UNIVERSITA' DEGLI STUDI DI MODENA E REGGIO EMILIA

DEPARTMENT OF ENGINEERING “ENZO FERRARI”

Ph.D. Course “Enzo Ferrari” in
Industrial and Environmental Engineering

Cycle XXXVII

Modeling and simulation of a small-scale side-by-side helicopter for Urban Air Mobility

Candidate: Francesco Mazzeo

PhD course coordinator:
Prof. Alberto Muscio

Supervisor:
Prof. Francesco Leali
Co-supervisors:
Prof. Alessandro Talamelli
Prof. Fabrizio Giulietti

Academic year 2024-2025

Modeling and simulation of a small-scale side-by-side helicopter for Urban Air Mobility
Author: Francesco Mazzeo
Supervisor: Prof. Francesco Leali
Co-Supervisors: Prof.Alessandro Talamelli, Prof. Fabrizio Giulietti
University of Modena and Reggio Emilia
Department of Engineering “Enzo Ferrari”
Via Pietro Vivarelli, 10, 41125 Modena, Italy

Abstract: Urban Air Mobility (UAM) is an advanced air transportation system for passengers and cargo that emerged in the last few years with the aim of moving part of urban transportation into the third dimension. Vertical Take-Off and Landing aircraft (VTOLs) are central to the UAM concept, because of their capability to operate within restricted areas and provide sustainable air transportation by addressing critical issues affecting modern society. While most of the research efforts have been dedicated to the conceptualization of multiple configurations and the analysis of conventional rotorcraft dynamics, a systematic approach for comparing different layouts and the definition of a modular tool for evaluating flight dynamics properties were still missing. To fill in this gap, this work aims to select, study, and evaluate the potential of a VTOL candidate, by providing a clear methodology to assess mission performance and stability characteristics. Starting from customer needs and project requirements, a set of analytical frameworks, based on momentum theory and semi-analytical models, are developed for designing propulsion systems and preliminary concepts. As a first step of the methodology, these tools are employed in the analysis of hybrid-electric powertrains, revealing that the optimization of the propulsion system must be aligned with the objective scenario in which the aircraft will be deployed. The second step is represented by a conceptual design study conducted by evaluating the endurance and range of three rotary wing configurations, i.e. a conventional helicopter, a multirotor, and a side-by-side helicopter: the analysis confirmed that the former remains the most efficient rotary wing layout, while a general discussion on the qualitative properties (design simplicity, societal acceptance, safety, noise..) of each VTOL, revealed that side-by-side rotors provide a more suitable balance between performance and inherent advantages. The core part of the thesis is focused on this last configuration and provides a flight dynamic analysis carried out on a small-scale prototype. The aircraft dynamics is described with two original modeling approaches: a 14 degrees of freedom (dof) analytical model and an advanced, 24 dof, numerical framework. While the first one is mainly adopted for steady-state computations and for evaluating the stability properties at variable forward flight conditions, the second provides deeper insights into the effect of rotor dynamics on rigid body stability and allows for cross-validation of the results. The identification of rotorcraft poles with the analytical approach verified the presence of standard aircraft dynamics, with slightly unstable phugoid and dutch-roll modes. The stability of these two oscillatory poles requires thorough investigation, as high forward speeds or unexpected center of gravity locations could result in dangerous lateral and longitudinal divergences. The numerical approach quantifies the beneficial effect of flap and lead-lag dynamics and addresses the negative influence of longitudinal inflow coupling. The manuscript converged on the side-by-side helicopter as a viable candidate for future UAM services among the considered layouts. The performance and dynamic properties revealed the potential of this configuration in a UAM context but also highlighted dangerous instabilities connected to specific flight conditions and rotor couplings. The innovative simulation platform and numerical tools developed in this study contribute to establishing a systematic research methodology that can be adapted for future evaluations of alternative VTOL configurations, the development of advanced control systems, and the execution of numerical simulations within a safe and controlled environment.

Keywords:
Urban Air Mobility, Flight Dynamics, Performance analysis, conceptual design, Simulation and modeling

Abstract (Ita.): La Mobilità Aerea Urbana (UAM) è un sistema avanzato di trasporto aereo per passeggeri e merci, nato negli ultimi anni con l'obiettivo di trasferire parte del trasporto urbano nella terza dimensione. Gli aeromobili a decollo e atterraggio verticale (VTOL) sono centrali nel concetto di UAM grazie alla loro sostenibilità e capacità di operare in aree congestionate. Nonostante la ricerca si sia finora dedicata principalmente a studi di design concettuale e dinamica di velivoli convenzionali, un approccio sistematico per confrontare diversi layout e un metodo per valutarne le proprietà dinamiche sono ancora carenti in letteratura. Al fine di colmare questa lacuna, questo lavoro si propone di selezionare, studiare e valutare il potenziale di un candidato VTOL, fornendo una metodologia per analizzare prestazioni di missione e stabilità. Partendo da esigenze della clientela e requisiti di progetto, vengono sviluppati una serie di strumenti basati sulla teoria del momento e modelli semi-analitici per progettare sistemi di propulsione e design preliminari. Come primo step della metodologia, questi strumenti vengono impiegati per l'analisi di sistemi di propulsione ibridi-elettrici, rivelando che l'ottimizzazione del sistema di propulsione deve essere allineata allo scenario operativo in cui l'aeromobile verrà impiegato. Il secondo passo consiste in uno studio di design concettuale che valuta autonomia e range di tre configurazioni ad ala rotante: un elicottero convenzionale, un multirotore e un elicottero side-by-side. L'analisi ha confermato la maggior efficienza del primo, mentre una discussione generale sulle proprietà qualitative (semplicità costruttiva, accettazione sociale, sicurezza, rumore, ecc) di ciascun VTOL ha evidenziato come una configurazione con rotori side-by-side offra un equilibrio più adeguato tra prestazioni e vantaggi intrinseci. La parte centrale della tesi si concentra su quest'ultima configurazione e fornisce un'analisi della dinamica del volo effettuata su un prototipo in scala. La dinamica del velivolo è descritta attraverso due approcci di modellazione: un modello analitico a 14 gradi di libertà (dof) ed uno numerico a 24 dof. Mentre il primo viene principalmente utilizzato in condizioni di trim e per valutarne la stabilità in volo rettilineo, il secondo offre una visione più approfondita dell'effetto della dinamica dei rotori sulla stabilità del corpo rigido e consente una parziale validazione dei risultati. L'identificazione dei poli del velivolo con approccio analitico ha verificato la presenza di dinamiche note per gli aeromobili, con modi oscillatori leggermente instabili come il fugoide e il dutch-roll. La stabilità di questi due poli deve essere attentamente calibrata, poichè un volo rettilineo ad alta velocità e/o la posizione del baricentro possono indurre pericolose divergenze laterali e longitudinali. L'approccio numerico quantifica l'effetto benefico delle dinamiche di flappeggio e brandeggio ed evidenzia l'influenza negativa dell'accoppiamento tra inflow longitudinale e stabilità dell'elicottero. La tesi converge, tra le configurazioni considerate, sull'elicottero side-by-side come candidato valido per i futuri servizi UAM. Le prestazioni e le proprietà dinamiche hanno rivelato il potenziale di questa configurazione nel contesto UAM, ma hanno anche evidenziato instabilità pericolose legate a specifiche condizioni di volo e accoppiamenti dei rotori. La piattaforma di simulazione e gli strumenti numerici sviluppati in questo lavoro contribuiscono alla definizione di una metodologia di ricerca sistematica, adattabile a valutare configurazioni VTOL alternative, progettare sistemi di controllo avanzati e condurre simulazioni numeriche in un ambiente sicuro e controllato.

Parole chiave:
Urban Air Mobility, Dinamica del volo, Analisi delle prestazioni, Design concettuale, Simulazione e modellazione

Acknowledgments

This study was carried out within the ”Programma Operativo Nazionale Ricerca e Innovazione” 2014-2020 (CCI 2014IT16M2OP005), resources FSE REACT-EU, Action IV.4 ”Dottorati e contratti di ricerca su tematiche dell’innovazione” and Action IV.5 ”Dottorati su tematiche Green”. The PhD scholarship was (co)funded by: ”PON Ricerca e innovazione” - ”Curti - Costruzioni Meccaniche S.P.A”. The project title was: ”Study and development of systems and technologies for the Urban Air Mobility”.

(ITA.) Tesi di dottorato di ricerca co-finanziata nell’ambito del Programma Operativo Nazionale Ricerca e Innovazione 2014-2020 (CCI 2014IT16M2OP005), risorse FSE REACT-EU, Azione IV.4 ”Dottorati e contratti di ricerca su tematiche dell’innovazione” e Azione IV.5 ”Dottorati su tematiche Green”.

A special acknowledgment to Curti S.p.A. for co-funding this Ph.D. studentship and for the continued support throughout the course of this research. The collaboration and commitment to advancing Urban Air Mobility have been fundamental in the successful development of this work.

Notation

A	State matrix
A_1, A_2	Constant coefficients for coupled flap and lead-lag dynamics
$\mathcal{A}_1$, $\mathcal{A}_2$	Viterna's post-stall lift curve coefficients
A_B, A_R, A_λ	Rigid body, rotor and inflow state matrices
AR	Blade's aspect ratio
A_r	Rotor disc area
a_w	Wake contraction factor due to shrouds
B	Control matrix
$\mathcal{B}_1$, $\mathcal{B}_2$	Viterna's post-stall drag curve coefficients
B_B, B_R, B_λ	Rigid body, rotor and inflow control matrices
c	Chord
C_0^b, C_0^c	Battery and cell nominal capacity
C_1, C_0	Coupling coefficients of the partially decoupled flap and lead-lag dynamic equations, in the numerical modeling approach
$\boldsymbol{C}_{aero} = [C_T\ C_{L^w}\ C_{M^w}]$	Aerodynamic coefficients vector, where C_T is the thrust coefficient while C_{L^w} and C_{M^w} are respectively the rolling and pitching moment coefficients
C_{D_2}, C_{D_1}	Pre-stall drag curve coefficients
$C_{D_{max}}$	Maximum airfoil drag coefficient
C_L, C_D	Lift and drag coefficients
C_{L_0}, C_{D_0}	Blade lift and drag coefficients at zero angle of attack
C_{L_s}, C_{D_s}	Blade lift and drag coefficients at stall angle of attack
C_{L_α}	Lift coefficient curve's slope in pre-stall region
$C_{m,x}$, $C_{m,y}$, $C_{m,z}$	Fuselage moment coefficients
C_{pr}	Profile power coefficient
C_T	Thrust coefficient
$C\text{-}rate$	Battery discharge rate
D	Coupling term of the second order ODE of the coupled flap-lead-lag dynamics, in the numerical modeling approach
D_f	Fuselage drag
dD, dL	Infinitesimal drag and lift of the blade section
DL	Disc loading
DoD	battery Depth of Discharge
$\boldsymbol{E}$	Excitation of the second order ODE of the partially decoupled flap and lead-lag dynamics, in the numerical modeling approach
e_0	Total hinge offset
E_b	Battery energy capacity
E_d	Battery energy density
e_F, e_L, e_P	Flap, Lag and Pitch hinges offsets
f, f_v	Equivalent flat plate frontal and vertical drag area
$\boldsymbol{F} = [X\ Y\ Z]$	Total external force: includes aerodynamic, centrifugal and inertial contributions
$\boldsymbol{F}_a$, $\boldsymbol{F}_i$, $\boldsymbol{F}_c$	Respectively: aerodynamic, inertial, and centrifugal forces in body f.o.r.
$\boldsymbol{F}_f$, $\boldsymbol{F}_g$	Fuselage and gravitational forces in body f.o.r.
g	Acceleration of gravity
h	Altitude
H_1, H_2, H_3	Analytical flap dynamic modeling matrices

$[H\ Y\ T]^{HW}$	Aerodynamic force in the hub-wind frame of reference (horizontal, lateral and thrust) in the analytical modeling approach
$\mathbb{I}_i$	Identity matrix of dimensions $i \times i$
I	Rotorcraft Inertia matrix
I_{xx}, I_{yy}, I_{zz}	Inertia moment wrt x_B, y_B and z_B axes
I_{yz}, I_{xz}, I_{xy}	Inertia product wrt x_B, y_B and z_B axes
i_s, i_c	Longitudinal and lateral hub incidence angles
k	Hybrid powertrain control factor
K_1, K_0	Constant matrices of the partially decoupled flap and lead-lag dynamic equations, in the numerical modeling approach
$k_{C_D,1}$, $k_{C_D,0}$	Correction coefficients for drag curve continuity
$k_{C_L,1}$, $k_{C_L,0}$	Correction coefficients for lift curve continuity
k_{ind}	Induced power factor
$K_{s\beta}$, $K_{s\xi}$	Spring restraint coefficients due to flap and lead-lag, respectively
$K_{t\beta}$, $K_{t\xi}$	Pitch-flap and pitch-lead-lag coupling ratios
K_v	Velocity ratio between the inlet and the outlet of the shroud
l_t	Distance between main and tail rotor centers
$[L\ M\ Q]^{HW}$	Aerodynamic moment in the hub-wind frame of reference (rolling, pitching, and torque) in the analytical modeling approach
LHV	Lower Heating Value
m_0	Empty mass
$\boldsymbol{M} = [L\ M\ N]$	Total external moment: includes aerodynamic, inertial and spring restraint contributions
$\boldsymbol{M}_a$, $\boldsymbol{M}_i$, $\boldsymbol{M}_s$	Respectively: aerodynamic, inertial and spring restraint moments in body f.o.r.
m_b	Battery mass
m_{bl}	Blade mass
m_c	Battery cell mass
m_e	Motor mass
m_{FC}	Fuel cell mass
$\boldsymbol{M}_f$	Fuselage moment in body f.o.r.
m_h	Mass of the hydrogen line
m_{H_2}	Hydrogen mass
m_{H_2res}	Hydrogen mass reserve
$m_{H_2,residual}$	Residual hydrogen mass
m_p	Maximum payload
m_{to}	Maximum take-off mass
$MTOW$	Maximum take-off weight
N_b	Number of blades
N_c	Number of blades' configurations
n_{cp}, n_{cs}	Number of parallel and series cells
P_b	Battery power
P_{BSE}, P_{BSR}	Power at the best specific endurance and best specific range
P_{FC}	Fuel cell power
$P_{FC_{max}}$	Maximum Fuel cell power
P_M, P_T	Main and tail rotor power
P_{max}	Maximum motor power
P_P, P_s	Parasite and systems power
P_{sh}	Power at the main shaft
P_{tot}	Total Power
$Q - F$	Excitation term of the second order ODE of the coupled flap-lead-lag dynamics, in the numerical modeling approach
R	Rotor radius
$\boldsymbol{r} = [r_x\ r_y\ r_z]$	Local blade section position wrt hub-body frame of reference

$\mathcal{R}_{n-m}$	Rotation matrix from the generic "m" to the "n" frame of reference
r_c	Blades' root cutout
$\boldsymbol{r}_{CP}$	Center of Pressure position wrt body axes frame of reference
Re	Reynolds number
r_G	Blade center of gravity linear coordinate from flap hinge
$\boldsymbol{r}_{HB}$	Hub position wrt body axes frame of reference
r_k	Duct lip radius
r_s	Blade section linear coordinate from flap hinge
S^f, S^s, S^t	Equivalent flat-plate fuselage surfaces
sls	Specific load factor
SoC	Battery state of charge
SP	Specific Power
T	Main rotor total thrust
T_c	Cruising time
T_{BSE}, X_{BSR}	Best specific endurance and best specific range
T_d	Rotor thrust due to shroud
T_{em}	Emergency landing time
T_t	Tail rotor thrust
T_{tot}	Mission duration
$\boldsymbol{U} = [u\ v\ w]$	Relative wind velocity expressed in body axes frame of reference
$U_\infty = \lvert\boldsymbol{U}\rvert$	Wind velocity magnitude
$\hat{\boldsymbol{U}} = \boldsymbol{U}/U_\infty$	Velocity versor
U_{BSE}, U_{BSR}	Best specific endurance and range velocities
U_v	Vertical speed
UED	Useful Energy Density
$\boldsymbol{V}_a$	Aerodynamic velocity at the blade section
$\boldsymbol{V}_g$	Gust velocity in hub-body f.o.r.
$\boldsymbol{V}_i$	Inertial velocity of the blade section
v_i	Induced inflow velocity
$v_{i_h} = \sqrt{\frac{MTOW}{2\rho A_r}}$	Induced inflow velocity at hover
v_{nom}	Nominal voltage
V_T	Tip speed
x	Generic state of the state vector
$\boldsymbol{x}$	State vector
$\hat{\boldsymbol{x}}$, $\hat{\boldsymbol{y}}$, $\hat{\boldsymbol{z}}$	Unit vectors perpendicular to the frontal, side and top surfaces of the fuselage approximation
X_{tot}	Mission range
$[x^B\ y^B\ z^B]$	Body axes frame of reference (f.o.r.)
$[x^{bl}\ y^{bl}\ z^{bl}]$	Local blade frame of reference (f.o.r.)
$[x^{HB}\ y^{HB}\ z^{HB}]$	Hub-body frame of reference (f.o.r.)
$[x^{HW}\ y^{HW}\ z^{HW}]$	Hub-wind frame of reference (f.o.r.)
$[x_G\ y_G\ z_G]$	Center of gravity (CG) coordinates in body axes f.o.r.
$\mathbb{Z}_{i\times j}$	Zeros matrix of dimensions $i \times j$

Greek symbols

α	Blade's angle of attack
α_f	Fuselage angle of attack
α_s	Airfoil stall angle of attack
α_T	Angle of attack of the tip-path plane
β	Flapping angle
β_f	Fuselage sideslip angle
$\boldsymbol{\beta} = [a_0\ a_1\ b_1]$	Vector of tip-path plane coordinates, thus coning angle (a_0), longitudinal (a_1) and lateral (b_1) disc tilt angles
β_w	Rotor sideslip angle
Γ	Rotor sense of rotation (-1 for clockwise, 1 for counterclockwise)
δx	Generic small perturbation
δ	Blade's tip clearance
δ_f	Blade's tip clearance factor

η_{DC}	DC-DC controller efficiency
η_m	Electric motor efficiency
η_M, η_T	Main and tail rotor transmission efficiency
η_{FC}	Fuel cell efficiency
η_ξ	Inertial force coefficient
θ_{bl}	Local twist angle
θ_w	Linear twist angle
λ_i	Induced inflow ratio in the analytical modeling approach
λ	Total inflow ratio in the analytical modeling approach
$\boldsymbol{\lambda} = [\lambda_0\ \lambda_s\ \lambda_c]$	Induced inflow ratio components: uniform (λ_0), lateral (λ_s) and longitudinal (λ_c) inflows in the numerical modeling approach
λ_m	Normal induced inflow due to the effect of rotor thrust
$\boldsymbol{\mu} = [\mu_x\ \mu_y\ \mu_z]$	Advance ratio
ξ	Lead-lag angle
$\boldsymbol{\xi} = [\xi_0\ \xi_c\ \xi_s]$	Rotor center of gravity coordinates: collective (ξ_0), advancing (ξ_c) and regressive (ξ_s) lead-lag
ξ_{in}, ξ_{out}	Inlet and outlet drag factor of the shroud
ρ	Air density
σ	Solidity ratio
$\boldsymbol{\tau}$	Control vector
$[\phi\ \theta\ \Psi]$	Euler's angles (roll, pitch, yaw)
ψ	Blade's azimuthal position
$\boldsymbol{\psi} = [\psi_1\ \psi_2\ \psi_3]$	Blades configuration
ψ_θ	Swashplate phase angle in the local twist definition
Ω	Rotor angular velocity
$\boldsymbol{\omega} = [p\ q\ r]$	Angular velocity in body axes

Superscripts

0	Trim condition
(1), (2)	Main rotor 1, and 2
B	Body frame of reference
b	Referred to the battery
bl	Local blade frame of reference
c	Referred to single cell
HB	Hub-body frame of reference
HW	Hub-wind frame of reference
e	Referred to the electric motor
f, s, t	Frontal, side and top equivalent flat-plate areas of the fuselage
fp	Referred to flat plate regime
p, i	Profile and induced power
$post$	Referred to post-stall regime
TPP	Tip-path plane frame of reference
TPP_w	Wind tip-path plane frame of reference
β	Referred to the flap dynamics
ξ	Referred to the lead-lag dynamics

Rotor controls

θ_0	Collective pitch control
A_{1s}	Lateral cyclic control
B_{1s}	Longitudinal cyclic control
ΔB_{1s}	Differential longitudinal cyclic control

Contents

Chapter 1

Introduction

1.1 State of the art of Urban Air Mobility

The global population reached 8 billion in 2022, with an average growth rate of approximately 1% per year in the last decade [1]. It was estimated by the Department of Economics and Social Affairs of the United Nations that 55% of the registered population (4.4 billion) is currently living in urban areas, a data that is expected to grow up to 70% in 2050 [2] (Figure 1.1). By assuming a constant growth rate, the world's inhabitants should reach approximately 10.7 billion in 2050, with 7.5 of them living in metropolitan regions. The overpopulation of cities is an alarming phenomenon that lies at the basis of many problems affecting modern societies. The increase in vehicle density is proportional to the number of traffic jams, leading to a degradation of the air quality, noise pollution, and climate change. The actual infrastructure capacity is put under pressure by the higher demand for public services and the constant need for renovation and maintenance. Overpopulation is also a factor in the reduction of life quality and possible rise of informal settlements in and around urban environments. The inevitable prospect of overpopulation makes a profound renewal of the urban and regional transport system, as well as infrastructure and services, necessary. Advanced Air Mobility (AAM) is a new concept of air transportation, which aims at moving part of the actual transportation methods into the third dimension. AAM promotes the emerging aviation markets and supports the next generation of sustainable aircraft: Unmanned Aerial Systems (UAS), autonomous vehicles, and Vertical Take-Off and Landing (VTOL) are the main characters of the AAM vision. Urban Air Mobility (UAM) is a branch of the AAM concept, which focuses on providing services for passengers and cargo in and around densely populated areas. According to the definition provided by the European Union Aviation Safety Agency (EASA), *"UAM is a new safe, secure and more sustainable air transportation system for passengers and cargo in urban environments, enabled by new technologies and integrated into multimodal transportation systems"* [3].

Figure 1.1: Urban Air Mobility in modern societies: critical issues and population growth

The main objective of UAM is to integrate aviation methodologies into urban environments, providing a faster, cleaner, and more efficient transportation method, enhancing connectivity between urban centers and regional areas, and impacting positively the global society. The services provided by UAM range from private air taxis to short- and long-range commuters, as well as last-mile delivery, cargo and medical transport, emergency services, and access to remote areas [4]. Adopting a UAM ecosystem in modern society would significantly reduce the average travel time and impact the amount of traffic congestion, which is responsible for noise pollution and low air quality. It has been estimated that 15 to 40 minutes could be saved on average on a standard city travel time and more than 70% of time could be saved for emergency and medical delivery [3]. Preis *et al.* [5] carried out an extensive analysis of the potential benefits in terms of time and energy savings of an efficient UAM ecosystem integrated into urban environments. In their study, the feasibility and actual advantage of different VTOL configurations were analyzed at a conceptual level by considering an entire fleet over thousands of UAM trips. It is concluded that UAM can potentially provide several advantages in those terms, but the effective gains are strictly related to the proposed mission.

Urban Air Mobility has the aim of promoting safety and security, and reduce the risk of fatal accidents. To this extent, Cokorilo [6] reviewed the main safety challenges linked to UAM, highlighting how technology innovation and safety rules play a fundamental role in guaranteeing the maximum level of safety during air transportation. Vehicle communication and advanced air traffic management systems will be fundamental to this goal. It was stated that 68% of aircraft accidents are caused by human factors: according to that, automation will play a crucial role in guaranteeing safety standards [7].

Sustainability is of primary importance. In 2022, the International Energy Agency (IEA) [8] affirmed that the transportation industry accounted for 23% of the global greenhouse gas emissions, having a great impact on climate change. Since UAM introduces new means of transportation, zero-carbon impact is a key requirement for aircraft operating in this context. A huge research effort is dedicated to studying new propulsion systems, such as hybrid and electric configurations, with the aim of providing an alternative to classical fossil fuel-based powertrains associated with significant CO_2 emissions. A consistent part of this thesis will be dedicated to this topic.

Urban Air Mobility will have a significant impact on the global market as well [9]. It is expected that 90000 jobs will be generated by 2030 by UAM [3] and global investments could create a \$1.5 trillion market by 2040 [10]. The NASA market study on Urban Air Mobility (UAM) [11] explores the potential economic impact of integrating UAM services, focusing on three primary markets: Airport Shuttle, Air Taxi, and Air Ambulance. The study estimates that in an unconstrained scenario, where regulatory, weather, and infrastructure challenges are minimized, the total available UAM market in the U.S. could reach from \$2.5, in the near term, to \$500 billion in a longer timescale. Key findings include:

- Economic Viability: The Airport Shuttle and Air Taxi services are identified as the most viable near-term markets, with significant potential for growth as infrastructure develops and costs decrease;
- Barriers to Adoption: High initial service costs, regulatory hurdles, public perception issues, and technological limitations (e.g., battery performance for eVTOLs) present major obstacles. Additionally, adverse weather conditions and air traffic management challenges could affect UAM operations.
- Infrastructure Needs: Expansion of vertiports and integration with existing transportation networks are critical for UAM scalability. Initial operations may rely on existing heliports and airports.
- Long-term Outlook: The market could expand with advancements in automation, battery technology, and favorable regulatory changes. Public acceptance and environmental

concerns, such as noise and emissions, will play a key role in the long-term success of UAM.

Overall, NASA highlighted the potential for UAM to revolutionize urban transportation but underscored the need for coordinated efforts between industry stakeholders, regulatory bodies, and the public to address the existing challenges [12].

When discussing Urban Air Mobility, it is more appropriate to refer to a UAM ecosystem. The general vision of UAM includes not only the aircraft providing services but also specific players and frameworks that enable the entire system to work properly. Some of these players are summarised in Figure 1.2

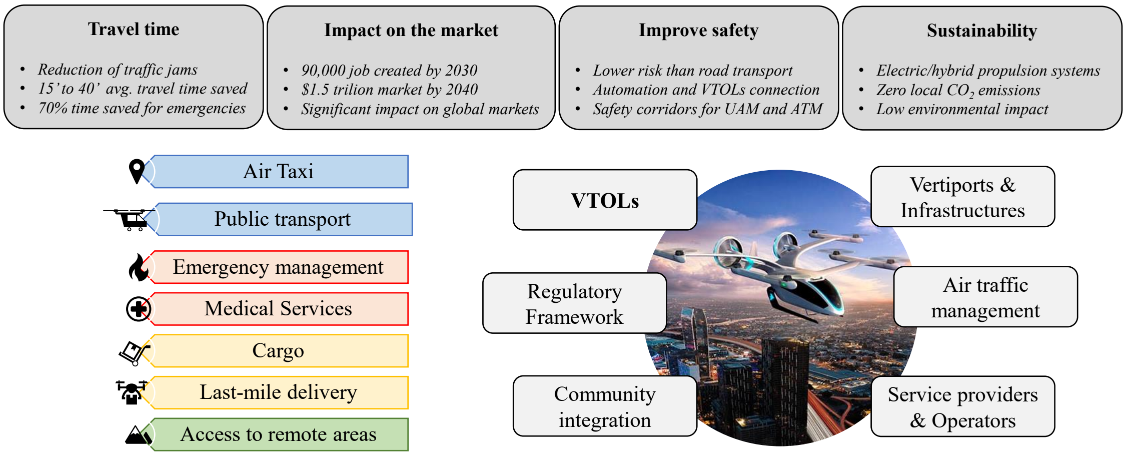

Figure 1.2: The Urban Air Mobility ecosystem: players, services and advantages.

- **VTOLs**: Vertical Take-Off and Landing aircraft are the major enabling factor for UAM. The whole ecosystem orbits around VTOLs and users' needs, with single players contributing to allow aircraft to operate in urban environments in the safest and most efficient way. This player will be further analyzed later in this Section.
- **Infrastructures and vertiports**: An extensive infrastructure network is essential for the successful integration of UAM services. UAM operations are carried out within specialized takeoff and landing facilities known as Vertiports, which provide charging, refueling, maintenance, and passenger handling services [13]. They can be further classified into vertihubs, vertipads, and standard vertiports based on their size and functionality (see Figure 1.3). Vertihubs are larger facilities located in central, high-traffic areas, serving as major transit points with multiple landing pads, passenger terminals, and maintenance stations. Vertipads, on the other hand, are smaller, single-landing sites designed for quick, on-demand services in decentralized or remote locations, offering minimal infrastructure. Standard vertiports fall between these two, supporting moderate traffic with basic services. Together, these infrastructure components form an integrated network that enables efficient, safe, and scalable UAM operations, connecting urban centers and regional areas. Private companies like Skyport, are collaborating with public entities and industrial partners to create vertiport networks in strategic locations [14].

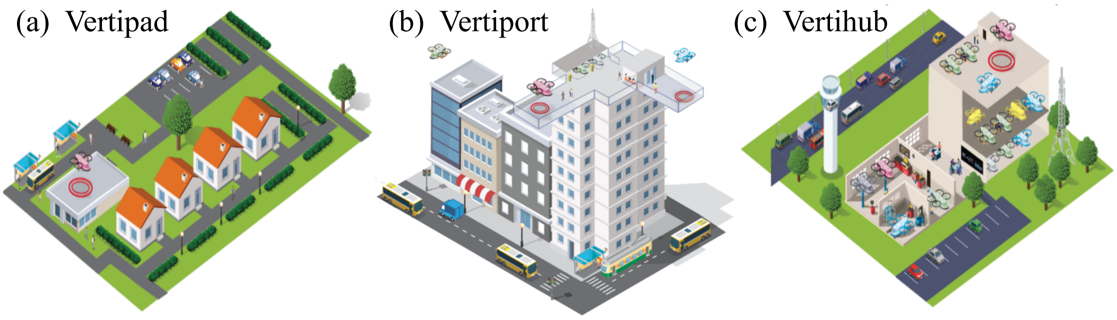

Figure 1.3: Conceptual design of different sizes' vertiports. [13]

- **Air traffic management**: air traffic management plays a crucial role in UAM ecosystems. Even if UAM operations will be carried out at relatively low altitudes and within urban and high-density regions, the integration with commercial aviation and UAS services will be fundamental to guarantee the maximum level of safety and efficiency [15]. In this context, the Federal Aviation Administration (FAA) released in 2023 the UAM concept of operations (ConOps) to support the development of new UAM ecosystems [16]. In their vision, UAM services will be carried out within specific "corridors" that enables an high density of complex operations. Aircraft must have the capability to communicate with each other, avoiding collisions without the need of an external air traffic controller, both in a piloted and an autonomous version. The introduction of remotely piloted and autonomous vehicles would certainly ease this task. Bauranov *et al.* [17] analyzed different airspace concepts to manage AAM traffic in urban environments, categorizing them according to safety, social, system, and aircraft parameters. They concluded that extensive ground infrastructures and further technological developments are fundamental to guarantee basic services and aircraft separation. [14].

Figure 1.4: UAM ecosystem illustration from NASA ATM-X project [18]

- **Service providers**: these entities and companies are responsible for enabling UAM operations and proper user experience. They include aircraft operators, air traffic and fleet management services, infrastructure developers, digital platform providers, navigation and surveillance services, energy providers, maintenance services, entities that guarantee compliance with safety standards, certifications, etc. Additionally, service providers facilitate integration with existing urban transportation networks and support critical infrastructure like vertiports and charging stations. By delivering reliable and efficient services, they help build public trust, enhance operational efficiency, and drive the adoption of UAM, making them a vital component in the growth of this emerging market [19].
- **Regulatory framework**: the development of a solid regulatory framework for a UAM ecosystem is essential to ensure safety, service efficiency, airworthiness, noise levels, and environmental impact. The primary focus areas of current regulations include establishing design standards, defining operational requirements, managing air traffic, and setting pilot certification criteria [20]. Regulatory bodies are also working on guidelines for vertiport infrastructure and the integration of eVTOLs into both controlled and uncontrolled airspace. In 2022 EASA released the world's first specifications for vertiport design (PTS-VPT-DSN), offering detailed descriptions of the physical characteristics of a vertiport, the necessary obstacle clearance zones, visual guidance systems etc. [21]. The FAA (Federal Aviation Administration) is the largest transportation agency in the United States, directing all aspects related to civil aviation in the country and over surrounding international waters. The FAA emits the FARs (Federal Aviation Regulations), which govern all aviation activities in the U.S., including Unmanned Aircrafts Systems (UAS) and VTOLs. The applicable parts for UAM are Parts 23, 27, 29, 33, 35, 61, 135. On the other hand, EASA is the European authority responsible for civil aviation safety, regulation, and certification. In 2019 it published the first complete set of dedicated technical specifications in the form of a Special Condition (SC) for VTOL aircraft, to establish the standards for the type certification of this type of product [22]. The special condition has been lately updated and the latest issue was released in 2024. The most relevant technical specifications for UAM are CS-23, CS-27, CS-29, CS-36, CS-P, CS-E, CS-VLR, and CS-UAS (which is specific for UAS). Lately, in 2023, EASA published 4 Means of Compliance (MOCs) [22] to address the applicants' requests for clarification on the objectives and standards set in the Special Condition for VTOL. Apart from several definitions, the two MOCs provide further specifications for the following aspects of VTOL vehicles for UAM: handling qualities, structural design, flight loads, risk analyses etc.
- **Community integration**: the integration of the community in UAM is probably the most complicated aspect of the ecosystem. It is fundamental to work on a solid societal acceptance of the users and citizens integrated into the environment where UAM operates [23]. According to the EASA survey on this matter [24], safety, noise, and emissions are the major concerns for European citizens. On the other hand, the solutions of UAM to reduce travel time, traffic jams, and air pollution were seen as attractive perspectives. The adoption of design features to address these criticalities is mandatory: ducted rotors, sustainable propulsion systems, low-noise rotors, and certified structures are some examples. In addition, social equity is another topic of concern: current on-demand aviation services are seen as expensive solutions dedicated to users with higher incomes and business travelers [25]. The objective of making UAM affordable to the majority of the population is another crucial point that involves an in-depth analysis of business models, operating and maintenance costs, and design optimization. Social equity is also one of the key findings of Shaheen's work on societal barriers to the adoption of UAM [26]. In the work, the authors highlighted how familiarity with UAM and classical aviation may decrease the general concern about safety and efficiency. A similar analysis was carried out by Çetin *et al.* [27] on the topic of drones and UAS flying at low altitudes. While VTOLs are expected to fly

through hypothetical corridors below general aviation, services such as last-mile delivery and cargo are provided by smaller aircraft that interact with ground activities.

The main characters of the UAM ecosystem are the Vertical Take-Off and Landing (VTOL) aircraft. Usually denoted as eVTOL or hVTOL (electric and hybrid VTOL), these vehicles are characterized by the ability to take off, land, hover, and fly vertically with the adoption of specific devices such as rotors and propellers. This allows operating in confined spaces, where the high urban density demands versatile and compact transportation solutions. VTOL aircraft can bypass road congestion, reduce travel times, and connect urban centers with remote locations. It plays a critical role in the development of efficient, sustainable, and accessible urban transportation networks. By leveraging innovative propulsion technologies, VTOLs also contribute to reducing noise and emissions, aligning with the sustainability goals of future UAM systems. VTOLs can be classified by their lift and thrust production systems: while the lift force sustains the aircraft weight during flight, thrust devices provide the necessary force to cruise and maneuver. These two forces can be generated by the same system or by separate ones.

- **Multirotor**: in this category, a set of fixed propellers with variable RPM control provides both lift and thrust during all flight phases. Multirotor are characterized by a rather simple mechanical design and large disc loadings, which make them suitable for hovering flight and less efficient in cruise [28]. Some examples of multirotor VTOLs are the Volocopter VoloCity [29], the EHang AAV [30] and the AIRBUS CityAirbus technology demonstrator [31]. Drones and small UAS fall into this category as well. Their role in a UAM ecosystem is fundamental for services such as goods delivery, cargo transportation, and inspections.

Figure 1.5: Multirotor VTOLs: Volocopter VoloCity (a) [29], EHang AAV (b) [30], hexacopter drone (c) [32]

- **Helicopters**: conventional helicopter can be included in the VTOL definition. As a matter of fact, the classical helicopters are the very first example and mostly adopted case of aircraft capable of hover and vertical flight. Even if their mechanical design is more complicated than a multirotor, the higher efficiency and different control methods have made this configuration the very first UAM rotorcraft. Apart from their military application, helicopters are widely used in a large amount of UAM applications such as emergency and rescue, business transportation, inspections, cinema, security, and private uses. Helicopters are characterized by a set of rotors providing both lift and thrust, controlled with a constant RPM and variable pitch system. While the conventional layout is characterized by a single main rotor with an anti-torque system mounted on the tail, tandem helicopters such as the Boeing CH-47 Chinook, side-by-side or coaxial configurations are also included in this category.

Figure 1.6: Helicopter VTOLs: Leonardo AW139 (a) [33], Boeing CH-47 Chinook (b) [34], Kamov Ka-27 (c) [35]

- **Lift+cruise**: this category adopts three separate systems for producing lift and thrust at different flight phases. A set of vertical propellers is adopted for producing lift during hover, take-off, landing, and vertical flight, while one or more horizontal propellers are adopted for producing thrust during cruise. Lift+cruise is equipped with fixed wings and aerodynamic surfaces to produce lift during the cruise and control the vehicle like a normal fixed-wing aircraft when flying at a high enough speed. With respect to the tiltrotor and tiltwing categories, lift+cruise have fixed wings and fixed propellers, which operate only during specific flight phases and transition periods. The propellers have a fixed pitch and they are controlled with a variable RPM control system. The aircraft is then controlled with a proper mix between aerodynamic surfaces and propellers RPM. Examples of lift+cruise VTOLs are the recently revealed AIRBUS NextGen [36], the Uber Elevate eCRM concepts [37] and the experimental Wisk 5$^{\text{th}}$ Generation [38] ("Kitty Hawk").

Figure 1.7: Lift+cruise VTOLs: AIRBUS NextGen (a) [36], Uber Elevate eCRM-003 concept (b) [39], Wisk 5$^{\text{th}}$ Generation "Kitty Hawk" [38]

- **Tiltrotors**: together with the helicopter, this is one of the most well-established VTOL configurations, and probably one of the most promising for future UAM transport. In this layout, two separate systems are used to provide lift and thrust at different flight phases. In particular, a set of tilting rotors is used in vertical flight to provide lift and thrust, while during a cruise a fixed-wing generates the necessary lift. The rotors can be either fixed or variable pitch and can operate at both constant or variable RPM. The characteristic of this vehicle is the capability of tilting the rotors to adapt the layout for hovering and cruise phases, where in the latter case rotors provide only thrust. The aircraft is controlled with a mix of rotor controls and aerodynamic surfaces, which is adapted for the actual flight phase. While they have been already adopted for a lot of military purposes (see for example the Leonardo AW609 [33] or the Boeing V-22 Osprey [40]), in the last few years tiltrotors are gaining popularity in civil applications due to their VTOL characteristics and average efficiency in both hover and cruise. Even if the tilting mechanism brings with it several complexities, this particular design has been exploited by important companies all over the world to propose their conceptual design and first prototypes. Examples of tiltrotor are the Archer VTOL [41], the Vertical Aerospace VX4 [42], the Joby S4 [43] or the Wisk 6th Generation [44].

Figure 1.8: Tiltrotor VTOLs: Vertical VX4 (a) [42], Leonardo AW609 (b) [33], Joby S4 (c) [43]

- **Tiltwings**: similar to tiltrotors, the tiltwings provide lift and thrust with two separate systems, a set of rotors or propellers and a set of fixed wings. What differentiates this configuration is the mechanism that rotates the rotors together with the wings. Tiltwings are also called "vectored thrust" since they provide propulsive forces with a set of distributed rotors along the blades. The Lilium Jet [45] and the Dufour Aero2 [46] are examples of this VTOL type.

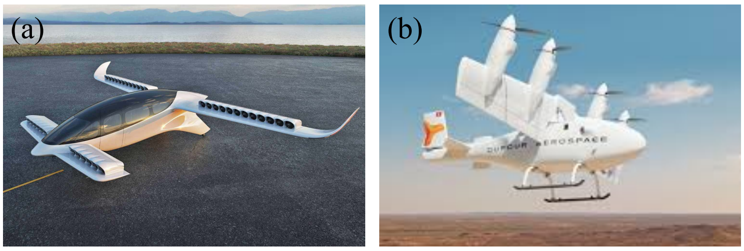

Figure 1.9: Tiltwing VTOLs: Lilium Jet (a) [45], Dufour Aero2 (b) [46]

In the last few years, the Vertical Flight Society (VFS) has created a detailed list of the designed and conceptualized VTOLs over history. The directory can be found in Ref. [39], along with datasets and additional information.

1.2 Objectives and motivation

Urban Air Mobility is emerging as a transformative solution to urban congestion, offering a third dimension to transportation that aims to enhance mobility efficiency, reduce emissions, and improve safety. The integration of VTOLs within urban environments presents several technological and operational challenges, ranging from vehicle design to infrastructure development and regulatory considerations. Due to the growing interest in this new transportation perspective, conceptual design, performance studies, and state-of-the-art analyses have become the main topics around which researchers and engineers have focused their energies in the last few decades. The analyses of Long *et al.* [9] and Cohen *et al.* [25] have provided a broad view of the conceptual UAM ecosystem, while Rothfeld [47] described the current state of the art of UAM technologies and the potential impact on modern societies. In parallel with the review studies about current technologies, the first step in the UAM research was provided by the conceptual design and performance studies carried out by Johnson. These works had the aim of providing preliminary results on the capabilities of multiple VTOL configurations, by studying their power, endurance, and range along specific mission scenarios. In Ref. [48], Johnson *et al.* designed and compared different conceptual VTOLs by analyzing the performance of electric, hybrid, and turboshaft propulsion systems. Power requirements, payload, and range capabilities are estimated on a regular UAM mission scenario [49]. Similar analyses were conducted by Kadhiresan *et al.* [50] and Palaia *et al.* [51], but without converging to a unique solution for UAM transport. The methodology behind these studies is mostly based on scaling design methods which allow to determination of the constructive parameters of different VTOLs. As a result, the performance studies compare rotorcraft having different architectures, payload capabilities, and propulsion systems. This approach leads to meaningful results on the specific aircraft designed but does not provide a clear answer on which configuration, or propulsion system, has to be selected when designing a VTOL to satisfy specific mission requirements. Similarly, Bacchini and Cestino [28], analyzed with an analytical approach the theoretical performance of multiple VTOLs available on the market, assessing which are the optimal configurations for specific missions, but without providing a solid design methodology that allows comparing VTOLs of similar characteristics. Despite these efforts, there is still little agreement on the optimal configuration for UAM operations, as mission-specific constraints play a significant role in determining the most suitable aircraft layout. Previous works have highlighted that the selection of an appropriate VTOL strongly depends on the operational scenario, with trade-offs existing between efficiency, safety, and sustainability. In addition, while numerous studies have assessed these trade-offs from a performance perspective, very few have examined them from a flight dynamics and control standpoint. Following the completion of the preliminary analysis stages, research efforts of the last few years are increasingly directed toward addressing specific and detailed aspects of VTOL design, such as structural design, aerodynamics, control, and flight dynamics. These aspects are critical for transitioning from theoretical and preliminary studies to practical, refined, and efficient VTOL solutions. For the sake of this thesis, flight dynamics is the aspect with the major interest. Research studies on this topic, applied specifically to VTOLs designed for the UAM are quite scarce and most of the efforts have been dedicated to classical configurations such as conventional helicopters [52]–[55], multirotor [56]–[59], and a few studies on tiltrotor or alternative layouts [60]–[63]. Alternative designs are relatively underexplored from this point of view and it is still unclear which of them provides the most promising results in terms of performance and flight dynamics characteristics.

The absence of a systematic approach to designing, comparing, and selecting an optimal VTOL configuration, combined with the limited flight dynamics studies on alternative designs, has prompted the formulation of specific research questions to address these research gaps. First, what are the main users' needs that a VTOL must satisfy to become a viable UAM transport solution? And what are the technical requirements correlated with these customer needs? Once the project requirements are established, the research methodology in this work initially focuses on the propulsion system type and aircraft configuration, as these are the primary factors influencing VTOL performance at the conceptual design stage, as highlighted in Johnson's studies. Considering a baseline configuration, how do different propulsion system architectures influence the overall performance and operational feasibility of a UAM rotorcraft? Which of the analyzed powertrains is suitable for a specific transportation service? These questions are fundamental to setting the basis of a conceptual design methodology constructed around a specific sustainable VTOL that ranges around the performance of that specific propulsion system. In this context, what are the main requirements to design different but comparable VTOLs starting from an initial benchmark? And among the considered ones, which one mostly suits with the UAM mission objectives both from a performance and a qualitative point of view? The evaluation of these inquiries with an analytical and systematic approach leads to the selection of a specific VTOL configuration that satisfies most of the requirements set by the industrial partner and the customer's needs. Advanced modeling and simulation are then required to characterize the VTOL from a flight dynamics point of view and to build up a numerical platform for testing and evaluating the capabilities under specific flight conditions. The first research question to address is what are the key mathematical tools required to evaluate VTOL trim, stability, and flight dynamics properties in realistic urban environments? Considering the different tools developed in this study, what are the main differences between them? And in which cases an advanced modeling approach is required to capture specific dynamic behaviors? In order to characterize the rotorcraft dynamics, which are the trim solutions at specific flight conditions, and which are the most critical instabilities arising from the analysis?

Considering the current state of the art of UAM and flight dynamics of alternative VTOL configurations, the above-mentioned research questions are still unresolved. For this reason, the thesis has the aim of studying, selecting, and evaluating viable candidates for specific UAM scenarios from a performance point of view and then focusing on its inherent flight dynamics properties. The work can be organized into three main objectives, strictly connected by the methodology and global aim of the thesis:

1. Evaluate the performance of multiple sustainable propulsion systems in a UAM context (fuel cell hybrid and battery-electric), and select a specific powertrain for conceptual design;
2. Compare different (rotary wing) VTOL configurations at a conceptual design stage and select a viable candidate for UAM services. The selection is made according to both quantitative and qualitative factors;
3. Develop and apply original mathematical tools for the simulation and study of the selected rotorcraft's trim, stability, and flight dynamics characteristics.

The expected output is a numerical platform, suitably developed for a specific configuration, that can be adapted for simulating UAM missions and studying the VTOL behavior. This thesis contributes to the scientific community by developing a systematic methodology for evaluating VTOL flight dynamics, integrating conceptual design and performance studies. By advancing the understanding of alternative VTOL designs, this research enhances the ability to design, model, and simulate, rotorcraft for UAM, promoting the development of the next generation of sustainable urban air transport solutions.

Chapter 2

Methodology

2.1 Methodology description

As already mentioned in Section 1.2, the objective of this thesis is to perform an in-depth analysis of the performance, capabilities, and flight dynamic characteristics of a potential candidate for Urban Air Mobility services. The methodological framework is structured into steps that integrate design considerations, analytical modeling, numerical simulations, and performance analyses. Each step builds upon the previous one, ensuring a systematic approach to achieving the research objectives. The flow chart in Figure 2.1 depicts this process. The analysis starts with an in-depth study of the current state of the art of Urban Air Mobility worldwide. Latest technological advancements and innovative configurations are considered as well as the current state of the regulations governing this new transportation sector. This initial stage of the methodology has the objective of providing a clear vision of the environment within which the adopted solutions will be deployed, understanding their limitations and principal research gaps to satisfy. In the second stage of the technical work, a set of requirements is defined by considering mission objectives and customer needs integrated with the "House of Quality" technique. A baseline configuration is selected at this stage, in order to carry out the following analyses. For the sake of this work, a conventional helicopter configuration is selected.Conceptual design and performance analysis are then required to define the potential candidate and its general characteristics for fulfilling UAM services. In particular, the propulsion system and configuration are the main arguments to discuss. The powertrain architecture is analyzed at first since this is the main factor that affects the aircraft's performance. A finite number of sustainable candidates is selected among all propulsion system solutions and analyzed with suitable models. Endurance, range, and power requirements are estimated for the baseline configuration with different propulsion layouts along specific UAM mission scenarios, properly designed to meet customer needs. The aim of the analysis is to select the powertrain configuration that will be adopted for the rest of the work. The second stage of the performance analysis is the conceptual design and comparison of alternative VTOL configurations: starting from the baseline design, different solutions are produced at a conceptual design stage, and their performance are computed along one specific UAM mission. A qualitative discussion on societal acceptance, noise emissions, safety, and design simplicity follows the calculations and allows for selecting one among the analyzed cases. Chapter 3 develops this part of the methodology. For the sake of this work, three plug-in hybrid helicopters powered by hydrogen fuel cells and a full battery-electric one are compared along three UAM mission scenarios with an analytical modeling approach. A similar mathematical framework is employed to design and compare the performance of three VTOL configurations: a conventional helicopter, a multirotor, and a side-by-side VTOL. Both quantitative results and intrinsic advantages are evaluated for selecting a battery-electric side-by-side configuration as representative for the next phases of this thesis. As soon as this step is completed, an in-depth modeling and simulation campaign is conducted to study the trim, stability, and flight dynamics characteristics of the selected VTOL. According to the requirements set for the mathematical frameworks, a simulation platform is developed: fuselage, shrouds, and blades' aerodynamics are modeled with semi-analytical, numerical, and experimental datasets.

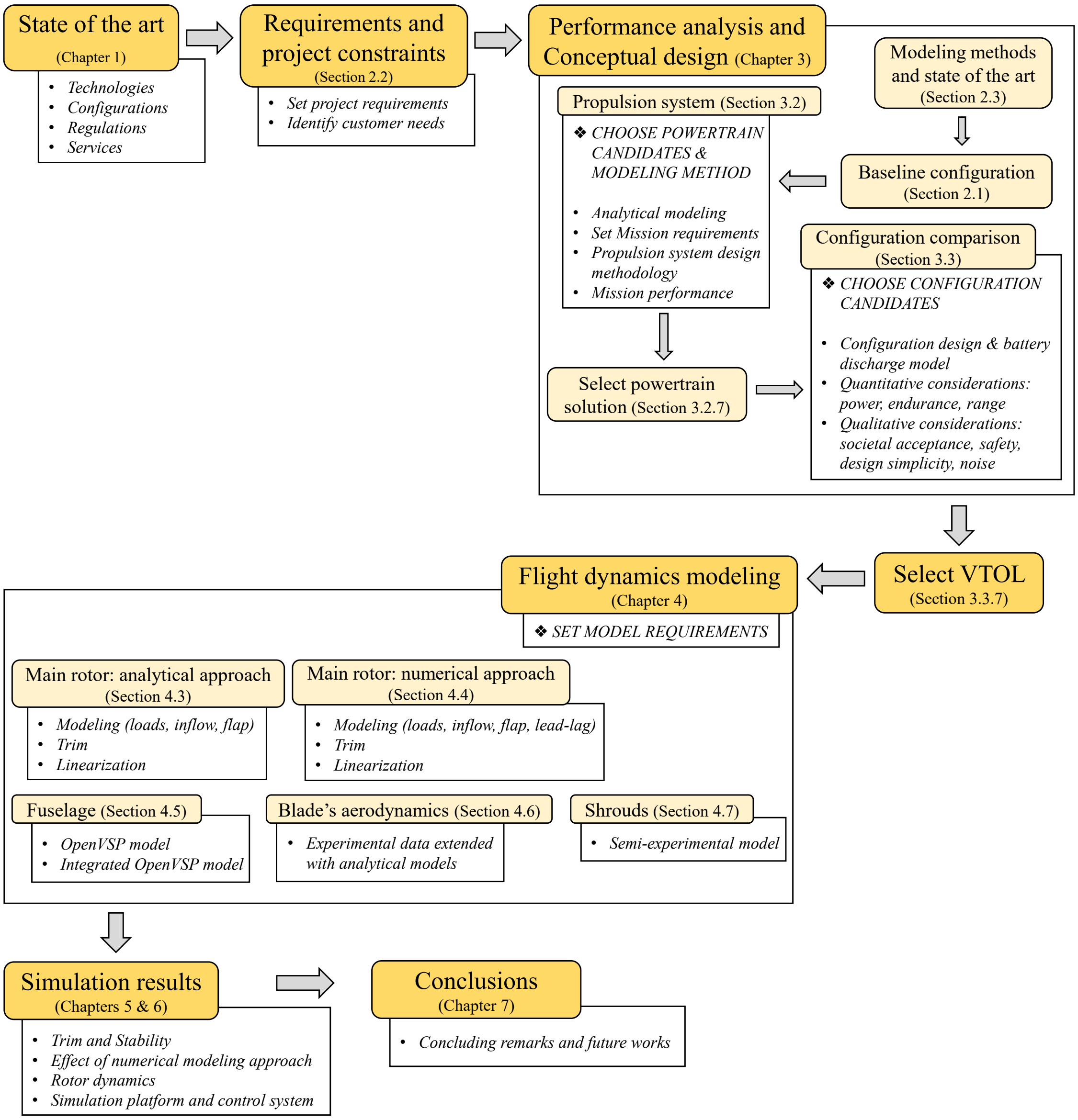

Figure 2.1: Flow chart of the project methodology

Concerning the main rotor, two different approaches are adopted: analytical and numerical. An analytical modeling approach is employed for describing a simplified mathematical framework based on a reduced number of degrees of freedom, where the rigid body dynamics is integrated with first-order uniform inflow dynamics and second-order flap dynamics. A numerical modeling approach is employed for developing an advanced mathematical framework, based on a higher number of degrees of freedom where the rigid body dynamics is integrated with first-order nonuniform inflow dynamics, second-order flap, and second-order lead-lag dynamics. This second approach requires advanced trim and linearization techniques that are suitably developed for this thesis. Chapter 4 develops this stage of the methodology, proposing 14 and 24 dof analytical and numerical models, developed for a small-scale side-by-side helicopter. The modeling section has the aim of providing a solid simulation platform for VTOLs and producing insights about their trim, stability, and dynamic properties. Trim curves are studied together with static stability and effects of forward speed and center of gravity position are accounted. In addition, the comparison between the modeling approaches provides fundamental remarks about the necessary degrees of freedom for modeling and replicating VTOL flight dynamics. Rotor dynamics and rotor stability are computed as well, by addressing the issues of rigid body and rotor dynamic coupling with a 38-state-space linear representation. The methodology ends up with concluding remarks and future works.

2.2 Requirements and project constraints

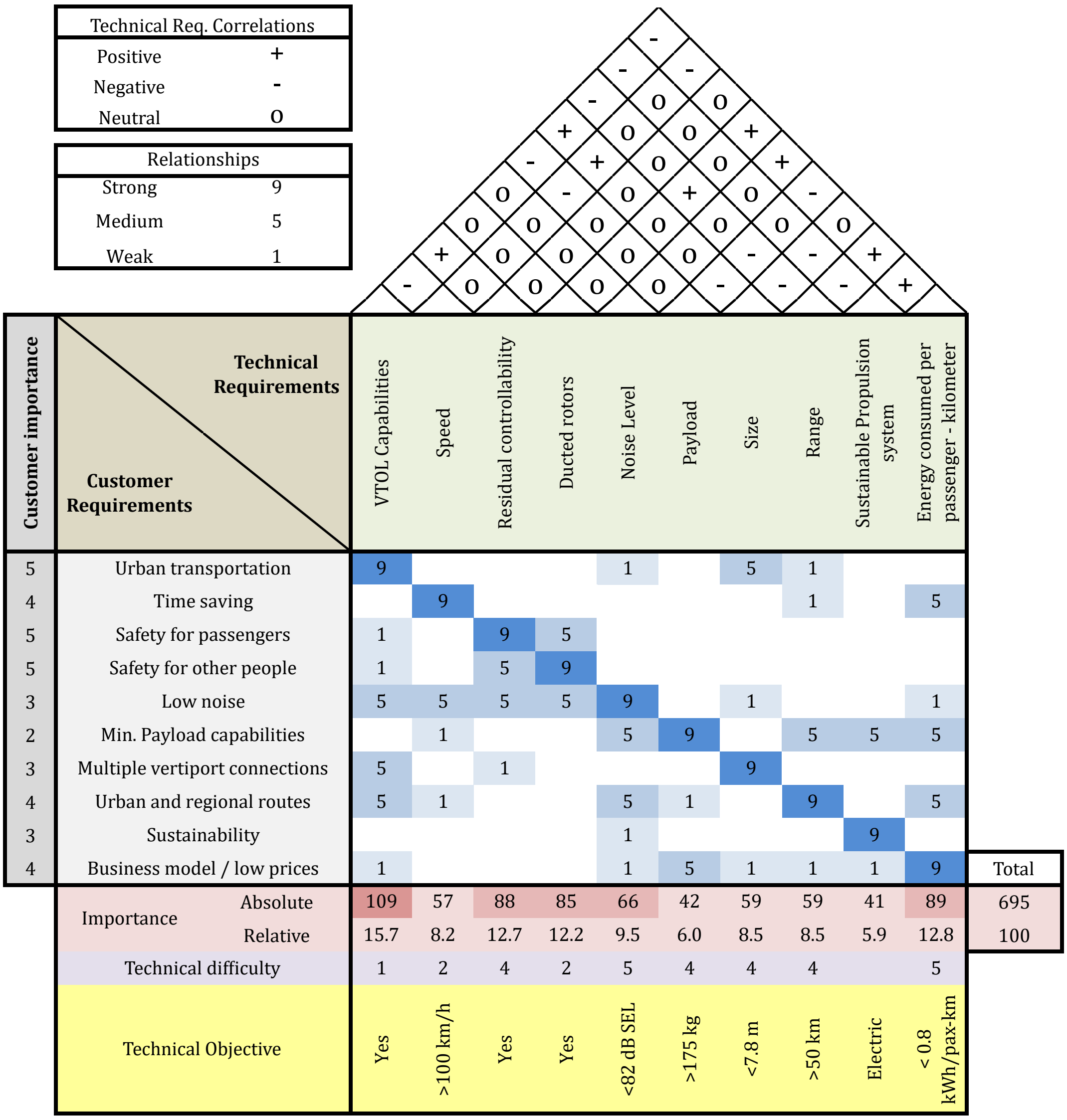

Technical Req. Correlations	
Positive	+
Negative	-
Neutral	o

Relationships	
Strong	9
Medium	5
Weak	1

Customer importance	Technical Requirements / Customer Requirements	VTOL Capabilities	Speed	Residual controllability	Ducted rotors	Noise Level	Payload	Size	Range	Sustainable Propulsion system	Energy consumed per passenger - kilometer	
5	Urban transportation	9				1		5	1			
4	Time saving		9						1		5	
5	Safety for passengers	1		9	5							
5	Safety for other people	1		5	9							
3	Low noise	5	5	5	5	9		1			1	
2	Min. Payload capabilities		1			5	9		5	5	5	
3	Multiple vertiport connections	5		1				9				
4	Urban and regional routes	5	1			5	1		9		5	
3	Sustainability					1				9		
4	Business model / low prices	1				1	5	1	1	1	9	Total
Importance	Absolute	109	57	88	85	66	42	59	59	41	89	695
	Relative	15.7	8.2	12.7	12.2	9.5	6.0	8.5	8.5	5.9	12.8	100
	Technical difficulty	1	2	4	2	5	4	4	4		5	
	Technical Objective	Yes	>100 km/h	Yes	Yes	<82 dB SEL	>175 kg	<7.8 m	>50 km	Electric	< 0.8 kWh/pax-km	

Figure 2.2: House of quality for the conceptual design of a VTOL for UAM services.

General requirements and project constraints adopted for selecting the most suitable aircraft for UAM services are summarised in this Section by adopting an essential tool of the Quality Function Deployment (QFD) methodology [64]: the House of Quality (HoF). This technique, reported in Figure 2.2, enables the systematic translation of customer needs into technical requirements, grading the product's specifications by their level of importance and technical difficulty. In this section, a HoQ analysis for an electrical VTOL designed for Urban Air Mobility (UAM) is presented, ensuring alignment between user expectations and engineering solutions. The target users are civilian passengers adopting an air taxi service to travel in and around urban areas: the customer needs and their level of importance can change if different targets are selected.

The analysis begins by identifying the key customer needs and their importance level in agreement with the current state of the art [11], [24] and recent surveys on the population. It was observed that the main property that a UAM vehicle must have is the capability to perform fast and sustainable urban transportation while maintaining high levels of safety. These and other customer needs, are translated into the most relevant technical requirements at the top of the diagram, while the core of the chart is filled with the relationships between customer expectations and technical design choices. At the bottom side, the level of importance, the technical difficulty, and the technical objectives are listed. The latter are selected according to the industrial standards, specifications for certifications, and the current state-of-the-art of lightweight helicopters and general VTOLs. VTOL capabilities, residual controllability, ducted rotors and sustainability of the propulsion system are intrinsic characteristics that a VTOL should possess to be aligned with the general view of a UAM ecosystem. A zero local CO_2 emissions propulsion system must be implemented and suitably designed to guarantee reasonable performance and compete with more classical turbine-powered layouts. The aircraft size, its BSE (Best Specific Endurance) speed, payload capabilities, and range performance are set up in agreement with the industrial partner of this work. Regarding the acceptable noise level, although this work does not focus on analyzing the noise emissions of specific configurations, an indicative value is provided as a technical objective. The Federal Aviation Administration (FAA) and the European Union Aviation Safety Agency (EASA) define noise certification standards for rotorcraft based on guidelines established by the International Civil Aviation Organization (ICAO). These standards, outlined in ICAO Annex 16, Volume I [65], specify the maximum permissible noise levels for various aircraft categories, including lightweight helicopters, using the Sound Exposure Level (SEL) metric. The maximum allowable noise level depends on multiple factors, such as aircraft type, maximum takeoff weight, number of engines, and flight conditions. According to ICAO regulations, for a light helicopter with a maximum takeoff mass not exceeding 788 kg, the noise limit is set at 82 dB SEL, measured on the ground at a reference point 150 meters below the flight path. The efficiency of the rotorcraft is measured through the Energy consumed per passenger-kilometer, which is a metric that captures the overall energy efficiency of the aircraft, considering both aerodynamic efficiency and propulsion system performance. The benchmark for this technical requirement is set according to the current state-of-the-art of eVTOLs operating in UAM ecosystems. The study by Sripad and Viswanathan [66] suggests that the energy consumption of eVTOLs designed for urban missions ranges between 0.08 kWh/pax-km to 0.75 kWh/pax-km depending on mission phases and the efficiency of the rotorcraft. Similarly, Shamiyeh et al. [67] set up performance standards for energy consumption of different VTOLs calculated along standard UAM scenarios, ranging from 0.3 to 1.2 kWh/pax-km in lift+cruise and multicopter layouts. For the sake of this work, the performance benchmark is set at 0.8 kWh/pax-km, calculated along the reference mission reported in Section 3.3.5.

From the analysis of the HoQ chart, several key insights emerge. The possibility to take off and land vertically is of course a fundamental requirement for UAM and this comes in a negative correlation with most of the technical specifications. Indeed, VTOL means adopting rotors, which are noisy devices that are more power-demanding than fixed wings to lift the same payload. Safety ranks among the highest-priority customer needs and this strongly correlates with both residual controllability and ducted rotors. While the first one is necessary for maneuverability in case of failure, the second property guarantees protection for both direct and external users, while impacting the noise emissions of the aircraft. Maintaining low energy consumption across all flight phases is a critical factor for ensuring the economic viability of an urban VTOL. Energy consumption per passenger-kilometer directly influences the operational costs and, consequently, the feasibility of the business model for UAM services. This parameter exhibits strong correlations with key performance indicators such as time savings, payload capabilities, and the ability to perform both urban and regional routes. Efficient energy management is essential for optimizing mission endurance and maintaining competitive operational costs. However, a major challenge arises from the negative correlation between energy consumption and other essential aircraft characteristics. Specifically, larger aircraft, higher payload capacities, and increased cruise speeds tend to increase energy consumption, necessitating careful trade-offs in design choices. Speed was found to have medium importance, suggesting that while faster transit is beneficial, operational feasibility (noise, energy consumption, and performance) may limit maximum cruise speeds.

The House of Quality analysis provides valuable insights into the design trade-offs necessary for an efficient and customer-centric VTOL. By systematically evaluating the correlations between customer requirements and technical specifications, it is possible to set up the requirements for a well-balanced configuration that meets urban mobility needs. Future iterations of the HoQ could integrate cost models and lifecycle analysis to further refine this balance.

2.3 Introduction to performance analysis methods

The analysis of the performance at a conceptual design stage of aircraft for UAM is critical for defining the vehicle's mission profile, energy requirements, and operational feasibility. A significant research effort was dedicated to this topic, with various approaches that were developed with the aim of providing a preliminary and fast overview on the capabilities of different VTOLs. The most common approaches are summarized below.

- **Analytical methods**: these are simplified analytical frameworks based on basic aerodynamic principles and they are adopted to estimate performance metrics, such as power requirements, lift and drag. These methods often employ blade element and momentum theories or actuator disk concepts to approximate the physical behavior of the rotors and the aerodynamic loads [68]. Analytical methods are useful for quick estimates and initial comparisons between design configurations, as they involve relatively simple calculations that provide valuable insights into performance trade-offs [69].
- **Semi-analytical methods**: these are analytical models extended by incorporating empirical data from existing rotorcraft. These are beneficial for increasing the accuracy without requiring a full numerical analysis and are commonly used in sizing and early design estimation [70], [71].
- **Numerical methods**: numerical simulations, such as Computational Fluid Dynamics (CFD) and Finite Element Methods (FEM), allow for more detailed estimations by simulating airflow around the rotor blades and structure. This approach captures complex aerodynamic effects like rotor wake interactions, turbulence, and three-dimensional flow characteristics that are not easily modeled by simpler methods. Although highly computationally demanding, simulations provide more reliable data for advanced design stages [72], [73].
- **Flight Dynamics simulations**: rotorcraft dynamics can be modeled by adopting ordinary differential equations that describe the evolution of the aircraft loads in time. This method is usually adopted to evaluate stability, control, and maneuverability properties, as well as performance characteristics. Programs like FLIGHTLAB [74], custom MATLAB-based models [75] of NASA's CAMRAD software [48], often simulate the aircraft response to control inputs, predicting behavior in realistic operational scenarios. This methodology will be further discussed in Chapter 4.

- **Experimental campaign**: while this method provides clear evidence of the performance of small- and full-scale models, it is typically the most resource-intensive approach. A substantial investment in terms of time, setup organization, hardware costs, and realization is required. Conducting experimental tests involves the fabrication of a physical platform, which means that an advanced design stage must be achieved prior to testing. Furthermore, ensuring similarity between the physical model and the final design is essential, both for small- and full-scale prototypes, to obtain meaningful and reliable results [76], [77].

In this work, an analytical approach is adopted (see Section 3.2.2): this allows for providing a large number of results with a fast and preliminary approach. The analytical framework is particularly suitable for this step of the methodology because of its simple adaptation to different configurations and powertrain solutions. The technical methods for performance analysis and conceptual design are reported in Chapter 3, as well as the main results and principal findings.

2.4 Introduction to flight dynamics modeling and requirements

Developing a mathematical model that accurately represents the dynamic behavior of the rotorcraft under specific flight conditions is a critical precursor to achieving an optimal design for UAM platforms. While physical prototyping and flight testing remain essential in the final validation of a configuration, these steps are both highly expensive and time-consuming. Therefore, simulation plays a fundamental role in bridging the gap between conceptual design and the realization of a physical demonstrator, enabling early-stage evaluations and refinements. The performance analysis conducted in Chapter 3 provided the motivations for selecting the side-by-side configuration and estimating its performance for targeted mission scenarios. However, flight dynamics modeling goes beyond this initial analysis by examining the rotorcraft response to pilot commands and environmental conditions, thus offering deeper insights into the stability and handling qualities of the rotorcraft. Over the past five decades, substantial research efforts have been dedicated to enhancing the accuracy of mathematical models for rotorcraft flight dynamics [78]–[80]. Different modeling approaches were developed and categorized based on their increasing levels of complexity. The most traditional method involves an analytical formulation of rotor non-linearities using blade elements and momentum theory [54]. A more advanced modeling technique adopts numerical methods to compute the rotor loads and to integrate the dynamics of the flexible blades in a mathematical framework based on the blade element motion [81], [82]. This approach enables an integral, non-linear representation of rotorcraft forces and moments, providing a more detailed understanding of the interactions between rotor and airframe dynamics. Multi-body dynamics is a third modeling approach. This type of models considers the rotorcraft as a system of interconnected bodies with a specific number of degrees of freedom, capturing the complex interactions between different components. This approach is exemplified by the widely recognized flight dynamics simulation software, FLIGHTLAB [74], [83], [84]. The most sophisticated modeling technique involves coupling computational fluid dynamics (CFD) with computational structural dynamics (CSD). This hybrid method provides a high-fidelity representation of the aerodynamic and structural phenomena affecting the rotorcraft, offering improved accuracy in predicting rotor loads and performance under varying operational conditions [85]. All of these methods have their pros and cons, with different levels of accuracy and computational costs. While the analytical approach may lack fidelity in the case of specific rotor dynamic behaviors, the CFD technique requires high computational costs and computing times.

The simulation platform developed in this work provides a versatile tool for multiple applications, including:

- Studying the trim and stability characteristics of the helicopter;
- Analyzing dynamic behavior under specific flight conditions;
- Designing control systems based on the rotorcraft dynamics;
- Training pilots and gathering feedback on handling qualities;

- Refining the rotorcraft design and study the effect of specific design features on the rotorcraft behavior.

These capabilities underscore the importance of a robust simulation platform, which can significantly accelerate the development process while reducing the costs and risks associated with prototyping and flight tests. The primary objective of this stage is to conduct a detailed trim and stability analysis of the side-by-side helicopter configuration. To achieve this, both analytical and numerical modeling approaches are necessary. These models will be complemented by algorithms to compute trim conditions and linearize the dynamics for open-loop stability assessment. The motivation for employing two distinct modeling approaches is multifaceted. The analytical model offers a fast and preliminary-oriented tool for analyzing the trim and stability characteristics of the rotorcraft. This approach adopts well-established methodologies that are both robust and validated at a low level of accuracy. Conversely, the numerical approach provides a more detailed and innovative method, introducing higher levels of complexity and enabling deeper studies of the rotor dynamic features. Given that the side-by-side helicopter configuration has still not been extensively studied, the use of two different models allows for cross-validation of the results, thereby providing greater confidence in the accuracy of the simulation. Additionally, this comparative approach has the aim of defining the necessary level of complexity that should be introduced for specific tasks of the simulation platform: indeed, it is recognized that introducing higher levels of complexity increases computational demands. The latter may not always be justified depending on the specific objectives of the study and ensuring that the computational resources are used efficiently for the overall goals of the study.

Both approaches must agree with the following requirements. Different levels of complexity can be added to a simulation model to capture multiple rotorcraft behaviors. Starting from a very simple material point description, one can include in the mathematical framework a more detailed description of each part composing the rotorcraft dynamics. For the sake of this work, a minimum level of complexity is set by the technical requirements of the numerical modeling approach: both the mathematical representations described in this manuscript must agree with the constraints in Table 2.1.

Description	**Requirement**
Rigid body representation	min. 6 dof
Rotor dynamics	Include blade flexibility effects
Inflow contribution	Include inflow dynamics

Table 2.1: Simulation models: technical requirements

Chapter 3

Performance analysis and conceptual design

In this Chapter, a performance analysis and conceptual design study are presented. The propulsion system architecture is investigated at first: the performance of three plug-in hybrid and one battery-electric powertrain system, ideally installed on a conventional helicopter, are evaluated along three specific UAM scenarios. Later, two alternative VTOL configurations (side-by-side helicopter and multirotor) are designed starting from the baseline layout and compared both from a quantitative and a qualitative point of view. The objective of this Chapter is to analyze the performance of VTOLs in a UAM context and select a specific configuration that can become a viable solution for future UAM services.

3.1 Baseline configuration

The most classical VTOL configuration is the helicopter, which does not satisfy all the requirements listed in Figure 2.2, but can be used as a reference configuration for conceptual design and performance analysis. The rationale behind this choice lies in the extensive data available in the literature regarding this configuration. In addition, technical datasets and preliminary performance analysis were available to the authors for validation of the results and comparison with experimental evidence. In the present study, a lightweight turbine-powered helicopter (Figure 3.1) with a Maximum Take-Off Mass (m_{to}) of 762.8 kg, and a maximum payload of 175 kg (2 passengers), is employed as a starting layout. In its original setup, the helicopter was powered by a PBS TS100 turboshaft engine fed by a fuel tank of 170 L capacity, and the total mass of the propulsion system (engine, fuel, tank, and auxiliary components) was 287.5 kg. Technical data are provided by de Angelis *et al.* [86] and summarised in Table 3.1.

Figure 3.1: Illustrative example of a 2-seat lightweight helicopter [87].

Description	**Symbol**	**Value**	
Maximum Take-Off Mass [kg]	m_{to}	762.8	
Empty mass (no powertrain, payload, and fuel) [kg]	m_0	300.4	
Maximum payload [kg]	m_p	175	
Disc loading [kg/m^2]	DL	12.97	
Equivalent flat plate drag area [m^2]	f	0.295	
Equivalent vertical flat plate drag area [m^2]	f_v	0.295	
Distance between main and tail rotor centers [m]	l_t	4.4	
Rotors		*Main*	*Tail*
Number of blades	N_b	2	2
Radius [m]	R	3.7	0.57
Blade aspect ratio	AR	19.5	4.75
Solidity ratio	σ	0.0327	0.0382
Tip speed [m/s]	V_T	210.3	182.8
Drag coefficient ($C_d = C_{d_0t} + k_t C_l^2$)	C_{d_0}	0.008	0.008
	k	0.008	0.008
Transmission efficiency	η	0.9	0.9

Table 3.1: Helicopter data

3.2 Propulsion system

3.2.1 Overview and aim of the study

A first step towards selecting a suitable VTOL for UAM services is the definition of an analytical framework to estimate the performance of different platforms. As outlined in Section 2.2, a primary requirement for future UAM vehicles is the sustainability of their propulsion systems. The aviation industry is a significant contributor to global CO_2 emissions: according to the latest report of the International Energy Agency (IEA) [8], in 2022 the transportation industry accounted for 23% of the global greenhouse gas emissions, and its impact on the climate change is substantial. The aviation sector contributes to 10% of this industry [88] and is expected to grow further in the near future due to the emerging branch of Urban Air Mobility. The integration of VTOLs in urban environments, although promising for reducing ground traffic congestion, could further increase aviation's environmental footprint unless sustainable technologies are adopted. For UAM to become a viable alternative for public transportation, sustainable propulsion systems are essential. Estimating the efficiency, range, and endurance of different powertrain solutions at a conceptual design stage, is fundamental for engineers and researchers to better understand the potential performance of VTOLs for UAM.

This section applies the case study presented in Table 3.1 to propose a conceptual design for four distinct propulsion system configurations: a battery-electric system and three hybrid layouts incorporating hydrogen fuel cells of different capacities. In the redesigned configuration, the helicopter must retain its Maximum Take-Off Mass and match the speed and climbing performance of the original model, while being integrated into a proposed zero-emission UAM ecosystem. The motivation for selecting these two types of propulsion systems among all possible alternatives is linked to the sustainability and reliability requirements set in Section 2.2. Fuel cell hybrid and battery electric design are well-established technologies, already adopted for a wide range of applications which guarantee available datasets, tested layouts, and zero impact on the local CO_2 emissions.

3.2.2 Model description

The analytical framework adopted to compute the power required by the helicopter in steady flight conditions is reported in this section. The mathematical formulation was described by Mazzeo *et al.* [89] and is here reported for this work. The model, inspired by Avanzini *et al.* [68], is based on the general momentum and blade element theories [78]. The total power required at the main shaft (P_{sh}), i.e. the power delivered by the electric motor, is computed for both forward and vertical flight as a sum of the main and tail rotor contributions (P_M and P_T), the parasitic power due to fuselage drag (P_P) and additional power required by auxiliary systems (P_s, assumed to be negligible in this study) such as avionics and conditioning. In particular

$$P_{sh} = \frac{P_P + P_M}{\eta_M} + \frac{P_T}{\eta_T} + P_s \tag{3.1}$$

where η_M and η_T are the main and tail rotor transmission efficiencies (Table 3.1). Concerning the forward flight condition, P_P is proportional to the fuselage drag (D_f) computed by means of an equivalent flat plate area f (Table 3.1), as

$$P_P = D_f U_\infty = \frac{1}{2}\rho f U_\infty^3 \tag{3.2}$$

where U_∞ is the forward speed and ρ the atmospheric density.

The terms P_M and P_T in Equation 3.1 include both the profile ($P^p_{M/T}$) and the induced ($P^i_{M/T}$) powers, that for a generic rotor are:

$$P_{M/T} = P^p_{M/T} + P^i_{M/T} \qquad \text{where} \qquad \begin{cases} P^p_{M/T} = \rho A_r C_{pr} (\Omega R)^3 \\ P^i_{M/T} = k_{ind} T v_i \end{cases} \tag{3.3}$$

where T is the thrust produced by the considered rotor, which is, according to a simple 1 dof model,

$$T = \sqrt{MTOW^2 + D_f^2} \qquad \text{for the main rotor, while} \qquad T_t = \frac{P_p + P_M}{U_\infty l_t} \tag{3.4}$$

for the tail. $MTOW$ is the maximum take-off weight, thus $m_{to}g$, with g as the acceleration of gravity. The induced speed v_i and profile power coefficient C_{pr} are computed numerically according to momentum theory (see Leishman [90]), as:

$$v_i \sqrt{(v_i - U_\infty \sin\alpha_T)^2 + (U_\infty \cos\alpha_T)^2} = \frac{T}{2\rho A_r} \tag{3.5}$$

where α_T is the angle of attack of the rotor plane, thus $\alpha_T = \sin^{-1}(-D_f/T)$. On the other hand, C_{pr} depends on the aerodynamic coefficients of the rotor blades and is expressed as

$$C_{pr} = \frac{\sigma \bar{C_D}}{8}\left(1 + 4\mu^2 + \frac{5}{8}\mu^4\right) \qquad \text{where} \qquad \begin{cases} \bar{C_D} &= C_{d_0} + k\bar{C_l}^2 \\ \bar{C_L} &= 6\dfrac{C_T}{\sigma(1+1.5\mu^2)} \\ C_T &= \dfrac{T}{\rho A_r (\Omega R)^2} \end{cases} \tag{3.6}$$

where μ is the rotor advance ratio, while the mean lift and drag coefficients ($\bar{C_L}$ and $\bar{C_D}$) depend on the rotor thrust coefficient C_T. The induced power factor k_{ind} (i.e. the ratio between the induced and ideal power according to momentum theory) is an empirical coefficient that accounts for various aerodynamic dissipation effects, including blade tip losses and nonuniform inflow. For the sake of simplicity, it is kept constant and equal to 1.25.

In vertical flight conditions, the model is modified by considering the incoming vertical flow occurring in steady climbing and descending phases. In particular, the parasitic power is

$$P_P = \frac{1}{2}\rho f_V U_V^2 |U_V| \tag{3.7}$$

where f_V represents the equivalent vertical flat plate area (Table 3.1), and U_V is the climbing/descending speed. For the sake of simplicity, the contribution of the induced speed to the vertical drag is neglected. On the other hand, the air density ρ is computed for each phase of flight according to the mathematical representation of the International Standard Atmosphere. The main and tail rotor powers are computed with the same expression as in forward flight (Equation 3.3), with the exception of the induced power contribution to the main rotor one, which is estimated as

$$P_M^i = k_{ind} T (U_V + v_i) \tag{3.8}$$

In this case, the semi-analytical model implemented by Johnson [78] is used to estimate the induced speed v_i within wake, vortex, and windmill brake regions for both climbing and descending phases. In particular

$$\frac{v_i}{v_{i_h}} = \frac{1}{2}\left[-\frac{U_V}{v_{i_h}} + \sqrt{4 + \left(\frac{U_V}{v_{i_h}}\right)^2}\right] \qquad \text{if} \qquad \frac{U_V}{v_{i_h}} \geq -1 \tag{3.9}$$

$$\frac{v_i}{v_{i_h}} = 0.3727\left(\frac{U_V}{v_{i_h}}\right)^3 - 1.9907\frac{U_V}{v_{i_h}} \qquad \text{if} \qquad -2 < \frac{U_V}{v_{i_h}} < -1 \tag{3.10}$$

$$\frac{v_i}{v_{i_h}} = -\frac{1}{2}\frac{U_V}{v_{i_h}} - \sqrt{\left(\frac{U_V}{2v_{i_h}}\right)^2 - 1} \qquad \text{if} \qquad \frac{U_V}{v_{i_h}} < -2 \tag{3.11}$$

$$\tag{3.12}$$

where v_{i_h} is the induced speed at hover.

In order to supply the power at the shaft, the electric motor has to require from the fuel cell/battery system the total power

$$P_{tot} = \frac{P_{sh}}{\eta_m} \tag{3.13}$$

where η_m is the electric motor efficiency, which is assumed to be constant, and equal to 0.887. This is the average value between climbing and cruising conditions of the selected motor (0.93, from Ref. [91]), multiplied by the motor's controller efficiency (assumed 0.95). The total power curve in steady forward flight for the selected helicopter, resulting from the above-described model, is reported in Figure 3.2. The helicopter requires, at the shaft level, approximately 120 kW to hover at 100 m altitude and 56 kW at the minimum power condition, which occurs when the helicopter cruises at 115 km/h.

As soon as the power required by the electric motor is known, the endurance and range of the helicopter at different flight conditions depend on the propulsion system and energy storage carried onboard. To estimate the performance, a simplified mathematical representation of the fuel cell system and the battery discharge is provided. The fuel cell system is represented using a performance curve that reflects typical PEM fuel cell characteristics. This curve, adapted from the data in Ref. [92], provides a reasonable approximation of fuel cell behavior and is illustrated in Figure 3.3. The fuel cell achieves a peak efficiency of 60% at 20% of its rated power, while at maximum power output, its efficiency is 50%.

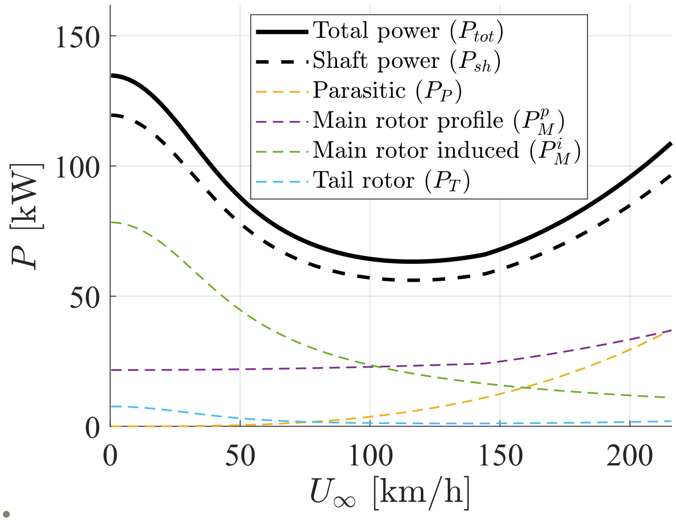

Figure 3.2: Helicopter's power curve at variable forward speed and 100 m of altitude

The hydrogen consumption, denoted as Δm_{H_2} is computed by integrating the fuel mass rate over time:

$$\Delta m_{H_2} = \int_t^{t+\Delta t} \frac{P_{FC}}{\eta_{FC} LHV} dt \qquad \text{with} \qquad \eta_{FC} = f\left(\frac{P_{FC}}{P_{FC_{max}}}\right) \tag{3.14}$$

where t and Δt are the current time and time interval, P_{FC} is the power supplied by the fuel cell, η_{FC} is its efficiency, and LHV stands for the Lower Heating Value of hydrogen. For the battery model, given limited experimental data, an ideal discharge model is used for simplicity. The State-of-Charge (SoC) variation over a time period is approximated as follows:

$$\Delta SoC = -\int_t^{t+\Delta t} \frac{P_b}{E_b} dt \tag{3.15}$$

where P_b and E_b are the battery power and energy capacity, respectively. The power distribution between the battery (P_b) and the fuel cell (P_{FC}) is governed by a control strategy that will be discussed later in Section 3.2.5.

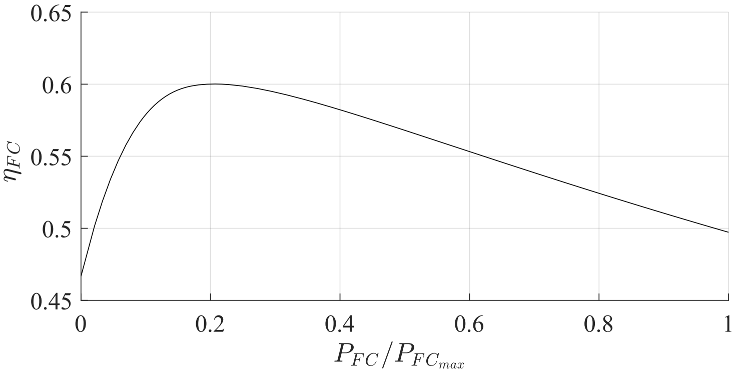

Figure 3.3: Fuel cell system efficiency at required power: data adapted from Ref. [92]

3.2.3 Mission scenarios

Three distinct mission scenarios are designed to evaluate and compare the performance of various propulsion systems. While an experimental campaign would ideally be conducted to gather data on realistic duty cycles (see for example Boukoberine et al. [93]), a simplified methodology is employed here due to the lack of empirical data specific to this transport category. The study includes a standard flight cycle and two representative UAM routes: an urban and a regional mission. The standard scenario is designed to be achievable by all propulsion configurations, while the urban and regional missions are intended to test the capabilities of one propulsion system over the other. All three mission scenarios include five consecutive flight phases:

- vertical climbing at 4 m/s from the ground (0 m a.s.l.) to the cruising altitude;
- hovering at cruising altitude;
- steady cruise performed at the maximum endurance speed of the helicopter (i.e. $U_{BSE} =$ 32.8 m/s);
- hovering at cruising altitude;
- vertical descending at 4 m/s down to the ground.

Specific data of each flight phase, including power and energy mission parameters, are reported in Table 3.2 for a single route. For the sake of this study, it is assumed that the eVTOL does not consume energy during the ’drop and go’ phases. In Table 3.2, the ”low-power” phases correspond to cruising segments, while ”high-power” defines hovering, climbing, and descending stages. Although these vertical climb and descent phases demand more power compared to conventional takeoff and landing maneuvers with a specified ramp angle, they offer a closer representation of eVTOL operations in an urban air mobility context, where these vehicles are expected to function within restricted urban areas. This approach also yields conservative performance estimates for high-power phases of the helicopter. Figure 3.4 plots power and altitude profiles for the standard mission as a representative example. In this study, the standard mission serves as a baseline for designing and comparing the performance of various propulsion systems. The urban mission simulates a route from G. Marconi Airport in Bologna, Italy, to the Bologna train station, adopting the helicopter as an air shuttle between two strategic hubs. Due to the higher percentage of time spent performing high-power phases, this mission exhibits the highest weighted average power requirement among all scenarios. On the other hand, the regional mission reproduces a journey from Bologna Airport to the Modena train station, representing an intercity air taxi service within the region. This mission emphasizes cruising, resulting in a lower weighted average power than the urban mission but demanding significantly higher energy to complete. Figure 3.5 displays the routes for both urban and regional missions on a map.

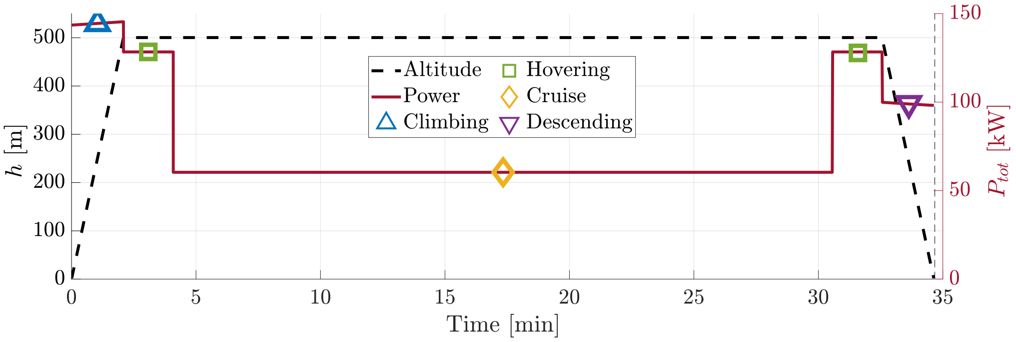

Figure 3.4: Standard mission profile: altitude (left axis), and power required (right axis).

		Standard	**Urban**	**Regional**
Payload	[kg]	175 (2 pax.)	175 (2 pax.)	175 (2 pax.)
Range	[km]	50	6	30.8
Cruising altitude	[m]	500	100	200
Hovering before cruise	[s]	120	30	30
Hovering after cruise	[s]	120	30	30
Total Duration	[min]	34.7	4.9	18.3
Total energy required	[kWh]	43.2	7.1	21.5
Weighted average power	[kW]	77.1	86.6	70.9
Minimum power	[kW]	60.4	60.7	60.8
Maximum power	[kW]	154.7	155.6	155.8
Low-power phases	[%]	75.7	62.5	85.4
High-power phases	[%]	23.3	37.5	14.6

Table 3.2: Propulsion system design: mission profiles

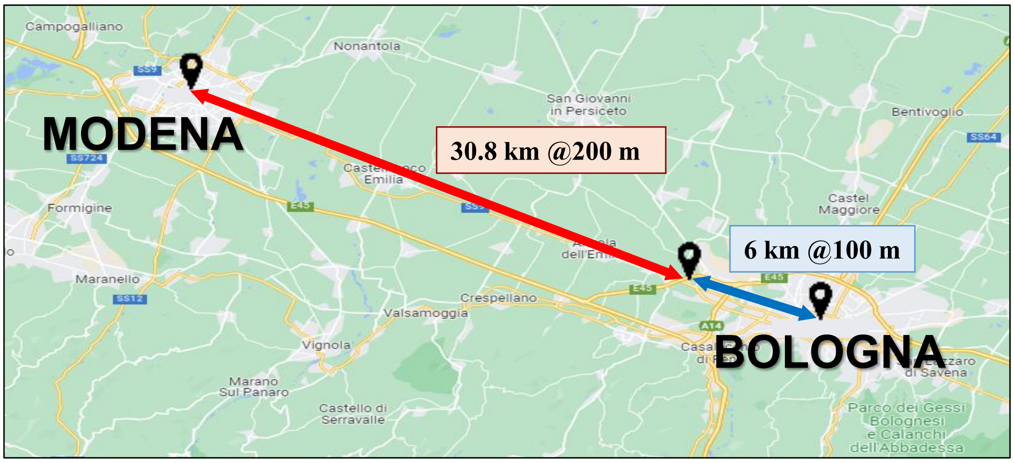

Figure 3.5: Illustration of urban (blue) and regional (orange) scenarios on a map [89]

While a comprehensive analysis would need to account for both energy consumption and emissions, it is clear that the eVTOL significantly reduces travel time compared to car transport in both urban and regional contexts. In the urban mission, a car takes approximately 20 minutes to travel from Bologna Airport to the Bologna train station, whereas the eVTOL could reduce this time by over 75%. Similarly, for the regional mission from Bologna Airport to Modena train station, which typically takes about 40 minutes by car, the eVTOL would provide a time savings of around 50%, not including the ”drop and go” phases.

3.2.4 Propulsion system design

A plug-in fuel cell/battery hybrid powertrain is proposed in three different configurations, comparing their performance against a purely battery-electric system. The hybrid powertrain architecture, shown schematically in Figure 3.6, includes an electric motor linked to both the main and tail rotors by a system of gearboxes and transmissions, and two ”energy delivery lines”. The motor is fed by a battery and a fuel cell connected in series. This allows either one or both systems to sustain the power demand and recharge the battery when the helicopter enters into low-power phases of flight. In contrast, the battery-electric configuration is simpler, relying on a single battery pack to power the motor.

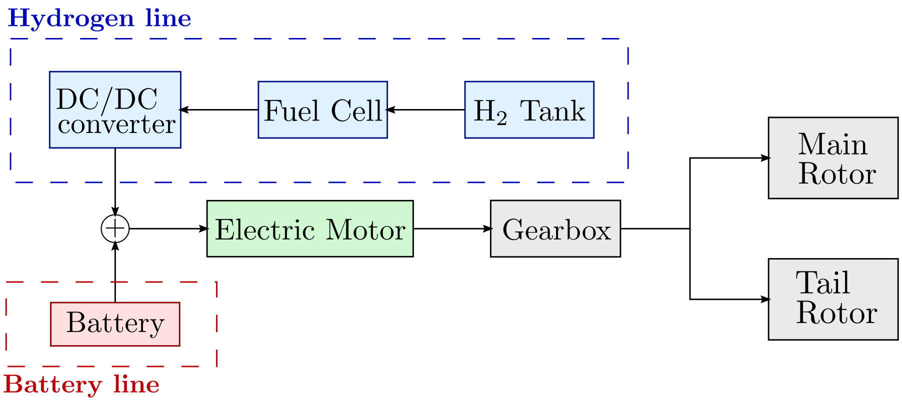

Figure 3.6: Schematic visualization of the plug-in hybrid propulsion system [89]

All propulsion configurations are designed to replace the helicopter's original turboshaft engine and fuel tank. Key design criteria include maintaining the electric powertrain within the original system's mass (287.5 kg) and ensuring it can support the rotorcraft through the standard mission profile (detailed in section 3.2.3). Table 3.3 summarizes the technical requirements for each configuration. Each component was sized based on commercial data and/or scaling methods, as discussed further in this chapter.

Electric motor
The H3X HPDM-250 electric motor [91] is an ultra-high power density motor drive for high-performance and aerospace applications. Its total mass is 21.6 kg, and it provides a peak power of 250 kW and a continuous power of 200 kW.

Fuel cell
A scaling approach is used to design the fuel cells and hydrogen tanks, with their power/energy capacity and size based on specific power and energy density reference values. Research on the state-of-art of hydrogen PEM fuel cells revealed that a conservative power-to-mass ratio of 0.6 kW/kg is consistent with recent studies [94], [95] and aligned with the U.S. Department of Energy (DOE) 2025 target [96].

Description	**Requirement**
Total mass of the propulsion system	287.5 [kg]
Completion of a reference mission	Standard mission
Electric motor type	H3X HPDM-250
Battery cell type	OXiS high-power Li-S
Battery pack nominal voltage	226.8 v (motor voltage in cruise)
Maximum Depth of Discharge (DoD)	60%
Minimum State of Charge (SoC)	30%
Minimum battery pack capacity	$\Delta SoC_{std}(\text{climb} + \text{hover}) > SoC_{lim}$
Fuel Cell Max. Power to mass ratio ($P_{FC_{max}}/m_{FC}$)	0.6 [kW/kg]
Hydrogen storage system gravimetric capacity	5.5 %
Safety Limit (SoC_{lim}, m_{H_2lim})	Emergency landing phase

Table 3.3: Propulsion system design: technical requirements

Hydrogen storage

For hydrogen storage, a compressed gas system is selected and sized to achieve a system gravimetric capacity of 5.5% (mass percentage of hydrogen fuel with respect to the total mass of the system given by tank and fuel), as defined by the DOE 2025 technical target [97]. According to this value, the hydrogen tank mass is approximately 17.2 times the weight of the onboard hydrogen fuel, m_{H_2}.

Battery

Data on the battery cell selected in this study [98] are summarized in Table 3.4. This battery cell is characterized by a good balance between energy density and discharge rate, making it highly suitable for aerospace applications, although it has a relatively limited charging rate. Conventional Li-Ion and Li-Po batteries can achieve even higher discharge rates but at the expense of a generally lower energy density. Across all configurations, the battery pack is designed to match the nominal voltage requirements of the electric motor during cruise, with its capacity tailored according to the propulsion system type. The individual cells act as "building blocks" for the battery pack, arranged in series and parallel to achieve the desired specifications. The capacity of the battery pack in the battery-electric setup enables the helicopter to complete a standard mission and attain a 50 km maximum range. On the other hand, in the plug-in fuel cell hybrid system, the battery pack capacity is determined by balancing contributions from both power sources: the battery and hydrogen fuel cell. Additionally, a conservative Depth of Discharge (DoD) of 60% is used in all cases for estimating the State-of-Charge (SoC).

Parameter	Value
Chemistry	Li-S
Nominal voltage [V]	2.1
Nominal capacity [Ah]	19
Max discharge rate [-]	6C
Max charge rate [-]	0.25C
Weight [g]	141
Energy density [Wh/kg]	283

Table 3.4: Battery cell data

A powertrain configuration where both the hydrogen and battery lines are capable of sustaining the helicopter along all flight conditions is not feasible, as their power/energy characteristics are not suitable for carrying the helicopter alone during the whole mission. Therefore, the proposed hybrid approach is conceived such that:

- the fuel cell provides a maximum power that is high enough to meet the requirements for the cruise phase while allowing the recharge of the battery at the maximum rate;
- the battery compensates power peak requests in the high-power segments;
- the battery capacity must be large enough for the aircraft to complete the first two flight phases of the standard mission (climbing from 0 to 500 m and 2 minutes hovering) without dropping below the safety limit;
- the helicopter must carry enough hydrogen to complete the minimum range of the standard mission and maximize the endurance.

According to the above-mentioned approach, and the technical requirements 3.3, three hybrid configurations plus a battery-electric one are designed. Their data are reported in 3.5. The number of battery cells in series defines the nominal voltage, which is a fixed parameter determined by the electric motor. For this reason, the battery packs are designed by tuning only the number of parallel modules. "Hybrid 70" consists in a 70 kW fuel cell coupled with a storage system for 4.9 kg of hydrogen. The fuel cell size corresponds to the minimum one that has a power high enough to recharge the battery at the maximum rate of charge when the helicopter is cruising in the standard scenario. ”Hybrid 80” mounts an 80 kW fuel cell coupled with 4 kg of hydrogen storage. This size approximately matches the weighted average power of the standard mission, but cannot be exploited for recharging the battery faster due to the limited battery charge rate. ”Hybrid 90” has a 90 kW fuel cell and 3 kg of hydrogen storage. This system has an oversized power with respect to the previous two. The hydrogen reserve (m_{H_2res}) represents the minimum quantity of hydrogen that must remain in the tank to ensure that the hydrogen pressure meets the requirements for fuel cell functionality. This reserve is not accessible for flight, and it is determined by calculating the mass of hydrogen at a conservative pressure of 10 bar (room temperature, 20°) within a tank designed for a nominal pressure of 350 bar.

	Battery-Electric	**Hybrid 70**	**Hybrid 80**	**Hybrid 90**
Powertrain mass [kg]	280.5	287.1	287.3	285.6
Useful battery energy [kWh]	44.0	10.3	10.3	10.3
Useful fuel energy [kWh]	-	68.3	55.7	41.8
Tot. useful energy on board [kWh]	44.0	78.6	66.1	52.2
Battery Pack				
Configuration [-]	108s17p	108s4p	108s4p	108s4p
Battery pack Capacity [kWh]	73.3	17.2	17.2	17.2
Nominal Capacity [Ah]	323	76	76	76
Nominal Voltage [V]	226.8	226.8	226.8	226.8
Mass [kg]	258.9	60.9	60.9	60.9
Depth of Discharge	60%	60%	60%	60%
Hydrogen Line				
Fuel cell rated power [kW]	-	70	80	90
Fuel cell system mass [kg]	-	115.5	132.0	148.5
Average Fuel cell efficiency	-	45%	45%	45%
H_2 capacity [kg]	-	4.9	4	3
H_2 tank empty mass [kg]	-	84.2	68.7	51.6
Reserve H_2 [kg]	-	0.17	0.14	0.11
DC/DC efficiency [-]	-	0.93	0.93	0.93

Table 3.5: Propulsion systems design parameters

To make some practical considerations on the different propulsion systems, two parameters are defined: the Useful gravimetric Energy Density (UED, expressed in kWh/kg) and the Specific Power (SP, expressed in kW/kg) related to the battery and hydrogen lines (subscripts $_{H_2}$ and $_b$) and the whole system (subscript $_{tot}$). In particular

$$\begin{cases} SP_b &= \dfrac{E_b C\text{-}rate|^d_{max}}{m_b} \\ SP_{H_2} &= \dfrac{P_{FC_{max}}}{m_h} \\ SP_{tot} &= \dfrac{m_b SP_b + m_h SP_{H_2}}{m_b + m_h} \end{cases} \qquad \begin{cases} UED_b &= \dfrac{E_b DoD}{m_b} \\ UED_{H_2} &= \dfrac{LHV m_{H_2} \eta_{DC} \eta_{FC}}{m_h} \\ UED_{tot} &= \dfrac{m_b UED_b + m_h UED_{H_2}}{m_b + m_h} \end{cases} \tag{3.16}$$

where E_b is the battery pack capacity, $C\text{-}rate|^d_{max}$ is the maximum discharge rate of the battery, m_b is the battery mass, η_{DC} and η_{FC} are respectively the reference average DC/DC controller and fuel cell efficiency, while m_h is the mass of the hydrogen line (converter, fuel cell, storage system, and fuel). The computed values are reported in Table 3.6.

		Battery-Electric	**Hybrid 70**	**Hybrid 80**	**Hybrid 90**
Battery line	SP_b	1.7	1.7	1.7	1.7
	UED_b	0.17	0.17	0.17	0.17
Hydrogen line	SP_{H_2}	-	0.34	0.39	0.44
	UED_{H_2}	-	0.33	0.27	0.21
Total	SP_{tot}	1.7	0.65	0.69	0.73
	UED_{tot}	0.17	0.30	0.25	0.20

Table 3.6: Specific power and useful gravimetric energy density of the electric and hybrid configurations.

It is quite clear that the battery exhibits significantly higher specific power when compared to the fuel cell. On the other hand, the hydrogen option provides greater energy density values in hybrid configurations than those achievable with a battery-electric system. For instance, the "Hybrid 70" configuration nearly doubles the UED realized by the battery-electric model, while the "Hybrid 90" configuration has the highest SP among all hybrid designs, but also the minimum amount of energy stored. This is because the m_{to} remains constant, therefore, if the helicopter utilizes a more powerful fuel cell, the quantity of hydrogen and the corresponding tank size must be decreased.

3.2.5 Power distribution strategy

The hybrid propulsion system configuration requires an energy management strategy to define the power distribution between the fuel cell and the battery during each flight phase. A control factor k defines the amount of power delivered by the battery and hydrogen lines, such that:

$$k = 1 - \eta_{DC} \frac{P_{FC}}{P_{tot}} \qquad \text{and} \qquad P_b = kP_{tot} \tag{3.17}$$

where η_{DC} is the efficiency of the DC/DC controller, assumed to be constant and equal to 0.93. The rule-based control strategy (Figure 3.7) is divided into two branches, depending on the power required by the rotorcraft:

- $P_{tot} > P_{FC_{max}}$: the battery is discharged and sustain the electric motor together with the fuel cell ($k > 0$);
- $P_{tot} < P_{FC_{max}}$: the fuel cell can provide enough power to both sustain the helicopter alone and recharge the battery pack ($k < 0$).

The fuel cell operates across a predefined set of constant-power operating points, depending on the battery SoC and the $P_{tot}/P_{FC_{max}}$ ratio. For the sake of this work, the definition of the operating points is based on an heuristic approach, and the energy management strategy proposed in this study does not rely on the application of optimization tools. According to this, as long as the battery SoC is higher than a predefined limit ($SoC_{FC,max}$), the fuel cell is regulated by the piece-wise linear function ($f_{control}$) depicted in Figure 3.8). Otherwise, if $SoC < SoC_{FC,max}$, P_{FC} is set to the maximum value. The feedback on the SoC has the aim of saving battery when the state of charge becomes too low, to the detriment of higher fuel consumption. In Figure 3.8, the parameters $x_1 = 2$, $x_2 = 1$, $y_1 = 1$, $y_2 = 0.8$ and $y_3 = 0.7$ are user-defined. During low-power phases, the battery can be either charged or discharged to maintain the level of SoC within two target levels (SoC_{max} and SoC_{sust}). With this approach, the battery is charged in the initial part of the low-power segment and then maintained at SoC levels within the user-defined bounds. Similarly to the high-power phases, when the battery is discharged, the fuel cell power is regulated by Equation 3.19, while the charging phase is set at the $P_{FC,charge}$ level. This is

$$P_{FC,charge} = min \left[P_{FC,max} \ , \ \frac{P_{tot} - P_b|^{c}_{max}}{\eta_{DC}} \right] \tag{3.18}$$

where $P_b|_{max}^c = E_b C\text{-}rate|_{max}^c$ is the battery power at the maximum rate of charge. Even if with a lack of physical meaning, in this analysis the battery power is defined as negative during battery charge phases. On the other hand, P_{FC} is limited by both its maximum level and the maximum rate at which the Li-S battery cells can be charged.

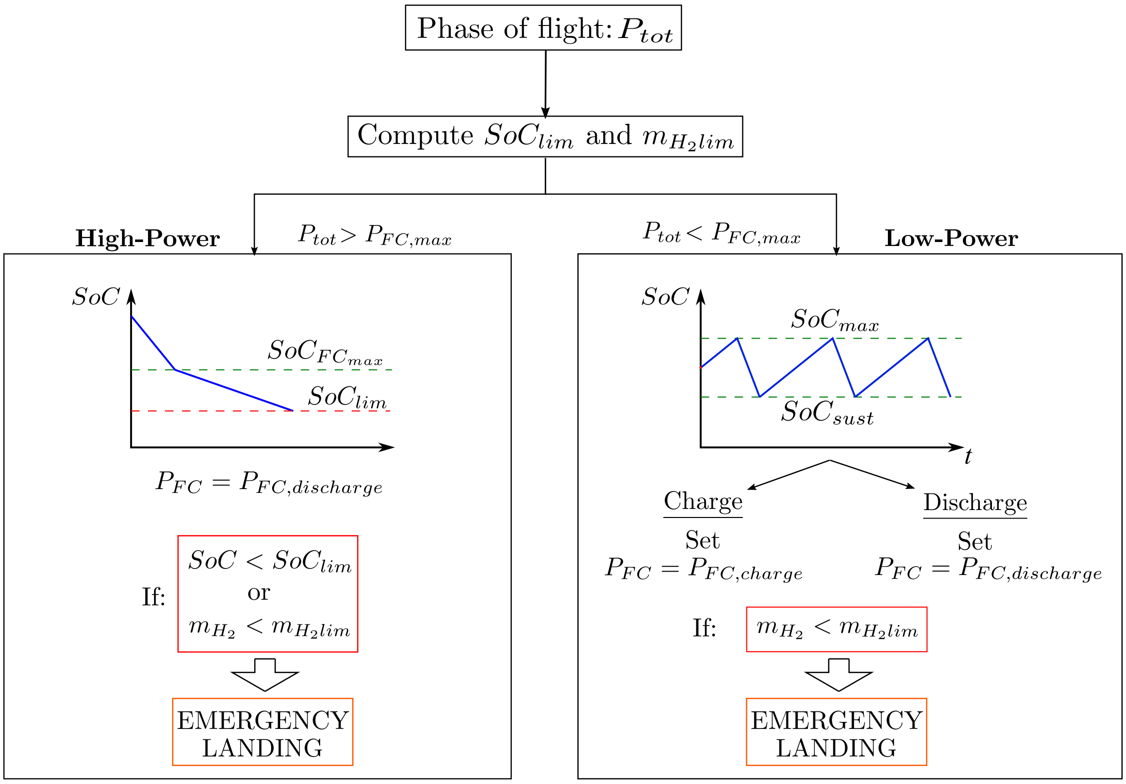

Figure 3.7: Scheme of the control strategy implemented on the hybrid powertrain [89]

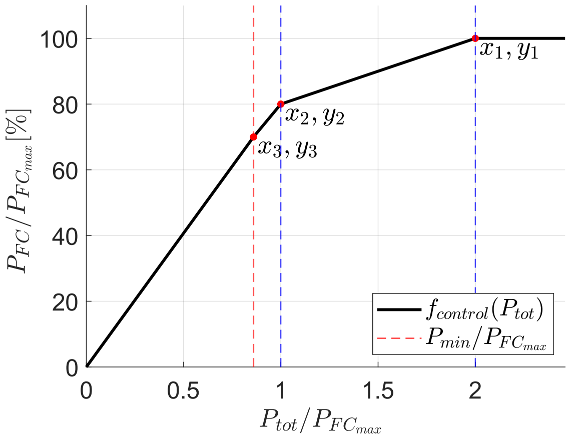

Figure 3.8: Piece-wise linear control function for the fuel cell power output [89]

During the high-power phases, the fuel cell power follow the equation:

$$P_{FC,discharge} = \begin{cases} f_{control}(P_{tot}) & \text{if } SoC > SoC_{FC,max} \\ P_{FC,max} & \text{if } SoC < SoC_{FC,max} \end{cases} \tag{3.19}$$

Further, during the flight, the controller constantly evaluates the mass of hydrogen, $\Delta m_{H_2}(T_{em})$, and battery energy, $\Delta SoC(T_{em})$, that are required to complete a standard emergency landing of a total duration of T_{em}. This consists of performing 2 minutes of hovering at the current altitude h and then descending to the ground (set at 0 meters for the sake of simplicity) at 4 m/s of vertical speed. The emergency landing time depends on the altitude at which the landing procedure starts. For this reason, two lower boundaries are set for the hydrogen mass (m_{H_2lim}) and the battery SoC (SoC_{lim}): in case one of these two limits is reached, the helicopter is running out of energy in one of the two propulsion lines and the mission is interrupted. Indeed, for safety reasons, the helicopter must carry enough energy on board to perform, at any time, a safe landing from the current altitude. The parameters for the feedback control are summarised in Table 3.7.

Feedback	**Value**	**Description**
SoC_{max}	90 %	Maximum battery SoC
SoC_{min}	30 %	Minimum battery SoC
SoC_{sust}	70 %	In the low-power phase, whenever the SoC hits this limit while decreasing, the battery charge phase is activated
$SoC_{FC,max}$	65 %	In battery discharge phases, it is the level of SoC below which the fuel cell is set at $P_{FC_{max}}$
SoC_{lim}	-	Emergency limit for SoC. It is computed as $SoC_{min} + \Delta SoC(T_{em})$
m_{H_2lim}	-	Emergency limit for m_{H_2}. It is computed as $m_{H_2res} + \Delta m_{H_2}(T_{em})$

Table 3.7: Control strategy feedback parameters

Regarding the helicopter's safety protocols, it's important to note that in hybrid configurations, neither the fuel cell nor the battery can independently support the helicopter during high-power flight phases. However, system redundancy is an inherent advantage of hybrid configurations, and in the case of an emergency descent, a suitable ramp angle can be selected to help the powertrain sustain the vehicle. In addition, while assessing the helicopter performance in this specific scenario is beyond the scope of this study, it is crucial to highlight that due to its mechanical design, the helicopter can always rely on the autorotation maneuver to perform a safe emergency landing without the need for an active propulsion system.

3.2.6 Results

The performances of the helicopter are studied, and the results of the four propulsion systems (designed in Section 3.2.4) are compared over the three mission scenarios (see Section 3.2.3). The initial test assesses the maximum range achievable in the standard scenario, by extending the duty cycle shown in Figure 3.4 and progressively increasing the cruising distance until the helicopter starts an emergency landing. The maximum range and residual battery SoC are reported in Figure 3.9, where the latter is

$$SoC_{residual} = SoC(T) - SoC_{min} \tag{3.20}$$

and T is the total duration of the mission. Among the configurations, "Hybrid 70" achieves the greatest range at BSE speed, covering 116 km, which is more than twice the range of the battery-electric configuration (50 km). As anticipated, due to the smaller hydrogen storage, "Hybrid 80" and "Hybrid 90" achieve shorter distances (93 km and 65 km, respectively), yet still exceed the range of the battery-electric design. All three hybrid setups complete the mission with a comparable $SoC_{residual}$, proving that, as soon as the battery can power the vehicle through the initial climb and hover phases, the maximum range can be extended by increasing the mass of hydrogen carried onboard.

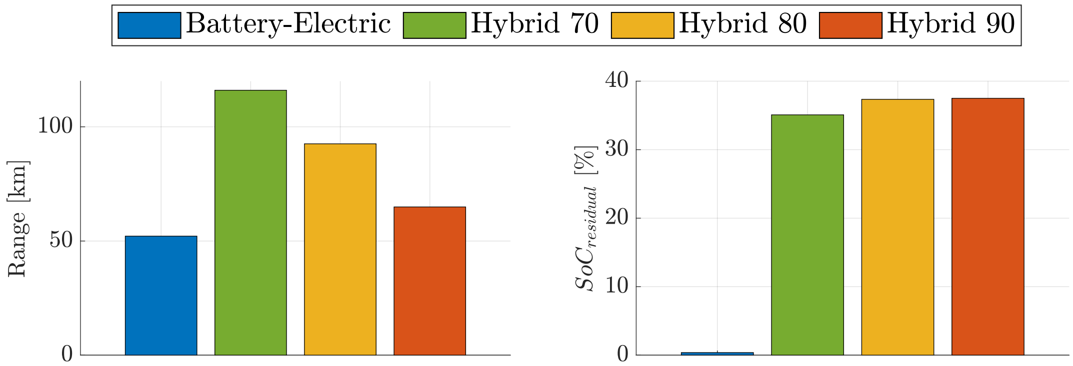

Figure 3.9: Maximum range on the extended standard mission (left), and residual battery SoC (right), for different powertrain layouts.

The second test is conducted along the urban and regional missions. In these scenarios, the helicopter repeats a single route until it runs out of energy and starts an emergency landing. This approach aims to determine the number of trips the rotorcraft can complete before requiring refueling or battery charging. The results are summarized in Table 3.8 and the residual amount of hydrogen is given by

$$m_{H_2,residual} = m_{H_2}(T) - m_{H_2res} \tag{3.21}$$

		Battery-Electric	**Hybrid 70**	**Hybrid 80**	**Hybrid 90**
Urban Scenario					
# Routes	[-]	5.7	4.9	5.9	7.1
$m_{H_2,residual}$	[kg]	-	2.9	1.6	0.13
$SoC_{residual}$	[%]	0.0	0.0	0.0	0.0
Regional Scenario					
# Routes	[-]	1.8	3.5	2.9	2.1
$m_{H_2,residual}$	[kg]	-	0.0	0.0	0.0
$SoC_{residual}$	[%]	0.0	10.6	29	29.5

Table 3.8: Rotorcraft performance results in the urban and regional scenarios

Considering the urban scenario, the battery-electric helicopter demonstrates significant performance by completing 5 trips between the airport and the train station, which is the same amount of "Hybrid 80" and one more than "Hybrid 70". Even if by carrying a lower amount of energy than the hybrid configurations, the low-range/high-power mission aligns well with the strengths of a battery-electric powertrain. Indeed, "Hybrid 70" and "Hybrid 80" ends up the mission with 2.9 kg and 1.6 kg of unused hydrogen because of the battery depletion. In these cases, the fuel cells cannot adequately support the battery to meet the motor power demands, as they are undersized for the mission's average power requirements. Additionally, the limited charging rate of the Li-S battery cells, combined with the short cruising time (and thus limited battery recharging opportunity), accelerates battery drain. Conversely, "Hybrid 90" achieves the highest number of trips, completing seven journeys with just 0.13 kg of residual hydrogen.

Its larger fuel cell enables it to deliver higher power during intense phases, preserving battery SoC and achieving a better balance between hydrogen and battery energy utilization. Figure 3.10 shows the battery SoC profiles for each design during the urban mission. The pink line indicates the safety threshold below which the helicopter initiates an emergency landing, continuously monitored throughout the mission to ensure descent occurs with the minimum necessary battery charge. When the battery SoC reaches this threshold, the mission is interrupted, and the helicopter descends following the standard emergency protocol. The system implements a charge-sustaining behavior at low-power, but, due to the limited duration of the cruise phases, the batteries are never fully replenished. Therefore, the range and endurance differences among the hybrid designs are primarily influenced by powertrain performance during high-power phases, where battery depletion occurs. Higher-power fuel cells are advantageous in these phases, conserving battery energy and extending both range and endurance. Figure 3.11 shows the power profiles for both fuel cell and battery systems. The energy management strategy keeps the fuel cell running at a nearly constant power output in the "Hybrid 70" configuration, as it is undersized relative to the mission requirements. Conversely, in configurations with a larger fuel cell, such as "Hybrid 90," the power output aligns more effectively with the demands of each flight phase, resulting in more efficient energy utilization. The urban mission specifically aims to stress the battery line more than the hydrogen branch, making the SoC the main limiting factor. By preserving battery energy through the use of a more powerful fuel cell like in "Hybrid 90", a more suitable balance is achieved. This trade-off enables comparable or greater ranges than the battery-electric design.

The regional mission was analyzed in a similar way. This scenario demands a longer range than the urban mission but with a lower average power requirement, favoring powertrains with higher UED. Specifically, "Hybrid 70" completes 3 full regional trips, outperforming the other two hybrid configurations (even if "Hybrid 80" comes close to finishing a third trip) and the battery-electric one, which completes only a single route (Table 3.8). For this scenario, battery SoC is no longer the limiting factor for hybrid designs; instead, each mission ends when fuel runs out, leaving a substantial amount of energy unused in the battery. This trend is evident in Figure 3.12, where none of the hybrid designs reach the battery's safety threshold. "Hybrid 70" delivers the best performance in terms of residual SoC, completing 3.5 travels with only 10 % of unused SoC, while "Hybrid 80" and "Hybrid 90" left around 30% of the total energy. Finally, Figure 3.13 shows the power distribution between battery and fuel cell. Given that the regional mission predominantly involves low-power operations (mainly cruising), the fuel cell maintains an almost constant power output across all three hybrid configurations. Among the four options, "Hybrid 70" appears to be the most suitable configuration for regional operations, as the near-complete utilization of onboard energy and the steady operation of the fuel cell suggest it is a well-balanced configuration for this type of transportation.

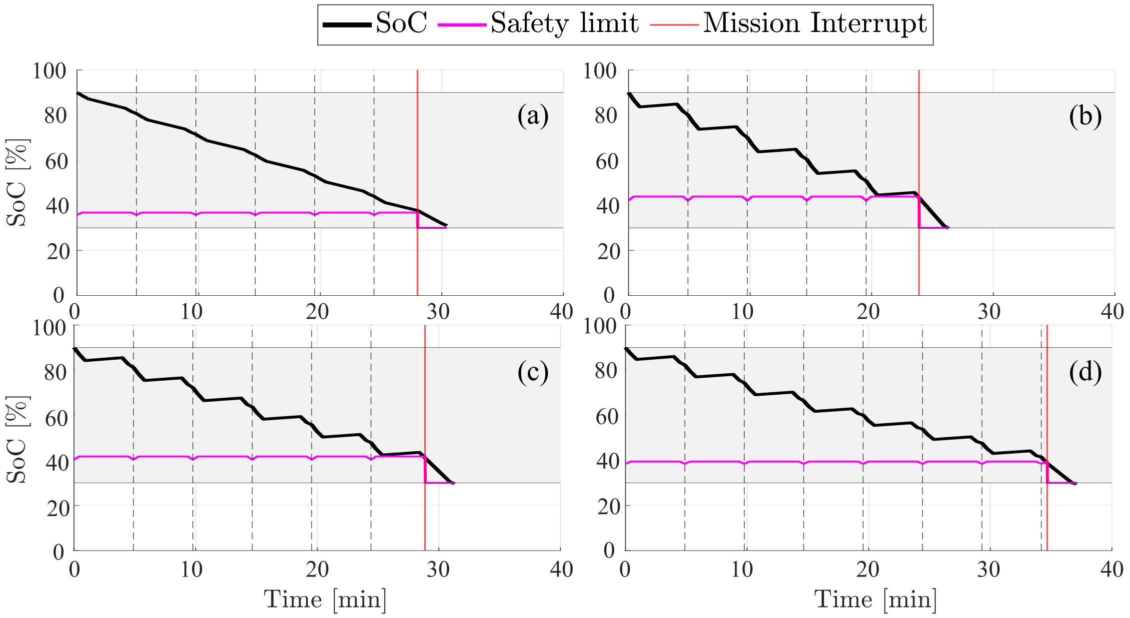

Figure 3.10: Battery *SoC* in the urban scenario. The grey region indicates the allowed *DoD* of the battery (from 90% to 30%) while the grey dashed lines represent the end of the single routes. a) Battery-electric; b) Hybrid 70; c) Hybrid 80; d) Hybrid 90

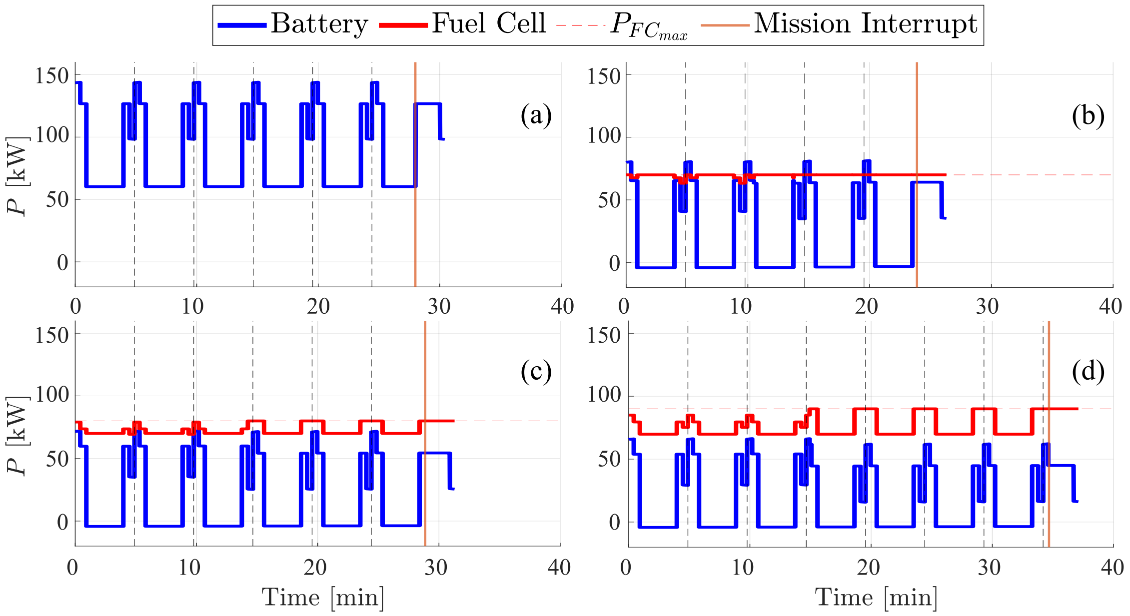

Figure 3.11: Power output profiles in the urban scenario. The grey dashed lines represent the end of the single routes. Battery-electric **(a)**, Hybrid 70 **(b)**, Hybrid 80 **(c)**, Hybrid 90 **(d)**

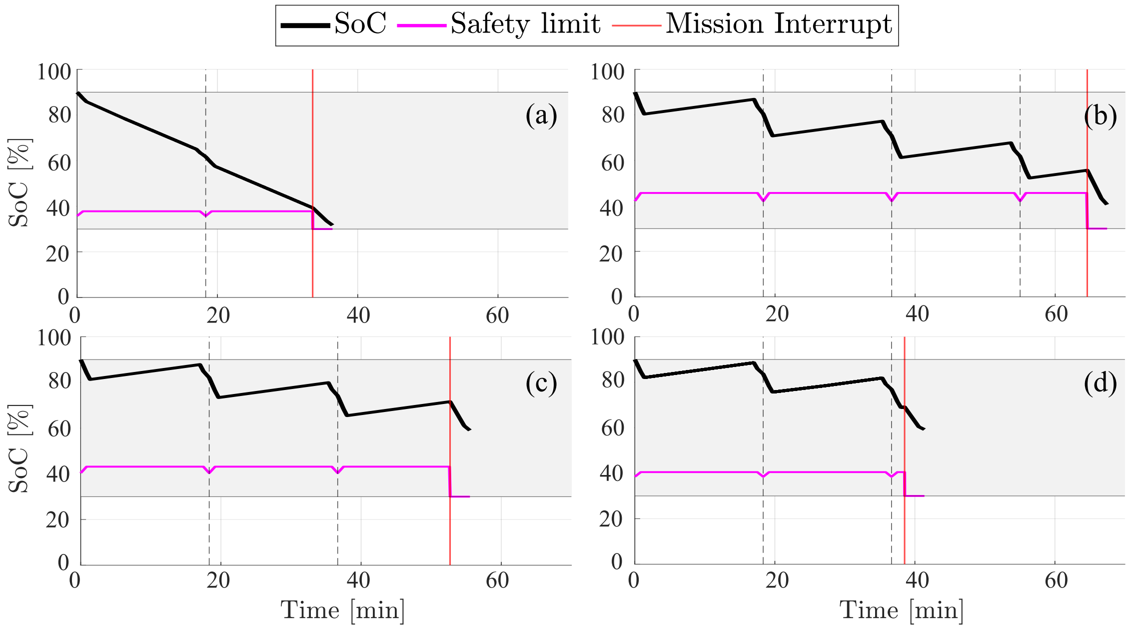

Figure 3.12: Battery *SoC* in the regional scenario. The grey region indicates the allowed *DoD* of the battery (from 90% to 30%) while the grey dashed lines represent the end of the single routes. a) Battery-electric; b) Hybrid 70; c) Hybrid 80; d) Hybrid 90

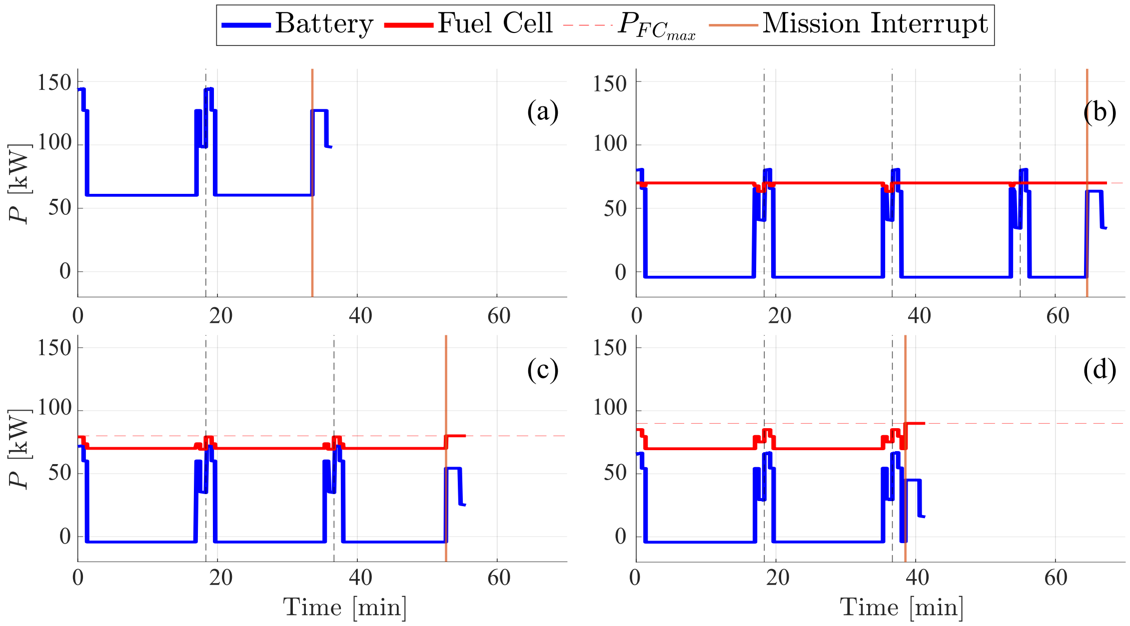

Figure 3.13: Power output profiles in the regional scenario. The grey dashed lines represent the end of the single routes. a) Battery-electric; b) Hybrid 70; c) Hybrid 80; d) Hybrid 90

3.2.7 Conclusions on the propulsion system

In this section, different propulsion systems for a lightweight helicopter were evaluated in an Urban Air Mobility context. The design approach replaces the original turboshaft engine with a sustainable powertrain by considering mass and performance constraints and adopting a suitable energy management strategy. In particular, 3 plug-in hybrid fuel cell systems and a full battery-electric design are compared along 3 mission scenarios. Key findings are:

- Both hybrid and battery-electric powertrains perform well in specific missions. The battery-electric system offers higher power density, making it ideal for short-range missions, while the fuel cell acts as an effective range extender for longer distances.
- As expected, the configuration with the highest UED reaches the maximum range in the standard mission but the same is not valid for all the UAM scenarios. "Hybrid 70" outperforms the other layouts in the regional travels whereas an oversized fuel cell ("Hybrid 90") proves more effective in urban missions, allowing a better exploitation of the energy onboard. In the latter case, the battery-electric helicopter reaches a remarkable number of routes.
- The best hybrid powertrain configuration depends on mission type. Short-range, high-power missions benefit from a larger fuel cell, while regional, low-power missions favor a smaller fuel cell paired with ample hydrogen storage.
- Optimal performance is achieved when all onboard energy is utilized by the end of a mission. Such a condition is unlikely to be verified in any situation by the hybrid layout, where either the battery capacity or the hydrogen mass cannot be fully exploited.

Considering a UAM scenario, the choice for the best propulsion system depends on the specific mission that the rotorcraft has to complete. For the sake of this thesis, urban missions are the prevalent goal for the studied cases, and the selection must fall between a battery-electric design and a hybrid configuration with an oversized fuel cell. While the second surely provides better performance, the first one brings inherent advantages linked to the simplicity of its architecture and the capability to perform experimental tests on small-scale models. Following in this manuscript, different VTOL configurations will be compared and an extensive mathematical representation of their flight dynamics will be performed. This requires validation through testing and simulations and for this reason, a battery-electric architecture is selected from now to the end of the thesis.

3.3 VTOL Configuration study

3.3.1 Overview and aim of the study

The analysis presented in Section 3.2, highlights the potential capabilities of hybrid and battery-electric helicopters in urban and regional scenarios. However, a large variety of rotorcraft configurations can populate a reliable and efficient UAM ecosystem. It then becomes crucial to select the optimal layout not only in terms of flight performance but also by considering qualitative aspects such as societal acceptance and its impact on the community. In this section, both a quantitative and qualitative analysis of the positive and negative aspects of rotary wing VTOLs is carried out to propose a suitable candidate for UAM services in the future. At first, VTOLs can be classified between rotary and mixed-wing configurations: while the first ones always rely on one or multiple rotors to produce both lift and thrust, the second category includes all the VTOLs that use a fixed-wing to provide lift during forward flight phases and a set of rotors to provide thrust in forward flight and enable VTOL capabilities at low speed. This second category includes tilt rotors, tilt wings, vectored thrust, and lift+cruise VTOLs. Those will not be included in this study since they are not purely rotary wing configurations and enable VTOL capabilities by passing through a transition time between forward and hovering flight conditions. For the sake of this study, three main categories of rotary wing VTOLs are investigated, i.e. the classical helicopter, the side-by-side helicopter, and the multirotor. The general characteristics of these VTOLs are here summarised.

Figure 3.14: Examples of rotary wing VTOLs. a) Curti Zefhir [99] conventional helicopter; b) McDonnell XHJD-1 Whirlaway [100] side-by-side helicopter; c) Volocopter Volocity [29] multirotor

Conventional helicopter

The conventional helicopter, often referred to as the single-rotor helicopter, represents the most widely adopted rotorcraft configuration, largely employed nowadays and in the past for most of the air transport which requires VTOL capabilities. Lift and thrust forces are both generated by a large main rotor which sustains the rotorcraft weight and provides the propulsive power to perform vertical and in-plane maneuvers. The main rotor torque is counteracted by a secondary rotor, generally placed on the tail of the helicopter, that is used to perform yaw maneuvers, thus rotations around the vertical axis. Classical helicopters are generally controlled by a system of swashplate and pitch links [101], [102] which allow the variation of pitch angle in each rotor blade and realize collective, lateral cyclic and longitudinal cyclic pitch controls. The collective pitch increases the main rotor thrust, while the lateral and longitudinal cyclic create rolling and pitching moments to tilt the helicopter for forward and lateral motion. The yaw motion is instead controlled by the tail rotor collective pitch angle. Both the main and tail rotors operate at constant angular speed, meaning that pitching, rolling, and yawing moments are generated only by the variation of the blade's pitch angles. Its history dates back to the early 20th century, with significant advancements occurring during the 1930s. Among the earliest examples of a fully operational single-rotor helicopter is the VS-300, designed by Igor Sikorsky in 1939. This prototype set the foundation for modern rotorcraft technology, introducing key innovations such as collective and cyclic pitch control, which allowed for precise maneuvering and stable hovering flight. In the context of UAM, the conventional helicopter offers a proven, reliable platform for short-range and medium-range missions. Although its larger rotor diameter can pose challenges in densely populated environments, its high aerodynamic efficiency and range make it a valuable asset for UAM operations [103].

Side-by-side helicopter

Dual-rotors are a particular category of helicopters made by arranging a couple of counterrotating rotors in tandem or side-by-side layout. In this case, the tail rotor is not necessary and the rotorcraft can be controlled simply by a proper mixing of the single rotor controls. Each rotor operates at constant RPM and is provided by collective and cyclic pitch controls. One of the most common examples of dual-rotor helicopters operating in tandem configuration is the Boeing CH-47 Chinhook developed in the 60s for the U.S. Army. Several studies can be found in the literature related to this vehicle, both with an experimental [104]–[106] and a numerical approach [107]–[109]. Although this configuration is highly accepted as a proper solution for a wide range of operations, especially related to heavy lift duties, it is known that it presents some criticalities related to the stability and aerodynamic properties of the two rotors. According to Newman [103], the presence of aft and rear rotors may induce potential mode couplings between longitudinal and lateral dynamics that can be detrimental to the rotorcraft's controllability. In addition, when the rotorcraft assumes a nose-up attitude during landing operations, the rear rotor may fall directly into the downwash of the aft one and induce pitch instability. A solution to reduce this effect can be found by rearranging the rotors in a side-by-side layout, with the longitudinal axis perpendicular to the rotor-rotor one. For these reasons, only the side-by-side configuration will be considered as a viable dual-rotor solution for UAM transport. Over the years, this configuration has periodically emerged as an alternative in various aviation projects. Its history started in the early 1930s, with one of the first prototypes built in Germany between the First and Second World Wars. The rotorcraft is known as the world's first operating helicopter with a system of collective and cyclic pitches and is named Focke-Wulf Fw 61. The rotorcraft was meant to operate as a military vehicle for observation, transport, and medical evacuation. Even if the configuration experienced intermittent development through the mid-20th century, research on side-by-side helicopters has gained momentum in recent years with the growing interest in the UAM concept and alternative VTOL design. The need for compact, efficient, and relatively quiet rotorcraft for intra-urban transport has prompted renewed investigations into the performance and flight dynamics of this configuration [110], [111]. The NASA Advanced Air Mobility (AAM) program focuses on the future of urban and regional aviation and includes studies on different VTOL configurations, including side-by-side rotorcraft. Their research highlights the potential benefits of lateral rotor placement in dense urban environments. Johnson et al. conducted several performance analysis and conceptual design studies to define optimal configurations for UAM purposes [48], [49]. In their studies, the side-by-side helicopter has intermediate performance between multirotor and lift+cruise configurations, partially confirming the conclusions drawn at the end of Section 3.3.5 in this work.

Multirotor

The last rotary-wing configuration analyzed in this study is the multirotor. Unlike the previous two, the multirotor operates by varying the angular speed of the rotors while maintaining a constant blade pitch. This approach is widely employed in commercial drones due to its ability to significantly reduce both the mechanical system's complexity and the aircraft's empty weight. Control of the individual rotors' rotational speeds is used to generate the moments required for maneuvering flight, enabling pitch, roll, and yaw movements. For instance, in a quadrotor, differential rotor speeds between the front and rear rotors create moments about the lateral axis, resulting in pitching maneuvers. Similarly, lateral rotor speed variations and rotor torque adjustments are used to produce rolling and yawing maneuvers. The origins of multirotor technology can be traced back to the early 20th century, with pioneering concepts such as Etienne Oehmichen's quadrotor and De Bothezat helicopter in 1922. However, the configuration gained attention only in the 21st century, driven by advancements in electric propulsion and lightweight materials. Today, multirotor are commonly associated with commercial drones and unmanned aerial systems (UAS), offering exceptional maneuverability in a rather simple design and providing services such as last-mile delivery, surveillance, and aerial photography. Multirotors are an essential component of the UAM vision: companies like EHang [30] and Volocopter [29] have developed prototypes specifically designed for UAM operations, demonstrating their potential for providing safe and efficient short-range urban transport. Their widespread use in commercial and recreational applications has also contributed to their societal acceptance, making them a key focus of ongoing research studies. In addition, this configuration is considered a promising candidate for short-range missions due to its compact size, minimal infrastructural requirements, and ability to operate in highly constrained urban environments [28].

3.3.2 Conceptual design methodology

In order to study the performance of different configurations, a proper design methodology has to be defined. The battery-electric helicopter presented in Section 3.2 is adopted as a baseline configuration for designing two alternative rotary wing eVTOL layouts: a side-by-side helicopter and a hexacopter drone (Figure 3.15).

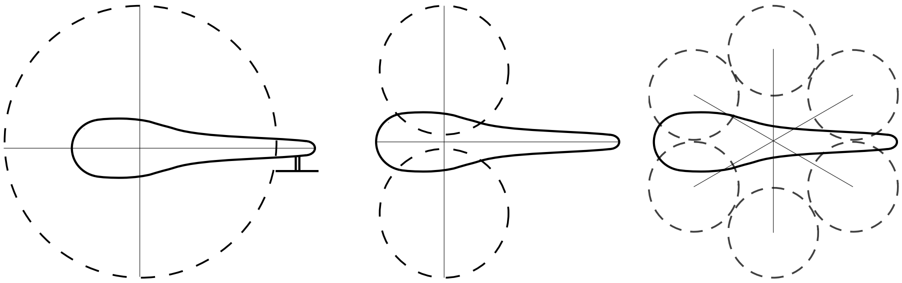

Figure 3.15: Rotorcraft's conceptual design illustration [112]

The technical requirements for the conceptual design are:

- a maximum take-off mass of 760 kg;
- two passengers of payload (175 kg);
- a maximum size of the rotorcraft not exceeding 7.6 m;
- battery discharge limit of $SoC = 30\%$;
- max. hovering throttle at 500 m: 65%;
- objective endurance: 50 min;
- same structure and fuselage;

Adopting the same fuselage in the three cases guarantees equivalent aerodynamic loads and constant weight and volumes. The methodology is summarised here:

- **Side-by-side helicopter**: the rotors are designed from the required maximum width, and the rotor angular speed was derived by keeping the same blade tip speed as the single-rotor configuration. The rotor blades maintained the same aspect ratio and a constant airfoil along their span;
- **Multirotor**: a specific motor + propeller system is selected [113] to operate at variable RPM. For the sake of this study, a hexacopter was considered, as the more classical quadrotor brings some criticalities in safety and residual controllability. While the constant RPM machines (helicopter and side-by-side) can rely on the autorotation maneuver in case of engine failure [114], drones implement safety measures through the redundancy of their rotors. Residual controllability of the system in case of engine failure is only guaranteed with systems having a minimum of six rotors, while in the case of a two-rotor failure, only if these two are not adjacent. It is straightforward the reason why the quadrotor configuration is directly neglected in this study and hexacopters are considered as representative of their VTOL category.

The helicopter's blades are scaled as $m_{bl} = \dfrac{m_{bl_0}}{R_0}R$, where the subscript $_0$ refers to the helicopter's baseline design. A scaled set of N_r electric motors is selected for the single and dual rotor layout. In particular, linear scaling is applied by considering the set of commercial motors produced by EMRAX (Kamnik, Slovenia) [115] (Figure 3.16). EMRAX produces a family of electric motors properly designed for aeronautical and high-power-density applications. Their relatively low weight and high-power characteristics make them an excellent candidate to sustain UAM vehicles and perform AAM services [116]. In addition, the different motor sizes designed with the same technology, and the availability of their technical datasets [117], make this product very suitable for analytical scaling, as proposed in this work. The scaled motors are selected by fixing the required maximum power for hovering (65% throttle at 500 m altitude) and computing the equivalent weight with a second-order polynomial interpolation (see Figure 3.16). A similar approach is applied for the derivation of the specific load factor and the equivalent power/RPM curves. Rotorcraft design specifications are summarized in Table 3.9.

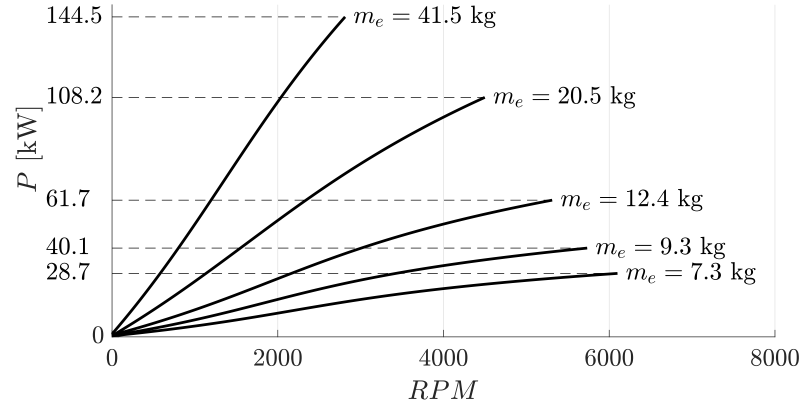

Figure 3.16: EMRAX motors scaling curves [112]

			Helicopter	**Side-by-side**	**Multirotor**
Max. take-off mass	m_{to}	[kg]	760	760	760
Empty mass	m_0	[kg]	301.2	299.4	306.3
Payload mass	m_p	[kg]	175	175	175
Motor mass	m_e	[kg]	74.4	23.1	11
Battery mass	m_b	[kg]	209.4	239.4	212.7
Tail rotor			yes	no	no
Max. width	$L(R)$	[m]	7.6 (3.8)	7.6 (1.9)	4.8 (0.8)
Electric motor					
Type			Scaled	Scaled	Commercial
Number of motors	N_r		1	2	6
Maximum motor power	P_{max}	[kw]	183.5	110.8	45
Specific load factor	sls	[RPM/Vdc]	1.22	6.08	16.4
Main Rotor					
Number of blades	N_b	-	2	2	2
Rotor radius	R	[m]	3.8	1.9	0.8
Chord	c	[m]	0.195	0.098	0.08
Angular velocity	Ω	[RPM]	528.5	1057	$1000 \div 2500$
Tip speed	V_T	[m/s]	210	210	$170 \div 420$
Disk loading	DL	[kg/m^2]	16.8	25.8	48.5
Blade's drag coeff.	C_{d_0}, k	-	0.008, 0.008	0.008, 0.008	0.008, 0.008

Table 3.9: Rotorcraft conceptual design specifications

3.3.3 Battery design methodology

The battery pack is designed by adopting the following methodology. The battery cells are arranged in a series and parallel layout in order to:

- maximize the total capacity;
- match the motor's voltage in the hovering situation;
- adhering to the maximum take-off mass requirement.

Figure 3.17 depicts a typical battery pack arrangement on the left. An iterative procedure is required, since every time the total number of cells is changed, the overall weight of the system changes accordingly, and with it the electric motor power demand. It is worth mentioning that, the number of cells in parallel (n_{cs}) defines the battery pack capacity, while the number of cells in series defines the battery voltage (n_{cp}). The methodology is depicted in Figure 3.17 on the right. The algorithm looks for the best combination of n_{cs} and n_{cp} to match the nominal voltage of the battery (V^b_{nom}) with that of the motor (V^e_{nom}) to maintain the rotorcraft in a hover. The rotorcraft power demand is computed at every iteration with the analytical model described in Section 3.3.4, while the characteristic power curve of the electric machine links the power required at the shaft P_{sh} and the rotational frequency of the motor RPM. An electrical motor's specific load speed sls is a metric that links voltage and frequency. At each iteration, the number of cells in series and parallel is computed as

$$n_{cs} = round\left(\frac{V^e_{nom}}{V^c_{nom}}\right) \tag{3.22}$$

$$n^{new}_{cp} = n^{old}_{cp} + floor\left(\frac{m_{to} - m_{to}(n^{new}_{cs}, n^{old}_{cp})}{n_{cs}m_c}\right) \tag{3.23}$$

where $m_{to}(n^{new}_{cs}, n^{old}_{cp})$ is the total weight computed with a battery having the new n_{cs} and the n_{cp} computed in the previous iteration.

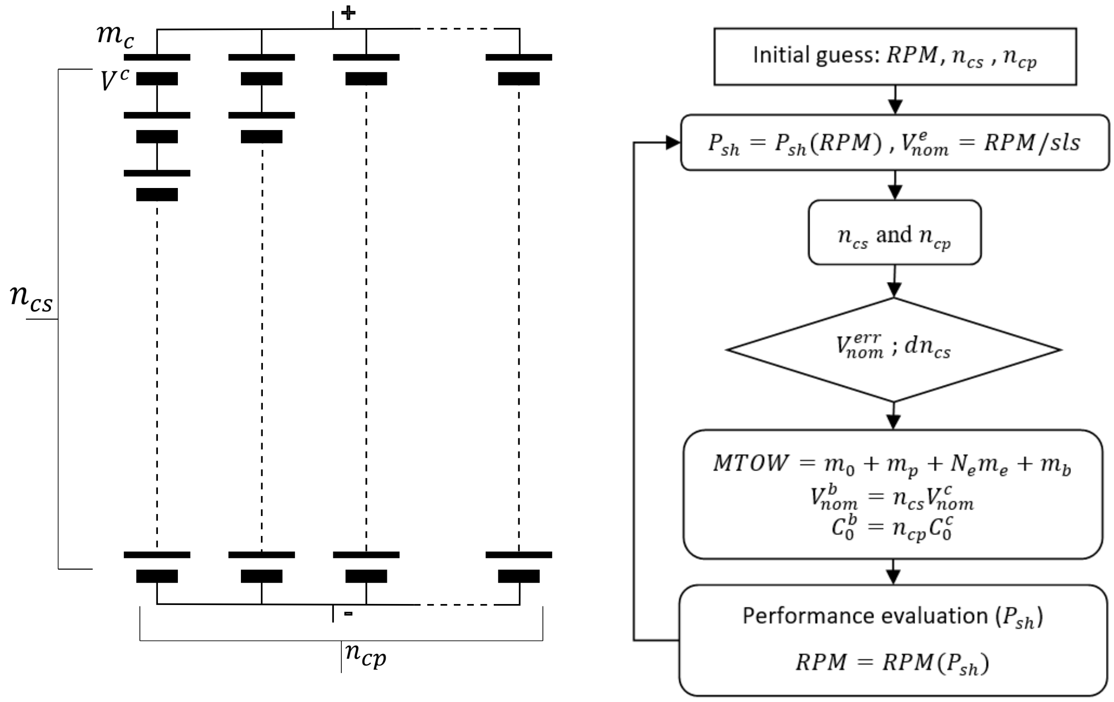

Figure 3.17: Battery pack design (left); Algorithm for battery pack design (right) [112]

In this sense, the n_{cs} tends to match the nominal voltages, while n_{cp} is used to fill up the remaining available mass and maximize the capacity, and thus the endurance. At every iteration, the mass of the rotorcraft is updated with the "new" battery cell arrangement, where the battery mass is $m_b = n_{ns}n_{cp}m_c$, its nominal voltage is V^b_{nom} and the nominal capacity is C^b_0. In Figure 3.17, the "empty mass" m_0 is the mass of the rotorcraft without payload and electric propulsion system (the rotor mass is included), while the mass occupied by the motors is $N_e m_e$. The algorithm stops when both the requirements for voltage error and variation in the number of series cells are achieved. The silicon anode battery (Si-A) cells produced by Amprius (Fremont, United States) [118] are selected for this study since they offer an improved energy density with respect to traditional lithium-ion (Li-Ion) batteries. This technology guarantees the maximum energy density currently available on the market, with an acceptable limit regarding the maximum discharge rate exploitable from the pack. Further descriptions of Amprius batteries and silicon anode technology can be referred to in the works of Feng [119] and Tang [120]. Table 3.10 reports the battery cell details.

Battery Type: Silicon Anode (Amprius Technologies [118])		
Nominal voltage	V^c_{nom}	3.7 V
Nominal capacity	C^c_0	3.8 Ah
Max. discharge rate	C_{rate}	3 C
Energy density	E_d	425 Wh/kg
Cell mass	m_c	33 g

Table 3.10: Battery cell parameters

Table 3.11 reports the battery pack designs produced by applying this methodology. The available space in each vehicle was different because of the different motor and rotor weights; therefore, the side-by-side helicopter is the rotorcraft with the highest energy carried onboard, while similar battery packs are produced for the helicopter and the multirotor, with a different cell arrangement.

			Helicopter	**Side-by-Side**	**Hexacopter**
Pack design	$n_{ncs} \times n_{cp}$	[-]	171 × 37	113 × 64	102 × 63
Battery mass	m_b	[kg]	209.4	239.4	212.7
Nominal voltage	V^b_{nom}	[v]	632.7	418.1	377.4
Nominal capacity	C^b_0	[Ah]	140.6	243.2	239.4
Ideal energy	E	[kwh]	89.0	101.7	90.4

Table 3.11: Battery packs design

3.3.4 Mathematical modeling

The analytical model to evaluate the power demand of each configuration is derived from the one presented in section 3.2.2. For the side-by-side helicopter, the main rotor is split into two separated ones, with negligible interaction and such that each of them provides half of the required thrust. The total power required by the rotorcraft is the sum of the single rotor power (equation 3.3), the parasite power due to fuselage drag, and the system power, such that

$$P_{sh} = \frac{P_P + N_r(P^i_M + P^p_M)}{\eta_M} + P_s \tag{3.24}$$

The side-by-side and classical helicopter work at constant rotor angular speed, thus the same modeling approach can be adopted for both configurations. On the other hand, the multirotor works with variable RPM control and fixed collective pitch, meaning that the rotor's angular speed depends on the flight condition. For preliminary performance analysis, Ω in equations 3.3 and 3.6 can be determined by the experimental thrust-RPM curve provided by the commercial electric motor coupled with high-performance propellers [113]. Similarly to the side-by-side helicopter case, the total thrust is distributed between the single rotors, each of them rotating at the specific RPM derived by the characteristic curve.

The battery is modeled with a constant-power battery discharge model extrapolated from the experimental study conducted by Avanzini et al. [70]. In their work, a series of tests on Li-Po batteries were carried out to determine the overall duration t, depending on the battery capacity C_0^b, the number of cells $N_c = n_{cs}n_{cp}$, and the constant battery discharge power P_b. An exponential model was implemented as

$$t = \alpha(N_c, P_b)C_0^b \tag{3.25}$$

where α is a function of the power and the number of cells. The values of α were obtained in experiments for variables P_b and N_c and interpolated by applying a variable separation method. Nevertheless, the interpolation adopted by Avanzini has the criticality of diverging when the number of cells increases and it could not be applied in this case. As such, an alternative interpolation method is proposed:

$$\alpha(N_c, P_b) = a(N_c)P_b^{b(N_c)} + c(N_c) \tag{3.26}$$

where

$$\begin{cases} a(N_c) & = 4.129N_c - 0.2241 \\ b(N_c) & = -1.003 \\ c(N_c) & = -0.03244N_c^{-1.43} + 3.161 \cdot 10^{-4} \end{cases} \tag{3.27}$$

so $a(N_c)$, $b(N_c)$, and $c(N_c)$ are, respectively, linear, constant, and exponential functions of N_c. In order to scale the results to the Si-A batteries employed in this study, a simple linear proportion is performed using the nominal voltage of the cells, to the experimental values of α, namely α_{exp}, such that

$$\alpha = \alpha_{exp}\frac{V^c_{nom}(\mathrm{Si-A})}{V^c_{nom}(\mathrm{Li-Po})} \quad . \tag{3.28}$$

The experimental data are reported in Figure 3.18.

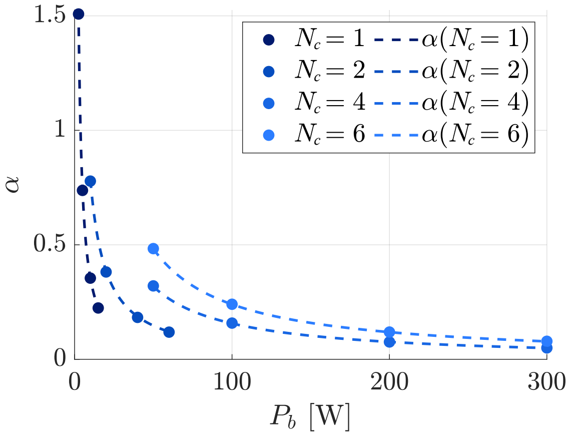

Figure 3.18: Experimental α values and small N interpolation [112]

3.3.5 Performance analysis

The performance of the three rotorcraft configurations is studied in terms of the power required, maximum endurance, range, and performance on the standard mission scenario described in Section 3.2.3. The power curves for each configuration at variable forward speed are reported in Figure 3.19. The plot provides the envelope of power curves from an empty ($m_p = 0$ kg) to a maximum load condition, showing the variation of power for different payloads. Different considerations can be made from this plot. In general, the multirotor design is the highest power-consuming configuration, with a hovering power in a fully loaded layout of 180.2 kW. The dual rotor configuration is a compromise between the others, requiring 140.9 kW to keep a steady hovering condition, while the helicopter's hovering power is 117.5 kW. Considering low-speed conditions (below the minimum power speed) the helicopter is the most efficient configuration, as it requires a minimum power to hover and perform forward flight in both empty and fully loaded layouts. Low-speed regimes are governed by the induced power, which is directly proportional to the disk loading, defined as the ratio between the thrust and the rotor-swept area ($DL = T/A_r$). A larger disk loading leads to low power efficiency at low speed. At flight regimes above the minimum power, the slopes of the side-by-side, and helicopter curves, merge until the first one becomes lower. It is known, indeed, that single-rotor layouts are suitable for low-speed operations, while a larger number of rotors brings advantages at higher speeds [121]. The plot also highlights the power sensibility to a weight variation of each configuration. The parameter ΔP_h is the power difference between a fully loaded and an empty configuration in hover and decreases with the disk loading. The envelope of the multirotor is larger than the others, indicating large power variations with variable loads. This effect is generally linked to two factors: the subdivision of the lifting surface, hence the increase of disk loading in a multirotor machine, and the lower efficiency of the variable RPM system. The latter is an important criticality of this system since the propeller design can be optimized to operate only at one specific flight condition, and becomes highly inefficient as soon as the rotorcraft changes speed or payload. However, being this effect connected to the variation of the induced power factor which is, for the sake of simplicity, kept constant and equal for the three configurations, the power jump highlighted in this Figure is mostly related to the disk loading effect. In general, from a power-required point of view, the more classical single-rotor configuration remains the best choice for an efficient UAM service operated with rotary wing layouts. Rotorcraft performance are also evaluated with their theoretical maximum endurance and range, computed by applying the battery discharge model described in Section 3.3.4 and reported in Figure 3.20. While for the best specific endurance (subscript $_{BSE}$) condition, the helicopter is undoubtedly the best configuration, from a maximum range perspective, the side-by-side and helicopter achieve similar results. The multirotor design described in this work has the main advantage of reducing the overall maximum width of the configuration, but on the other hand, it has the highest hovering power and a very limited maximum endurance. Best specific endurance and range parameters are summarised in Table 3.12.

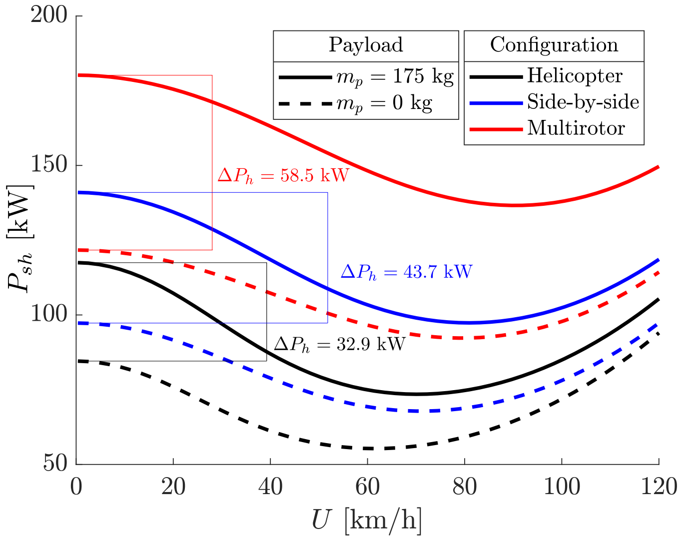

Figure 3.19: Power curves in a fully loaded and empty configuration.

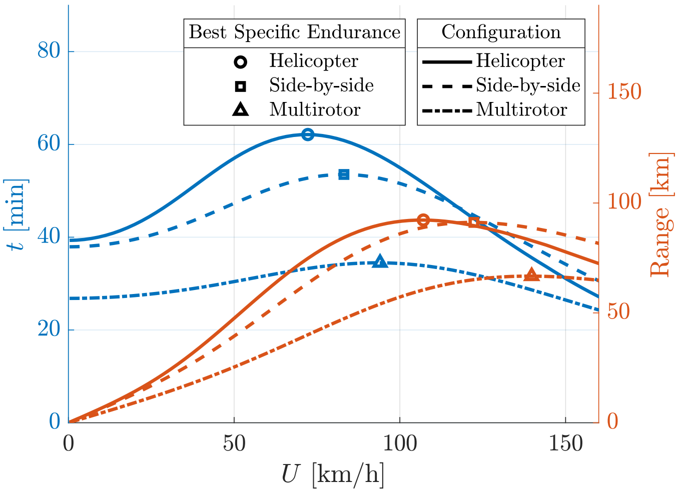

Figure 3.20: Endurance and range at variable forward speed and VTOL configurations

			Helicopter	**Side-by-Side**	**Multirotor**
Hovering power ratio	$P_h/(N_r P_{max})$		64 %	64 %	67 %
Hovering efficiency	$MTOW/P_h$	[N/kW]	6.5	5.4	4.2
Best specific endurance	P_{BSE}	[kw]	74.1	99.4	141.7
	T_{BSE}	[min]	62.1	53.5	34.5
	U_{BSE}	[km/h]	72.2	83.1	94.0
Best specific range	P_{BSR}	[kw]	89.6	120.5	174.2
	X_{BSR}	[km]	92.2	91.2	66.7
	U_{BSR}	[km/h]	107.1	122.3	139.8

Table 3.12: Endurance and range performance parameters

It should be highlighted that the maximum endurance and range described in Figure 3.20 consider a rotorcraft operating at a constant speed and consuming the maximum available energy. However, in a realistic scenario, vertical flight and hovering phases must be considered. Figure 3.21 represents the battery state of charge (SoC) during the standard UAM mission designed in Section 3.2.3 for the three cases. The SoC is constantly decreased with a quasi-linear trend during the different phases of the mission. The higher the power demand, the higher the rate of discharge, and thus the steeper slope in that range. The helicopter is the rotorcraft that achieves the maximum endurance during the mission, followed by the side-by-side and the multirotor. Concerning the range, the helicopter and side-by-side reach similar values. Indeed, while the first is more suitable for low-speed operations, the second configuration has higher U_{BSR}. The multirotor has the worst performance in the analysis and very limited endurance capabilities. The mission results are reported in Table 3.13. It is highlighted that all the designs satisfy the maximum discharge rate limit of 3C imposed by Si-A technology for the entire duration of the mission. The energy consumed per passenger-kilometer is computed as a parameter to evaluate the efficiency of the configuration along the standard mission. It was mentioned at first in the house of quality analysis in Section 2.2, where the metric was strictly correlated with the cost efficiency of the transportation system. In this case, the parameter is calculated as the total energy consumed during the mission, divided by the number of passengers and total range achieved. In particular

$$E_{pax-km} = \frac{\sum_{i=1}^{N_{ph}} P_i \Delta t_i}{2X_{tot}} \tag{3.29}$$

where P_i and Δt_i are the power and time interval of each phase of flight, and N_{ph} is the number of flight phases that are included in the mission. As expected, the helicopter configuration reaches the minimum value, confirming that a single rotor layout remains the most efficient rotary wing VTOL, while the side-by-side helicopter fits into the benchmark set in the house of quality.

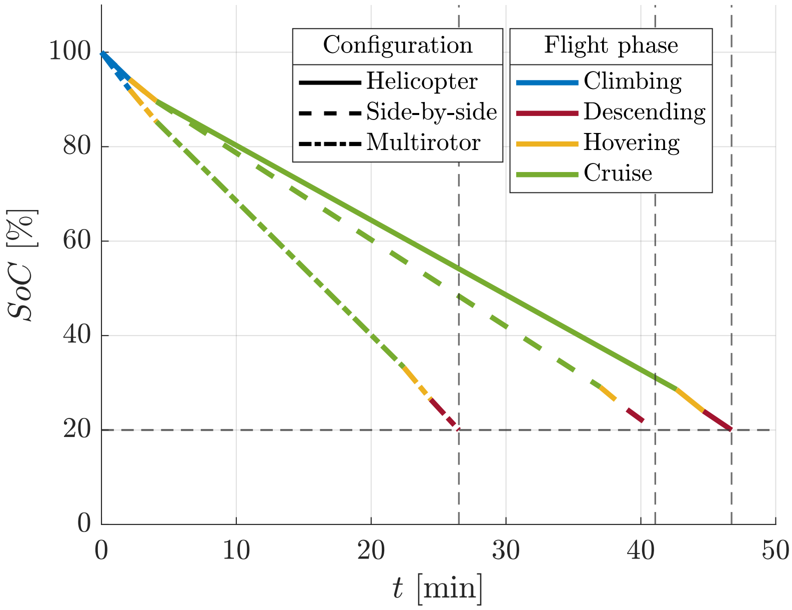

Figure 3.21: Standard mission SoC of different VTOL configurations

Parameter			**Heli.**	**SbS.**	**Multi.**
Discharge rate in hover	$C\text{-}rate_h$	[C]	1.32	1.39	1.99
Discharge rate in cruise	$C\text{-}rate_{BSE}$	[C]	0.83	0.98	1.57
Discharge rate in climbing	$C\text{-}rate_{cli}$	[C]	1.60	1.62	2.30
Discharge rate in descending	$C\text{-}rate_{des}$	[C]	1.11	1.21	1.85
Total mission duration	T_{tot}	[min]	47	41	26
Cruising time	T_c	[min]	39	33	18
Range	X_{tot}	[km]	46.4	45.6	28.7
Energy consumed per passenger-kilometer	E_{pax-km}	$\left[\frac{\text{kWh}}{\text{pax} - \text{km}}\right]$	0.6	0.8	1.2

Table 3.13: Endurance and range performance parameters in the standard mission scenario

3.3.6 Qualitative discussion

Introducing air mobility services for citizens within urban environments requires evaluating different aspects beyond that of rotorcraft performance. The impact of VTOLs on society has to be assessed in a qualitative discussion as well as the inherent characteristics in terms of design simplicity, noise, and safety.

Considering the typical architecture of the analyzed cases, multirotor, as well as side-by-side helicopters, are symmetric machines. This means that they do not require a tail rotor to keep the rotorcraft steady and do not suffer from induced moments generated by the aerodynamic load distribution in steady flight conditions. In the helicopter case, for example, during a forward flight, the main rotor blades experience different relative wind velocities when advancing and retreating from the flight direction, creating a lift gap between the lateral sides of the rotor disc. This asymmetry creates a rolling moment which has to be counteracted by the blade's natural flapping motion [122] together with the tail rotor effect. It is straightforward to highlight that asymmetric rotor configurations bring to the whole design a higher level of complexity in terms of flight dynamic properties and mechanical systems, which are as well related to a higher empty weight. The empty mass ratio, defined as the mass of the rotorcraft without payload, cargo, and energy storage (fuel or batteries in case of a fully electric vehicle) divided by its maximum take-off weight, is strictly related to the design simplicity of the rotorcraft. Table 3.14 shows some examples of helicopters, dual rotors, and multirotors evaluated with their empty mass ratio. Data are taken from the following references: as helicopters are taken typical light and medium weight models such as the one described by de Angelis *et al.* [86], the Robinson R22 and R44 [87], [123]; for the dual-rotor configuration are considered the side-by-side helicopters designed by Johnson *et al.* [48], [49] and the well-known, heavy-lift, tandem helicopter Chinhook CH47 [34]; for the multirotor configuration, vehicles of different sizes are compared, including the commercial VTOL E-Hang 184 [28], the heavy lift drone FB3 produced by Flying Basket [124] and the quadrotor designed by Kadhiresan and Duffy in [50].

Helicopter		**Dual-Rotor**		**Multirotor**	
Zefhir	0.55	Johnson's SbS (1)	0.48	E-Hang 184	0.47
R22	0.62	Johnson's SbS (2)	0.55	FP3	0.41
R44	0.69	CH47	0.49	Quad.	0.55
Average	*0.59*	*Average*	*0.51*	*Average*	*0.47*

Table 3.14: Empty mass ratio of different rotorcraft.

On average, due to the complexity of its systems, the helicopter configuration is the one with a higher empty mass ratio, meaning that for a fixed maximum take-off weight, a smaller space can be reserved to payload and energy storage. The latter is indeed an indicator of the maximum endurance achievable by the rotorcraft and a trade-off between battery/fuel on board and number of passengers is generally performed. Even if the side-by-side helicopter merges two helicopter rotors together, the overall complexity of the system can be considered lower. Indeed, no transmission has to be implemented for the tail and the rotors operate semi-autonomously (generally, a drive belt connects them). Finally, as already mentioned, the multirotor is the simplest configuration and allows to reserve of a larger "mass fraction" to the payload and battery. However, although its design complexity is lower than the other two configurations, the multirotor presents some criticalities in the power efficiency at variable flight conditions (Section 3.3.5), and some safety and societal acceptance considerations have to be made.

A fundamental aspect is the confidence that a UAM ecosystem generates in its direct users. An extensive analysis of the societal acceptance of UAM operations was conducted by the European Aviation Safety Agency (EASA) in 2021 [24], with the consulting firm McKinsey & Company. Based on thorough research, literature review, local market analysis, surveys, and interviews, the study inspects the major concerns and expectations of European citizens concerning UAM: a generally positive attitude was observed, as it was seen as a new attractive solution to reduce travel time, traffic jams, and urban pollution. On the other hand, safety and security were the major concerns, together with noise and environmental impact. To this extent, the three configurations considered in this study present different characteristics. The constant RPM and variable collective pitch system adopted by helicopters and side-by-side, guarantee the capability of performing an autorotation maneuver in case of propulsion system failure [114]. The autorotation is a condition where zero power is required by the rotor and the VTOL can descend with a controlled vertical speed. The energy to drive the rotor comes from the relative airflow passing through the rotor during the descent phase and allows it to produce a sufficient thrust to limit the vertical speed of the rotorcraft [90]. Autorotation is a maneuver that can be used to recover the VTOL to the ground in case of an engine failure or transmission problems and requires a variable collective pitch to be performed. An additional level of safety can be introduced in the side-by-side configuration by operating the two rotors semi-autonomously. Indeed, when each rotor is driven by a specific motor, the redundancy of the system guarantees that, whenever one of the two fails, the other one can drive both of them to a safe landing. Multirotors, instead, implement safety measures through the redundancy of the rotors. Residual controllability of the system in case of one rotor failure is guaranteed only with systems having a minimum of six rotors, while in the case of two rotors failure, only if these two are not adjacent.

Safety and societal acceptance can be improved by implementing shrouded rotors as well. The design of ducts protecting and isolating the rotors would be a fundamental requirement for VTOLs operating in a UAM ecosystem. The latter would avoid the presence of open rotors and even improve blade aerodynamic efficiency at the cost of increased take-off mass [90]. Indeed, the presence of rotating blades near future passengers is of major concern for the safety of both the professional and nonprofessional public. Safety procedures for boarding and disembarking would be fundamental to avoid collision with rotating propellers and dangers related to the inflow velocity produced by the rotors. However, while this solution is not practical on classical helicopters with a single main rotor, and of difficult implementation in multirotors, side-by-side configurations can provide a perfect fit with this measure. An example of a side-by-side helicopter with ducted fans is proposed by SAB s.r.l. in a small-scale prototype [75].

A final aspect to be considered for selecting the most suitable configuration for UAM services is the noise generated by the VTOL. The acoustic footprints generated by single or multiple rotors can be evaluated by adopting analytical [125], [126], numerical [127]–[129] or experimental methods [130], [131]. Smith *et al.* [132] compared multirotor noise characteristics with an increasing number of rotors and variable disc loading. A general observation was that for higher disk loadings, the overall noise levels increased significantly. The latter leads to conclusions on the optimal number of rotors for minimizing the acoustic levels. Considering a constant maximum take-off weight and a fixed maximum width, operating with a single, larger, main rotor, would be beneficial for the overall noise produced by the VTOL. Multirotors and side-by-side have generally higher disk loadings than helicopters [50], requiring larger power during low-speed flight phases and producing stronger noises. An additional drawback of these configurations is the noise generated by the aerodynamic interaction of the rotors with the fuselage and the rotors themselves. Most of the side-by-side helicopters studied in the literature, present two overlapped and intermeshing rotors. An acoustic prediction of the background noise generated by side-by-side rotors in hovering conditions, with different levels of overlap, was conducted by Sagaga *et al.* [111] by employing numerical simulations. It was found that the noise level, which is mainly related to the tip vortex interactions between the two rotors, can be decreased by reducing the level of overlap between the two rotors. Nevertheless, the rumor intensity still remained above the maximum threshold set by Uber for air taxi services in a UAM ecosystem (67 dB at 500 ft altitude [133]. Considering the rotor-fuselage interaction, this is strictly inevitable in a classical single-rotor configuration, while it can be avoided in multiple rotors VTOLs (see Refs. [134] and [135]). This would increase the total width of the rotorcraft but avoid the impact between the fuselage and the rotor inflow. In general, the overall noise produced by a specific VTOL depends on several factors such as the number of rotors and their rotational speed, the fuselage design, the presence of ducts, and the relative location, and thus interaction, between the rotors themselves.

A unique solution to which of the three analyzed configuration produces higher noise disturbances cannot be found at a conceptual design stage and requires advanced investigations on more realistic design. However, if neglecting the aerodynamic interactions between rotors and fuselage, and the tail rotor contribution, it can be concluded that a single-rotor design can provide lower disturbances to citizens and users with respect to multiple rotors restricted to the same width.

3.3.7 Configuration selection

The considerations made in this section can be summarised in Table 3.15. All the qualitative and quantitative aspects are evaluated by assigning a grade (A, B, C) to the respective configuration. According to the analysis, the side-by-side helicopter is selected as a reference configuration for future services in an Urban Air Mobility ecosystem. From a design point of view, it represents a trade-off between classical helicopters and multirotor, merging the better performance of a constant RPM system with the design simplicity of a symmetric machine. The house of quality developed in Section 2.2 is recalled to verify whether all the technical objectives are satisfied. Concerning the design parameters, the three configurations are designed in order to satisfy the maximum size and payload capabilities set in the HoD, while the minimum speed at BSR and range capabilities are satisfied as well at the best specific range condition. The three layouts are electrically driven and guarantee VTOL capabilities and residual controllability due to their inherent design concept. Safety and security were the major users' concerns about VTOLs and the side-by-side helicopter satisfies both redundancy requirements and the capability to perform emergency maneuvers in case of failure. Ducted rotors improve safety for external users and increase the level of societal acceptance by covering the rotating blades. Finally, the energy consumed per passenger-kilometer is calculated on the standard mission scenario, completed at the best specific endurance speed, highlighting that only the multirotor does not fit into the initial requirement. This can be translated into higher operational costs and lower efficiency of this rotorcraft system with respect to the other two. From a noise level point of view, the satisfaction of the technical objective has not been fully proven, as an in-depth noise assessment of the system was out of the scope of this work. In general, the side-by-side configuration is theoretically less efficient than a classical helicopter, but its performance should be re-evaluated by considering the low level of aerodynamic interactions occurring by placing the main rotors out of the fuselage boundaries.

	Helicopter	**Side-by-side**	**Multirotor**
Performance	A	B	C
Design simiplicity	C	B	A
Empty mass fraction	C	B	A
Societal acceptance	B	A	C
User's safety	B	A	C
Fail safe	B	A	C
Noise	A*	B*	C*

Table 3.15: Configuration's grade. The * symbol means that the property has to be re-evaluated at an advanced design stage

Chapter 4

Side-by-side helicopter flight dynamics modeling

This Chapter focuses on the flight dynamics modeling of a small-scale side-by-side helicopter, the configuration identified as a viable candidate for Urban Air Mobility (UAM) services in the previous sections. The Chapter aims to propose two different main rotor modeling approaches (analytical and numerical) and provide suitable trim and linearization routines. The mathematical frameworks are complemented with the fuselage, shrouds, and blade aerodynamics models.

4.1 Case study

The case study for the development of a flight dynamics simulation model is a small-scale side-by-side helicopter (Figure 4.1) available at the University of Bologna and produced by SAB Group S.R.L. Rotorcraft's data are summarised in Table 4.1. The fuselage is a lightweight carbon fiber structure, symmetric with respect to its longitudinal plane, and designed to allocate two 22000 mAh Li-Po batteries underneath.

Figure 4.1: Small-scale side-by-side helicopter, courtesy of SAB Group S.R.L.

Two custom-made electric motors are placed at the very end parts of the upper beam, which connects the main rotors. Those are two identical helicopter rotors, counter-rotating and operating at constant angular speed to avoid the need for a tail rotor or other anti-torque systems. The rotors are assembled on the two sides of the central body with zero overlap and minimum aerodynamic interference with the fuselage. Two shrouds surround each rotor, to improve safety, noise, and aerodynamic properties. As already mentioned in Section 3.3.6, all of these properties make the VTOL a perfect candidate to operate in a UAM ecosystem. The presence of the shrouds improves the societal acceptance and safety for both external citizens and direct users, especially during embarking/disembarking procedures, while bringing a beneficial effect on the overall thrust produced (see Section 4.7). The positioning of the rotors is optimal to reduce the rotor-rotor and rotor-fuselage aerodynamic interactions, thus minimizing the level of noise.

Description	**Unit**	**Symbol**	**Value**
Maximum Take-Off Mass	kg	m_{to}	20.62
Inertia moment wrt x_B	kgm^2	I_{xx}	3.532
Inertia moment wrt y_B	kgm^2	I_{yy}	2.222
Inertia moment wrt z_B	kgm^2	I_{zz}	5.342
Inertia product wrt x_B	kgm^2	I_{yz}	0
Inertia product wrt y_B	kgm^2	I_{xz}	-0.052
Inertia product wrt z_B	kgm^2	I_{xy}	-0.001
Rotors			
Airfoil name		*NACA0015*	
Sense of rotation		Γ	± 1
Number of blades		N_b	3
Radius	m	R	0.505
Mean Chord	m	c	0.051
Solidity ratio		σ	0.0964
Angular velocity	rpm	Ω	2400
Total Hinge offset $(\overline{0F})$	m	e_0	0.075
Flap Hinge offset $(\overline{LF})$	m	e_F	0.0075
Lag Hinge offset $(\overline{PL})$	m	e_L	0.045
Pitch Hinge offset $(\overline{0P})$	m	e_P	0.0225
Blade mass	kg	m_{bl}	0.1613
Blade center of gravity wrt the hub	m	r_G	0.224
Spring restraint coefficient due to flap	Nm/rad	$K_{s\beta}$	162
Spring restraint coefficient due to lag	Nm/rad	$K_{s\xi}$	0
Pitch-Lag coupling ratio		$K_{t\xi}$	0
Pitch-Flap coupling ratio		$K_{t\beta}$	0
Blade twist coefficient	rad	θ_w	0
Longitudinal incidence angle	rad	i_s	0
Lateral incidence angle	rad	i_c	0
Hub position of the MR1 wrt body axes	m	$\boldsymbol{r}_{HB}^{(1)}$	[0 -0.645 0.066]
Hub position of the MR2 wrt body axes	m	$\boldsymbol{r}_{HB}^{(2)}$	[0 0.645 0.066]

Table 4.1: Small-scale side-by-side helicopter data

The rotors are semi-rigid, with lead-lag hinges and blade flapping due to the blade's flexibility. A classical swashplate system with three equispaced pitch links is used to control the collective pitch and lateral/longitudinal cyclic controls of each rotor. A suitable control mix is adopted to reduce the over-actuation of the VTOL from 6 single rotor controls to 4 global controls, which allows the pilot to operate the system as a classical helicopter configuration. In particular, the main rotor 1 (MR1, superscript $^{(1)}$) is referred to as the right-hand side clockwise rotor, while the main rotor 2 (MR2, superscript $^{(2)}$) is referred to as the left-hand side counterclockwise rotor. The global collective pitch (θ_0) is used to control the vehicle along the vertical axis and it is a constant value in the two rotors. Similarly, the global lateral cyclic control (A_{1s}) is adopted to control the lateral motion and rolling moment of the rotorcraft and it is actuated by the same value in the two rotors. The longitudinal motion and pitch moment are actuated by a global longitudinal cyclic, which is represented by the average value between the two rotors. Finally, the yaw motion of the VTOL is controlled by a differential longitudinal cyclic such that each tip-path plane is rotated to create a yawing moment. In mathematical terms, the global controls and their relationships are

$$\theta_0 = \theta_0^{(1)} = \theta_0^{(2)} \qquad A_{1s} = A_{1s}^{(1)} = A_{1s}^{(2)} \tag{4.1}$$

$$B_{1s} = \frac{B_{1s}^{(1)} + B_{1s}^{(2)}}{2} \qquad \Delta B_{1s} = \frac{B_{1s}^{(2)} - B_{1s}^{(1)}}{2} \tag{4.2}$$

4.2 Modeling scheme

The side-by-side helicopter is modeled under the hypothesis of a rigid body moving in a flat and non-rotating Earth under the action of propulsive, aerodynamic, and gravity effects. The rigid body motion is governed by the 6 first order ordinary differential equations

$$m_{to}\dot{\boldsymbol{U}} = -m_{to}\boldsymbol{\omega} \times \boldsymbol{U} + \boldsymbol{F_g} + \boldsymbol{F} \tag{4.3}$$

$$I\dot{\boldsymbol{\omega}} = \boldsymbol{M} - \boldsymbol{\omega} \times I\boldsymbol{\omega} \tag{4.4}$$

$$\tag{4.5}$$

where the external forces and moments are provided by the main rotors and fuselage contributions. The overall structure of the mathematical frameworks is depicted in the open-loop block diagram in Figure 4.2. Pilot inputs, which may be preceded by a control system in closed-loop dynamics, are processed by a control mixer, which distributes the inputs to individual rotor commands. These rotor commands, along with the current rotorcraft state, determine the forces and moments generated by the two main rotors as well as the fuselage. Each rotor's dynamics are modeled separately, incorporating blade flexibility and inflow models. The forces and moments produced by the rotors are corrected to account for the contribution of the rotor shrouds and combined with the aerodynamic forces acting on the fuselage. These cumulative forces and moments serve as the external inputs required to solve the equations of motion, determining the helicopter's attitude and velocity over time. The simulation model is time-dependent, and specific input signals can be supplied to simulate various maneuvers and flight conditions.

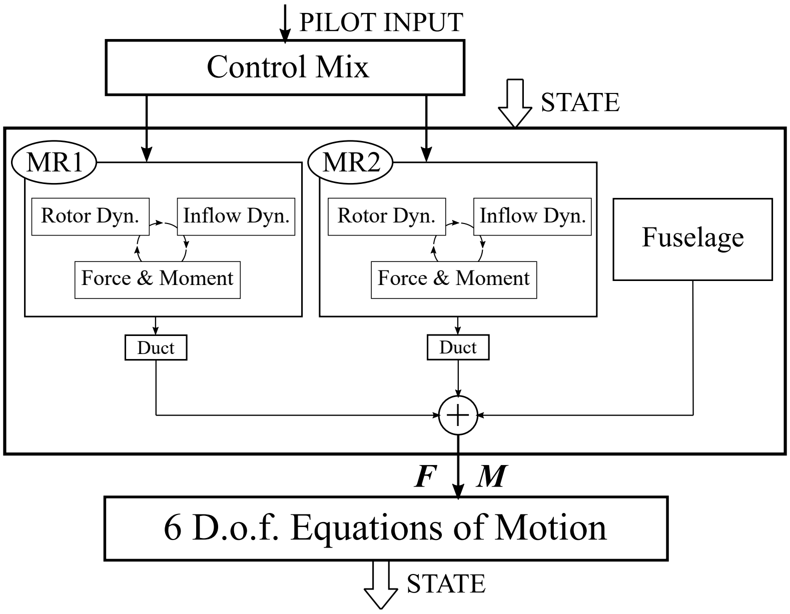

Figure 4.2: Side-by-side helicopter simulation model scheme

As already mentioned, two distinct modeling approaches have been developed for the main rotor contributions. The first is a low-complexity, analytical framework characterized by a reduced number of degrees of freedom and simplified rotor dynamics. The second is a high-complexity, numerical model based on a blade element method, which computes the contribution of each rotor blade over time. This introduces additional degrees of freedom and allows for the analysis of specific blade designs, as well as the study of rotor dynamics phenomena such as flapping, lead-lag motion, and nonuniform inflow, and their effects on the rigid body stability of the rotorcraft.

4.3 Main rotor: analytical modeling approach

4.3.1 Overview of the model

In this section, an analytical modeling framework for the main rotor forces and moments is described. This approach leads to the definition of a 14 dof (degrees of freedom) model, made of 14 nonlinear ordinary differential equations:

- 6 equations for the first-order rigid body motion (Section 4.2);
- 6 equations for the second-order main rotor flapping (3 for each rotor, stated in Section 4.3.5);
- 2 equations for the first order, uniform dynamic inflow (1 per each rotor, stated in Section 4.3.4.

The rotor angular velocity is kept constant and the analysis will focus on flight conditions that are generally operated at constant RPM, thus excluding the autorotation procedure. The model was validated by comparing the trim and stability results with the formulation provided by Talbot [54] on a small-scale helicopter configuration. The side-by-side layout was developed afterward with an identical main rotor modeling approach.

4.3.2 Frames of reference

The mathematical framework adopts three main frames of reference (f.o.r.), as shown in Figure 4.3. The first one is the right-handed body f.o.r. ($[x^B\ y^B\ z^B]$). In this work, whenever the f.o.r. of a vector is not identified, it is implied that the vector is represented in the body frame. This is centered in the center of gravity (CG) and coherent with the rotorcraft attitude: the lateral axis y^B is directed towards the right-hand side rotor, while z^B is directed towards the underneath of the vehicle.

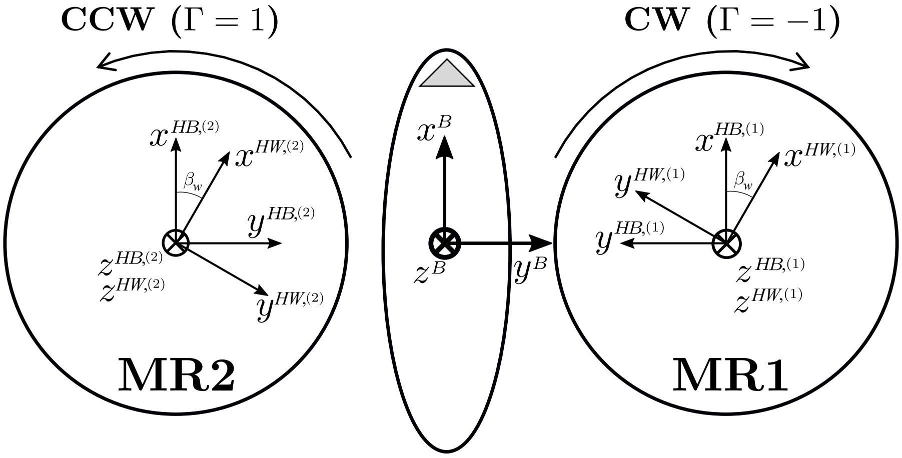

Figure 4.3: Coordinate systems of the analytical modeling framework

The second f.o.r. to be described is the hub-body frame ($[x^{HB}\ y^{HB}\ z^{HB}]$). This f.o.r. is centered on the main rotor center of rotation, with the vertical axis z^{HB} directed downwards and parallel to the rotor shaft. The horizontal axis x^{HB} is instead perpendicular to the rotor shaft and pointed towards the nose of the rotorcraft. The lateral axis is defined differently in the two rotors, generating a right-handed f.o.r. in the counterclockwise rotor (MR2) and a left-handed one in the clockwise (MR1) (see Figure 4.3). The third f.o.r. to be defined is the hub-wind frame of reference ($[x^{HW}\ y^{HW}\ z^{HW}]$, along with the aerodynamic forces are computed with the analytical expressions. This f.o.r. is similar to the hub-body one but rotated with the sideslip angle created by the freestream velocity (β_w).

4.3.3 Main rotor

The analytical framework to describe the main rotor loads is based on the formulation proposed by Talbot [54]. The two rotors are identical, with the only differences related to their location and sense of rotation. For the sake of simplicity, in this section, the framework is presented for a generic Γ-rotating rotor which, as already mentioned in Section 4.3.2, requires two different hub-body frames depending on the sense of rotation of the rotors. Following the method proposed by Choi *et al.* [136], the wind and angular velocities in hub-body frames for a generic rotor are expressed as (considering that no incidence is applied to the rotors)

$$\boldsymbol{\omega}^{HB} = \begin{bmatrix} \Gamma & 0 & 0 \\ 0 & 1 & 0 \\ 0 & 0 & \Gamma \end{bmatrix} \boldsymbol{\omega} \qquad \text{and} \qquad \boldsymbol{U}^{HB} = \begin{bmatrix} 1 & 0 & 0 \\ 0 & \Gamma & 0 \\ 0 & 0 & 1 \end{bmatrix} \boldsymbol{U} + \boldsymbol{\omega}^{HB} \times \boldsymbol{r}_{HB} \tag{4.6}$$

where $\Gamma = 1$ is used for the right-handed counter-clockwise rotor, $\Gamma = -1$ for the left-handed clockwise one, and $\boldsymbol{r}_{HB}$ is the rotor hub position with respect to the body f.o.r. Similarly, the lateral cyclic control input has to be corrected when expressed in the hub-body frame specific for a Γ-rotating rotor, such that

$$A_{1s}|^{HB} = \Gamma A_{1s}|^{B} \tag{4.7}$$

The values of $\boldsymbol{\omega}^{HB}$, $\boldsymbol{U}^{HB}$ and the cyclic control of each rotor are needed to evaluate the total force and moment created by the main rotors at specific flight conditions. This force and moment are modeled by assuming a constant and unique value around one rotor revolution and rigid blades. The analytical expression of the loads in the hub-wind frame can be found in Ref. [54], and the components are: H, Y, T, L, M, and Q. These loads are analytical functions of the rotor design, the flight condition, the pilot control, the blades flapping, and the local inflow velocity (see Sections 4.3.5 and 4.3.4), and they include aerodynamic, inertial and centrifugal contributions from the rotor blades. In the rotor design dependency, are included as well the average aerodynamic coefficients of the blades, which are described in Section 4.6, and the effect of the shrouds (Section 4.7). The total main rotor force and moment vectors, represented for the j-th rotor in the hub-wind frame, are

$$\boldsymbol{F}^{(j),HW} = [H\ Y\ T]^{(j),HW} \qquad \text{and} \qquad \boldsymbol{M}^{(j),HW} = [L\ M\ Q]^{(j),HW} \tag{4.8}$$

The loads are rotated from hub-wind to body f.o.r. by means of the following transformation:

$$\boldsymbol{F}^{(j)} = \begin{bmatrix} \cos i_s & 0 & -\sin i_s \\ 0 & 1 & 0 \\ \sin i_s & 0 & \cos i_s \end{bmatrix} \begin{bmatrix} \cos\beta_w & \sin\beta_w & 0 \\ -\Gamma\sin\beta_w & \Gamma\cos\beta_w & 0 \\ 0 & 0 & 1 \end{bmatrix} \boldsymbol{F}^{(j),HW} \tag{4.9}$$

$$\boldsymbol{M}^{(j)} = \begin{bmatrix} \cos i_s & 0 & -\sin i_s \\ 0 & 1 & 0 \\ \sin i_s & 0 & \cos i_s \end{bmatrix} \begin{bmatrix} \Gamma\cos\beta_w & \Gamma\sin\beta_w & 0 \\ -\sin\beta_w & \cos\beta_w & 0 \\ 0 & 0 & \Gamma \end{bmatrix} \boldsymbol{M}^{(j),HW} + \boldsymbol{r}_H^{(j)} \times \boldsymbol{F}^{(j),HW} \tag{4.10}$$

where $\beta_w = \mathrm{atan}_2(v^{HB}, u^{HB})$. The total external force and moment generated by the main rotors of the side-by-side helicopter modeled with the analytical approach, plus the fuselage contribution are

$$\boldsymbol{F} = \boldsymbol{F_f} + \boldsymbol{F}^{(1)} + \boldsymbol{F}^{(2)} \tag{4.11}$$

$$\boldsymbol{M} = \boldsymbol{M_f} + \boldsymbol{M}^{(1)} + \boldsymbol{M}^{(2)} \tag{4.12}$$

4.3.4 Inflow

The rotor inflow is the airflow induced by the rotor at the disc level, which contributes to the dynamic pressure of the blades and the generation of the aerodynamic loads. Modeling the rotor inflow is a fundamental aspect of the mathematical framework and requires ODEs to define its dynamics. For the sake of this Section, the inflow is modeled with a first-order ODE, describing a uniform, nonlinear, induced inflow ratio, derived from general momentum theory [78]. In particular

$$\dot{\lambda}_i = \frac{3\pi}{4}\left(\frac{C_T}{2} - \lambda_i\sqrt{\mu^2 + \lambda}\right) \qquad \text{where the total inflow ratio} \qquad \lambda = \lambda_i + \frac{w^H}{\Omega R} \tag{4.13}$$

and the uniform, time-dependent, rotor-induced velocity is defined as $v_i = \lambda_i \Omega R$.

4.3.5 Flap dynamics

The blade's flapping dynamics describe the vertical bending of the blades subjected to the aerodynamic, centrifugal, and inertial forces on the hinge that connects the blades' root to the rotor shaft. The flapping angle of the i-th blade β_i is approximated by the tip path plane (TPP) representation described by the first harmonic of the Fourier expansion. In particular

$$\beta_i = a_0 - a_1 \cos\psi_i - b_1 \sin(\psi_i) \tag{4.14}$$

where the time-varying coefficients a_0, a_1, and b_1 follow the second-order dynamics law developed by Chen [137], [138] and ψ_i describes the azimuthal position of the i-th blade. The TPP dynamics is expressed as

$$\ddot{\boldsymbol{\beta}} + H_1\dot{\boldsymbol{\beta}} + H_2\boldsymbol{\beta} = H_3 \qquad \text{where} \qquad \boldsymbol{\beta} = [a_0 \; a_1 \; b_1]^T \tag{4.15}$$

and the expression of matrixes H_1, H_2 and H_3 can be found in Ref. [138] with a different notation. a_0, a_1, and b_1 are the coning angle, longitudinal, and lateral tip-path plane coefficients.

4.4 Main rotor: numerical modeling approach

4.4.1 Overview of the model

In this Section, a numerical model for the main rotor forces and moments is described. This approach leads to the definition of a 24 dof mathematical model, made of 24 ordinary differential equations:

- 6 equations for the first-order rigid body motion
- 12 equations for the second-order main rotor dynamics, including flap and lead-lag motion
- 6 equations for the first-order, non-uniform dynamic inflow.

Similarly with the analytical representation, the rotor angular frequency is kept constant and the analysis will focus on flight conditions generally operated at constant RPM. The numerical modeling approach introduces a higher level of complexity in the mathematical framework but also allows for more accurate studies. Each blade is modeled separately, with its design changing from section to section and the loads numerically integrated along the span. Specific blade and airfoil design can be performed with this approach, as well as studying vibrations, particular chord distributions, non-conventional blade designs, and unbalanced rotors. However, as already mentioned, this approach brings different complexities into the formulation, and dealing with a numerical approach in flight dynamics requires the formulation of suitable trim and linearization methodologies. To this extent, three major issues were identified:

1. the single-blade representation of the rotor dynamics leads to a loss of physical meaning when developing linear state-space representations;
2. the rotor dynamics formulated with a Lagrangian approach on the single-blade produces a high level of coupling between flap and lead-lag dynamics, and the two effects cannot be isolated;
3. the presence of complex, nonlinear terms derived by numerical integration, makes the linearization process impractical with an explicit version of the equations, thus additional approximations should be applied.

In order to study the trim, stability, and flight dynamics properties of the rotorcraft, a linearized state space representation must be produced and the three issues addressed by implementing a set of guidelines. The implementation of the numerical model aims also at isolating the effects of the single rotor dynamics and studying their influence on rigid body stability. This secondary goal arises whenever an analytical representation such as the one presented in Section 4.3 becomes unable to predict the rotorcraft behavior under specific flight conditions. The idea of comparing the two models is indeed carried out to validate the two representations and define whether one or the other is more suited for specific studies.

The mathematical framework and trim methodology were initially validated by comparing the results with the Taamallah [55] formulation for a classical helicopter configuration. The linearization methodology and results were instead compared with the analytical modeling approach.

4.4.2 Frames of reference

Five main frames of reference are defined in the numerical representation, as shown in Figures 4.4 and 4.5. The body f.o.r. is defined in the same way as in Section 4.3.2, while the two hub-body f.o.r. are both right-handed and centered on each rotor center of rotation. A third f.o.r. is defined in this framework, the local blade f.o.r., identified by the superscript ^{bl}. This frame is specifically centered on the center of pressure of each blade section and it is rotated (starting from the hub-body directions) with the typical angles of the blade, thus its azimuthal position ψ_i, local twist θ_{bl}, flap β_i and lead-lag angles ξ_i. Figure 4.5 shows the positive direction of each angle, with respect to a clockwise rotor. The rotation from the hub-body to the local blade f.o.r. is made of a sequence of rotations that starts from a constant rotation matrix ($\mathcal{R}_{HB_0-HB}$ and $\mathcal{R}_{HB-HB_0}$) and subsequently rotate the frame of the specific angle at that hinge. Considering Figure 4.5, the P hinge is the local pitch one, F stands for flapping, and L for lead-lag. The rotation matrix from a generic frame/hinge m to another one n is represented by the notation $\mathcal{R}_{n-m}$. In particular,

$$\mathcal{R}_{HB-bl} = \mathcal{R}_{bl-F} \cdot \mathcal{R}_{F-L} \cdot \mathcal{R}_{L-P} \cdot \mathcal{R}_{P-HB_0} \cdot \mathcal{R}_{HB_0-HB} \tag{4.16}$$

and

$$\mathcal{R}_{bl-HB} = \mathcal{R}_{HB-HB_0} \cdot \mathcal{R}_{HB_0-P} \cdot \mathcal{R}_{P-L} \cdot \mathcal{R}_{L-F} \cdot \mathcal{R}_{F-bl} \tag{4.17}$$

where

$$\mathcal{R}_{HB_0-HB} = \begin{bmatrix} 0 & 1 & 0 \\ -1 & 0 & 0 \\ 0 & 0 & 1 \end{bmatrix} \quad \text{and} \quad \mathcal{R}_{HB-HB_0} = \begin{bmatrix} 0 & -1 & 0 \\ 1 & 0 & 0 \\ 0 & 0 & 1 \end{bmatrix} \quad , \tag{4.18}$$

$$\mathcal{R}_{bl-F}(\beta_i) = \mathcal{R}_{F-bl}(-\beta_i) = \begin{bmatrix} 1 & 0 & 0 \\ 0 & \cos\beta_i & -\sin\beta_i \\ 0 & \sin\beta_i & \cos\beta_i \end{bmatrix} , \tag{4.19}$$

$$\mathcal{R}_{F-L}(\xi_i) = \mathcal{R}_{L-F}(-\xi_i) = \begin{bmatrix} \cos\xi_i & \Gamma\sin\xi_i & 0 \\ -\Gamma\sin\xi_i & \cos\xi_i & 0 \\ 0 & 0 & 1 \end{bmatrix} , \tag{4.20}$$

$$\mathcal{R}_{L-P}(\theta_{bl_i}) = \mathcal{R}_{P-L}(-\theta_{bl_i}) = \begin{bmatrix} \cos\theta_{bl_i} & 0 & -\Gamma\sin\theta_{bl_i} \\ 0 & 1 & 0 \\ \Gamma\sin\theta_{bl_i} & 0 & \cos\theta_{bl_i} \end{bmatrix}, \text{and} \tag{4.21}$$

$$\mathcal{R}_{P-HB_0}(\psi_i) = \mathcal{R}_{HB_0-P}(-\psi_i) = \begin{bmatrix} \cos\psi_i & -\Gamma\sin\psi_i & 0 \\ \Gamma\sin\psi_i & \cos\psi_i & 0 \\ 0 & 0 & 1 \end{bmatrix}. \tag{4.22}$$

On the other hand the rotation between hub-body and body f.o.r. is regulated by the lateral (i_c) and longitudinal (i_s) incidence angles. In particular

$$\mathcal{R}_{HB-B}(i_s, i_c) = \mathcal{R}_{B-HB}(-i_s, -i_c) = \begin{bmatrix} \cos i_s & 0 & -\sin i_s \\ \sin i_c \sin i_s & \cos i_c & \sin i_c \cos i_s \\ \cos i_c \sin i_s & -\sin i_s & \cos i_c \cos i_s \end{bmatrix} \tag{4.23}$$

Two additional f.o.r. have to be defined in this approach. The first one is the tip-path plane (TPP) rotor coordinate system, identified by the superscript ^{TPP}, and whose x^{TPP} and y^{TPP} axes lay on the plane connecting the three blade tips. The TPP plane is the equivalent of the rotor disc, tilted according to the blades' flapping coefficients (see Section 4.4.5), and the rotation from hub-body to TPP is

$$\mathcal{R}_{TPP-HB} = \begin{bmatrix} \cos a_1 & 0 & -\sin a_1 \\ 0 & \cos b_1 & \Gamma\sin b_1 \\ \sin a_1 & -\Gamma\sin b_1 & \cos a_1 \cos b_1 \end{bmatrix} \tag{4.24}$$

By rotating the TPP towards the wind speed direction, the wind-tip-path plane rotor coordinate system is obtained (superscript ^{TPP_w}). Considering the sideslip angle at the tip-path plane

$$\beta_w = \arctan\left(\frac{v^{TPP}}{u^{TPP}}\right) \quad \text{where} \quad \boldsymbol{U}^{TPP} = \begin{bmatrix} u^{TPP} \\ v^{TPP} \\ w^{TPP} \end{bmatrix} = \mathcal{R}_{TPP-HB}\mathcal{R}_{HB-B}\left[\boldsymbol{U} + \boldsymbol{\omega} \times \boldsymbol{r}_{HB}\right] \tag{4.25}$$

the rotation matrix from TPP to TPP_w is

$$\mathcal{R}_{TPP_w-TPP} = \begin{bmatrix} \cos\beta_w & \sin\beta_w & 0 \\ -\sin\beta_w & \cos\beta_w & 0 \\ 0 & 0 & 1 \end{bmatrix} \tag{4.26}$$

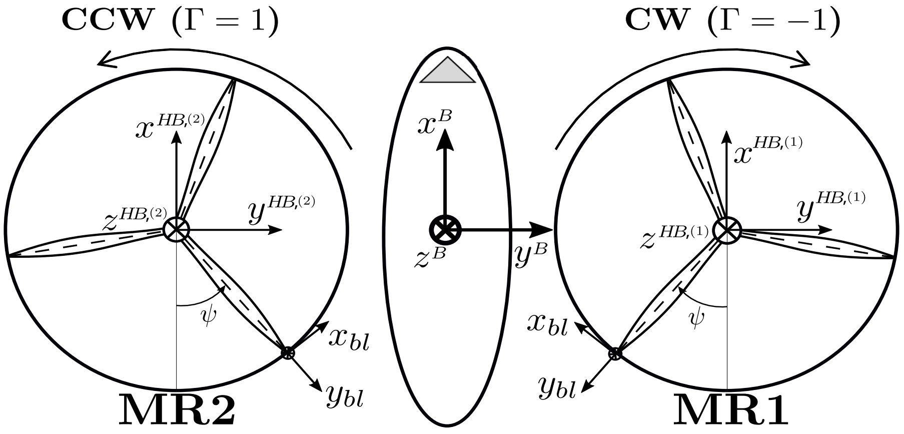

Figure 4.4: Coordinate systems of the numerical modeling framework

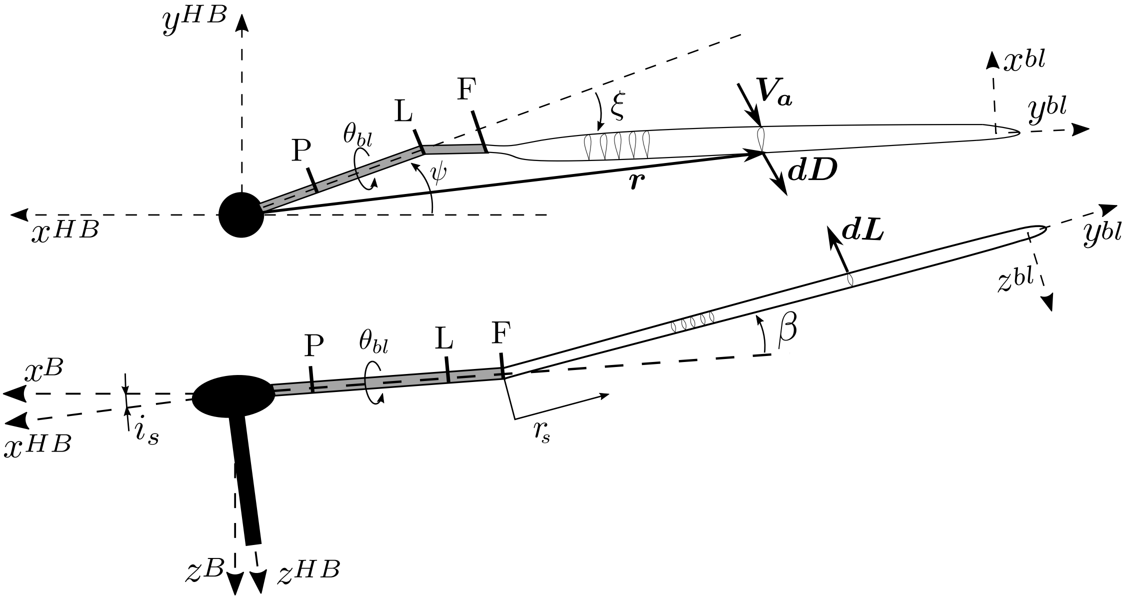

Figure 4.5: Blade's frame of reference in a P-L-F sequence rotor [139]

4.4.3 Main rotor

Describing the main rotor loads with a numerical model requires a blade element approach: each blade is divided into a finite number of sections, each of them governed by 2D aerodynamics, whose infinitesimal contributions are integrated along the blade span. The main rotor forces are divided into three contributions: aerodynamic ($\boldsymbol{F_a}$), inertial ($\boldsymbol{F_i}$), and centrifugal ($\boldsymbol{F_c}$). The main rotor moments are provided by their aerodynamic ($\boldsymbol{M_a}$), inertial ($\boldsymbol{M_i}$), and flap hinge stiffness ($\boldsymbol{M_s}$) components. Considering the single-blade contribution of a Γ-rotating rotor (where $\Gamma = 1$ for a counter-clockwise rotor and $\Gamma = -1$ for a clockwise rotor), the aerodynamic force in the hub-body frame of the i-th blade (subscript $_i$) is computed as

$$\boldsymbol{F_{a_i}}^{HB} = \int_{r_c}^{R-e_0} \mathcal{R}_{HB-bl}(\boldsymbol{dL}^{bl} + \boldsymbol{dD}^{bl})dr_s \tag{4.27}$$

where the infinitesimal force given by the sum of lift and drag ($\boldsymbol{dL}$ and $\boldsymbol{dD}$), rotated from local blade to hub-body frame of reference, is integrated along the blade span, from the root cutout to the blade tip. The infinitesimal lift and drag contributions are computed as

$$\boldsymbol{dL}^{bl} = \frac{1}{2}\rho|\boldsymbol{V_a}|^2 C_L(\alpha, Re)c \begin{bmatrix} \Gamma \sin\alpha \\ 0 \\ -\cos\alpha \end{bmatrix}, \tag{4.28}$$

$$\boldsymbol{dD}^{bl} = \frac{1}{2}\rho|\boldsymbol{V_a}|^2 C_D(\alpha, Re)c \begin{bmatrix} -\Gamma \cos\alpha \\ 0 \\ -\sin\alpha \end{bmatrix} \tag{4.29}$$

where C_L and C_D are the aerodynamic lift and drag coefficients of the specific blade section subjected to a Reynolds number Re and an angle of attack α. The modeling approach for airfoil's aerodynamics is described in Section 4.6, while α and Re are computed from the relative aerodynamic velocity at that specific blade section. In particular

$$\alpha = \arctan\left(\frac{V_{a,z}}{V_{a,x}}\right) \qquad \text{and} \qquad Re = \frac{|\boldsymbol{V_a}|c}{\nu} \tag{4.30}$$

where ν is the kinematic viscosity of air. $\boldsymbol{V_a}^{bl} = [V_{a,x}\ V_{a,y}\ V_{a,z}]$ is the relative wind speed observed by the blade section at a radial location r_s of the i-th blade at the azimuthal coordinate ψ_i. It is a combination of inertial $\boldsymbol{V_i}$ and inflow v_i (see Section 4.4.4) velocities, plus the gust contribution $\boldsymbol{V_g}$. Estimating $\boldsymbol{V_a}^{bl}$ requires the knowledge of the rotor flap and lead-lag angles, the location of their hinges, and the flight condition. In particular

$$\boldsymbol{V_a}^{bl} = \mathcal{R}_{bl-HB}\left(\boldsymbol{V_i}^{HB} - \begin{bmatrix} 0 \\ 0 \\ v_i \end{bmatrix} - \boldsymbol{V_g}^{HB}\right) \tag{4.31}$$

The formulation of the inertial velocity $\boldsymbol{V_i}^{HB} = [V_{i,x}\ V_{i,y}\ V_{i,z}]$ was inspired by Taamallah [82], and is here reported for a generic rotor (superscript $^{(j)}$ is here omitted for the sake of simplicity):

$$\begin{aligned} V_{i,x} = {} & u + \Omega(\sin\psi_i[e_L + e_P + \cos\xi_i(e_F + r_s\cos\beta_i)] - \cos\psi_i[\cos\theta_{bl_i}\sin\xi_i(e_F + r_s\cos\beta_i) \\ & + r_s\sin\beta_i\sin\theta_{bl_i}]) + \dot{\xi}_i(e_F + r_s\cos\beta_i)[\cos\psi_i\sin\xi_i - \sin\psi_i\cos\theta_{bl_i}\cos\xi_i] \\ & + \dot{\beta}_i r_s[\cos\psi_i\cos\xi_i\sin\beta_i + \sin\psi_i(\cos\theta_{bl_i}\sin\xi_i\sin\beta_i - \cos\beta_i\sin\theta_{bl_i}] \\ & + \dot{\theta}_{bl_i}\sin\psi_i[\sin\theta_{bl_i}\sin\xi_i(e_F + r_s\cos\beta_i) - r_s\sin\beta_i\cos\theta_{bl_i}] \\ & + q\,(z_H - r_s\cos\theta_{bl_i}\sin\beta_i + (e_F + r_s\cos\beta_i)\sin\xi_i\sin\theta_{bl_i}) \\ & - r(y_H - \Gamma\cos\psi_i(\cos\theta_{bl_i}\sin\xi_i(e_F + r_s\cos\beta_i) + r_s\sin\beta_i\sin\theta_{bl_i}) \\ & + \Gamma\sin\psi_i(e_L + e_P + \cos\xi_i(e_F + r_s\cos\beta_i))) \end{aligned} \tag{4.32}$$

$$\begin{aligned} V_{i,y} = {} & v + \Omega\Gamma((e_L + e_P)\cos\psi_i + r_s\sin\psi_i\sin\beta_i\sin\theta_{bl_i} \\ & + (e_F + r_s\cos\beta_i)(\cos\psi_i\cos\xi_i + \sin\psi_i\cos\theta_{bl_i}\sin\xi_i)) \\ & - \dot{\xi}_i\Gamma(e_F + r_s\cos\beta_i)[\cos\psi_i\cos\xi_i\cos\theta_{bl_i} + \sin\psi_i\sin\xi_i] \\ & + \dot{\beta}_i r_s\Gamma(\cos\psi_i\cos\theta_{bl_i}\sin\xi_i\sin\beta_i - \cos\psi_i\cos\beta_i\sin\theta_{bl_i} - \sin\psi_i\cos\xi_i\sin\beta_i) \\ & + \dot{\theta}_{bl_i}\Gamma\cos\psi_i[\sin\theta_{bl_i}\sin\xi_i(e_F + r_s\cos\beta_i) - r_s\sin\beta_i\cos\theta_{bl_i}] \\ & - p(z_H - (r_s\cos\theta_{bl_i}\sin\beta_i - (e_F + r_s\cos\beta_i)\sin\xi_i\sin\theta_{bl_i})) \\ & + r(x_H - (\cos\psi_i(e_L + e_P + \cos\xi_i(e_F + r_s\cos\beta_i)) + \sin\psi_i(\cos\theta_{bl_i}\sin\xi_i(e_F + r_s\cos\beta_i) \\ & + r_s\sin\beta_i\sin\theta_{bl_i}))) \end{aligned} \tag{4.33}$$

$$\begin{aligned} V_{i,z} = {} & w + \dot{\xi}_i\cos\xi_i\sin\theta_{bl_i}(e_F + r_s\cos\beta_i) - \dot{\beta}_i r_s(\cos\beta_i\cos\theta_{bl_i} + \sin\beta_i\sin\xi_i\sin\theta_{bl_i}) \\ & + \dot{\theta}_{bl_i}[r_s\sin\theta_{bl_i}\sin\beta_i + (e_F + r_s\cos\beta_i)\sin\xi_i\cos\theta_{bl_i}] \\ & + p(y_H - \Gamma\cos\psi_i(\cos\theta_{bl_i}\sin\xi_i(e_F + r_s\cos\beta_i) + r_s\sin\beta_i\sin\theta_{bl_i}) \\ & + \Gamma\sin\psi_i(e_L + e_P + \cos\xi_i(e_F + r_s\cos\beta_i))) - q(x_H - \cos\psi_i(e_L + e_P + \cos\psi_i(e_F + r_s\cos\beta_i)) \\ & - \sin\psi_i(\cos\theta_{bl_i}\sin\xi_i(e_F + r_s\cos\beta_i) + r_s\sin\beta_i\sin\theta_{bl_i})) \end{aligned} \tag{4.34}$$

The local twist angle θ_{bl_i} is instead the parameter where the pilot controls enter into the computation. It is a time-dependent parameter, specific for the i-th blade of the j-th rotor, which changes according to the blade's location, the pilot controls, and the design of the blades. It is determined as

$$\theta_{bl_i}^{(j)} = \theta_0^{(j)} + A_{1s}^{(j)}\cos(\psi_i + \psi_\theta) + B_{1s}^{(j)}\sin(\psi_i + \psi_\theta) + \frac{r_s}{R}\theta_w - K_{t\xi}\xi_i - K_{t\beta}\beta_i \tag{4.35}$$

where the parameter ψ_θ is used to consider the swashplate's phase angle in the local twist definition. Additional force contributions are the inertial and centrifugal components, which are modeled as, respectively,

$$\boldsymbol{F_{i_i}}^{HB} = m_{bl}\eta_\xi\ddot{\xi}_i \begin{bmatrix} \Gamma\cos\psi_i \\ -\sin\psi_i \\ 0 \end{bmatrix}, \qquad \text{and} \qquad \boldsymbol{F_{c_i}}^{HB} = \frac{1}{2}m_{bl}(\Omega R)^2 \begin{bmatrix} \Gamma\sin\psi_i \\ \cos\psi_i \\ 0 \end{bmatrix} \tag{4.36}$$

where $\eta_\xi = R - e_P - e_L$.

The aerodynamic moment in the hub-body frame of the i-th blade is computed as the integral of the infinitesimal moment contributions at each blade section (r_s), given by the cross product between the section position vector with respect to the hub center $\boldsymbol{r}$ and the aerodynamic force. In mathematical terms

$$\boldsymbol{M_{a_i}}^{HB} = \int_{r_c}^{R-e_0} \boldsymbol{r} \times [\mathcal{R}_{HB-bl}(\boldsymbol{dL}^{bl} + \boldsymbol{dD}^{bl})]dr_s \tag{4.37}$$

where $\boldsymbol{r} = [r_x\ r_y\ r_z]$ and

$$\begin{aligned} r_x &= -\cos\psi_i(e_L + e_P + \cos\xi_i(e_F + r_s\cos\beta_i)) - \sin\psi_i(\cos\theta_{bl_i}\sin\xi_i(e_F + r_s\cos\beta_i) + r_s\sin\beta_i\sin\theta_{bl_i}) \\ r_y &= -\Gamma\cos\psi_i(\cos\theta_{bl_i}\sin\xi_i(e_F + r_s\cos\beta_i) + r_s\sin\beta_i\sin\theta_{bl_i}) + \Gamma\sin\psi_i(e_L + e_P + \cos\xi_i(e_F + r_s\cos\beta_i)) \\ r_z &= -r_s\cos\theta_{bl_i}\sin\beta_i + (e_F + r_s\cos\beta_i)\sin\xi_i\sin\theta_{bl_i} \end{aligned} \tag{4.38}$$

Additional moments come from the flap hinge stiffness and inertial contributions and depend on the rotor disc tilt coordinates a_1 and b_1 (see Section 4.4.5). Those are respectively

$$\boldsymbol{M_{s_i}}^{HB} = \frac{1}{1-\frac{e_0}{R}}\frac{N_b K_{s\beta}}{2}\begin{bmatrix} \Gamma b_1 \\ a_1 \\ 0 \end{bmatrix}, \qquad \text{and} \qquad \boldsymbol{M_{i_i}}^{HB} = \frac{N_b}{2}m_{bl}e_0 r_G\Omega^2 \begin{bmatrix} \Gamma b_1 \\ a_1 \\ 0 \end{bmatrix} \tag{4.39}$$

Finally, the total external force and moment in the body f.o.r. applied by the j-th rotor is computed by the sum of the contributions of each blade plus the moment derived by the cross product between the rotor hub position and the external force. In particular,

$$\boldsymbol{F}^{(j)} = \mathcal{R}_{B-HB}\sum_{i=1}^{N_b}(\boldsymbol{F_{a_i}}^{HB} + \boldsymbol{F_{c_i}}^{HB} + \boldsymbol{F_{i_i}}^{HB}) \tag{4.40}$$

$$\boldsymbol{M}^{(j)} = \boldsymbol{r}_{HB} \times \boldsymbol{F}^{(j)} + \mathcal{R}_{B-HB}\sum_{i=1}^{N_b}(\boldsymbol{M_{a_i}}^{HB} + \boldsymbol{M_{s_i}}^{HB} + \boldsymbol{M_{i_i}}^{HB}) \tag{4.41}$$

The two rotors share the same design and operate at equal and constant angular speed; their only differences are their location with respect to the rotorcraft's CG and the sense of rotation. The total external force and moment acting on the VTOL, expressed in body f.o.r., are

$$\boldsymbol{F} = \boldsymbol{F}^{(1)} + \boldsymbol{F}^{(2)} + \boldsymbol{F_f} \tag{4.42}$$

$$\boldsymbol{M} = \boldsymbol{M}^{(1)} + \boldsymbol{M}^{(2)} + \boldsymbol{M_f} \tag{4.43}$$

4.4.4 Inflow

The dynamics of the rotor inflow, modeled in the numerical framework, follows a different approach than the one presented in the previous Sections. In particular, a nonuniform dynamic inflow is described by a set of three first-order ODEs, describing the time-dependent inflow ratio coordinates $\boldsymbol{\lambda} = [\lambda_0\ \lambda_c\ \lambda_s]$. In particular, considering a generic rotor, the inflow velocity ad a specific blade section (r_s, ψ_i) is

$$v_i = \Omega R\left(\lambda_0 + \lambda_s\frac{r_s}{R}\sin\psi_i + \lambda_c\frac{r_s}{R}\cos\psi_i\right) \tag{4.44}$$

where λ_0, λ_c and λ_s are respectively the uniform, lateral and longitudinal inflow ratios. The dynamics of $\boldsymbol{\lambda}$ is described by the Peters-Ha [140] formulation of the well-known Pitt-Peters inflow model, and is here reported as arranged for the sake of this paper. In particular

$$M\dot{\boldsymbol{\lambda}} = -\Omega(L_1 L_2)^{-1}\boldsymbol{\lambda} + \Omega\boldsymbol{C}_{aero} \tag{4.45}$$

where

$$M = \begin{bmatrix} \frac{8}{3\pi} & 0 & 0 \\ 0 & \frac{16}{45\pi} & 0 \\ 0 & 0 & \frac{16}{45\pi} \end{bmatrix} \quad , \quad L_1 = \begin{bmatrix} \frac{1}{2} & 0 & -\frac{15\pi}{64}\sqrt{\frac{1-\sin\alpha_T}{1+\sin\alpha_T}} \\ 0 & \frac{4}{1+\sin\alpha_T} & 0 \\ \frac{15\pi}{64}\sqrt{\frac{1-\sin\alpha_T}{1+\sin\alpha_T}} & 0 & \frac{4\sin\alpha_T}{1+\sin\alpha_T} \end{bmatrix} \tag{4.46}$$

$$\text{and} \quad L_2 = \begin{bmatrix} \mathcal{G}\sqrt{(\lambda_m-\mu_z)^2+\mu_{xy}^2} & 0 & 0 \\ 0 & \frac{\mu_{xy}^2+(2\lambda_m-\mu_z)(\lambda_m-\mu_z)}{\sqrt{(\lambda_m-\mu_z)^2+\mu_{xy}^2}} & 0 \\ 0 & 0 & \frac{\mu_{xy}^2+(2\lambda_m-\mu_z)(\lambda_m-\mu_z)}{\sqrt{(\lambda_m-\mu_z)^2+\mu_{xy}^2}} \end{bmatrix} \tag{4.47}$$

The rotorcraft advance ratio defined at the rotor disc is

$$\boldsymbol{\mu} = \begin{bmatrix} \mu_x \\ \mu_y \\ \mu_z \end{bmatrix} = \mathcal{R}_{TPP-HB}\mathcal{R}_{HB-B}\frac{\boldsymbol{U}}{\Omega R} \qquad \text{and} \qquad \mu_{xy} = \sqrt{\mu_x^2+\mu_y^2} \tag{4.48}$$

while λ_m is the normal induced inflow due to the effect of the rotor thrust coefficient C_T. It is computed by solving the nonlinear equation

$$\lambda_m = \frac{2C_T}{\sqrt{\mu_{xy}^2+(\lambda_m-\mu_z)^2}} \tag{4.49}$$

The value of L_1 depends on the angle α_T, which is the angle of attack of the tip-path plane, with respect to the incoming flow, and it is computed, given the advance ratios, as

$$\alpha_T = \arctan\frac{|\lambda_m-\mu_z|}{\mu_{xy}} \tag{4.50}$$

Finally, the known term of equation 4.45, depends on the aerodynamic coefficients of the thrust (C_T), rolling (C_{L^w}) and pitching moments (C_{M^w}) written in the wind-tip-path plane coordinate system. In particular, considering the j-th rotor

$$\boldsymbol{F}^{TPP_w,(j)} = \mathcal{R}_{TPP_w-TPP}\mathcal{R}_{TPP-HB}\mathcal{R}_{HB-B}\boldsymbol{F}^{(j)} \tag{4.51}$$

$$\boldsymbol{M}^{TPP_w,(j)} = \mathcal{R}_{TPP_w-TPP}\mathcal{R}_{TPP-HB}\mathcal{R}_{HB-B}\boldsymbol{M}^{(j)} \tag{4.52}$$

The thrust (T) is the third component of $\boldsymbol{F}^{TPP_w}$, while the rolling (L^w) and pitching moments (M^w) are respectively the first and second component of $\boldsymbol{M}^{TPP_w}$. The vector

$$C_{aero} = [C_T \; C_{L^w} \; C_{M^w}] \qquad \text{and} \tag{4.53}$$

$$C_T = \frac{T}{\rho A(\Omega R)^2} \quad , \quad C_{L^w} = \frac{L^w}{\rho A(\Omega R)^2 L_{ref}} \quad \text{and} \quad C_{M^w} = \frac{M^w}{\rho A(\Omega R)^2 L_{ref}} \tag{4.54}$$

where L_{ref} is a reference length for moments normalization.

4.4.5 Flap and lead-lag dynamics

The numerical modeling approach described in this section accounts for an additional rotor dynamic feature. While the blades' flapping has already been described by the analytical framework (Section 4.3.5), the rotor lead-lag motion is taken into account on an advanced modeling stage. The blades' lead lag describes the in-plane motion of the blades around the lag hinge due to the equilibrium between aerodynamic and centrifugal forces. The full rotor dynamics is described by a system of second-order ordinary differential equations derived with a Lagrangian method by Tamallah [55] for the P-L-F (Pitch-Lag-Flap) small-scale helicopter rotor. The system has 6 degrees of freedom for each rotor and describes the coupled flap and lead-lag dynamics in a rotating frame of reference. In particular, for the i-th blade

$$\begin{cases} \ddot{\beta}_i &= \dfrac{1}{A_1}(-D_i^{\beta}\dot{\xi}_i + Q_i^{\beta} - F_i^{\beta}) \\ \ddot{\xi}_i &= \dfrac{1}{A_2}(-D_i^{\xi}\dot{\beta}_i + Q_i^{\xi} - F_i^{\xi}) \end{cases} \tag{4.55}$$

where $A_1 = \dfrac{m_{bl}(R-e_0)^2}{3}$ and $A_2 = m_{bl}\left(e_F^2 + 2e_F r_G + \dfrac{(R-e_0)^2}{3}\right)$ are constants which depend on the blade's inertia. The terms D_i^{β} and D_i^{ξ} are non-linear coupling terms whose expression can be found in Ref. [82] and is specific for the i-th blade. Similarly, $Q_i - F_i$ is the excitation of each ODE and represents the generalized force that creates the flapping and lead-lag motion [82]. A numerical approach such as the one described in this section, eliminates the need for complex algebraic expansions of the blade's nonlinear structural dynamics, but it also requires a methodology for in-place linearization and trim analysis. It has been observed that the flap-lag equations derived in this form present some criticalities. Three major issues can be identified:

1. The single-blade representation of the rotor dynamics is suitable for the rotorcraft simulation, but leads to a loss of physical meaning when developing linear state-space representations;
2. Rotor dynamics obtained by a Lagrangian approach on the single-blade representation, produce a high level of coupling between flap and lead-lag dynamics;
3. The presence of complex, nonlinear terms derived by numerical integration, makes the linearization process impractical with an explicit version of the equations.

The first step for addressing the criticality number 1, is to transform equation 4.55 in a non-rotating frame, by describing the rotor flap and lead-lag angles with the Coleman representation for a 3-bladed rotor [141]. In particular, for the i-th blade,

$$\begin{cases} \beta_i = a_0 - a_1\cos\psi_i - b_1\sin\psi_i \\ \dot{\beta}_i = \dot{a}_0 - \dot{a}_1\cos\psi_i - \dot{b}_1\sin\psi_i + a_1\Omega\sin\psi - b_1\Omega\cos\psi \\ \ddot{\beta}_i = \ddot{a}_0 - \ddot{a}_1\cos\psi_i - \ddot{b}_1\sin\psi_i + (a_1\Omega^2 - 2\dot{b}_1\Omega - b_1\dot{\Omega})\cos\psi_i + (b_1\Omega^2 + 2\dot{a}_1\Omega + a_1\dot{\Omega})\sin\psi_i \\ \xi_i = \xi_0 - \xi_c\cos\psi_i - \xi_s\sin\psi_i \\ \dot{\xi}_i = \dot{\xi}_0 - \dot{\xi}_c\cos\psi_i - \dot{\xi}_s\sin\psi_i + \xi_c\Omega\sin\psi - \xi_s\Omega\cos\psi \\ \ddot{\xi}_i = \ddot{\xi}_0 - \ddot{\xi}_c\cos\psi_i - \ddot{\xi}_s\sin\psi_i + (\xi_c\Omega^2 - 2\dot{\xi}_s\Omega - \xi_s\dot{\Omega})\cos\psi_i + (\xi_s\Omega^2 + 2\dot{\xi}_c\Omega + \xi_c\dot{\Omega})\sin\psi_i \end{cases} \tag{4.56}$$

where the tip-path plane dynamics is described by the coned-shaped rotor coordinates, i.e. the coning angle a_0 and the lateral and longitudinal flap coordinates a_1 and b_1. The motion of the rotor center of gravity is instead described by the lead-lag coordinates in the non-rotating frame, i.e. the collective ξ_0, and the advancing/regressive lag, ξ_c and ξ_s. By substituting equations 4.56 into equations 4.55, the rotor dynamics can be then expressed in the following form:

$$\begin{cases} \ddot{\boldsymbol{\beta}} = -K_1^{\beta}\dot{\boldsymbol{\beta}} - K_0^{\beta}\boldsymbol{\beta} + C_1^{\beta}\dot{\boldsymbol{\xi}} + C_0^{\beta}\boldsymbol{\xi} + \boldsymbol{E}^{\boldsymbol{\beta}} \\ \ddot{\boldsymbol{\xi}} = -K_1^{\xi}\dot{\boldsymbol{\xi}} - K_0^{\xi}\boldsymbol{\xi} + C_1^{\xi}\dot{\boldsymbol{\beta}} + C_0^{\xi}\boldsymbol{\beta} + \boldsymbol{E}^{\boldsymbol{\xi}} \end{cases} \tag{4.57}$$

where $\boldsymbol{\beta} = [a_0 \; a_1 \; b_1]$ and $\boldsymbol{\xi} = [\xi_0 \; \xi_c \; \xi_s]$ are, respectively the vector of tip path plane and rotor center of gravity coordinates. The expression of the K, C, and $\boldsymbol{E}$ terms is derived manually and reported below. In particular, K_0 and K_1 are constant matrices (at each time step) derived from the frame transformation, while C_0 and C_1 are representative of the level of coupling between flap and lead-lag dynamics. Those matrixes are highly non-linear, and an explicit transformation from a rotating to a non-rotating frame was not feasible. $\boldsymbol{E}^{\boldsymbol{\beta}}$ and $\boldsymbol{E}^{\boldsymbol{\xi}}$ are instead the excitation of the second order ODE, represented by the flapping and lead-lag moments computed with numerical integration. The mathematical formulation of the K terms, considering the same transformation applied for flap and lead-lag, is

$$K_1^{\beta} = K_1^{\xi} = \begin{bmatrix} 1 & -\cos\psi_1 & -\sin\psi_1 \\ 1 & -\cos\psi_2 & -\sin\psi_2 \\ 1 & -\cos\psi_3 & -\sin\psi_3 \end{bmatrix}^{-1} \begin{bmatrix} 0 & 2\Omega\sin\psi_1 & -2\Omega\cos\psi_1 \\ 0 & 2\Omega\sin\psi_2 & -2\Omega\cos\psi_2 \\ 0 & 2\Omega\sin\psi_3 & -2\Omega\cos\psi_3 \end{bmatrix} \tag{4.58}$$

$$K_0^{\beta} = K_0^{\xi} = \begin{bmatrix} 1 & -\cos\psi_1 & -\sin\psi_1 \\ 1 & -\cos\psi_2 & -\sin\psi_2 \\ 1 & -\cos\psi_3 & -\sin\psi_3 \end{bmatrix}^{-1} \begin{bmatrix} 0 & \Omega^2\cos\psi_1 + \dot{\Omega}\sin\psi_1 & \Omega^2\sin\psi_1 - \dot{\Omega}\cos\psi_1 \\ 0 & \Omega^2\cos\psi_2 + \dot{\Omega}\sin\psi_2 & \Omega^2\sin\psi_2 - \dot{\Omega}\cos\psi_2 \\ 0 & \Omega^2\cos\psi_3 + \dot{\Omega}\sin\psi_3 & \Omega^2\sin\psi_3 - \dot{\Omega}\cos\psi_3 \end{bmatrix} \tag{4.59}$$

Similarly, for the coupling and forcing terms C and E, the formulation is equivalent for flap and lead-lag, but with a different expression of the internal coefficients

$$C_1^{\beta} = \frac{1}{A_1} \begin{bmatrix} 1 & -\cos\psi_1 & -\sin\psi_1 \\ 1 & -\cos\psi_2 & -\sin\psi_2 \\ 1 & -\cos\psi_3 & -\sin\psi_3 \end{bmatrix}^{-1} \begin{bmatrix} -D_1^{\beta} & 0 & 0 \\ 0 & -D_2^{\beta} & 0 \\ 0 & 0 & -D_3^{\beta} \end{bmatrix} \begin{bmatrix} 1 & -\cos\psi_1 & -\sin\psi_1 \\ 1 & -\cos\psi_2 & -\sin\psi_2 \\ 1 & -\cos\psi_3 & -\sin\psi_3 \end{bmatrix} \tag{4.60}$$

$$C_0^{\beta} = \frac{1}{A_1} \begin{bmatrix} 1 & -\cos\psi_1 & -\sin\psi_1 \\ 1 & -\cos\psi_2 & -\sin\psi_2 \\ 1 & -\cos\psi_3 & -\sin\psi_3 \end{bmatrix}^{-1} \begin{bmatrix} -D_1^{\beta} & 0 & 0 \\ 0 & -D_2^{\beta} & 0 \\ 0 & 0 & -D_3^{\beta} \end{bmatrix} \begin{bmatrix} 0 & \Omega\sin\psi_1 & -\Omega\cos\psi_1 \\ 0 & \Omega\sin\psi_2 & -\Omega\cos\psi_2 \\ 0 & \Omega\sin\psi_3 & -\Omega\cos\psi_3 \end{bmatrix} \tag{4.61}$$

$$C_1^{\xi} = \frac{1}{A_2} \begin{bmatrix} 1 & -\cos\psi_1 & -\sin\psi_1 \\ 1 & -\cos\psi_2 & -\sin\psi_2 \\ 1 & -\cos\psi_3 & -\sin\psi_3 \end{bmatrix}^{-1} \begin{bmatrix} -D_1^{\xi} & 0 & 0 \\ 0 & -D_2^{\xi} & 0 \\ 0 & 0 & -D_3^{\xi} \end{bmatrix} \begin{bmatrix} 1 & -\cos\psi_1 & -\sin\psi_1 \\ 1 & -\cos\psi_2 & -\sin\psi_2 \\ 1 & -\cos\psi_3 & -\sin\psi_3 \end{bmatrix} \tag{4.62}$$

$$C_0^{\xi} = \frac{1}{A_2} \begin{bmatrix} 1 & -\cos\psi_1 & -\sin\psi_1 \\ 1 & -\cos\psi_2 & -\sin\psi_2 \\ 1 & -\cos\psi_3 & -\sin\psi_3 \end{bmatrix}^{-1} \begin{bmatrix} -D_1^{\xi} & 0 & 0 \\ 0 & -D_2^{\xi} & 0 \\ 0 & 0 & -D_3^{\xi} \end{bmatrix} \begin{bmatrix} 0 & \Omega\sin\psi_1 & -\Omega\cos\psi_1 \\ 0 & \Omega\sin\psi_2 & -\Omega\cos\psi_2 \\ 0 & \Omega\sin\psi_3 & -\Omega\cos\psi_3 \end{bmatrix} \tag{4.63}$$

$$\boldsymbol{E}^{\boldsymbol{\beta}} = \frac{1}{A_1} \begin{bmatrix} 1 & -\cos\psi_1 & -\sin\psi_1 \\ 1 & -\cos\psi_2 & -\sin\psi_2 \\ 1 & -\cos\psi_3 & -\sin\psi_3 \end{bmatrix}^{-1} \begin{bmatrix} Q_1^{\beta} - F_1^{\beta} \\ Q_2^{\beta} - F_2^{\beta} \\ Q_3^{\beta} - F_3^{\beta} \end{bmatrix} \tag{4.64}$$

$$\boldsymbol{E}^{\boldsymbol{\xi}} = \frac{1}{A_2} \begin{bmatrix} 1 & -\cos\psi_1 & -\sin\psi_1 \\ 1 & -\cos\psi_2 & -\sin\psi_2 \\ 1 & -\cos\psi_3 & -\sin\psi_3 \end{bmatrix}^{-1} \begin{bmatrix} Q_1^{\xi} - F_1^{\xi} \\ Q_2^{\xi} - F_2^{\xi} \\ Q_3^{\xi} - F_3^{\xi} \end{bmatrix} \tag{4.65}$$

The subscripts $_1$, $_2$ and $_3$ are used to identify the single blade.

The second criticality related to this formulation arises when solving the system of rotor dynamic equations. The system in equation 4.57 represents the rotor dynamics in a non-rotating frame and can be solved with classical numerical methods [142]. However, to fundamentally understand the effects of isolated rotor dynamics on the overall stability of the rotorcraft and identify the major responsible for dangerous instabilities, a highly coupled system such as the one reported above is not suitable, being the flap and lead-lag effects highly influenced by each other. To this extent, a partially decoupled solution must be found. To do so, the dynamic is solved with a Simulink scheme depicted in Fig. 4.6. At each time-step, t, the flap and lead-lag equations are solved separately by approximating the coupling and forcing terms with value of rotor flap and lead-lag coordinates at the previous time-step ($t - \Delta t$). In the algorithm, $\boldsymbol{\psi} = [\psi_1\ \psi_2\ \psi_3]$ is the vector of single blade's azimuthal coordinates used to compute the constant matrixes (K_0 and K_1). With the same azimuthal positions and the single blade flap and lead-lag angles, derived from the inverse Coleman transformation, the C_0, C_1 and $\boldsymbol{E}$ terms of the equations are computed and used to solve the dynamics. The algorithm allows for solving the rotor equations with a partial decoupling so one or the other dynamics can be excluded by simply cutting off its branch and isolating its effect on the overall system.

The third criticality will be addressed by the linearization process, described in Section 4.9.2

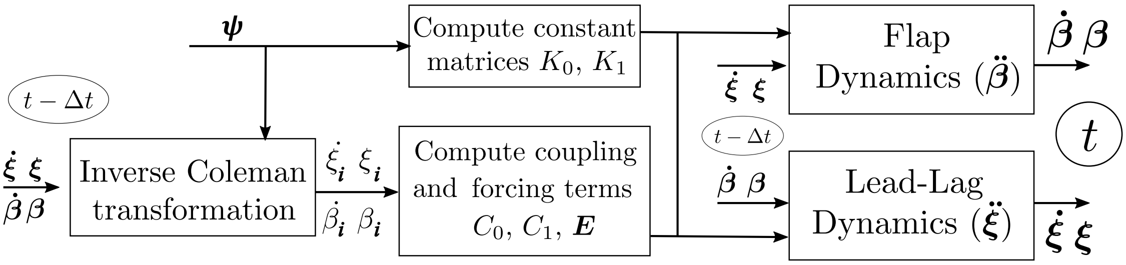

Figure 4.6: Simulink algorithm to partially decouple and solve rotor dynamics in a non-rotating frame of reference [139]

4.5 Fuselage modeling

The fuselage aerodynamic loads are included in a separate block and represented with a continuous, analytical, model. Several approaches can be adopted to characterize the forces and moments generated by the airframe under freestream conditions, each having different accuracy and computational costs. The most common methods are based on computational fluid dynamics and experimental testing [143], [144]. However, while in the second case, a wind tunnel facility would be needed, the first one requires very high computational costs and the capability to setup numerical simulations to solve the full Navier-Stokes equations. In general, a critical requirement for modeling the fuselage loads is to provide an analytical representation that is continuous around a 3D space, and numerically stable when implemented in a Matlab routine. Two different methods are presented in this thesis, both providing a fast and complete estimation of the aerodynamic loads around the airframe of the rotorcraft.

Method 1: Open VSP model
This method is based on the equivalent flat plate area definition: the fuselage is approximated by an equivalent parallelepiped, having a specific frontal, lateral, and upper surface (S), each characterized by a drag coefficient (C_D). It is assumed that the fuselage does not produce any lift force and the parasite drag provides its unique aerodynamic contribution. The approximation can be considered reliable as soon as the airframe behaves as a bluff body, thus the contribution of the lift is negligible with respect to the drag. With such an approximation, the aerodynamic force of the fuselage follows the direction of the relative airspeed. Figure 4.7 depicts the fuselage flat plate approximation, with $\hat{\boldsymbol{x}}$, $\hat{\boldsymbol{y}}$ and $\hat{\boldsymbol{z}}$ representing the versors perpendicular to each surface and $\hat{\boldsymbol{U}}$ the versor of the airspeed. The total drag is the sum of the contributions from each flat plate, while the aerodynamic moment produced by the fuselage was determined by placing the center of pressure (CP) in an arbitrary position. According to different analyses, it was observed that a positive pitching behavior of both tiltrotor [145] and multirotor [146] configurations at variable α_f was present. Nonetheless, even if a comprehensive aerodynamic analysis would be required, for the sake of the simplicity of this method, and based on the symmetry planes characterizing the vehicle, it is assumed that the aerodynamic force is applied ahead of the center of gravity (CG),

along the longitudinal axis. Under this assumption, the fuselage contributes only to pitching and yawing moments, respectively, in response to varying angles of attack and sideslip (α_f and β_f).

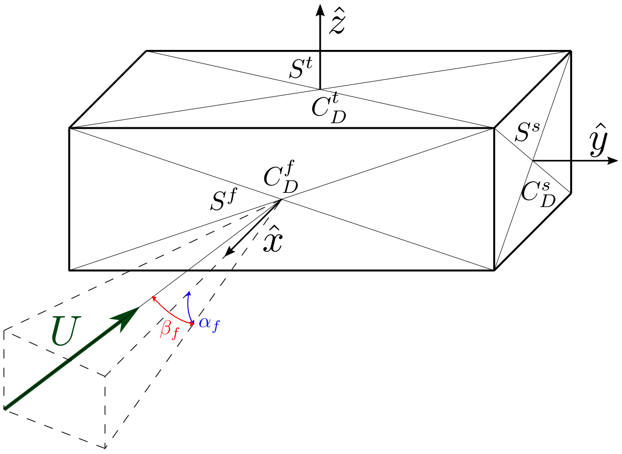

Figure 4.7: Equivalent flat-plate fuselage approximation. The fuselage angle of attack α_f and sideslip β_f are depicted [75]

This hypothesis is in agreement with the fuselage modeling approach presented by Padfield (see pp. 148 of Ref. [147]), where the fuselage moment contribution was reduced to its pitching moment due to α_f, rolling and yawing moments due to β_f. According to flat-plate aerodynamic theory, the center of pressure (CP) is assumed to be located at one-third of the fuselage's depth, corresponding to 0.26 meters ahead of the CG. In particular

$$\begin{aligned} \boldsymbol{F}_f &= -(F_f^f + F_f^t + F_f^s)\hat{\boldsymbol{U}} \\ \boldsymbol{M}_f &= \boldsymbol{r}_{CP} \times \boldsymbol{F}_f \end{aligned} \qquad \text{where} \qquad \begin{cases} F_f^f = \dfrac{1}{2}\rho U_\infty^2 S^f C_D^f \hat{U} \cdot \hat{x} \\ F_f^s = \dfrac{1}{2}\rho U_\infty^2 S^s C_D^s \hat{U} \cdot \hat{y} \\ F_f^t = \dfrac{1}{2}\rho U_\infty^2 S^t C_D^t \hat{U} \cdot \hat{z} \end{cases} \tag{4.66}$$

For a preliminary analysis, the values of the equivalent surfaces and drag coefficients are computed by adopting the panel method implemented in the software OpenVSP (Release 3.34.0), using a simplified geometry. The geometry and the body frame of reference are depicted in Figure 4.8, while the values of the coefficients are reported in Table 4.2. OpenVSP is an open-source software based on low-order aerodynamic models. The reliability of these models for the evaluation of aerodynamic loads around bluff bodies was discussed by Zhu et al. [148]. In their work, the authors compared different methods to compute the aerodynamic loads around the fuselage of the Eurocopter DGV rotorcraft, including panel methods, CFD, and experimental results. An overall good agreement was observed between the models even if an underestimated drag comes out at low Reynolds numbers from the panel method, because of the inviscid approximation. In general, the model is concluded to be suitable for isolated fuselages.

	Frontal	Lateral	Top/Bottom
S [m]	0.3426	0.2065	0.8034
C_D	0.3854	0.6356	0.1645

Table 4.2: Reference surfaces and drag coefficients of the equivalent flat plate approximation

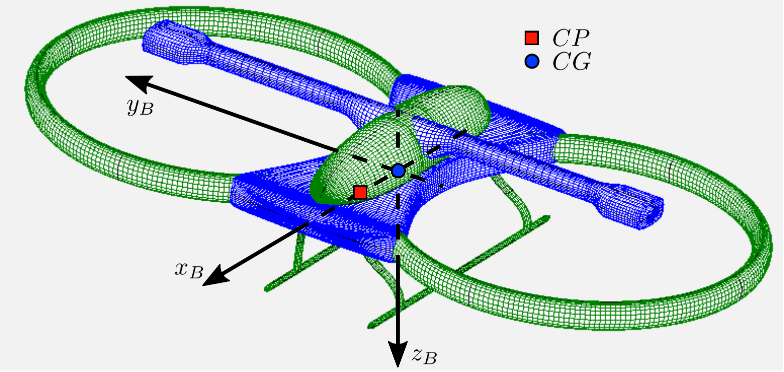

Figure 4.8: Side-by-side helicopter geometry approximation with OpenVSP [75].

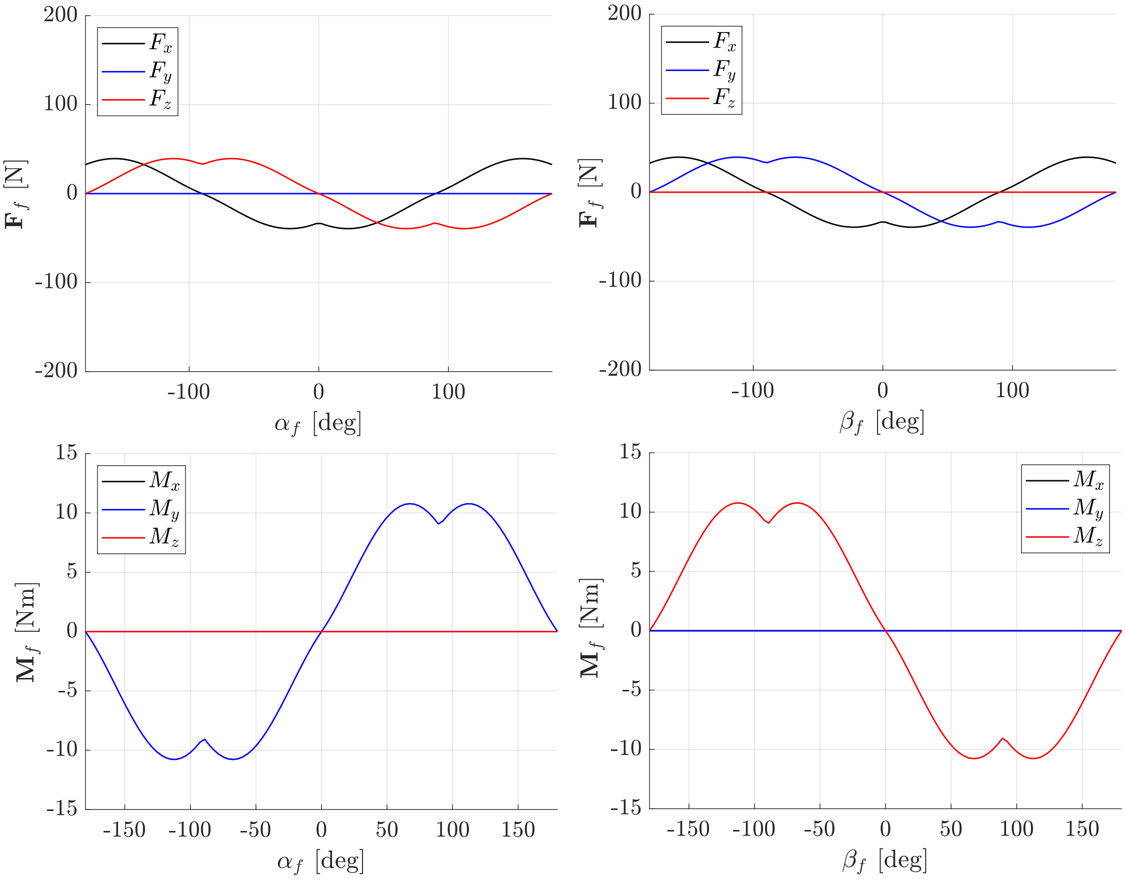

Figure 4.9: OpenVSP aerodynamic loads estimation at $|\boldsymbol{U}|= 20$ m/s

The first methodology presented in this Section, based on the OpenVSP estimations, produces the aerodynamic load estimation reported in Figure 4.9, where $\boldsymbol{F}_f = [F_x \; F_y \; F_z]$ and $\boldsymbol{M}_f = [M_x \; M_y \; M_z]$. The loads are periodic and symmetric, due to the symmetry planes characterizing the rotorcraft. It is assumed that the angle of attack does not affect the lateral force, and the sideslip does not change the vertical component. In addition, the zero-lift approximation leads to a zero vertical force component at $\alpha_f = 0$. Considering the moment estimation, this model is quite rough and simplistic, since the center of pressure is kept constant for each flow condition and always aligned with the center of gravity. This approximation leads to $\boldsymbol{M}_f(\alpha_f, \beta_f) = [0 \ M_y(\alpha_f) \ M_z(\beta_f)]$, where the moment about the x-axis remains always zero. Even if this methodology is coherent with the physical direction and the order of magnitude of forces and moments, it provides a quite rough and simplistic view of the aerodynamics around the fuselage. In order to improve the accuracy of these loads, an advanced modeling approach is proposed in this Section.

Method 2: integrated Open VSP model

This method integrates the Open VSP results, with the numerical evidence produced by Amadio [149] and Pantieri [150] in their thesis, adopting CFD tools to estimate the fuselage forces and moments at specific flight conditions. The results of their work are reported in Figure 4.10, and compared with the integrated Open VSP model presented in this Section. The latter is an analytical representation based on the one presented in method 1 and corrected to fit with the CFD results. The first observation made by comparing method 1 with CFD, was that the aerodynamic forces were initially underestimated. The reason for that is probably traceable to the zero-lift assumption and the approximation of drag due to only its parasite component. In addition, the estimation of moments, even if coherent with signs and magnitude, does not reproduce the trend highlighted by the CFD. The CP is placed in a reasonable position only for specific flight conditions, and for a variable attitude, the curves follow a different fashion. For these reasons, an integrated VSP model (iVSP) is developed by modifying the results from method 1, to reach a better agreement with the CFD results. Concerning the forces, the drag coefficients reported in Table 4.2 are corrected with empirical factors. This allows to keep the continuous trend of forces in method 1 but reach a better agreement with CFD. In particular, the integrated VSP drag coefficients ($|_i$) are

$$C_D^f|_i = 1.5C_D^f \qquad C_D^s|_i = 1.7C_D^s \qquad C_D^t|_i = 4.5C_D^t \tag{4.67}$$

where the frontal and side drag coefficients are increased, respectively, of 50% and 70%, while the most underestimated factor was the top drag. On the other hand, a different approach was followed for integrating CFD into the moment calculation, as the estimation of the center of pressure is a complicated task that strictly depends on the flight condition. Due to the symmetry planes of the rotorcraft, the aerodynamic moments of the fuselage are periodic functions of α_f and β_f with period 2π, which are symmetric with respect to the origin and can be approximated by an analytic trigonometric function. To this extent, the theory of the Fourier series is recalled [151]. A periodic function $f(x)$ of period 2π, can be approximated by a series of sine and cosine components cut at the N number of harmonics. In general

$$f(x) \approx a_0 + \sum_{n=1}^{N} (a_n \cos(nx) + b_n \sin(nx)) \tag{4.68}$$

where a_0 is the average value, while a_n and b_n are the Fourier coefficients for cosine and sine terms, respectively, and they are calculated as follows:

$$a_0 = \frac{1}{2\pi} \int_{-\pi}^{\pi} f(x) dx \tag{4.69}$$

$$a_n = \frac{1}{\pi} \int_{-\pi}^{\pi} f(x) \cos(nx) dx \tag{4.70}$$

$$b_n = \frac{1}{\pi} \int_{-\pi}^{\pi} f(x) \sin(nx) dx \tag{4.71}$$

(4.72)

The integrals are computed numerically with a trapezoidal method [152], by using the CFD results extended along a 2π period and by considering the symmetry planes of the rotorcraft. As already mentioned by Padfield [147], the most relevant moments around rotorcraft fuselage are the ones considered in this study, i.e. $M_y(\alpha_f)$, $M_x(\beta_f)$, and $M_z(\beta_f)$. These are computed as

$$M_x(\beta_f) = \frac{1}{2}\rho|\boldsymbol{U}|^2 S^f l_{ref} C_{m,x}(\beta_f) \tag{4.73}$$

$$M_y(\alpha_f) = \frac{1}{2}\rho|\boldsymbol{U}|^2 S^s l_{ref} C_{m,y}(\alpha_f) \tag{4.74}$$

$$M_z(\beta_f) = \frac{1}{2}\rho|\boldsymbol{U}|^2 S^t l_{ref} C_{m,z}(\beta_f) \tag{4.75}$$

$$\tag{4.76}$$

where $l_{ref} = 1$ m, and the coefficients $C_{m,x}(\beta_f)$, $C_{m,y}(\alpha_f)$, and $C_{m,z}(\beta_f)$ are approximated with the above mentioned Fourier series approach. In particular, $C_{m,x}(\beta_f)$ is approximated by a Fourier series cut at the $N = 7$ harmonic, while $C_{m,y}(\alpha_f)$ was cut at the $N = 6$ harmonic and $C_{m,z}(\beta_f)$ at the $N = 9$. The results of the integrated VSP model are reported in Figure 4.10, compared with the CFD outcomes. The model has in general a good agreement with the numerical analysis, it is analytical and continuous and provides a reliable estimation of the fuselage loads.

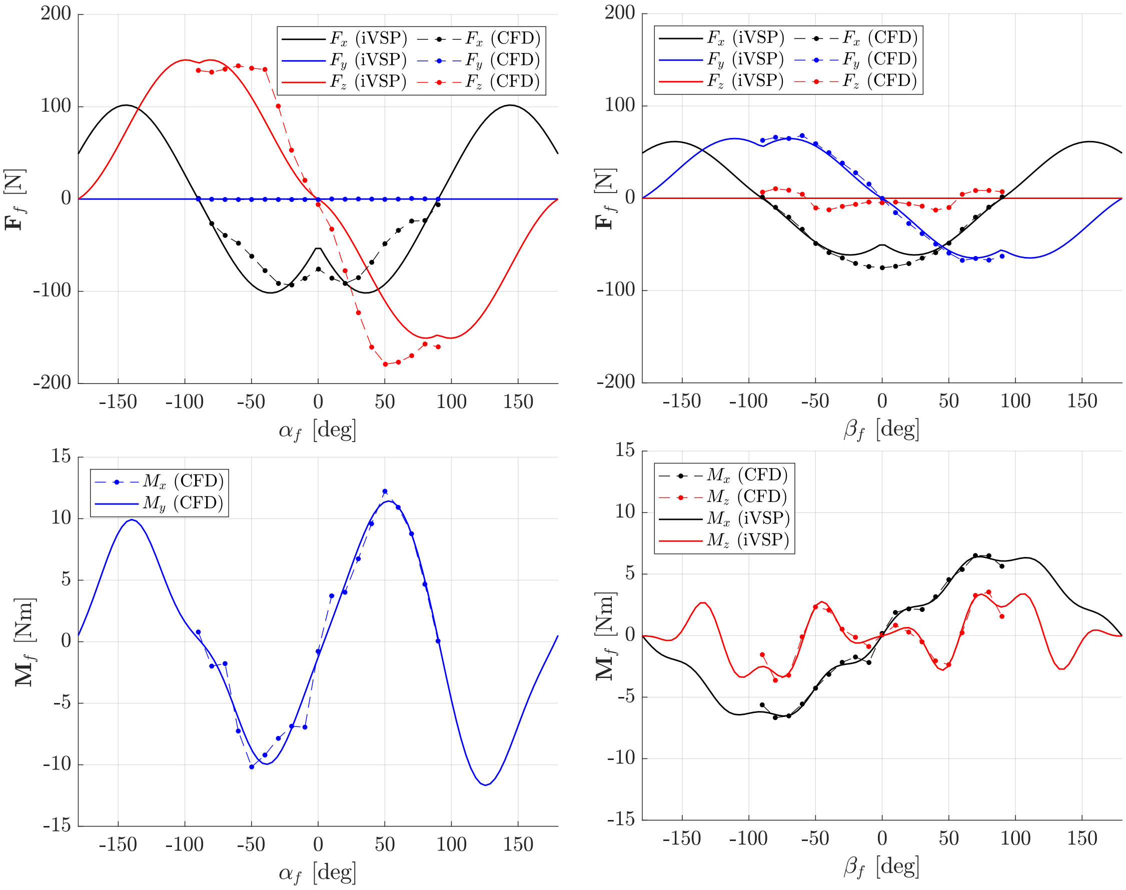

Figure 4.10: OpenVSP vs CFD geometry approximation at $|\boldsymbol{U}|$= 20 m/s

4.6 Blade's aerodynamics

Modeling the blade's aerodynamic loads is fundamental for developing reliable flight dynamics models. Both the analytical and numerical representations of the main rotor deal with the 2-dimensional aerodynamics of the airfoil and characterize the section characteristics through its lift and drag coefficients, respectively C_L and C_D. For the sake of the mathematical frameworks developed in this work, the algorithm for the computation of the aerodynamic coefficients must satisfy the following requirements:

1. the model must be defined and continuous around the entire interval of angles between $-180°$ and $+180°$;
2. the model must be simple and robust, allowing a fast computation while running flight simulations;
3. the model has to be numerical and not symbolic, to be able to solve the equations of motion with different approaches;
4. the dependency with the Reynolds number and angle of attack has to be considered;
5. the model has to be sufficiently reliable and work also on stall regimes,

Computational fluid dynamics is certainly the most common and widely used method, involving numerical algorithms to solve the Navier-Stokes equations around the 2 or 3-dimensional profiles [153], [154]. However, even if this methodology would provide quite accurate estimations and reliable results, it does not satisfy the requirements of simplicity and robustness needed in this work. The need for long computational times and the dependency of the results from the convergence of the routine, make it a not viable solution. Alternative, simpler, methods such as panel method [155], vortex lattice [156] or strip theories [157] can be considered. However, again, these theories do not fully match all the requirements set for this part, being not fully reliable around stall conditions and requiring more complex, and computational demanding, implementations than the one proposed in this work.

For these reasons, the aerodynamic loads of the airfoil adopted in this flight dynamics model, are extrapolated from experimental look-up tables provided by Abbott [158] for a *NACA0015* airfoil, and extended with the Viterna equations [159] on a continuous set of angles of attack (α, also called AoA) and Reynolds number (Re). In particular, the domain is divided into 3 regimes:

1) pre-stall, which goes from $\alpha = 0°$ to $\alpha = \alpha_s$, where α_s is the stall angle of attack identified as the AoA at which the airfoil reaches the maximum C_L, also named C_{L_s}. In this regime, the C_L is assumed to follow a linear trend until reaches the stall conditions and the C_D has a quadratic dependency with the C_L.
2) post-stall, which goes from $\alpha = \alpha_s$, to $\alpha = 90°$. Viterna equations are applied in this regime;
3) flat plate regime, which goes from $\alpha = 90°$, to $\alpha = 360°$, where it is assumed that the airfoil behaves as a flat plate.

The equations provided by Viterna guarantee an analytical and very simple continuous model that can be tuned with several parameters including the Reynolds number dependency and different airfoil characteristics. In particular, the adopted system is the following:

$$\text{Pre} - \text{stall regime}: \begin{cases} C_L = C_{L_\alpha}\alpha + C_{L_0} \\ C_D = C_{D_2}C_L^2 + C_{D_1}C_L + C_{D_0} \end{cases} \qquad \text{if} \qquad \alpha \in [0°,\ \alpha_s] \tag{4.77}$$

$$\text{Post} - \text{stall regime}: \begin{cases} C_L = k_{C_L,1}^{post}\left[\mathcal{A}_1 \sin 2\alpha + \mathcal{A}_2 \dfrac{\cos^2\alpha}{\sin\alpha}\right] + k_{C_L,0}^{post} \\ C_D = k_{C_D,1}^{post}\left[\mathcal{B}_1 \sin^2\alpha + \mathcal{B}_2 \cos\alpha\right] + k_{C_D,0}^{post} \end{cases} \qquad \text{if} \qquad \alpha \in [\alpha_s,\ 90°] \tag{4.78}$$

$$\text{Flat plate regime :} \begin{cases} C_L = k^{fp}_{C_L,1}\left[2\sin\alpha\cos\alpha\right] + k^{fp}_{C_L,0} \\ C_D = k^{fp}_{C_D,1}\left[2\sin^2\alpha\right] + k^{fp}_{C_D,0} \end{cases} \qquad \text{if} \qquad \alpha \in [90^\circ \ 360^\circ] \tag{4.79}$$

where

$$\mathcal{A}_1 = \frac{\mathcal{B}_1}{2} \qquad , \qquad \mathcal{A}_2 = (C_{L_s} - C_{D_{max}}\sin\alpha_s\cos\alpha_s)\frac{\sin\alpha_s}{\cos^2\alpha_s}, \tag{4.80}$$

$$\mathcal{B}_1 = \frac{C_{D_{max}}}{2} \qquad , \qquad \mathcal{B}_2 = \frac{(C_{D_s} - C_{D_{max}}\sin^2\alpha_s)}{\cos\alpha_s}. \tag{4.81}$$

The constant coefficients $k^{post}_{C_L,1}$, $k^{post}_{C_L,0}$, $k^{post}_{C_D,1}$, $k^{post}_{C_D,0}$, $k^{fp}_{C_L,1}$, $k^{fp}_{C_L,0}$, $k^{fp}_{C_D,1}$, and $k^{fp}_{C_D,0}$ are used to guarantee continuity of the model. They are evaluated for every different Re, and they are the result of the system imposing continuity on the stall point and the $\alpha = 90^\circ$ condition. In particular, it is solved

$$\begin{cases} C_L(\alpha_s)|_{pre} = C_L(\alpha_s)|_{post} = C_{L_s} \\ C_D(\alpha_s)|_{pre} = C_D(\alpha_s)|_{post} = C_{D_s} \\ C_L(90^\circ)|_{post} = C_L(90^\circ)|_{fp} = 0 \\ C_D(90^\circ)|_{post} = C_D(90^\circ)|_{fp} = C_{D_{max}} \end{cases} \tag{4.82}$$

where it is assumed that the airfoil produces zero lift and its maximum drag when $\alpha = 90^\circ$. The dependency from the Reynolds number is instead included into the parameters tuning the Viterna equations. While it is fixed that the airfoil behaves as a flat plate in all Re conditions, and its maximum C_D is independent of the incoming flow, the low AoA and post-stall parameters are influenced by Re. In particular, an analytical interpolation of these parameters is provided to guarantee simplicity and continuity, and

$$C_{L_\alpha} = C_{L_\alpha}(Re) = 2.18 \cdot 10^{-7} Re + 4.96 \tag{4.83}$$

$$C_{L_0} = C_{L_0}(Re) = 0 \tag{4.84}$$

$$C_{L_s} = C_{L_s}(Re) = -24.34 Re^{-0.33} + 1.63 \tag{4.85}$$

$$C_{D_0} = C_{D_0}(Re) = 412.6 Re^{-0.89} + 0.004 \tag{4.86}$$

$$C_{D_s} = C_{D_s}(Re) = 0.056\exp(-1.70 \cdot 10^{-7} Re) \tag{4.87}$$

$$C_{D_2} = C_{D_2}(Re) = -1.13 Re + 0.021 \tag{4.88}$$

$$C_{D_1} = C_{D_1}(Re) = 1.39 \cdot 10^{-9} Re + 5.67 \cdot 10^{-4} \tag{4.89}$$

According to Viterna [159], a simple estimation of the maximum drag coefficient in flat plate regimes is $C_{D_{max}} = 1.11 + 0.018AR$.

The result of this modeling approach is reported in Figure 4.12. Lift and drag coefficients are calculated with a continuous model that replicates with a simple and robust analytical framework, the trend of the aerodynamic forces around a 2 dimensional airfoil. The stall angle of attack increases with the Reynolds number, as well as the C_{Ls}. On the other hand, the minimum drag condition in the pre stall regime, which is the C_{D_0}, has an inverse behavior with respect to Re. The interpolation described in equation 4.89, is depicted in Figure 4.11, compared to the experimental data from Abbott [158].

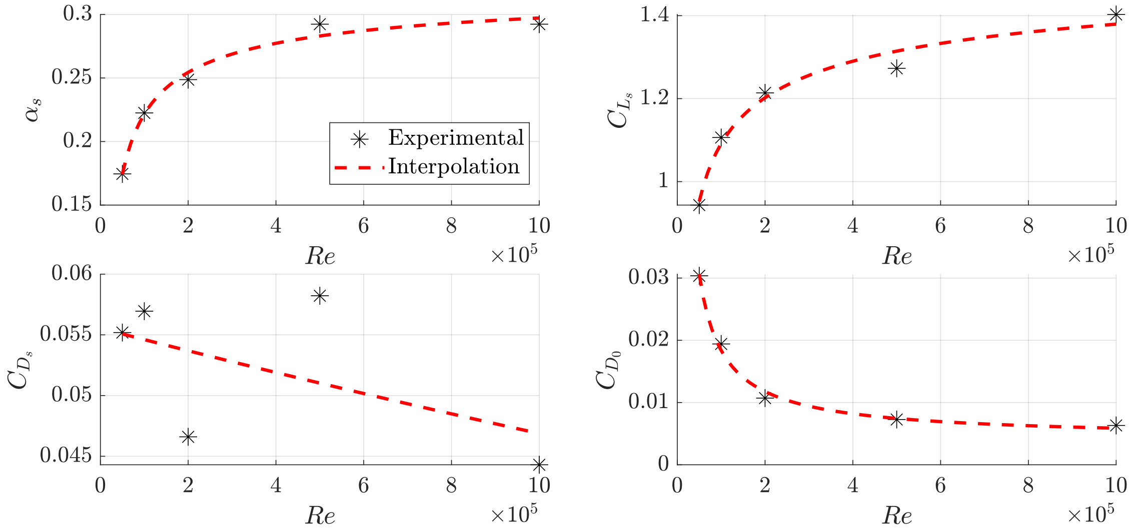

Figure 4.11: Lift and drag coefficient parameters: interpolation at variable Reynolds number

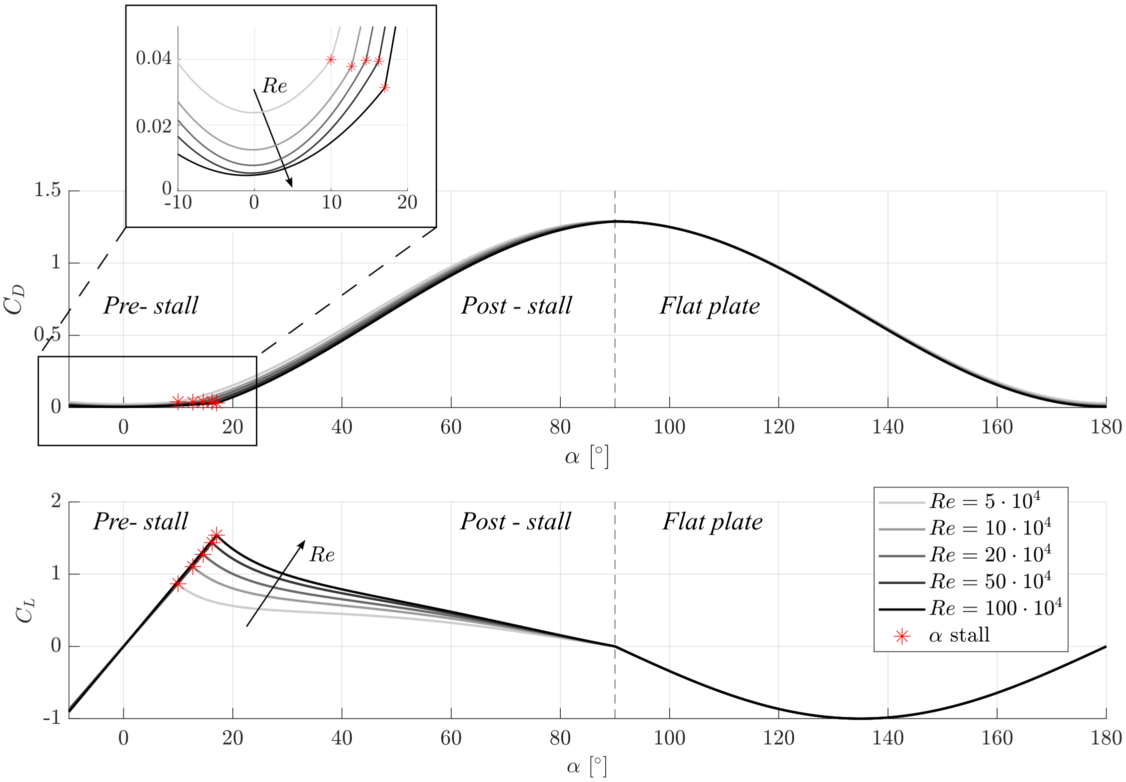

Figure 4.12: Lift and drag coefficient curves at variable angle of attack and Reynolds number

4.7 Shroud modeling

The side-by-side helicopter analyzed in this work has two shrouded rotors. The effect of the shroud on the generation of the airloads is taken into account by extending momentum theory to the analysis of a ducted fan. It has to be highlighted that this modeling approach does not take into account the aerodynamic interaction between the shroud and the surrounding flow, which would become of major importance when considering forward flight conditions. Computational fluid dynamics or wind tunnel tests can be performed in order to take those aspects into account. For the sake of this study, only the effect of the shroud on the rotor thrust was considered, by assuming an isolated and fixed rotor. To this extent, Kruger [160] showed that the presence of a duct surrounding the rotor can benefit the overall performance by decreasing the amount of power required to produce the needed thrust. Leishman [90] quantified this effect analytically by introducing a wake contraction factor a_w in the computation, such that

$$T = T^{HW} + T_d \qquad \text{where} \qquad \frac{T_d}{T} = 1 - \frac{1}{2a_w} \, . \tag{4.90}$$

T_d is an additional thrust contribution that arises from the presence of the duct and depends on the geometry of the shroud itself. Accurate estimation of a_w is a challenging task from both a numerical and an experimental point of view. Different analyses can be found in the literature for improving the accuracy of fan-in-fin tail rotor models or ducted fans [161], [162] and an extensive aerodynamic study would be required. However, for the sake of this study, an analytical and simple model is preferred. Bourtsev *et al.* [163] presented a semi-analytical model derived from experimental tests to connect the shroud geometry to its theoretical contraction factor. Different types of inlet/outlet were considered, as well as the "lip" radius (r_k) and the blades' tip clearance (δ). The wake contraction factor is

$$a_w = \frac{1}{2}\left(1 + \delta_f\left[\frac{K_v}{2} + \frac{(\xi_{in} + \xi_{out})}{2K_v} - 1\right]\right)^{-1} \tag{4.91}$$

where $\delta_f = 1 - 109\dfrac{\delta}{R}\sqrt{\dfrac{\delta}{R}}$, ξ_{in} is evaluated as a function of the lip radius according to the experimental data provided by Bourtsev *et al.* [163], and ξ_{out} is equal to zero.

4.8 Trim

4.8.1 Analytical model trim routine

The trim condition of an aircraft is the equilibrium state at which the rotorcraft accelerations are reduced to zero. A trim solution can be found per each flight condition, revealing the attitude and controls necessary to keep the rotorcraft at a certain steady-state condition. Considering the analytical representation of the main rotor, an iterative algorithm based on the Newton-Raphson method [164] is implemented to compute the trim solutions of the vehicle at different velocities. Equation 4.92 reports the full set of 16 dynamic equations of the analytical framework, which is solved in a steady-state condition by setting its first and second-order derivatives equal to zero. For the sake of simplicity, the angular rates are kept zero as well, thus $p = q = r = 0$, computing trim solution for variable forward and lateral speed. The system has 16 equations because the rotorcraft is over-actuated, meaning that the six controls operating on the two rotors are mixed to be reduced to the global four. The two additional equations accounts for the control mix law, and close the system of ODEs with 16 unknowns:

$$\begin{cases} m_{to}\dot{\boldsymbol{U}} = -m_{to}\boldsymbol{\omega} \times \boldsymbol{U} + \boldsymbol{F_g} + \boldsymbol{F} \\ I\dot{\boldsymbol{\omega}} = \boldsymbol{M} - \boldsymbol{\omega} \times I\boldsymbol{\omega} \\ \left[\ddot{\boldsymbol{\beta}} + H_1\dot{\boldsymbol{\beta}} + H_2\boldsymbol{\beta} - H_3\right]^{(1)} = 0 \\ \left[\ddot{\boldsymbol{\beta}} + H_1\dot{\boldsymbol{\beta}} + H_2\boldsymbol{\beta} - H_3\right]^{(2)} = 0 \\ \left[\dot{\lambda}_i - \frac{3\pi}{4}\left(\frac{C_T}{2} - \lambda_i\sqrt{\mu^2 + \lambda}\right)\right]^{(1)} = 0 \\ \left[\dot{\lambda}_i - \frac{3\pi}{4}\left(\frac{C_T}{2} - \lambda_i\sqrt{\mu^2 + \lambda}\right)\right]^{(2)} = 0 \\ A_{1s}^{(1)} = A_{1s}^{(2)} \\ \theta_0^{(1)} = \theta_0^{(2)} \end{cases} \quad \text{where} \quad \begin{cases} \dot{\boldsymbol{U}} = \dot{\boldsymbol{\omega}} = \boldsymbol{\omega} = 0; \\ \ddot{\boldsymbol{\beta}}^{(1)} = \dot{\boldsymbol{\beta}}^{(1)} = 0; \\ \ddot{\boldsymbol{\beta}}^{(2)} = \dot{\boldsymbol{\beta}}^{(2)} = 0; \\ \dot{\boldsymbol{\lambda}}_i^{(1)} = 0; \\ \dot{\boldsymbol{\lambda}}_i^{(2)} = 0; \end{cases} \tag{4.92}$$

and the vector of unknowns is

$$\left[a_0^{(1)}\ a_1^{(1)}\ b_1^{(1)}\ a_0^{(2)}\ a_1^{(2)}\ b_1^{(2)} \lambda^{(1)}\ \lambda^{(2)}\ \theta_0^{(1)}\ A_{1s}^{(1)}\ B_{1s}^{(1)}\ \theta_0^{(2)}\ A_{1s}^{(2)}\ B_{1s}^{(2)}\ \theta\ \phi\right]^T \tag{4.93}$$

The first six equations describe the dynamics of the rigid body. In steady state conditions, those are reduced to a sum of external forces and moments, plus the gravity contribution, equalized to zero. The gravity force, applied to the rotorcraft CG, thus not generating any moment in body f.o.r., is

$$\boldsymbol{F}_g = m_{to}\begin{bmatrix} -g\sin\theta \\ g\sin\phi\cos\theta \\ g\cos\phi\cos\theta \end{bmatrix} \tag{4.94}$$

The second six equations are the steady-state tip-path plane dynamics, while the following two are for the inflow. The yaw angle ψ is equal to zero, while the last two equations are additional relations added to close the system: a constraint on the control mix is set, such that the two rotors operate at the same collective pitch and lateral cyclic, both commanded by the pilot input (see Section 4.1). The solutions for the trim are reported in Section 5.1.1.

4.8.2 Numerical model trim routine

Computing the trim conditions with a numerical modeling framework is not as straightforward as in the case of the analytical model and requires a nonconventional, innovative, approach. The system of 26 equations describing the full dynamics of the rotorcraft is described in equation 4.95, where the rigid body accelerations, angular rates, and unsteady rotor dynamics are set to zero. Two additional relations describing the control mix are included to close the system, as already mentioned in Section 4.8.1. The full set of equations to be solved is

$$\begin{cases} m_{to}\dot{\boldsymbol{U}} & = -m_{to}\boldsymbol{\omega} \times \boldsymbol{U} + \boldsymbol{F_g} + \boldsymbol{F} \\ I\dot{\boldsymbol{\omega}} & = \boldsymbol{M} - \boldsymbol{\omega} \times I\boldsymbol{\omega} \\ A_{1s}^{(1)} & = A_{1s}^{(2)} \\ \theta_0^{(1)} & = \theta_0^{(2)} \\ \ddot{\boldsymbol{\beta}}^{(1)} & = \left[-K_1^\beta \dot{\boldsymbol{\beta}} - K_0^\beta \boldsymbol{\beta} + C_1^\beta \dot{\boldsymbol{\xi}} + C_0^\beta \boldsymbol{\xi} + \boldsymbol{E^\beta}\right]^{(1)} \\ \ddot{\boldsymbol{\beta}}^{(2)} & = \left[-K_1^\beta \dot{\boldsymbol{\beta}} - K_0^\beta \boldsymbol{\beta} + C_1^\beta \dot{\boldsymbol{\xi}} + C_0^\beta \boldsymbol{\xi} + \boldsymbol{E^\beta}\right]^{(2)} \\ \ddot{\boldsymbol{\xi}}^{(1)} & = \left[-K_1^\xi \dot{\boldsymbol{\xi}} - K_0^\xi \boldsymbol{\xi} + C_1^\xi \dot{\boldsymbol{\beta}} + C_0^\xi \boldsymbol{\beta} + \boldsymbol{E^\xi}\right]^{(1)} \\ \ddot{\boldsymbol{\xi}}^{(2)} & = \left[-K_1^\xi \dot{\boldsymbol{\xi}} - K_0^\xi \boldsymbol{\xi} + C_1^\xi \dot{\boldsymbol{\beta}} + C_0^\xi \boldsymbol{\beta} + \boldsymbol{E^\xi}\right]^{(2)} \\ \left[M\dot{\boldsymbol{\lambda}}\right]^{(1)} & = \left[-\Omega(L_1 L_2)^{-1}\boldsymbol{\lambda} + \Omega\boldsymbol{C}_{aero}\right]^{(1)} \\ \left[M\dot{\boldsymbol{\lambda}}\right]^{(2)} & = \left[-\Omega(L_1 L_2)^{-1}\boldsymbol{\lambda} + \Omega\boldsymbol{C}_{aero}\right]^{(2)} \end{cases} \quad \text{where} \quad \begin{cases} \dot{\boldsymbol{U}} = \dot{\boldsymbol{\omega}} = \boldsymbol{\omega} = 0; \\ \ddot{\boldsymbol{\beta}}^{(1)} = \dot{\boldsymbol{\beta}}^{(1)} = 0; \\ \ddot{\boldsymbol{\beta}}^{(2)} = \dot{\boldsymbol{\beta}}^{(2)} = 0; \\ \ddot{\boldsymbol{\xi}}^{(1)} = \dot{\boldsymbol{\xi}}^{(1)} = 0; \\ \ddot{\boldsymbol{\xi}}^{(2)} = \dot{\boldsymbol{\xi}}^{(2)} = 0; \\ \dot{\boldsymbol{\lambda}}^{(1)} = 0; \\ \dot{\boldsymbol{\lambda}}^{(2)} = 0; \end{cases} \tag{4.95}$$

The higher complexity of the equations and time-dependency of the results, make the application of classical numerical methods highly impractical and the results do not fully satisfy the zero-acceleration condition. The system of equations cannot be solved with a symbolic routine, since the blade element decomposition requires numerical integration to obtain the rotor forces and moments. In addition, it was observed that the trim solution is not unique per each flight condition, with the rotor loads being dependent on the azimuthal location of the blades. Having a single-blade representation of the rotor disc leads to a dependency between the rotor dynamics and the current blades' configuration ($\boldsymbol{\psi}$), while the tip-path plane and rotor CG coordinates depend on the blade location at which the numerical algorithm has started. Flap wobbling and rotor vibrations are observed such that $\boldsymbol{\beta}$ and $\boldsymbol{\xi}$ change during one revolution. For these reasons, a general solution to the trim problem that keeps the rotorcraft in a real steady-state equilibrium cannot be found if considering a unique blade setup. In order to find a solution that minimizes the average rotor accelerations, the trim has to be computed based on an average rotor force and moment in a N_c number of blade symmetric configurations. For example, by setting the parameter $N_c = 3$, the trim is solved as an average between the equispaced blade configurations depicted in Figure 4.13.

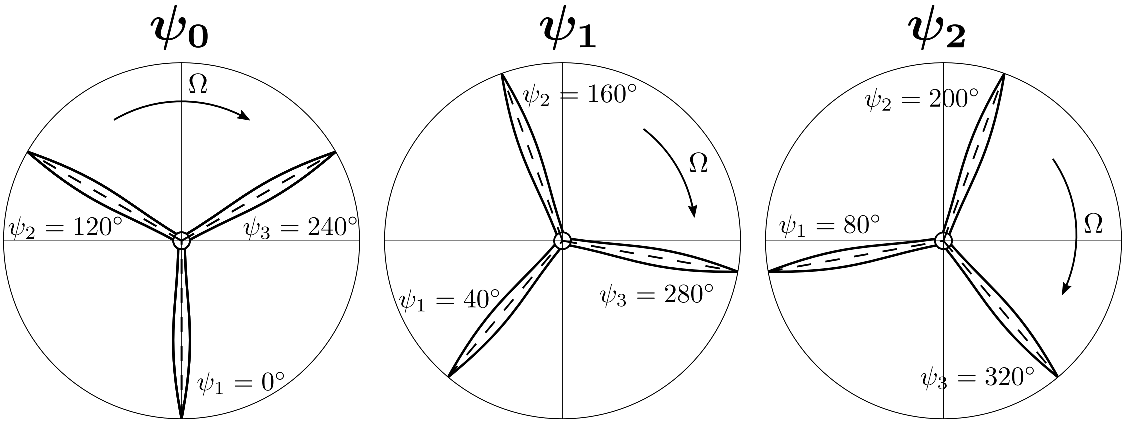

Figure 4.13: Blade configurations for a clockwise rotor with $N_b = 3$ and $N_c = 3$ [139]

Considering $\boldsymbol{\psi_0} = [\psi_1\ \psi_2\ \psi_3]_0$ the vector containing the initial position of each blade, the k-th configuration can be computed as

$$\boldsymbol{\psi_k} = \boldsymbol{\psi_0} + k\frac{2\pi}{N_b N_c} \qquad \text{where} \qquad k = 0, 1, 2, ...N_c - 1; \tag{4.96}$$

The trim algorithm is depicted in Figure 4.14. The solution to the problem is found by iteratively solving the steady-state flap-lag equations, the steady-state 6 dof equations of motion (EoM) coupled with control mix relations, and the non-uniform steady-state inflow. It was observed that to help the convergence of the algorithm, the solution of the entire system should be split into an internal and an external loop: in general, the internal loop iteratively solves the EoM and steady-state inflow for fixed rotor coordinates, while steady rotor dynamics is updated within an external routine. Each block of nonlinear equations is solved with a Newton-Raphson method. The algorithm works as follows:

a) the algorithm starts with an initial condition of the 26 unknowns (6 tip-path plane coordinates, 6 rotor CG coordinates, 6 inflow coefficients, 2 collective pitch, 4 cyclic controls, roll, and pitch attitudes);

b) the rotor dynamic equations are solved for an N_c finite number of equispaced blades' configurations and the disc tilt and rotor CG coordinates are derived for each of them. At this stage, the system of equations 4.57 is solved in a steady-state condition, for the vector of unknowns

$$\left[\ a_0^{(1)}\ a_1^{(1)}\ b_1^{(1)}\ a_0^{(2)}\ a_1^{(2)}\ b_1^{(2)}\ \xi_0^{(1)}\ \xi_c^{(1)}\ \xi_s^{(1)}\ \xi_0^{(2)}\ \xi_c^{(2)}\ \xi_s^{(2)}\ \right] \tag{4.97}$$

c) the average value of $\boldsymbol{\beta}_k$ and $\boldsymbol{\xi}_k$ is computed;

d) Knowing the average rotor coordinates and the initial condition for the inflow and rotorcraft's state, the main rotor loads are computed with equations 4.40 and 4.41. Again, this computation is repeated for N_c blade configurations.

e) the average main rotors forces and moments are computed;

f) with the average rotor disc tilts, CG coordinates and main rotor loads, the system of steady-state equations of motion, coupled with the two control mix relations, is solved (first 8 equations in system 4.95). The vector of unknowns in this block is

$$\left[\ \theta_0^{(1)}\ A_{1s}^{(1)}\ B_{1s}^{(1)}\ \theta_0^{(2)}\ A_{1s}^{(2)}\ B_{1s}^{(2)}\ \theta\ \phi\ \right] \tag{4.98}$$

g) with the new average state obtained at stage f), and the average rotor coordinates, the steady inflow dynamics for the two rotors is solved. The system is reported for a single rotor in equation 4.45, with the vector of unknowns being

$$\left[\ \lambda_0^{(1)}\ \lambda_c^{(1)}\ \lambda_s^{(1)}\ \lambda_0^{(2)}\ \lambda_c^{(2)}\ \lambda_s^{(2)}\ \right] \tag{4.99}$$

h) the internal loop that solves EoM and inflow is repeated until the following stopping criteria (maximum relative error between the rotorcraft state, inflow, and controls at each internal iteration) is satisfied:

$$err_{int} = \max\left[\frac{|SI^{ii} - SI^{ii-1}|}{|SI^{ii}|}\right] \leq tolerance \tag{4.100}$$

where SI^{ii} is the current vector of solutions (state, inflow, and controls) at the internal iteration ii, and SI^{ii-1} is the one at the previous iteration.

i) once the internal loop has converged, the rotorcraft state is updated and a new external iteration is started with the steady rotor dynamic equations. The external loop is repeated until a stopping criteria (maximum relative error between the TPP and rotor CG coordinates at each external iteration) is satisfied:

$$err_{ext} = \max\left[\frac{|SE^{ei} - SE^{ei-1}|}{|SE^{ei}|}\right] \leq tolerance \tag{4.101}$$

where SE^{ei} is the vector of solutions of the external loop (tip-path plane and rotor CG coordinates) at the external iteration ei, and SE^{ei-1} is the one at the previous iteration.

The results at a variable forward speed are reported in Section 5.2.2

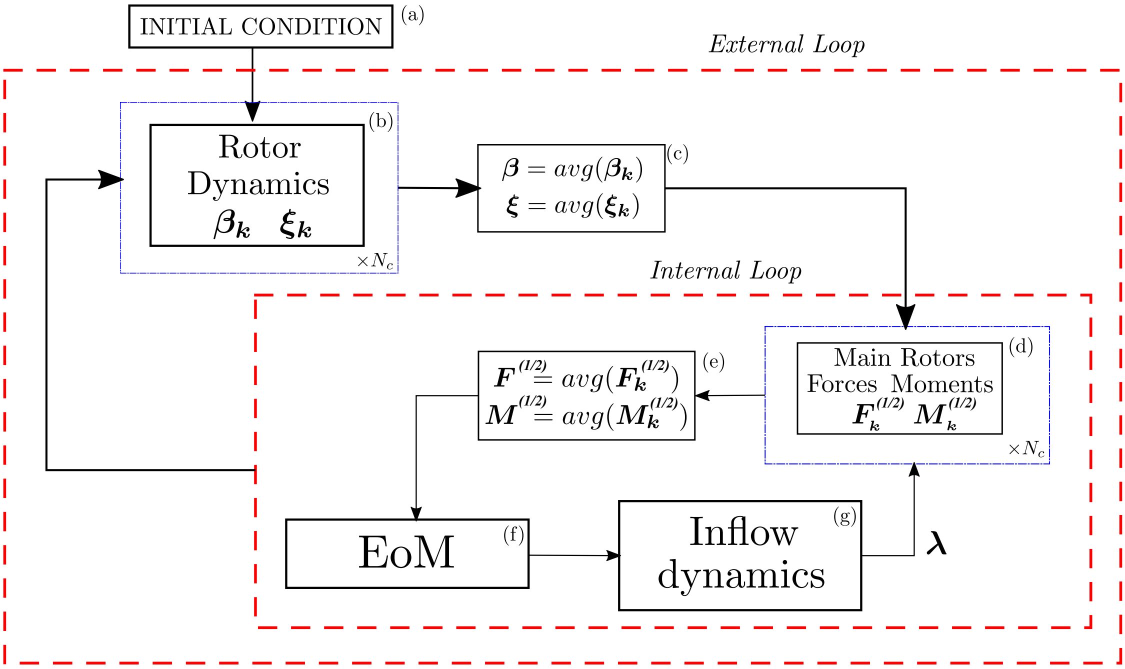

Figure 4.14: Iterative algorithm for trim computation with numerical modeling approach [139]

4.9 Linearized state-space model

4.9.1 8-states linearized model

The flight dynamic properties of an aircraft are defined by the open-loop stability assessed by linearizing its dynamics around a steady-state condition. From an experimental perspective, the stability of a system can be characterized by post-processing specific flight test data with identification tools [165], [166]. However, in case of a lack of empirical evidence, the mathematical framework can be adopted to study the analogous characteristics from a numerical perspective [62], [167], [168]. In this work, the open-loop stability of the system is studied by employing a numerical methodology: the ordinary differential equations describing the flight dynamics of the system are linearized around a specific trim condition and reduced to a linear state-space representation of the system behavior. An 8-state model can be obtained by linearizing the 6 d.o.f. rigid body equations of motion and the Euler angle definition (the heading angle Ψ is neglected as it does not affect the dynamics of the rotorcraft), which are

$$\begin{cases} m_{to}\dot{\boldsymbol{U}} & = -m_{to}\boldsymbol{\omega} \times \boldsymbol{U} + \boldsymbol{F}_g + \boldsymbol{F} \\ I\dot{\boldsymbol{\omega}} & = \boldsymbol{M} - \boldsymbol{\omega} \times I\boldsymbol{\omega} \\ \dot{\phi} & = p + q\sin\phi\tan\theta + r\cos\phi\tan\theta \\ \dot{\theta} & = q\cos\phi - r\sin\phi \end{cases} \tag{4.102}$$

where $\boldsymbol{F} = [X \ Y \ Z]$ and $\boldsymbol{M} = [L \ M \ N]$ are the excitation of the system, and include the aerodynamic loads of both the rotors and the fuselage contribution. Considering the state vector

$$\boldsymbol{x} = [u \ w \ q \ \theta \ v \ p \ \phi \ r] \qquad \text{and the control vector} \qquad \boldsymbol{\tau} = [\theta_0 \ A_{1s} \ B_{1s} \ \Delta B_{1s}] \tag{4.103}$$

the system can be reduced to the linear form

$$\dot{\boldsymbol{x}} = A_{B-B}\boldsymbol{x} + B_{B-B}\boldsymbol{\tau} \tag{4.104}$$

where A_{B-B} is the 8×8 state matrix and B_{B-B} is the 8×4 control matrix [147]. To do so, small perturbation theory and Taylor's theorem for analytic functions can be applied. Each state is described as a perturbation from its trim condition (identified by superscript ^{0}), thus, for a generic state x, $x = x^0 + \delta x$, where δx is a small perturbation. The excitation is approximated by Taylor's theorem cut at the first-order derivative such that a generic force/moment F can be expressed as its trim value (F^0) plus a sum of contributions from each state and control variable, such that

$$\boldsymbol{F} = \boldsymbol{F}^0 + \boldsymbol{F}_u u + \boldsymbol{F}_w w + ... + \boldsymbol{F}_{B_{1s}} B_{1s} + \boldsymbol{F}_{\Delta B_{1s}} \Delta B_{1s} \tag{4.105}$$

where the first-order derivative about a generic perturbation δx of the state x is computed numerically with a central finite difference formula as

$$\boldsymbol{F}_x = \left.\frac{\partial \boldsymbol{F}}{\partial x}\right|_{x^0} = \frac{\boldsymbol{F}(x^0 + \delta x) - \boldsymbol{F}(x^0 - \delta x)}{2\delta x} \tag{4.106}$$

The first-order derivatives computed with this formula, describing the behavior of a specific load around a trim condition, are called "stability derivatives", and they provide fundamental information about the stability and dynamics of the system. The value of the perturbation is chosen by performing a convergence check on the derivatives to not affect their computation. In particular, 10% of the forward velocity is chosen for the forward speed perturbation, 0.1 m/s is used for the other two components while a perturbation of 0.01 rad/s is applied to the angular velocities and 0.1 degrees for the attitude and control angles. The stability derivatives are computed manually by perturbing the dynamic system implemented in a Simulink environment and by recording the perturbed loads. On the other hand, by substituting the small perturbation description in equations 4.102, the linearized version around a trim condition with no angular rates ($p^0 = q^0 = r^0 = 0$) is described by the system

$$\begin{cases} \dot{u} &= -w^0 q - g\theta\cos\theta^0 + v^0 r + X_u u + X_w w + ... + X_{\Delta B_{1s}}\Delta B_{1s} \\ \dot{w} &= u^0 q - g\theta\cos\phi^0\sin\theta^0 - v^0 p - g\phi\sin\phi^0\cos\theta^0 + Z_u u + Z_w w + ... + Z_{\Delta B_{1s}}\Delta B_{1s} \\ \dot{q} &= M_u u + M_w w + ... + M_{\Delta B_{1s}}\Delta B_{1s} \\ \dot{\theta} &= q\cos\theta^0 - r\sin\theta^0 \\ \dot{v} &= -g\theta\sin\phi^0\sin\theta^0 + pw^0 - ru^0 + Y_u u + Y_w w + ... + Y_{\Delta B_{1s}}\Delta B_{1s} \\ \dot{p} &= L'_u u + L'_w w + ... + L'_{\Delta B_{1s}}\Delta B_{1s} \\ \dot{\phi} &= p + q\sin\phi^0\tan\theta^0 + r\cos\phi^0\tan\theta^0 \\ \dot{r} &= N'_u u + N'_w w + ... + N'_{\Delta B_{1s}}\Delta B_{1s} \end{cases} \tag{4.107}$$

from which the state and control matrices can be easily derived. The force derivatives (X, Y, and Z) are normalized with m_{to}, while the pitching moments (M) are normalized with the inertia moment with respect to the pitch axis I_{yy}. The lateral-directional derivatives L' and N' are normalized and coupled as

$$L'_{x_i} = \frac{I_{zz}L_{x_i} + I_{xz}N_{x_i}}{I_c} \tag{4.108}$$

$$N'_{x_i} = \frac{I_{xz}L_{x_i} + I_{xx}N_{x_i}}{I_c} \tag{4.109}$$

where $I_c = I_{xx}I_{zz} - I_{xz}^2$. The dynamic stability of the system can be assessed by considering the eigenvalues of the state matrix A, while the identification of the main dynamic modes through the eigenvectors analysis. The methodology presented in this Section, is applied to the analytical modeling approach.

4.9.2 38-states linearized model

The linearization process for the analytical framework has been described in Section 4.9.1, and produces an 8-state linear representation of the side-by-side helicopter flight dynamics. In this Section, a methodology for linearizing the numerical model with highly-coupled body-rotor-inflow dynamics is described. The method produces a 38-state-space representation of the side-by-side helicopter flight dynamics, including the effects of the blade's flexibility in the calculation of the open-loop stability. The core motivations for developing an alternative linearization methodology are substantially two:

- The presented methodology allows us to address the third criticality related to the numerical modeling approach, highlighted in Section 4.4.5: the presence of complex, nonlinear terms derived by numerical integration, makes the linearization process impractical with an explicit version of the equations. The system of equations describing the rotor dynamics contains coupling and forcing terms that are highly nonlinear and do not allow obtaining an explicit version such as the one adopted in the analytical representation;
- One of the objectives for developing an advanced modeling approach, with higher degrees of freedom, is to analyze the isolated effects of rotor dynamics on the rigid body stability. To this extent, a higher number of states have to be included in the linear representation, in order to be able to isolate the coupling effects and study the system stability.

The system of 38 ordinary differential equations describing the rigid body motion, rotor, and inflow dynamics is

$$\begin{cases}
m_{to}\dot{\boldsymbol{U}} & = -m_{to}\boldsymbol{\omega} \times \boldsymbol{U} + \boldsymbol{F_g} + \boldsymbol{F} \\
I\dot{\boldsymbol{\omega}} & = \boldsymbol{M} - \boldsymbol{\omega} \times I\boldsymbol{\omega} \\
\dot{\phi} & = p + q\sin\phi\tan\theta + r\cos\phi\tan\theta \\
\dot{\theta} & = q\cos\phi - r\sin\phi \\
\dot{\boldsymbol{\beta}}^{(1)} & = [\boldsymbol{d\beta}]^{(1)} \\
\dot{\boldsymbol{\beta}}^{(2)} & = [\boldsymbol{d\beta}]^{(2)} \\
\dot{\boldsymbol{d}}\boldsymbol{\beta}^{(1)} & = \left[-K_1^{\beta}\boldsymbol{d\beta} - K_0^{\beta}\boldsymbol{\beta} + C_1^{\beta}\boldsymbol{d\xi} + C_0^{\beta}\boldsymbol{\xi} + \boldsymbol{E}^{\boldsymbol{\beta}}\right]^{(1)} \\
\dot{\boldsymbol{d}}\boldsymbol{\beta}^{(1)} & = \left[-K_1^{\beta}\boldsymbol{d\beta} - K_0^{\beta}\boldsymbol{\beta} + C_1^{\beta}\boldsymbol{d\xi} + C_0^{\beta}\boldsymbol{\xi} + \boldsymbol{E}^{\boldsymbol{\beta}}\right]^{(2)} \\
\dot{\boldsymbol{\xi}}^{(1)} & = [\boldsymbol{d\xi}]^{(1)} \\
\dot{\boldsymbol{\xi}}^{(2)} & = [\boldsymbol{d\xi}]^{(2)} \\
\dot{\boldsymbol{d}}\boldsymbol{\xi}^{(1)} & = \left[-K_1^{\xi}\boldsymbol{d\xi} - K_0^{\xi}\boldsymbol{\xi} + C_1^{\xi}\boldsymbol{d\beta} + C_0^{\xi}\boldsymbol{\beta} + \boldsymbol{E}^{\boldsymbol{\xi}}\right]^{(1)} \\
\dot{\boldsymbol{d}}\boldsymbol{\xi}^{(2)} & = \left[-K_1^{\xi}\boldsymbol{d\xi} - K_0^{\xi}\boldsymbol{\xi} + C_1^{\xi}\boldsymbol{d\beta} + C_0^{\xi}\boldsymbol{\beta} + \boldsymbol{E}^{\boldsymbol{\xi}}\right]^{(2)} \\
\left[M\dot{\boldsymbol{\lambda}}\right]^{(1)} & = \left[-\Omega(L_1L_2)^{-1}\boldsymbol{\lambda} + \Omega\boldsymbol{C}_{aero}\right]^{(1)} \\
\left[M\dot{\boldsymbol{\lambda}}\right]^{(2)} & = \left[-\Omega(L_1L_2)^{-1}\boldsymbol{\lambda} + \Omega\boldsymbol{C}_{aero}\right]^{(2)}
\end{cases} \tag{4.110}$$

where the first 8 equations represent the rigid body motion plus the Euler angle definition. The second-order flap and lead-lag dynamics are described in a non-rotating frame of reference in equation 4.57, with a set of 6 equations per each rotor, are reduced to 24 first-order ODE by applying a separation of variables. In particular, $\boldsymbol{d\beta} = [\dot{a}_0 \; \dot{a}_1 \; \dot{b}_1]$ and $\boldsymbol{d\xi} = [\dot{\xi}_0 \; \dot{\xi}_c \; \dot{\xi}_s]$ are the variables added to reduce the second to first order ODEs. Again, the system of equations is linearized and reduced to the form

$$\dot{\boldsymbol{x}} = A\boldsymbol{x} + B\boldsymbol{\tau} \tag{4.111}$$

where A and B are the full state and control matrices, while in this case the state and control vectors, $\boldsymbol{x}$ and $\boldsymbol{\tau}$, are

$$\boldsymbol{x} = \left[u\ w\ q\ \theta\ v\ p\ \phi\ r\ \boldsymbol{\beta}^{(1)}\ \boldsymbol{\beta}^{(2)}\ \boldsymbol{d\beta}^{(1)}\ \boldsymbol{d\beta}^{(2)}\ \boldsymbol{\xi}^{(1)}\ \boldsymbol{\xi}^{(2)}\ \boldsymbol{d\xi}^{(1)}\ \boldsymbol{d\xi}^{(2)}\ \boldsymbol{\lambda}^{(1)}\ \boldsymbol{\lambda}^{(2)}\right] \tag{4.112}$$

$$\tau = [\theta_0\ A_{1s}\ B_{1s}\ \Delta B_{1s}] \tag{4.113}$$

Similarly to Section 4.9.1, small perturbation theory and Taylor's theorem are applied to the full set of dynamic equations to reduce system 4.110 into the linear system 4.111. Manual linearization is applied to the equations of motion and the stability derivatives of rigid body forces and moments are computed with the central finite difference formula, with respect to the full set of states in equation 4.113.

However, as already mentioned, rotor dynamics equations are in an implicit version, with coupling and forcing terms containing a nonlinear dependency with the states and numerical integration. To this extent, small-perturbation theory is only applied to the terms that are explicit in the equation above, while both forcing ($\boldsymbol{E^{\beta}}$ and $\boldsymbol{E^{\xi}}$) and coupling (C_0^{β}, C_1^{β}, C_0^{ξ} and C_1^{ξ}) terms are linearized by means of Taylor's theorem. A new set of stability derivatives is introduced with such a method, describing the level of coupling between flap and lead-lag, and flapping/lead-lag moments perturbed by each state. The state matrix A will indeed be a function of the trim condition and the full set of stability derivatives, including classical rigid body derivatives, the coupling body-rotor-inflow ones, and the term related to flap and lead-lag forcing and coupling. The general structure of the A matrix is

$$A = \begin{bmatrix} A_B(8 \times 38) \\ A_R(24 \times 38) \\ A_\lambda(6 \times 38) \end{bmatrix} = \begin{bmatrix} A_{B-B}(8 \times 8) & A_{B-R}(8 \times 24) & A_{B-\lambda}(8 \times 6) \\ A_{R-B}(24 \times 8) & A_{R-R}(24 \times 24) & A_{R-\lambda}(24 \times 6) \\ A_{\lambda-B}(6 \times 8) & A_{\lambda-R}(6 \times 24) & A_{\lambda-\lambda}(6 \times 6) \end{bmatrix} \tag{4.114}$$

where A_B, A_R and A_λ are respectively the linearized version of the rigid body, rotor, and inflow dynamics, and they are composed by a set of 3 sub-matrices for each of them. Considering, for example, the rigid body dynamics, A_{B-B} represents the 8-state linear model described in Section 4.9.1, while A_{B-R} and $A_{B-\lambda}$ represent the coupling effect of the flap, lead-lag and inflow dynamics on the body motion. On the other hand, A_{R-B} for example, represents the coupling effect of the rigid body motion on the rotor dynamics (flap and lead-lag). A_{B-R} (and similarly $A_{B-\lambda}$) is made by the stability derivatives derived by the total forces and moments, perturbed with a flap or lead-lag perturbation, i.e.

$$A_{B-R} = \begin{bmatrix} X_{a_0^{(1)}} & X_{a_1^{(1)}} & X_{b_1^{(1)}} & \cdots & X_{\xi_0^{(1)}} & \cdots \\ Z_{a_0^{(1)}} & \cdots & & & Z_{\xi_0^{(1)}} & \cdots \\ M_{a_0^{(1)}} & \cdots & & & M_{\xi_0^{(1)}} & \cdots \\ 0 & \cdots & & & 0 & \cdots \\ L_{a_0^{(1)}} & \cdots & & & L_{\xi_0^{(1)}} & \cdots \\ 0 & \cdots & & & 0 & \cdots \\ N_{a_0^{(1)}} & \cdots & & & N_{\xi_0^{(1)}} & \cdots \end{bmatrix} \tag{4.115}$$

The flap and lead-lag dynamics, instead, are represented by the linearized version of the rotor dynamics equations, i.e. A_R. This matrix is made of pure rotor-rotor dynamics (A_{R-R}) plus the coupling effects of body and inflow on the rotor itself. The structure of this matrix is

$$A_R = \begin{bmatrix} \mathbb{Z}_{24\times 8} & \begin{matrix} \mathbb{Z}_{6\times 6} & \mathbb{I}_6 & \mathbb{Z}_{6\times 6} & \mathbb{Z}_{6\times 6} \\ -K_0^{\beta} & -K_1^{\beta} & C_0^{\beta,0} & C_1^{\beta,0} \\ \mathbb{Z}_{6\times 6} & \mathbb{Z}_{6\times 6} & \mathbb{Z}_{6\times 6} & \mathbb{I}_6 \\ -K_0^{\xi} & -K_1^{\xi} & C_0^{\xi,0} & C_1^{\xi,0} \end{matrix} & \mathbb{Z}_{24\times 6} \end{bmatrix} + \begin{bmatrix} \mathbb{Z}_{6\times 1} & \cdots \\ \left[C_{0_x}^{\beta}\boldsymbol{\xi}^{\mathbf{0}} + \boldsymbol{E}_{\boldsymbol{x}}^{\boldsymbol{\beta}}\right]^{(1)} & \cdots \\ \left[C_{0_x}^{\beta}\boldsymbol{\xi}^{\mathbf{0}} + \boldsymbol{E}_{\boldsymbol{x}}^{\boldsymbol{\beta}}\right]^{(2)} & \cdots \\ \mathbb{Z}_{6\times 1} & \cdots \\ \left[C_{0_x}^{\xi}\boldsymbol{\beta}^{\mathbf{0}} + \boldsymbol{E}_{\boldsymbol{x}}^{\boldsymbol{\xi}}\right]^{(1)} & \cdots \\ \left[C_{0_x}^{\xi}\boldsymbol{\beta}^{\mathbf{0}} + \boldsymbol{E}_{\boldsymbol{x}}^{\boldsymbol{\xi}}\right]^{(2)} & \cdots \end{bmatrix} \tag{4.116}$$

where $C_0^{\beta,0}$ and $C_0^{\xi,0}$ are the coupling coefficients of flap and lead-lag equations evaluated in the trim condition, while $C_{0_x}^{\beta}$, $C_{0_x}^{\xi}$, $\boldsymbol{E}_{\boldsymbol{x}}^{\boldsymbol{\xi}}$ and $\boldsymbol{E}_{\boldsymbol{x}}^{\boldsymbol{\xi}}$ are the stability derivatives of the coupling and forcing terms, computed with respect to the generic perturbed state x as mentioned by equation 4.106. Symbols $\mathbb{Z}_{i\times j}$ and $\mathbb{I}_i$ represent, respectively, a zero matrix of dimensions $i \times j$ and an identity matrix of dimensions $i \times i$. All of those terms are derived for both main rotor 1 and 2, thus they are structured as, for example,

$$K_0^{\beta} = \begin{bmatrix} K_0^{\beta^{(1)}} & \mathbb{Z}_{3\times 3} \\ \mathbb{Z}_{3\times 3} & K_0^{\beta^{(2)}} \end{bmatrix} \tag{4.117}$$

It can be observed that A_R is split, for the sake of clarity, into two matrixes: the first one depends exclusively on the trim condition, while the second depends on the stability derivatives. It is indeed a 24×38 matrix and the general notation applied for both terms is with the x perturbed state in the last subscript. In addition, $\boldsymbol{\beta}^0$ and $\boldsymbol{\xi}^0$ are the flap and lead-lag coordinates at trim, considering the average solution found in the trim section. In general, in the j-th column of this matrix the derivatives are computed for the i-th perturbed state and for the rotor indicated by the superscript. A similar methodology is applied to the inflow dynamics to derive the linearized version of the inflow equations represented by matrix A_λ.

Chapter 5

Results on the side-by-side helicopter flight dynamics

5.1 Flight dynamics with analytical modeling

5.1.1 Trim

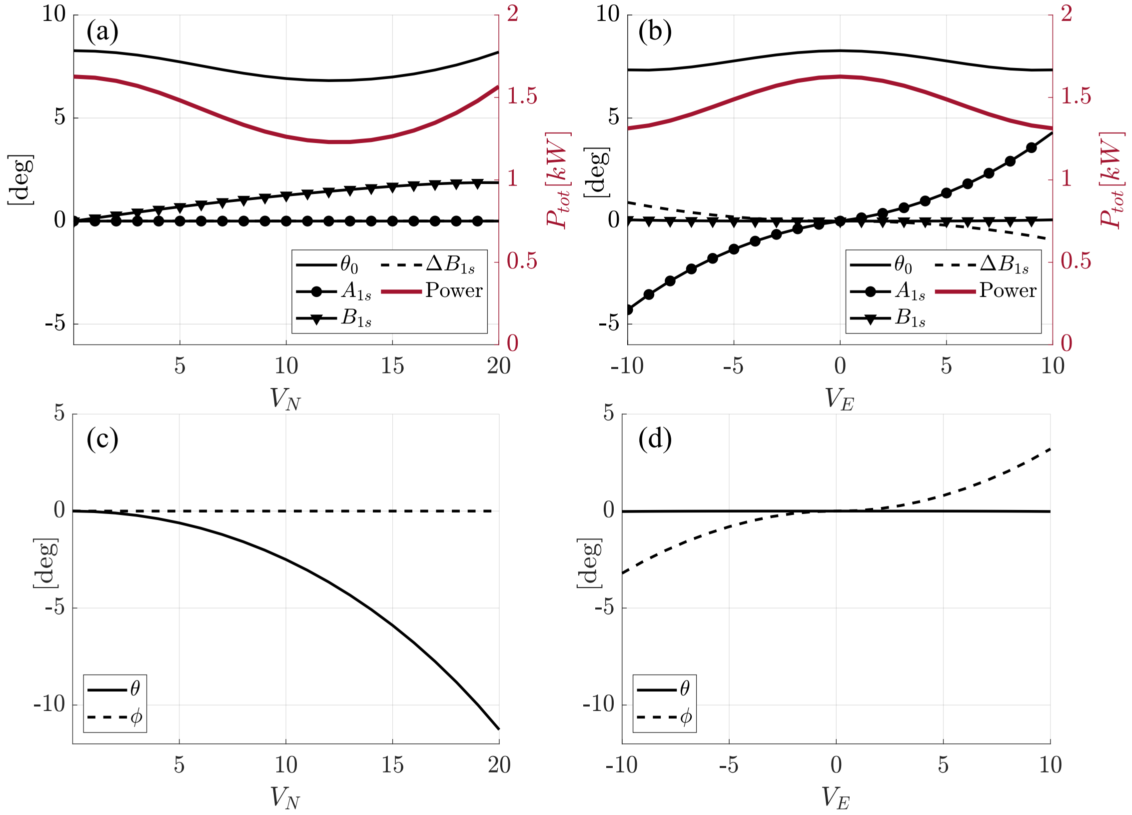

Figure 5.1: Trim conditions with an analytical modeling approach. a) Power and control inputs at variable forward speed; b) Power and control inputs at variable lateral speed; c) Rotorcraft attitude at variable forward speed; d) Rotorcraft attitude at variable lateral speed.

Section 4.8.1 described the numerical process for computing the trim conditions with an analytical modeling approach. The results are summarised in Figure 5.1. Subfigures a) and c) report the rotorcraft control inputs, power, and attitude at variable forward speed in a range of 0 to 20 m/s. As expected, the aircraft assumes a pitch-down attitude to move forward, together with a positive longitudinal cyclic control input. B_{1s} is the average value of the longitudinal cyclic applied in the two rotors and mixed with the control mixer described in Section 4.1. It is noted that, according to the mathematical model, a positive longitudinal cyclic is intended to be a "push effort" on the stick by the pilot, while the right-handed body axes system defines the attitude signs. The case study absorbs approximately 1.6 kW at hover and remains in a neutral condition with 8.2° of collective pitch applied in both rotors. It has a minimum power of 1.2 kW at 12 m/s of forward speed.

From a lateral movement perspective, the trim is computed from 0 to 10 m/s on both sides. The aircraft has symmetric behavior, decreasing the power required with the speed, and applying a lateral cyclic control in the direction of the motion. A small correction from the differential longitudinal cyclic control (ΔB_{1s}) is applied to counteract the yawing moment generated by the fuselage with the center of pressure in a forward position with respect to the CP. The $\boldsymbol{r}_{CP}$ position in front of the CG generates an unstable moment about the z-axis when the rotorcraft is subjected to a sideslip angle. The rotorcraft assumes a rolled attitude by lowering the main rotor placed in the direction of the motion.

5.1.2 Stability analysis at variable forward speed

The flight dynamic properties of the side-by-side helicopter are described by the eigenvalues and eigenvectors of the state matrix obtained from the linearized equations of motion (equations 4.107). The system poles are indeed representative of the natural responses of the aircraft to small disturbances around an equilibrium point. These poles provide crucial insights into the stability, controllability, and dynamic behavior of the vehicle and correspond to specific flight dynamics modes. Poles having a negative real part describe a stable dynamic mode, while a non-zero imaginary part is representative of an oscillatory response. Mode participation quantifies how the state variables (e.g., pitch angle, roll rate) contribute to a particular mode, enabling a deeper understanding of the dynamics and how design changes or control inputs influence stability and performance. Analyzing these poles is essential for ensuring safe and predictable behavior across a range of flight conditions, particularly for advanced rotorcraft configurations in complex operational scenarios like Urban Air Mobility.

The linearized equations of the analytical modeling approach account for 8 states participating in the 8 system poles representing the rigid body dynamics on a complex plane. For the sake of this work, the poles are identified through eigenvectors and frequency analysis and classical aircraft nomenclature is adopted. Mode participation in the system poles is represented in Figure 5.2 at a forward speed of $V_N = 5$ m/s, to show the dynamic behavior of the rotorcraft under specific state perturbations. In addition, Figure 5.3 represents the poles' frequency at variable forward speed. The system is characterized by four longitudinal poles and four lateral poles, identified by the participation of longitudinal (u, w, q, and θ) and lateral (v, p, ϕ, and r) states. From a longitudinal perspective, the rotorcraft behavior is defined by a high-frequency (around 3.7 rad/s at hover) stable and real pole, participated mainly by the vertical speed and pitch rate. This pole is referred to as short-period dynamics, which is a fast and well-damped motion involving the aircraft's pitch angle and pitch rate. An oscillatory and slightly unstable phugoid mode is instead identified by its low frequency (0.6 rad/s at hover) and a major contribution from the forward and lateral speed, and the pitch angle. The phugoid refers to a slow oscillatory motion characterized by coupled changes in airspeed and altitude. Longitudinal dynamics is also characterized by a stable and low-frequency pole, referable to a heave subsidence mode due to the prominent contribution of the vertical speed. The heave subsidence mode is indeed a fundamental, non-oscillatory motion associated with vertical (heave) movement. It represents the rotorcraft's response to disturbances or control inputs that affect its vertical velocity and primarily involves the rotor's thrust dynamics.

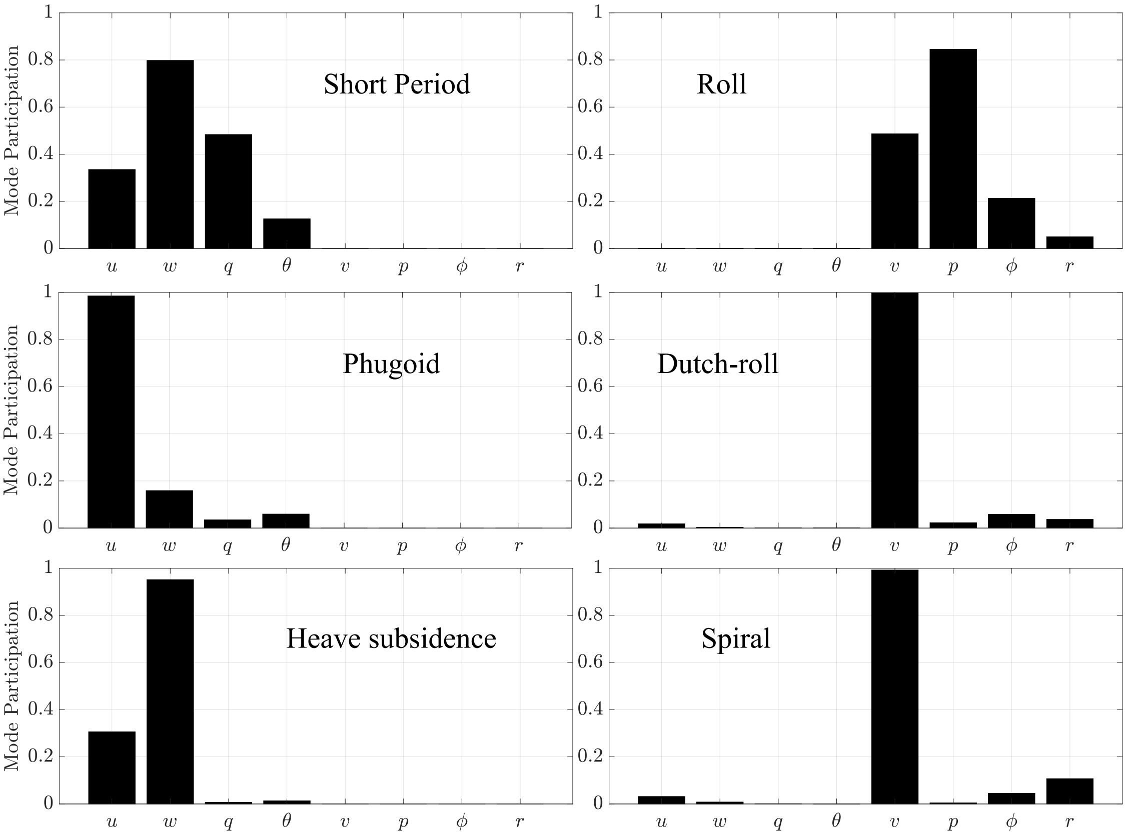

Figure 5.2: Module of the system eigenvectors at $V_N = 5$ m/s

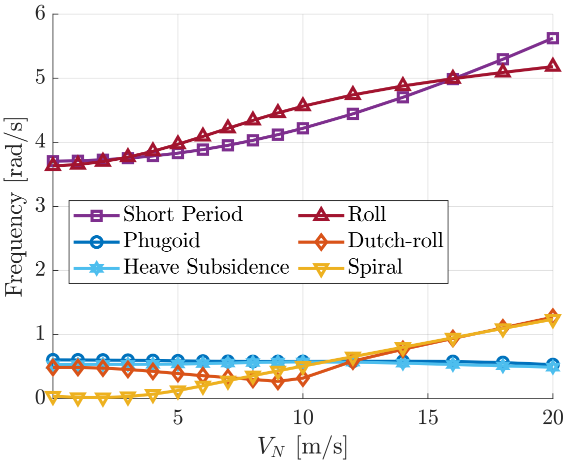

Figure 5.3: Frequency of the main rotorcraft dynamics, at variable forward speed.

Similarly, the lateral dynamics at low speed is characterized by a couple of oscillatory and low-frequency Dutch-roll poles and a couple of real stable eigenvalues at low and high frequency, representing a roll and spiral behavior. Dutch-roll dynamics is a characteristic oscillatory motion of an aircraft involving the coupled yawing and rolling motions and it arises due to the interaction between lateral-directional stability characteristics. Dutch-roll is typically participated by the lateral speed, coupled with bank angle, roll, and yaw rates. Similarly, spiral dynamics is a slow, unstable motion in which the rotorcraft gradually rolls and yaws in a coordinated manner, potentially leading to an increasing bank angle and eventual loss of control if left to diverge. Spiral is typically participated by the lateral speed and the yaw rate. The fast and stable lateral pole is instead representative of the roll dynamics: typical state participations are the roll rate and bank angles. Roll dynamics play a critical role in lateral stability and maneuverability. A well-damped roll mode ensures that the rotorcraft responds predictably to control inputs and external disturbances. The lateral and longitudinal poles are summarised in Table 5.1 at different forward speed conditions.

	$V_N = 0$ m/s	$V_N = 5$ m/s	$V_N = 10$ m/s	$V_N = 20$ m/s
Short Period	-3.705	-3.831	-4.219	-5.6251
Phugoid	$0.044 \pm 0.604i$	$0.010 \pm 0.590i$	$0.048 \pm 0.578i$	$0.457 \pm 0.271i$
Heave subsidence	-0.530	-0.540	-0.574	-0.491
Roll	-3.632	-3.970	-4.563	-5.181
Dutch-roll	$0.032 \pm 0.485i$	$0.076 \pm 0.384i$	0.320 , 0.173	1.272 , -0.089
Spiral	-0.040	-0.127	-0.508	-1.239

Table 5.1: Rotorcraft poles computed with the analytical modeling approach at different forward speed

The evolution of the rigid body poles is represented on a complex plane in Figure 5.4, with the forward speed that varies from hovering (0 m/s, plain markers) to 20 m/s (empty markers). In addition, the mode participation retrieved from the system's eigenvectors is represented in Figure 5.5 at a variable forward speed. From this plot, it can be observed how the contribution of the rigid body states to the rotorcraft dynamics changes with the speed.

An increased forward speed has a beneficial effect on the high-frequency modes, as the short period and roll dynamics increase their damping and stability. Both of them maintain the contribution of the respective angular rate and body velocity (q and u in the short period and p and v in the roll) as a fundamental part of the mode participation, even if the vertical speed arises in the short period. A similar behavior is observed in the stable spiral mode, which increases its damping and maintains the contribution of lateral speed, angular rate, and forward speed. Heave subsidence is the less affected pole from a stability perspective, even if the dynamics of this mode change with the increase of forward speed, which becomes a major contributor in the heave participation plot. The oscillatory poles are the most affected ones. The phugoid increases its damping ratio and decreases its natural frequency, evolving the poles closer to the real, unstable, axis. On the other hand, an increase of forward speed may become highly detrimental for the dutch-roll dynamics. The oscillatory and slightly unstable poles evolve closer to the real axis, until at around 9 m/s, they become a couple of lateral divergences. This behavior can lead to dangerous instabilities in the system when the forward speed becomes high enough to decouple the complex conjugate Dutch-roll dynamics. The mode participation at this point becomes quite confusing, and both lateral and longitudinal states contribute to the unstable behavior.

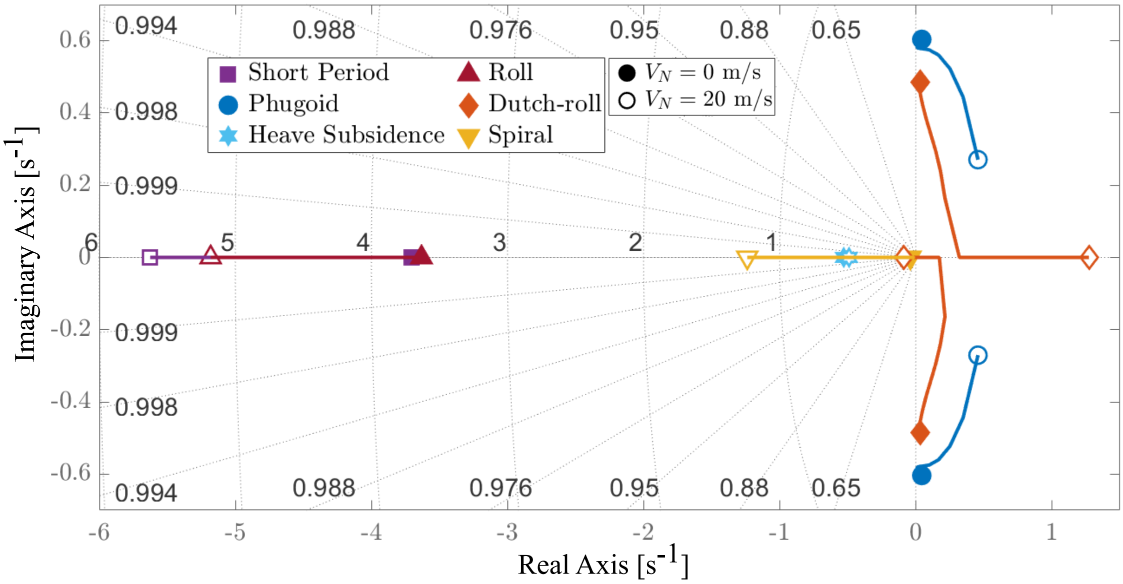

Figure 5.4: Evolution of the rigid body poles at variable forward speed, from 0 m/s (plain markers) to 20 m/s (empty markers).

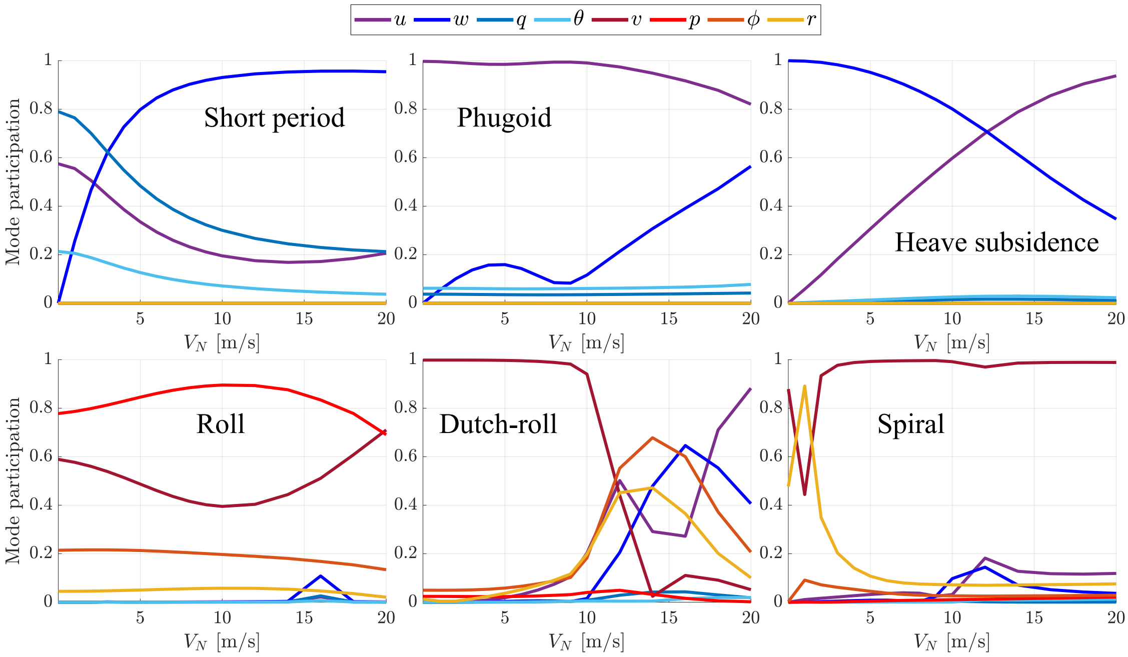

Figure 5.5: Mode participation of the rigid body poles at variable forward speed.

5.1.3 Stability analysis at variable center of gravity

This section elaborates on the effect of the CG location on vehicle stability. The side-by-side prototype considered in this work is designed by locating two 6s battery packs on the longitudinal axis of the rotorcraft. By shifting the batteries along their cases, it is possible to move back and forth the center of gravity of the whole system and alter its stability properties. It then becomes important to address the effects of moving the CG in order to draw conclusions on the optimal location for the batteries and understand how the rotorcraft behaves when its center of mass is shifted with respect to the nominal position. A schematic view of the rotorcraft is provided in Figure 5.6, to define the variation of center of gravity ΔCG with respect to the nominal position. A positive ΔCG refers to a center of mass shifted forward along the longitudinal body axis x^B.

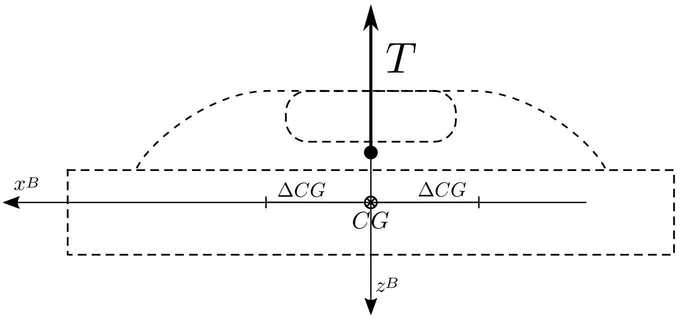

Figure 5.6: Schematic representation of the ΔCG definition [75]

Figures 5.7 and 5.8 show the effect of a variable center of gravity on the rigid body poles at, respectively, hover and $V_N = 5$ m/s. Considering the hovering case, ΔCG has a minimum effect on the high-frequency poles, i.e. short period and roll, while it can be crucial for the stability of the low-frequency dynamics, and in particular for the lateral poles. As can be observed in Figures 5.7, both a positive and negative shifting of the cG have the effect of moving the phugoid modes toward the real axis, impacting the already slightly unstable oscillatory mode and transforming it to a divergence. A similar behavior is observed on the heave subsidence mode, but with the final result of improving its stability and damping. On the other hand, the stability of spiral and dutch-roll strictly depends on the CG position, with an inverse effect on the two dynamics. Indeed, when the CG is shifted backward ($\Delta CG < 0$), the spiral mode tends to become unstable, while the dutch-roll frequency decreases and the poles move towards a stable configuration. In the most retreated layout considered in this study ($\Delta CG = -0.2$ m, see Table 5.2) the dutch-roll becomes stable, while the spiral becomes unstable. However, spiral dynamics tends to be slow and progressive and the motion divergence becomes significant after a long time. Its stability depends on the balance between lateral and directional stability, and in this case the retreated location of the CG enhance the unstable directional effect of the fuselage. Nevertheless, a slightly unstable spiral does not lead to seriously dangerous situations and its divergence can be easily corrected with stability augmentation systems. In general, for stable hover, it is recommended to shift the CG backward and avoid unstable lateral oscillations.

	$\Delta CG = -0.2$ m	$\Delta CG = 0$ m	$\Delta CG = 0.2$ m
Short Period	-3.472	-3.705	-3.472
Phugoid	0.372 , 0.346	$0.044 \pm 0.604i$	0.365 , 0.352
Heave subsidence	-1.628	-0.530	-1.628
Roll	-3.523	-3.632	-3.454
Dutch-roll	$-0.133 + 0.370i$	$0.032 \pm 0.485i$	$0.089 \pm 0.635i$
Spiral	0.146	-0.034	-0.393

Table 5.2: Rotorcraft poles computed with the analytical modeling approach at different center of gravity locations, in hovering conditions

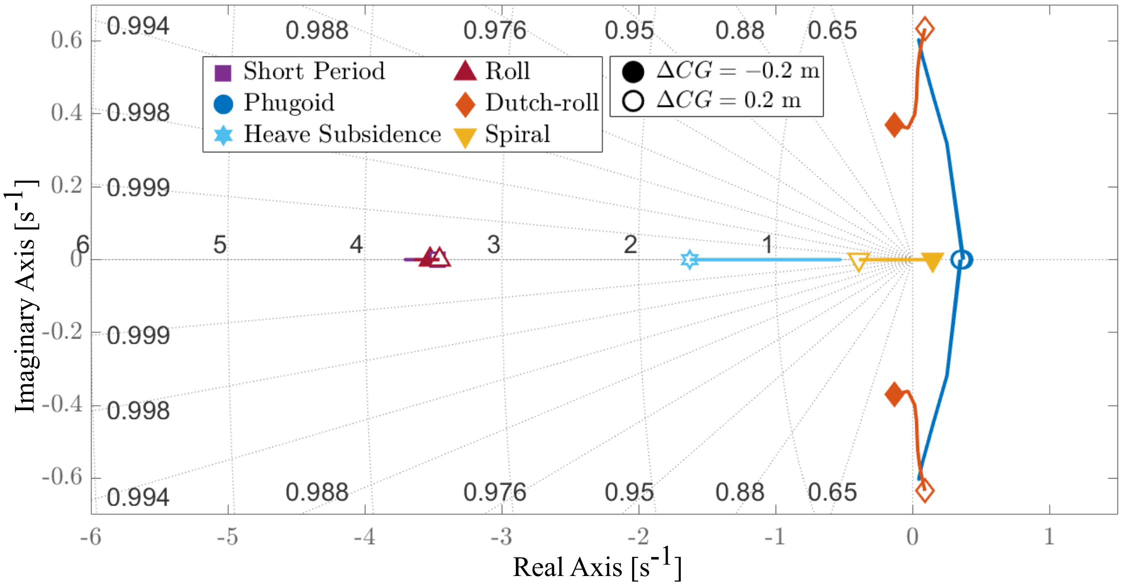

Figure 5.7: Evolution of the rigid body poles at variable CG location, from $\Delta CG = -0.2$ m (plain markers) to $\Delta CG = 0.2$ m (empty markers), in hovering condition.

In forward flight, the evolution of the poles changes. Figure 5.8 reports the rigid body poles at variable CG locations at $V_N = 5$ m/s, while Table 5.3 summarises the cases of $\Delta CG = -0.2$, 0, and 0.2. A similar trend with respect to the hovering case is observable in the roll, spiral, and dutch-roll poles: the $\Delta CG < 0$ condition leads to a slightly unstable spiral and a stabilization of the oscillatory modes. On the other hand, longitudinal dynamics evolves differently with respect to the hovering case. The phugoid remains unstable for all the CG configurations, and it becomes real, thus divergent, with a very much retreated CG. The main difference occurs with the short period and heave subsidence mode. Both of them remain stable for the entire CG range, but moving the CG forward has the effect of reducing the short period frequency and increasing the heave subsidence one. At $\Delta CG = -0.1$ m, these two poles merge into a couple of high-frequency, complex conjugate and oscillatory modes, which increase their frequency with the backward location of the CG. It is evident from Figure 5.9, that the mode participation in the heave subsidence at $\Delta CG < 0$, gradually becomes closer to the short period one, with the contribution of the pitch angle θ and rate q that arises as soon as the CG is shifted backward.

	$\Delta CG = -0.2$ m	$\Delta CG = 0$ m	$\Delta CG = 0.2$ m
Short Period	$-2.599 + 2.417i$	-3.831	-5.407
Phugoid	0.477 , 0.091	$0.010 \pm 0.590i$	$0.488 \pm 0.704i$
Heave subsidence	$-2.599 - 2.417i$	-0.540	-0.253
Roll	-3.809	-3.970	-3.832
Dutch-roll	$-0.186 + 0.731i$	$0.076 \pm 0.384i$	$0.001 \pm 0.595i$
Spiral	0.220	-0.127	-0.183

Table 5.3: Rotorcraft poles computed with the analytical modeling approach at different center of gravity locations, at $V_N = 5$ m/s

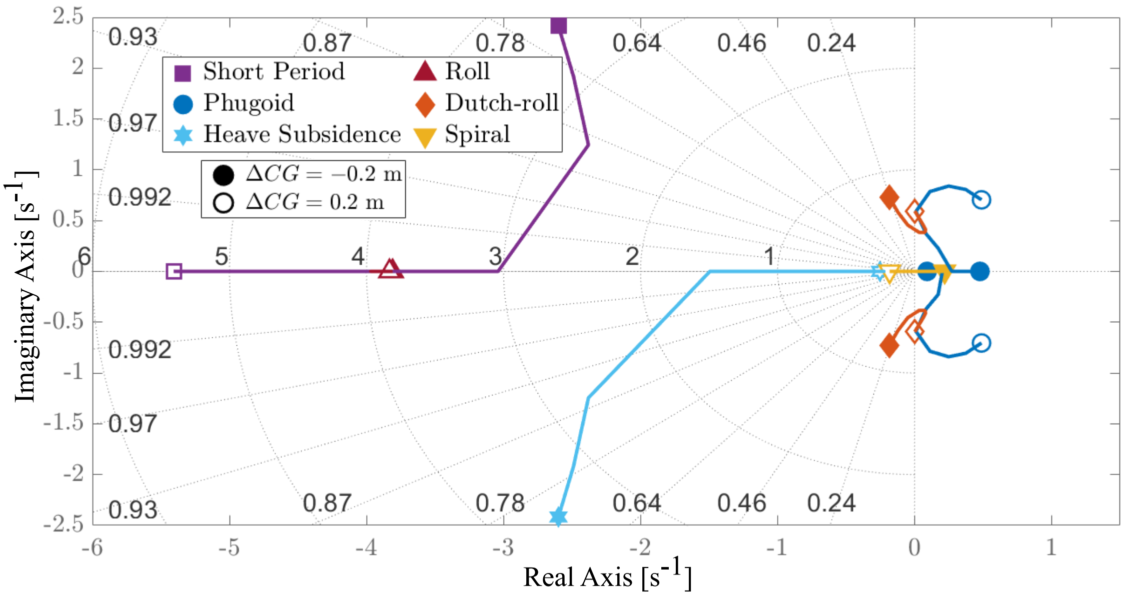

Figure 5.8: Evolution of the rigid body poles at variable CG location, from $\Delta CG = -0.2$ m (plain markers) to $\Delta CG = 0.2$ m (empty markers), at $V_N = 5$ m/s.

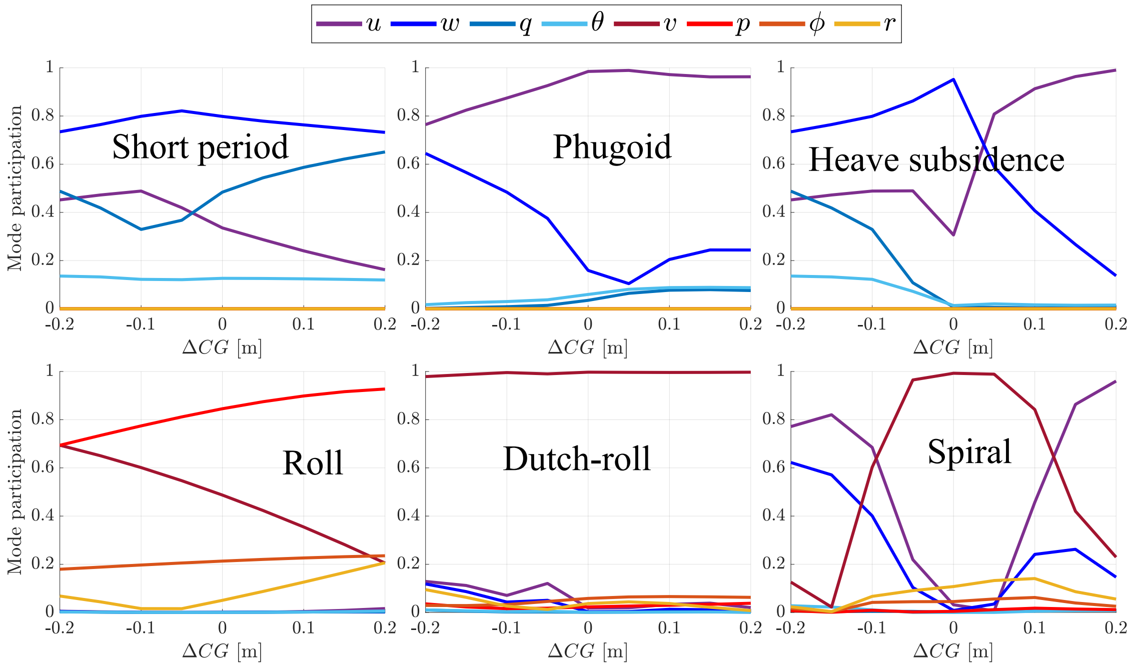

Figure 5.9: Mode participation of the rigid body poles at variable CG location and $V_N = 5$ m/s.

Finally, Figure 5.10 reports the frequency of the rigid body poles at variable CG locations in the cases of hovering (left) and $V_N = 5$ m/s. Concerning the hovering case, the heave subsidence mode is the one that experiences the largest frequency variation, with a symmetric trend for positive and negative ΔCG. Dutch-roll frequency gradually increases by moving the CG forward. On the other hand, in forward flight heave and short-period modes merge with a negative enough CG location, while the phugoid frequency is generally higher with the CG in a forward location.

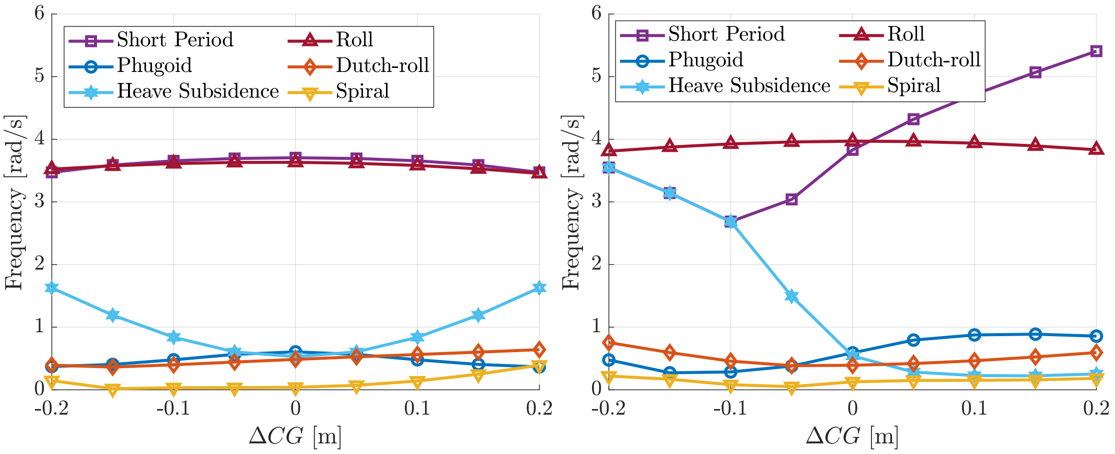

Figure 5.10: Rigid body poles frequency at hovering (left) and $V_N = 5$ m/s.

5.2 Flight dynamics with numerical modeling

5.2.1 Overview of the analysis

In this section, the flight dynamics characteristics of the side-by-side helicopter are studied with the numerical modeling approach (see Section 4.4) at hovering conditions. The objective is to provide an in-depth analysis of the stability and dynamic properties of the rotorcraft, by introducing different degrees of complexity in the modeling approach and understanding how the separate dynamic features affect the rigid body stability. In addition, cross-validation with the analytical model is provided by comparing the trim and stability outcomes. The only hovering condition will be taken into account in this study.

The methodology is summarised here:

1. Trim calculation at variable forward speed and comparison with the analytical modeling results;
2. Definition of a standard, lowest complexity, modeling configuration and comparison with the analytical approach:
   - Uniform and dynamic inflow ($\boldsymbol{\lambda} = [\lambda_0 \quad 0 \quad 0]$ in both rotors);
   - Uniform flap dynamics ($\boldsymbol{\beta} = [a_0 \quad 0 \quad 0]$ in both rotors);
   - Lead-lag neglected ($\boldsymbol{\xi} = [0 \quad 0 \quad 0]$ in both rotors).
3. Starting from this condition, different levels of complexity are included, and their effects on the rotorcraft stability (system poles and eigenvectors) are highlighted. At first, complete flapping dynamics is considered in both models ($\boldsymbol{\beta} = [a_0 \quad a_1 \quad b_1]$), then the lead-lag effect ($\boldsymbol{\xi} = [\xi_0 \quad \xi_c \quad \xi_s]$), and finally, the influence of a dynamic, non-uniform inflow ($\boldsymbol{\lambda} = [\lambda_0 \quad \lambda_s \quad \lambda_c]$).

5.2.2 Trim

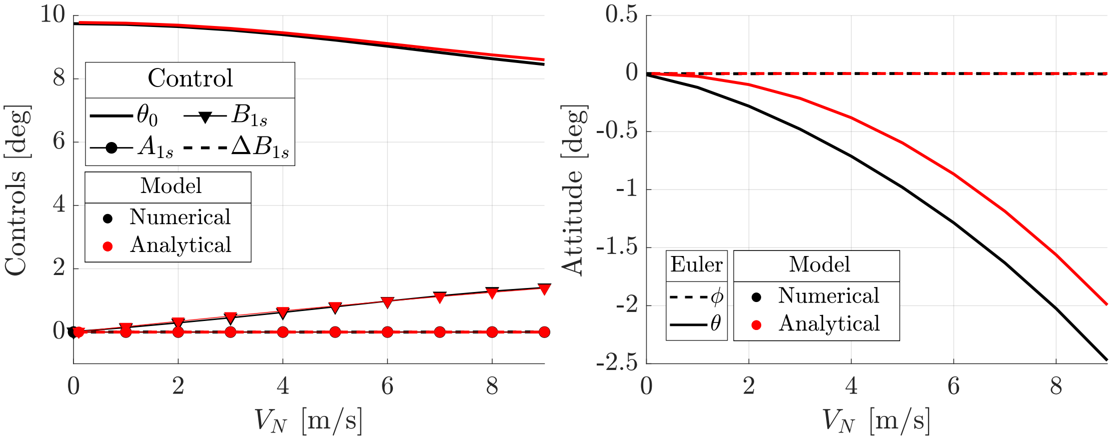

Figure 5.11: Trim results for the numerical modeling approach (black) compared with the analytical results (red).

Similarly to the results reported in Section 5.1.1 for the trim conditions computed with the analytical main rotor modeling approach, this Section shows the steady state solutions of rotorcraft dynamics described with the numerical modeling approach. Figure 5.11 compares the trim solution at variable forward speed, computed with the algorithm for the numerical model and the results from the analytical representation. The two models have a very good agreement on the controls applied to fly forward, with a small discrepancy on the collective pitch. Figure 5.11 right, reports the aircraft trimmed attitude at variable advancing speed, and the result is that with a numerical modeling approach, the aircraft tends to pitch more. In general, in the absence of experimental evidence, the computation of trim solution with two different models allows for partially validating the two representations in steady conditions.

5.2.3 Rotorcraft stability: flap dynamics

Figures 5.12 and 5.13 report the rigid body poles and their frequency affected by uniform and non-uniform flap dynamics in both the analytical and numerical modeling frameworks. These two plots provide several information regarding the flight dynamic properties of the side-by-side in hover, the comparison between modeling approaches, and the effect of lateral and longitudinal disc tilts on rigid body stability. The black/red colors identify the numerical/analytical framework, while the empty/plain markers distinguish between the standard condition and the first level of complexity introduced in the computation (complete flap dynamics). The symbols identify the poles. The mode identification is made through eigenvector analysis and by recalling classical aircraft nomenclature for low- and high-frequency modes. The frequency of the poles is represented in Figure 5.13, highlighting a clear difference between six low-frequency modes and two higher-frequency ones. Two couples of oscillatory dynamics identify slightly unstable, low-frequency phugoid and dutch-roll modes. The low-frequency behavior is also characterized by stable spiral and heave subsidence. From the high-frequency point of view, a couple of stable short-period and roll dynamics are reported.

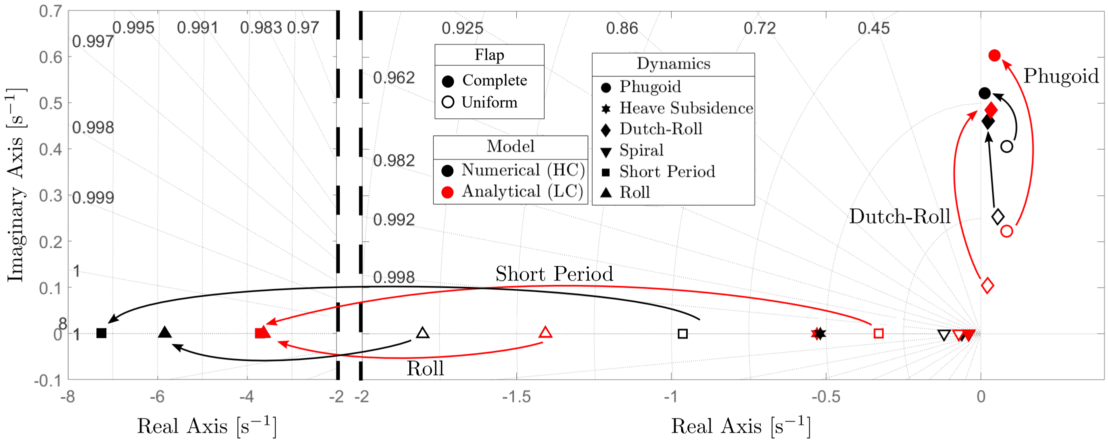

Figure 5.12: Rigid body poles affected by lateral and longitudinal disc tilts, according to the numerical (black markers) and analytical (red markers) frameworks

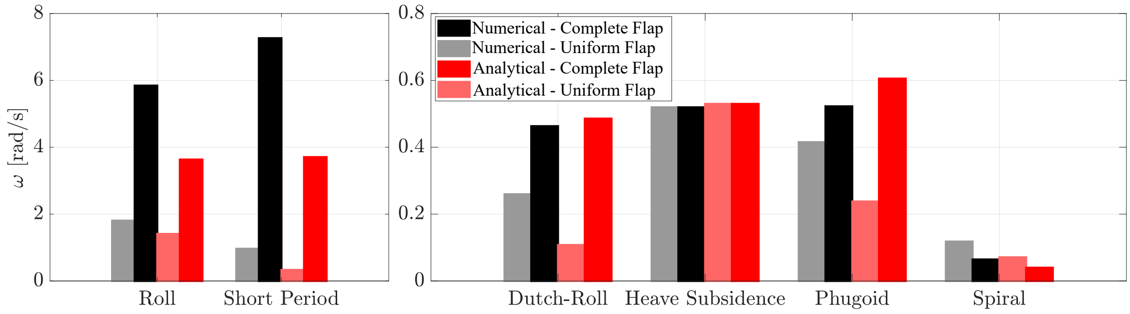

Figure 5.13: Frequency (ω) of the rigid body poles affected by lateral and longitudinal disc tilts

Considering the standard condition (empty markers in the plot, $\boldsymbol{\beta} = [a_0 \;\; 0 \;\; 0]$), the two models provide similar results, even if with some differences in the frequency estimation. It appears that the frequency of both the oscillatory modes (phugoid and dutch-roll) and the high-frequency poles (roll and short period) is underestimated by the analytical model with respect to the more refined numerical one. A substantial difference is obtained in the phugoid and short-period modes, whose ω value is almost doubled and tripled in the numerical model. Similarly, the Dutch-roll has a halved frequency when the rotorcraft is described by an analytical approach. However, although with a scaling factor in the frequency estimation, the two models at a standard level of complexity agree on the overall stability of the rotorcraft, both of them predicting the slightly unstable oscillatory modes and the mode participation of the 8 rigid body dynamics. Table 5.4 summarises the poles and their frequency at a standard level of complexity. The relative error is computed as the relative discrepancy between frequencies in the two models with respect to the more refined one (numerical), as

$$err_{\%} = 100\frac{\omega_{num} - \omega_{ana}}{\omega_{num}} \tag{5.1}$$

	Analytical		**Numerical**		**Relative error**
	Pole	Frequency	Pole	Frequency	
Short Period	-0.33	0.33	-0.96	0.96	66%
Phugoid	$0.08 \pm 0.22i$	0.24	$0.08 \pm 0.22i$	0.42	43%
Heave subsidence	-0.53	0.53	-0.52	0.52	2%
Roll	-1.41	1.41	-1.80	1.80	22%
Dutch-roll	$0.02 \pm 0.11i$	0.11	$0.06 \pm 0.25i$	0.26	58%
Spiral	-0.07	0.07	-0.12	0.12	40%

Table 5.4: Rigid body poles and frequencies at standard level of complexity

The first dynamic feature included in the computation is the complete, second-order, flapping dynamics, (solid markers in the plot, $\boldsymbol{\beta} = [a_0 \;\; a_1 \;\; b_1]$) which introduces the effect of the lateral and longitudinal disc tilts on the rigid body. The two models behave similarly, with the tip-path plane dynamics affecting the oscillatory poles by increasing their frequency and adding lateral and longitudinal damping to the high-frequency ones (short period and roll). Overall, the lateral and longitudinal disc tilts have a beneficial effect on the rotorcraft stability, moving all the poles towards the negative real axis. Short period and roll frequencies are directly linked to the lateral and longitudinal damping derivatives M_q and L'_p [147] which are reported in Table 5.5 for the two cases, together with the rotor disc coordinates with a perturbed pitch rate q. The rotorcraft reacts to a disturbance in angular rate with a damping moment around the perturbed axis. The different modeling approach to the flap dynamics leads to different disc tilts which are directly proportional to the damping derivative. Indeed, the flap hinge stiffness and inertial moments described in Equation 4.39 are proportional to a_1 and b_1 which are, for a small perturbation of pitch rate (the same happens with a perturbation of roll rate p), different in the two models (see Table 5.5). The discrepancy is, in absolute values, quite small, and the disc tilts maintain the same order of magnitude, as well as the damping derivatives. The relative discrepancy between short-period frequencies is reduced with respect to the standard case, where the numerical model almost tripled the analytical one, while here doubles the lower order framework. In addition, the relative error between the two models in the oscillatory modes is very much improved, with only 16% and 5% on the phugoid and dutch-roll modes. Short period and spiral have also decreased their relative errors by approximately 20%; the only dynamic mode that increases the discrepancy between analytical and numerical approaches is the roll. Table 5.6 summarises the poles, frequencies and relative errors between the two frameworks with complete tip-path plane dynamics.

	Analytical	**Numerical**
M_q [deg]	-3.60	-7.22
L'_p [deg]	-3.57	-5.83
$a_0(\Delta q)$ [deg]	0.55	0.53
$a_1(\Delta q)$ [deg]	-0.0041	-0.0047
$b_1(\Delta q)$ [deg]	0.0103	0.0144

Table 5.5: Stability derivatives with complete flap dynamics. The tip-path plane coefficients are provided with a pitch rate perturbation of $\Delta q = 0.01$ rad/s

	Analytical		**Numerical**		**Relative error**
	Pole	Frequency	Pole	Frequency	
Short Period	-3.70	3.71	-7.26	7.26	49%
Phugoid	$0.04 \pm 0.60i$	0.61	$0.01 \pm 0.52i$	0.52	16%
Heave subsidence	-0.53	0.53	-0.52	0.52	2%
Roll	-3.63	3.63	-5.84	5.84	38%
Dutch-roll	$0.03 \pm 0.48i$	0.49	$0.02 \pm 0.46i$	0.46	5%
Spiral	-0.04	0.04	-0.06	0.06	38%

Table 5.6: Rigid body poles and frequencies with complete flap dynamics

5.2.4 Rotorcraft stability: lead-lag dynamics

The effect of lead-lag dynamics on the rigid body stability is analysed in this Section. The mathematical representation of rotor dynamics and the linearization methodology presented for the numerical modeling approach, allow to partially decouple the flap and lead-lag dynamics in a nonlinear system of second-order ODEs. Figure 4.6 illustrated the algorithm for neglecting the lead-lag effect on both the rigid body and the rotor dynamics itself.

Figure 5.14 reports the rigid body poles in the cases with and without blades' lead-lag motion. The poles and their frequencies are also reported in Table 5.7. Low-frequency dynamics are the less affected by the lead-lag, with a small stabilizing effect observed on the oscillatory modes (phugoid and dutch-roll) and a very small influence on the frequency of these poles (Figure 5.15). The roll and short period are instead more affected by the presence of the lead-lag, and the frequency of these two stable and real dynamics moves, respectively, from 5.8 to 10.7 rad/s and from 7.2 to 15 rad/s. The reason why this higher level of modeling complexity affects the high-frequency poles is related to the coupling between the tip-path plane and the rotor center of gravity. The lead-lag angle is not directly responsible for an additional load acting on the blades but affects the value of the lateral/longitudinal disc tilt. Table 5.8 reports the values of flap and lead-lag coordinates with a pitch rate perturbation $\Delta q = 0.01$ rad/s, together with the lateral and longitudinal damping derivatives, affected by lead-lag. It is observed that, while b_1 is similar in the two cases, a_1 significantly changes in the case of coupled lead-lag dynamics. The latter is directly proportional to the absolute value of hinge stiffness and inertial moments computed by Equation (4.39) and increases the longitudinal damping M_q when the lead-lag is "on". The same process occurs with a roll rate perturbation p, and L'_p. In addition, the small variation in oscillatory poles can be linked to the variation in the coning angle, which is, in the case of a lagging rotor, larger.

	Lead-Lag OFF		**Lead-Lag ON**	
	Pole	Frequency	Pole	Frequency
Short Period	-7.26	7.26	-15.0	15.0
Phugoid	$0.01 \pm 0.52i$	0.52	$0.003 \pm 0.53i$	0.53
Heave subsidence	-0.52	0.52	-0.52	0.52
Roll	-5.84	5.84	-10.7	10.7
Dutch-roll	$0.02 \pm 0.46i$	0.46	$0.008 \pm 0.50i$	0.50
Spiral	-0.06	0.06	-0.04	0.04

Table 5.7: Rigid body poles and frequencies affected by lead-lag

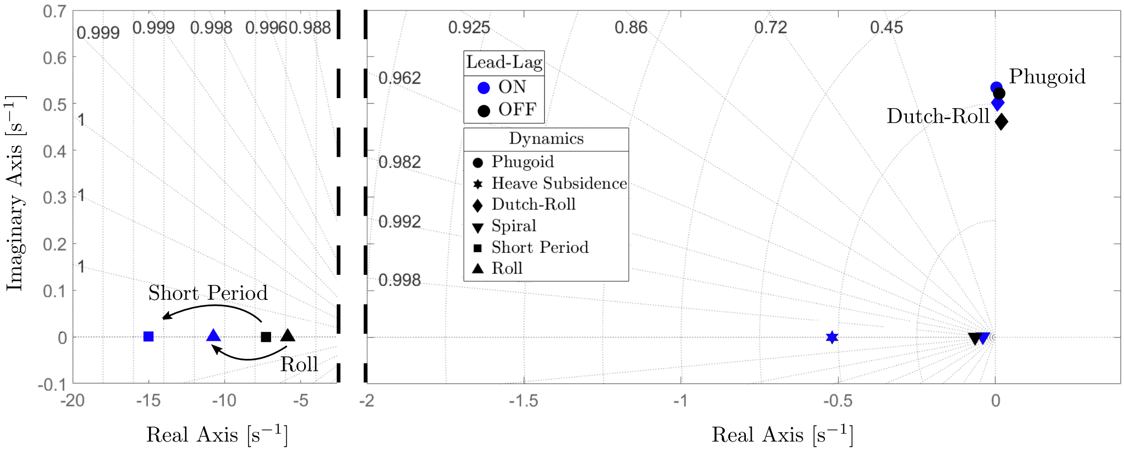

Figure 5.14: Rigid body poles affected by dynamic lead-lag, according to the numerical framework

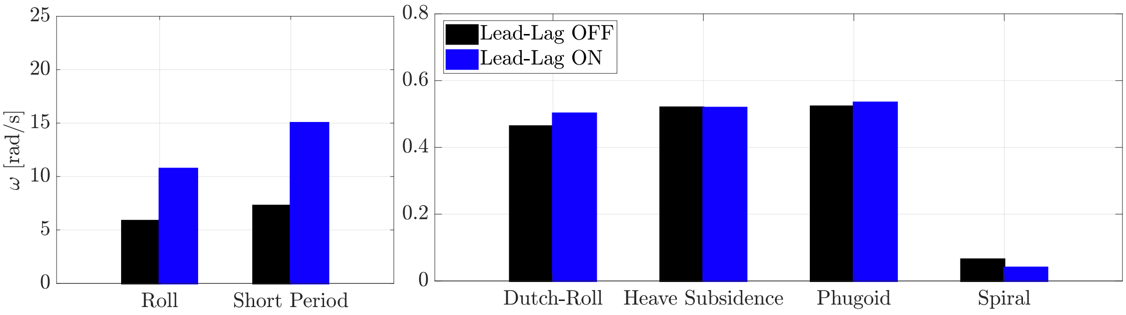

Figure 5.15: Frequency (ω) of the rigid body poles affected by dynamic lead-lag

		Lead-Lag OFF	**Lead-Lag ON**
M_q	[-]	-7.2	-15
L'_p	[-]	-5.8	-10.7
a_0	[deg]	0.53	0.69
a_1	[deg]	-0.0047	-0.023
b_1	[deg]	0.0144	0.0125
ξ_0	[deg]	0	1.56
ξ_c	[deg]	0	-0.065
ξ_s	[deg]	0	0.009

Table 5.8: Stability derivatives with the effect of lead-lag dynamics. The rotor CG coefficients are provided with a pitch rate perturbation of $\Delta q = 0.01$ rad/s

5.2.5 Rotorcraft stability: inflow dynamics

The inflow dynamics is described by a system of first-order ODEs and its distribution around the rotor disc can be either modeled as uniform ($\boldsymbol{\lambda} = \lambda_0$, like in the analytical framework) or non-uniform ($\boldsymbol{\lambda} = [\lambda_0\ \lambda_s\ \lambda_c]$, like in the numerical framework). In this Section, the effect of a non-uniform inflow distribution on the rotorcraft flight dynamics is studied by comparing the two approaches applied to the numerical modeling framework. Figure 5.17 shows the rigid body poles in the cases of uniform and non-uniform dynamic inflow. It is observed that the presence of lateral and longitudinal inflow components has an effect on the short period, dutch-roll, and phugoid dynamics. Considering the first one, an increase in the longitudinal damping is observed, linked to the mode coupling between the short period and longitudinal inflow λ_c. The mode participation of these poles is depicted in Figure 5.18, where the coupling between rigid body modes and inflow states is highlighted. A similar coupling effect that is highly detrimental for the longitudinal stability of the rotorcraft, is the one between the longitudinal inflow and the phugoid mode. Even with a small participation, the longitudinal inflow contribution has the effect of shifting the phugoid poles from a pure oscillatory, slightly unstable, situation, to a couple of real stable/unstable poles of similar frequency, as shown in Figure 5.16. This is effectively a dangerous coupling that transforms a low-frequency oscillatory mode, into a divergence. On the other hand, the dutch-roll stability remains unchanged although its frequency decreases by about 50% (see Table 5.9). Coupling with both lateral and longitudinal inflows is observed in the dutch-roll and roll poles as well, although without significant changes in the lateral stability. It is assumed that, being the configuration symmetrical with respect to the longitudinal plane, the effects of the lateral inflows of the two rotors balance themselves.

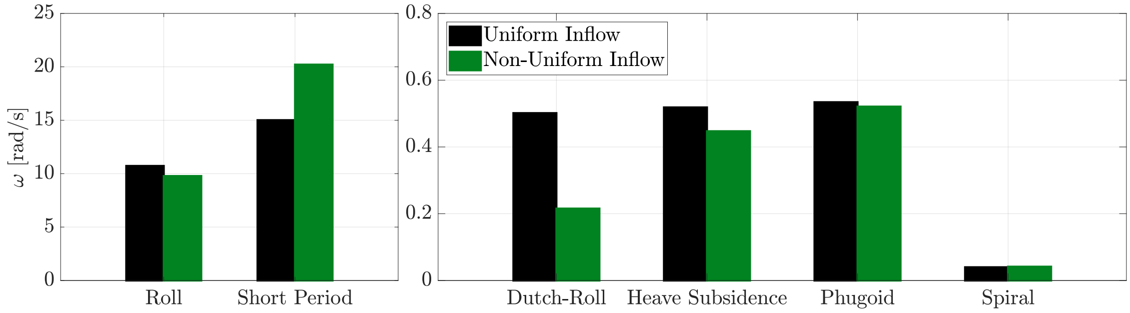

Figure 5.16: Frequency (ω) of the rigid body poles with a uniform and non-uniform dynamic inflow

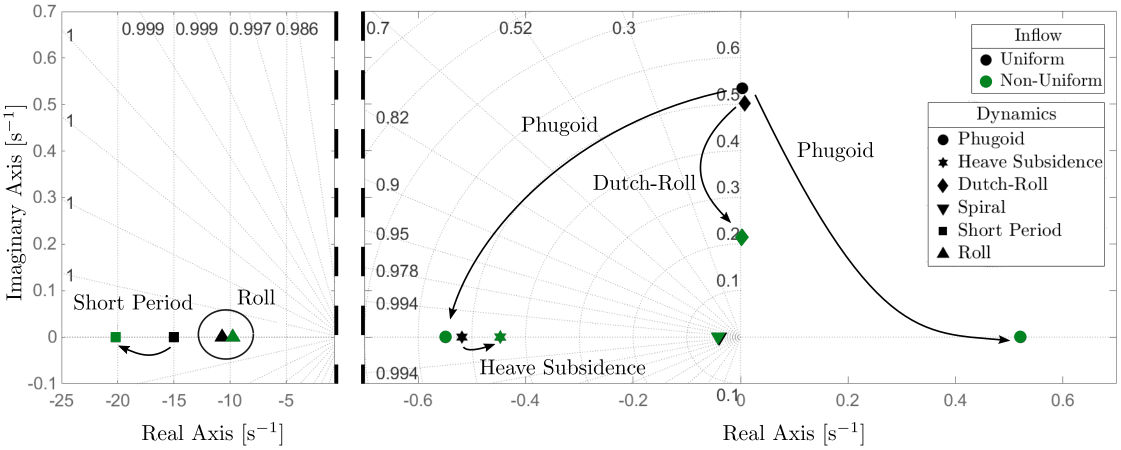

Figure 5.17: Rigid body poles with a uniform and non-uniform dynamic inflow

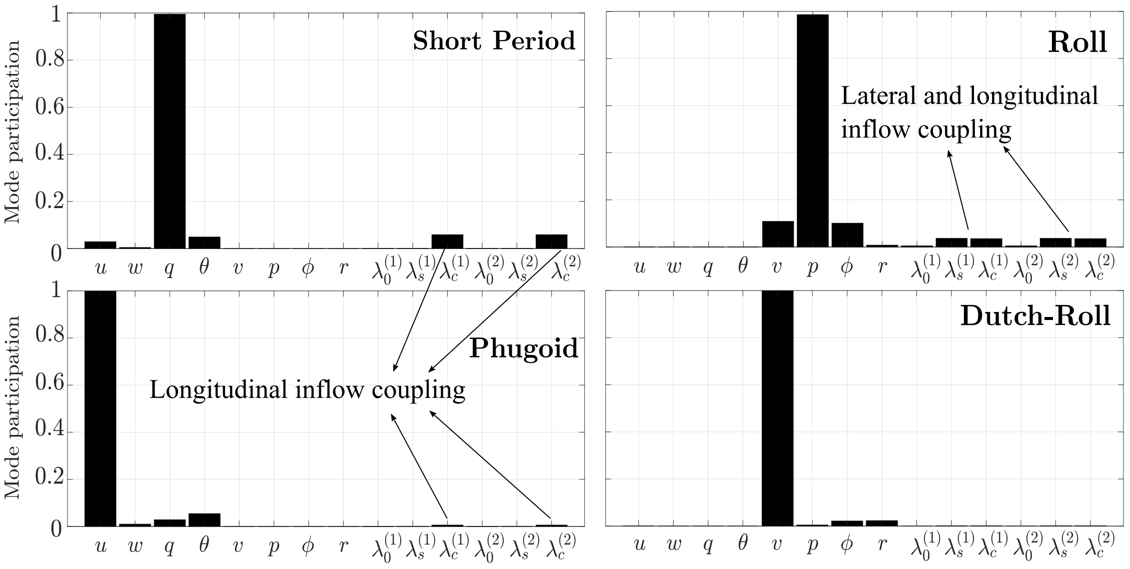

Figure 5.18: Rigid body eigenvectors, coupled with lateral and longitudinal inflow components

	Unifrom inflow		**Non-uniform inflow**	
	Pole	Frequency	Pole	Frequency
Short Period	-15.0	15.0	-20.2	20.2
Phugoid	$0.003 \pm 0.53i$	0.53	-0.55/0.52	0.52/0.55
Heave subsidence	-0.52	0.52	-0.45	0.45
Roll	-10.7	10.7	-9.78	9.78
Dutch-roll	$0.008 \pm 0.50i$	0.50	$0.003 \pm 0.22i$	0.22
Spiral	-0.04	0.04	-0.04	0.04

Table 5.9: Rigid body poles and frequencies with uniform and non-uniform inflow modeling

5.2.6 Rotor dynamics

Section 4.9.2 presented a linearization methodology to produce a 38 state-space representation of the side-by-side helicopter flight dynamics, including the rigid body, rotor, and inflow modes. Considering the state matrix A (Equation (4.114)), the out-of-diagonal terms describe the coupling between these three dynamics, while A_{B-B}, A_{R-R}, and $A_{\lambda-\lambda}$ are the pure linearized motion. This section focuses on the analysis of the rotor-rotor modes: it is noted that under hovering conditions, no significant differences are observed between MR1 and MR2, and no notable coupling effects are present. For this reason, the results depicted from now on are related to a generic rotor. The study is based on the numerical framework and includes fully coupled second-order flap-lead-lag dynamics, along with a first-order non-uniform inflow model. For each rotor, 12 oscillatory and stable poles are computed, including 6 associated with flap dynamics and 6 with lead-lag dynamics. Figure 5.19 shows the coupled collective, advancing, and regressive modes on the complex plane, while their corresponding frequencies and damping ratios are listed in Table 5.10. The results indicate that the system exhibits stable collective flap dynamics at the rotor's angular frequency, along with pairs of advancing and regressive modes characterized by identical real parts and imaginary components located at $\pm\Omega$ with respect to the collective mode. A similar trend is observed for the lead-lag dynamics, which is a stable high-frequency dynamic with greater damping compared to the flap. The significant damping of the lead-lag dynamics is attributed to the spring damping coefficient (K_{D_ξ}) adopted in this model, as detailed in Table 4.1. The identification of the rotor poles was achieved through the eigenvector analysis. The collective modes are characterized by the main contribution of the collective flap and lead-lag coefficients (a_0 and ξ_0), while the advancing and regressive modes are mainly related to the rotor disc tilt and non-uniform lead-lag coefficients (a_1, b_1, ξ_c, and ξ_s). As showed in the mode participation plots (Figure 5.20), a strong coupling between rotor dynamics is quite evident and the identification of the flap and lead-lag poles requires further discussions. Indeed, even if with a strong participation of the lead-lag states, the flap poles can be identified by the frequency of the collective mode (close to Ω) and the advancing/regressive poles located at approximately 0 and 2Ω. Coupling with rigid body modes (mainly p and q) is also present in the regressive flap. In addition, Figure 5.21 depicts the mode participation of the uniform inflow poles (also plotted in Figure 5.19). These poles demonstrated strong coupling with the collective flap and lead-lag dynamics, as well as with the rigid body modes. Notably, one of the inflow poles exhibited a contribution from the roll rate (p), while the other showed coupling with the heave velocity (w). This behavior aligns with the characteristics of the side-by-side rotor configuration, where variations in inflow can induce both heave and roll motions.movement.

	Pole	**Frequency [rad/s]**	**Damping [s]**
Uniform Inflow (w coupling)	-55.7	55.7	-
Uniform Inflow (p coupling)	-57.6	57.6	-
Collective Flap	$-34 \pm 265i$	267	0.12
Regressive Flap	$-34 \pm 15i$	37	0.9
Advancing Flap	$-34 \pm 518i$	519	0.07
Collective Lead–lag	$-223 \pm 607i$	647	0.34
Regressive Lead–lag	$-223 \pm 356i$	420	0.53
Advancing Lead–lag	$-223 \pm 859i$	887	0.25

Table 5.10: Rigid body poles and frequencies affected by lead-lag

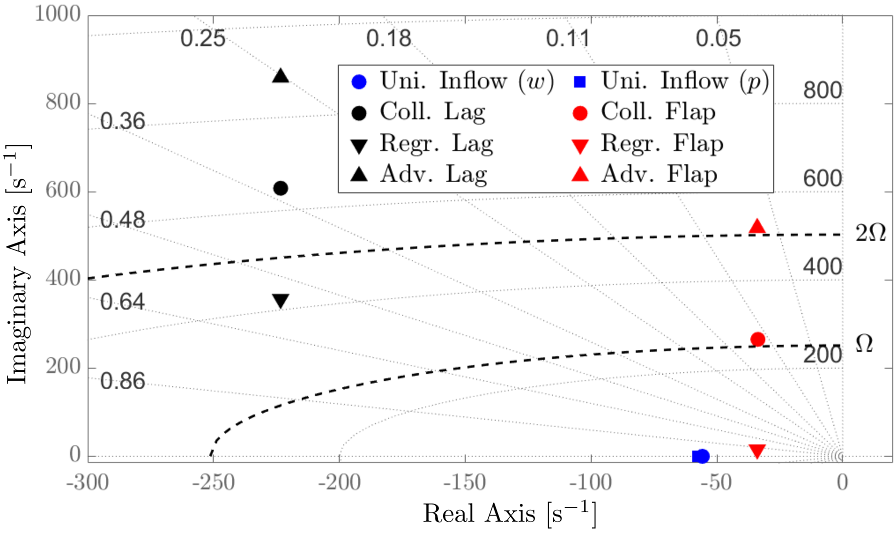

Figure 5.19: Main rotor poles in the complex plane

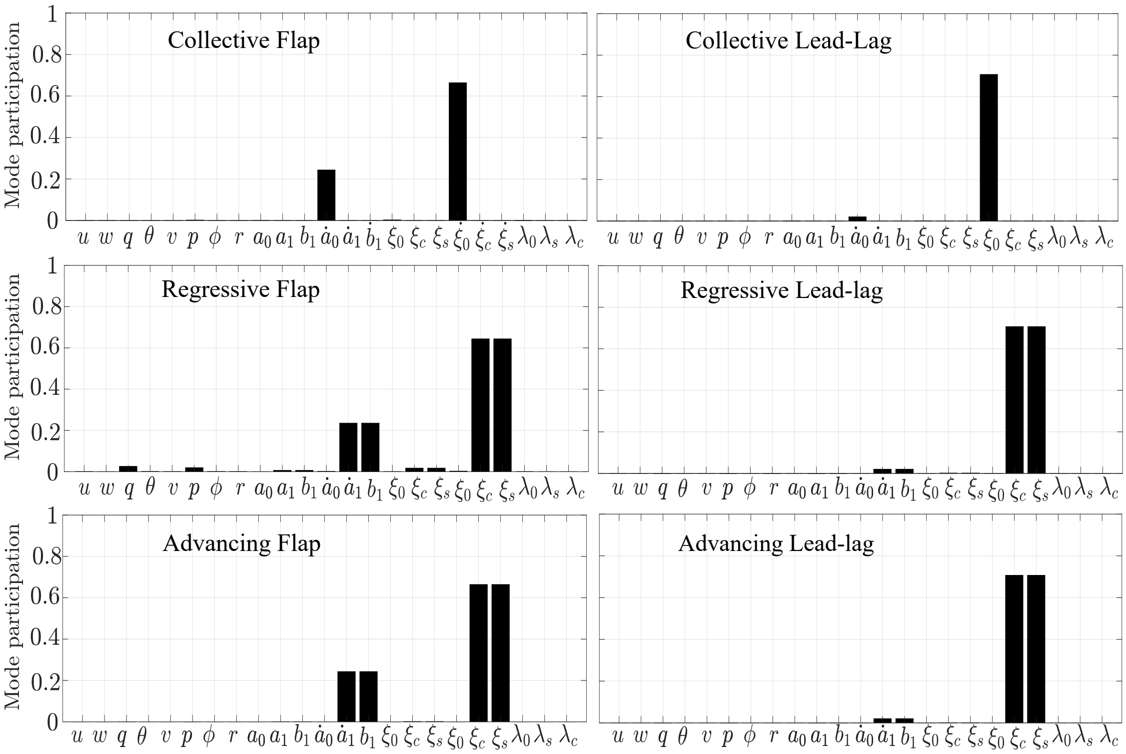

Figure 5.20: Mode participation of the rotor-coupled poles.

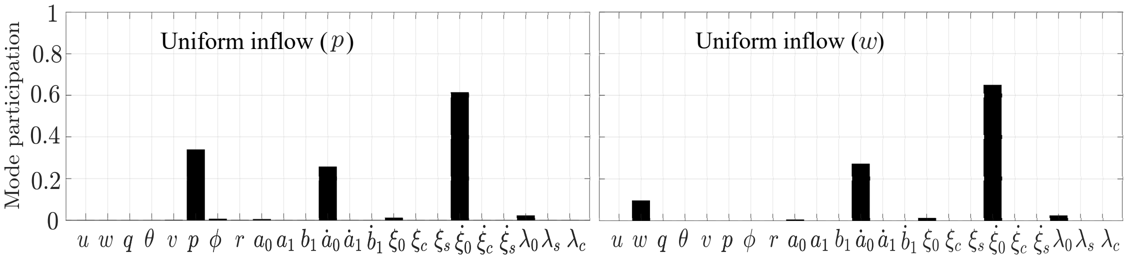

Figure 5.21: Mode participation of the uniform inflow poles.

Chapter 6

Additional research and future works

6.1 Future works

The analysis of side-by-side helicopters and, more broadly, VTOL configurations for Urban Air Mobility (UAM) is not concluded with the outcomes of this thesis. Several enhancements can be applied to the current mathematical models, particularly in the areas of fuselage loads, blade aerodynamics, and the effects of shrouds. Addressing these aspects in greater detail will be essential to further improve the accuracy of the existing formulations. Advanced Computational Fluid Dynamics (CFD) tools and experimental testing will play a pivotal role in refining the aerodynamic load predictions for these structures.

Special attention should be given to the aerodynamic effects of shrouds. At this stage, the contribution of shrouds is incorporated through a simplified semi-analytical model, which does not account for aerodynamic interactions in forward flight. This limitation should be addressed, as the presence of a duct surrounding the rotor can significantly alter the flow characteristics, particularly during forward flight operations. Investigating this phenomenon in greater detail will enhance the understanding of the interaction between shrouded rotors and the surrounding flow field.

Future work should also focus on the development of an advanced control system to improve stability and enable the piloted operation of the aircraft in realistic scenarios. A preliminary control architecture is proposed in Section 6.2 of this thesis. Once a fully functional closed-loop simulation model is developed, the framework can be tested in software-in-the-loop (SIL) or hardware-in-the-loop (HIL) environments. A comprehensive description of these architectures and their role as intermediate steps between simulations and experimental testing is provided in Section 6.3, along with an outline of a typical experimental setup.

Finally, validating the simulation results through experimental evidence will be a critical step. To this end, the construction and testing of a physical prototype will be required. Such an experimental campaign will provide valuable data on the flight performance, handling qualities, and dynamic behavior of the aircraft. These properties can be evaluated using appropriate pole and derivative identification methods. The insights gained from the experimental campaign, combined with the capabilities of a validated simulation model, could pave the way for the development of a full-scale prototype. This final stage would enable testing in real urban scenarios, advancing the understanding and applicability of side-by-side helicopters within the UAM ecosystem.

6.2 Preliminary control system design

In this Section, a theoretical control system design is proposed for the side-by-side helicopter modeled using the numerical approach. It is worth mentioning that the proposed layout is preliminary and it has the only aim of stabilizing the rotorcraft at trim and following quite simple step maneuvers. A deeper analysis of the controllability properties would be necessary to propose a more realistic and optimized control system, with detailed requirements and performance. The actual design generally has low performance, and its tuning and layout are based only on empirical knowledge and a trial-and-error approach. However, its definition provides meaningful insights into the main problems that occur when controlling such a configuration and the dynamics behavior of side-by-side VTOLs.

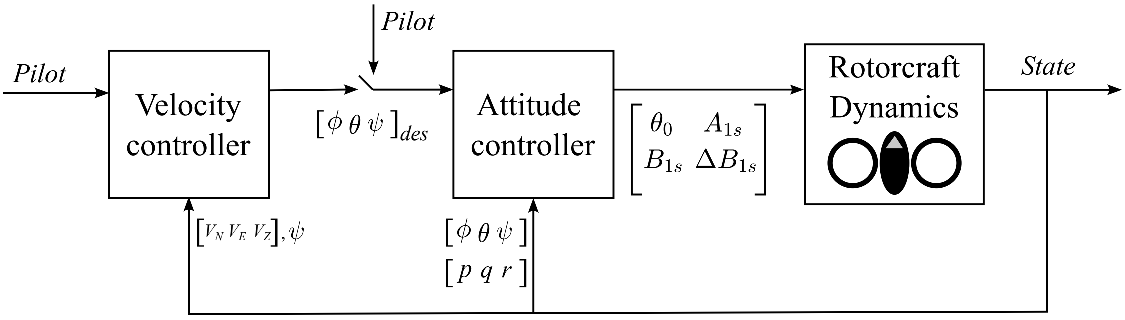

Figure 6.1: Control system

The control system is structured as depicted in Figure 6.1: the inner loop is an attitude controller, which aims at minimizing the error between a desired set of Euler angles and the actual rotorcraft state. The feedback branch is retrieved from the aircraft dynamics modeled with the numerical approach, while the target attitude can be either provided by the pilot or as the output of the outer loop. In particular, this is a classical PID controller that uses the feedback from the aircraft's attitude and angular rates to provide the swashplate controls necessary to follow the objective values. Figure 6.2 reports the PID structure of the pitch, roll, and yaw rate controls, where the subscript $_{des}$ identifies the desired values, the constants K, P, I, D are the control system's gains, N is the filter's constant and e is the error between the desired and the actual value. The control action is limited with a saturation block: the aim of this block is to avoid uncontrolled angular accelerations when the aircraft is subjected to quick inputs. It also limits the range provided by the controls on the swashplate. The controller commands the pitch and roll angles with feedback on the respective angular rates, providing the longitudinal and lateral cyclic commands as a function of the angular difference. Considering the roll angle controller and ignoring the filter dynamics, the output dynamics is, in the frequency domain,

$$A_{1s}(s) = P_\phi(K_\phi e_\phi - p) + \frac{I_\phi}{s}(K_\phi e_\phi - p) + D_\phi p \tag{6.1}$$

which is, in the time domain,

$$A_{1s}(t) = P_\phi K_\phi e_\phi(t) - P_\phi \dot{\phi} + I_\phi \int_0^t [K_\phi e(\tau) - \dot{\phi}] d\tau + D_\phi \dot{\phi} \tag{6.2}$$

An equivalent function can be derived for the pitch angle controller. On the other hand, the differential longitudinal cyclic control is determined by a yaw rate controller, and its dynamics in the frequency and time domain is

$$\Delta B_{1s}(s) = P_r e_r + \frac{I_r}{s} e_r + D_r r \tag{6.3}$$

and

$$\Delta B_{1s}(t) = P_r e(t) + I_r \int_0^t e(\tau) d\tau + D_r \dot{\Psi} \tag{6.4}$$

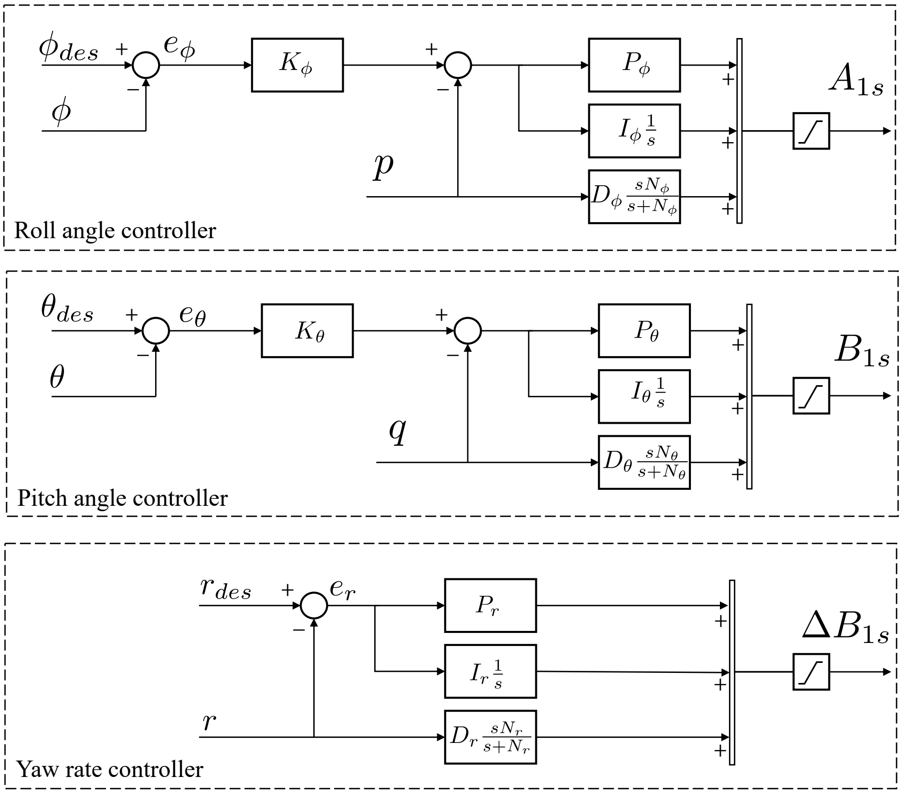

Figure 6.2: Attitude control system

The outer loop is a velocity controller: lateral and longitudinal speeds are commanded by the pilot and the controller provides the necessary acceleration for minimizing the error. The yaw rate control ΔB_{1s} is left unconnected from the velocity loop, as well as the collective pitch θ_0, is left free to be managed directly by the pilot to control the vertical velocity. The layout of the velocity control system is reported in Figure 6.3, with a similar structure to the yaw rate control. The lateral and longitudinal accelerations (a_{lat} and a_{lon}) computed by the controller are translated into desired angles as

$$\theta_{des} = \arctan\left(-\frac{a_{lon}}{g}\right) \qquad \text{and} \qquad \phi_{des} = \arctan\left(\frac{a_{lat}}{g}\cos\theta_{des}\right) \tag{6.5}$$

while the lateral and longitudinal velocities are computed from the inertial velocity rotated with the heading, thus

$$\begin{bmatrix} V_{lon} \\ V_{lat} \\ V_{vert} \end{bmatrix} = \begin{bmatrix} \cos\Psi & \sin\Psi & 0 \\ -\sin\Psi & \cos\Psi & 0 \\ 0 & 0 & 1 \end{bmatrix} \begin{bmatrix} V_N \\ V_E \\ V_v \end{bmatrix} \tag{6.6}$$

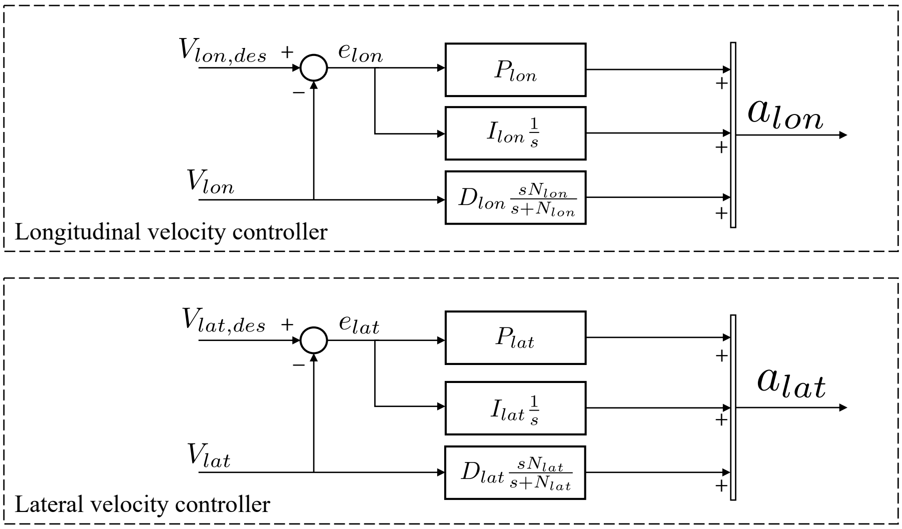

Figure 6.3: Velocity control system

Setting up the PID controller gains is a fundamental part of control system design. While at an advanced stage different systematic approaches can be applied, such as the Ziegler-Nichols method or the analysis of closed-loop poles [169], for the sake of this work an heuristic method is preferred. The system is fed by a set of step inputs of different entities, starting from the steady hover condition, and the gains are tuned in order to satisfy three main requirements:

1. Percentage error at regime (10 sec) $< 5\%$ of the target;
2. Maximum overshoot tolerance $< 10\%$ of the target;
3. Time delay at 90 % of the target < 1 second;

In particular, requirement 1. sets the maximum acceptable discrepancy between the actual and the desired signals after 10 seconds from the step input. Requirement 2. fixes the maximum overshoot limit for the actual signal, while requirement 3. imposes that the actual signal reaches 90% of the target step in less than 1 second. The gains are selected with a trial and error approach, in order to fulfill the three requirements. The values are summarised in Table 6.1, together with the saturation limits. Targets and requirements are selected empirically, with the only intention of proving the correct functioning of the control architecture and the dynamic behavior of the rotorcraft. The targets, in particular, do not reflect the aircraft performance neither in terms of controllability nor in terms of handling qualities or maximum speed/rate.

	K	P	I	D
Pitch angle controller	6	-0.20	-0.25	0.01
Roll angle controller	6	0.1	0.25	0
Yaw rate controller	-	1.15	0.05	-0.2
Lon. Velocity controller	-	1.8	0.25	-0.01
Lat. Velocity controller	-	2.5	0.2	-0.01
Roll control saturation	Min. $= -30°$; Max. $= 30°$			
Pitch control saturation	Min. $= -40°$; Max. $= 40°$			
Yaw rate control saturation	Min. $= -5°$; Max. $= 5°$			

Table 6.1: Control system gains

The attitude controller is tuned at first, by neglecting the outer loop and feeding the system with a set of step inputs on the roll and pitch angles, respectively 4 deg and 10 deg, and the yaw rate. For the latter, two different simulations are performed: a step input of 5 deg/s, and a finite step of 5 deg/s for 5 seconds, which has the aim of rotating the heading of the rotorcraft of 25 deg in 5 seconds. As a matter of fact, the yaw control is a criticality of this rotorcraft. The adopted control mix which applies a differential longitudinal cyclic pitch to change the heading of the rotorcraft guarantees quite low responsiveness on the yaw control. While it is true that this would represent a viable and simple solution for preliminary analysis, a deeper study on the controllability properties and optimization of the control mix would be required to improve the heading control. In addition, a strong roll/yaw coupling limits the controller capabilities and highlights the necessity to reexamine the control method. The simulation results are reported in Figures 6.4, 6.5, 6.6, and 6.7, while the compliance with the fixed requirements is provided in Table 6.2. Concerning the Pitch and Roll performance, the system behaves similarly: the dynamics follows the step input, reaching the 90% of the target in approximately 0.3 seconds, keeping the regime error very low and the overshoots contained in the limit. However, it is worth mentioning that the rolled attitude generates an uncontrollable yaw rotation, which is hardly stabilized by the yaw rate controller. The latter indeed represents the major criticality of the design. Even if the controller follows a desired step input, the yaw rate does not reach the target in an accepted time: the target set is a very small yaw rate and nevertheless the system reacts with 1.5 seconds delay with respect to the 90 % target value, not fulfilling the requirement 3. (highlighted in red in the Table). Pushing the gains above the selected value is not an option, since an unstable behavior has been observed in that case. However, a finite step simulation is tested as well, with the aim of reaching 25 degrees of heading in 5 seconds. The system reacts to the input by following the step, and reaches the 90% of the target with 0.66 seconds of delay with respect to the input, maintaining the error at regime within the limits.

	Target	Error at regime	Max. Overshoot	Time delay
Pitch angle sim.	10° step	0.17 %	3.6 %	0.29 s
Roll angle sim.	4° step	0.95 %	2.5 %	0.28 s
Yaw rate sim.	5° step	3.01 %	3.5 %	1.51 s
Yaw angle sim.	25° in 5 sec (finite step)	1.17 %	-	0.66 s
Lat. velocity sim.	2 m/s step	1.37 %	2.38 %	0.98 s
Lon. velocity sim.	3 m/s step	2.25 %	6.05 %	1.14 s s

Table 6.2: Attitude control system performance: the % are computed with respect to the target step, while the time delay is intended as the delay to reach 90% of the target value

With the fixed gains in the attitude controller, the outer loop is tuned with the same approach. The system is fed by a couple of step inputs on the lateral and longitudinal velocity, respectively 2 m/s and 3 m/s. The simulation starts at hover and the rotorcraft accelerates in order to achieve the target speed within one second. The simulation results are depicted in Figures 6.8 and 6.9, and the compliance with the requirements is reported in Table 6.2. Both targets are reached with acceptable overshoots and errors at regime, while the longitudinal controller does not match requirement 3 on the maximum time to reach 90% of the objective speed. This limits the longitudinal acceleration: it is observed that increasing either the proportional and integral gains leads to a longitudinally unstable behavior, with the rotorcraft that reaches the target before diverging in the pitch angle. Setting the target on the speed and tuning the controller to match requirement 3 means setting a desired acceleration. It is noticeable from this study that the longitudinal control, as well as the masses and inertia of the system, should be revised if the aircraft is required to perform higher accelerations.

The control system design presented in this Section is preliminary, but still provides meaningful information on the characteristics of the side-by-side helicopter. A general difficult tuning of the control parameters is highlighted, being the rotorcraft subjected to possible divergences when the controller gains are pushed too much. In addition, both pith and roll coupling with the yaw angle makes the rotorcraft directionally critical also during forward and lateral movements. Heading control requirements are not totally fulfilled, and the responsiveness of the yaw rate command appears to be limited. This suggests that both the control mix strategy and the heading controller architecture must be revised. Similarly, lateral and longitudinal velocity responsiveness is bounded by the appearance of unstable behaviors. This is not necessarily a limit in the rotorcraft acceleration performance, but suggests that a more detailed controllability analysis should be carried out to implement a more aggressive control strategy.

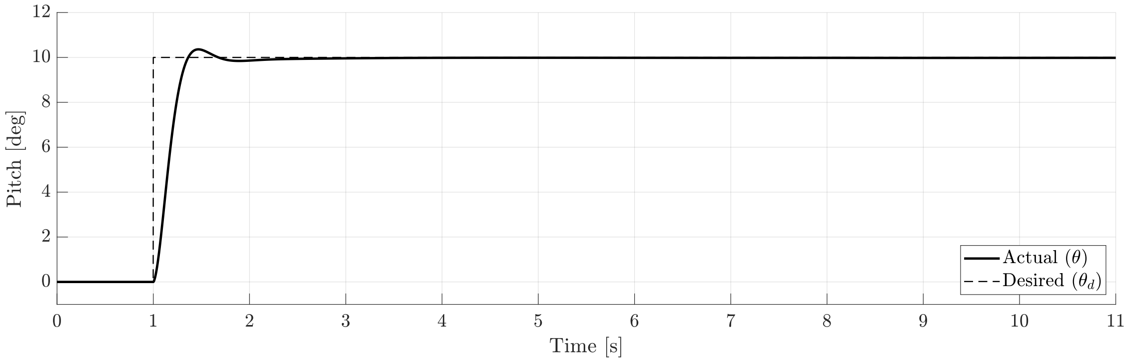

Figure 6.4: Pitch angle controller: step input of 10 deg

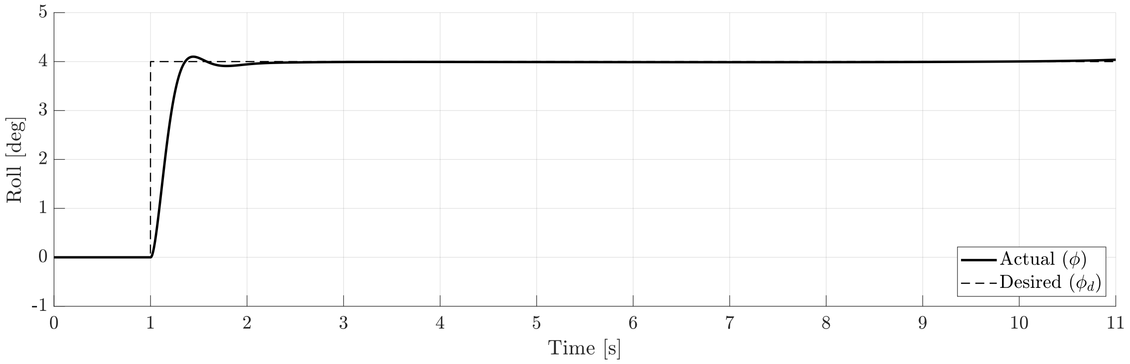

Figure 6.5: Roll angle controller: step input of 4 deg

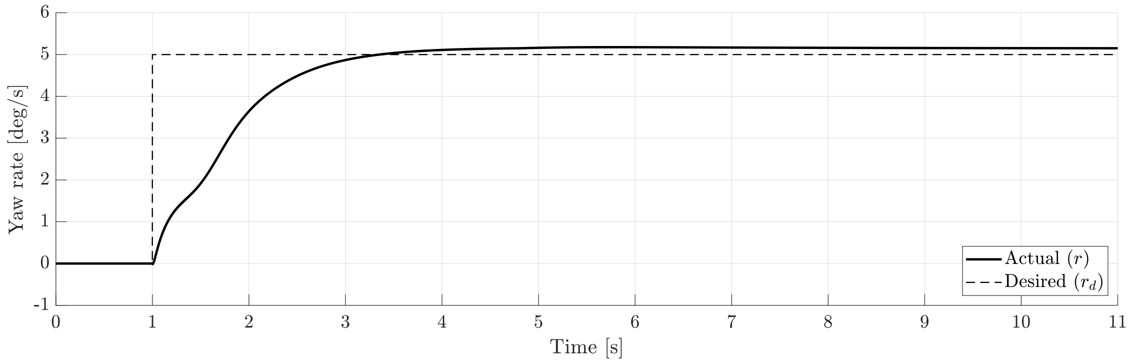

Figure 6.6: Yaw rate controller: step input of 5 deg/s

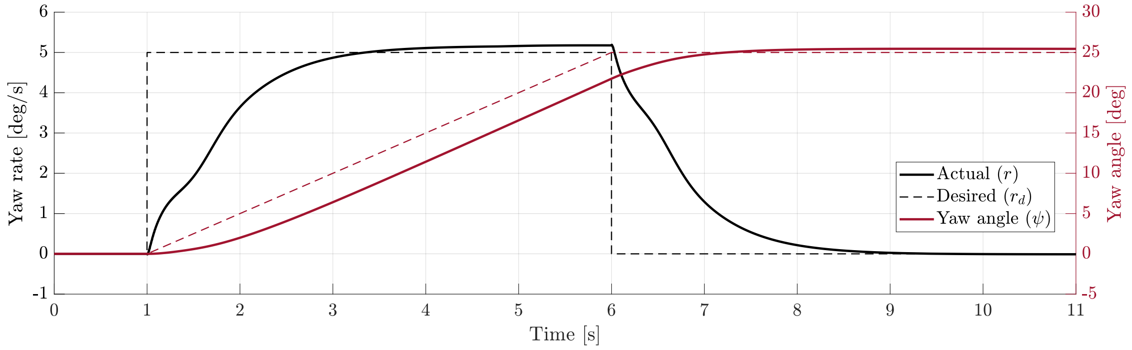

Figure 6.7: Yaw rate controller: finite step input of 25 degrees in 5 seconds

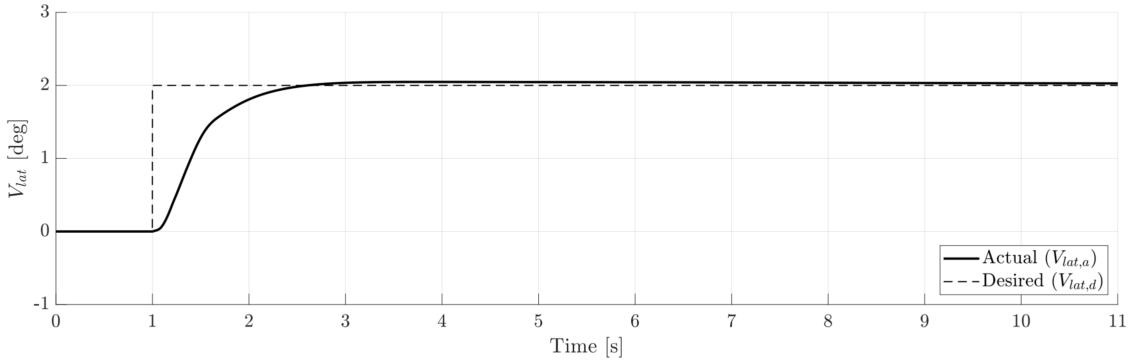

Figure 6.8: Lateral velocity controller: step input of 2 m/s

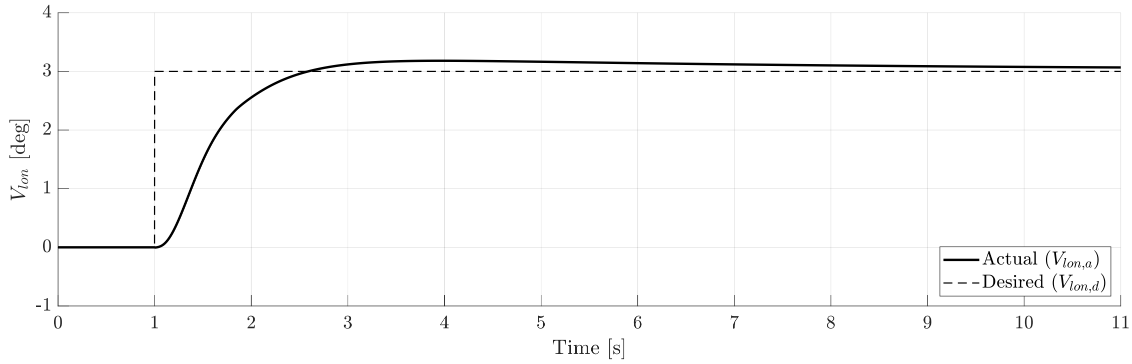

Figure 6.9: Longitudinal velocity controller: step input of 3 m/s

6.3 Hardware-in-the-loop (HITL) simulation setup

Simulation plays a crucial role in the development and validation of complex systems, control logics, and flight dynamics models [170]. Among all simulation techniques, Software-in-the-Loop (SITL) and Hardware-in-the-Loop (HITL) are the most widely used [171]–[175]. These methods are fundamental for studying aircraft's flight dynamics, as they offer an initial understanding of its behavior and stability across a range of conditions. By conducting simulations within a controlled and well-defined environment, these techniques help mitigate risks and significantly reduce the costs associated with physical testing. SITL simulation involves testing both aircraft dynamics and control system algorithms within a virtual environment. In this method, the software is tested with simulated inputs and outputs, allowing for the evaluation of the aircraft's performance without the need for physical hardware. SITL is often used in early development stages to verify the logic and functionality of control systems, detect software bugs, and verify the physical accuracy of a dynamic model. On the other hand, HITL is a more refined simulation technique that allows for taking into account hardware dynamics and some real-world uncertainties. HITL extends SITL with the integration of physical components, such as sensors, actuators, or controllers, into the testing loop. The hardware interacts with a real-time simulated environment, enabling the analysis of both flight systems' behavior and their integration with the software.

Figure 6.10: Hardware-in-the-loop setup

HITL bridges between purely numerical simulations and experimental campaigns: the control system architecture can be tested on real flight controllers, and the agreement between the computational burden and hardware capabilities can be assessed. A further extension of the HITL setup, is the Pilot-in-the-Loop simulation technique, which integrates a human operator into the feedback loop. The pilot interacts with the system through a user interface (e.g., flight controls, vehicle cockpit, or VR/AR systems), and its inputs influence the simulated environment. The system provides real-time feedback, allowing the operator to experience and react to specific scenarios. The operator of the PITL plays an active role in the system, while the software and hardware components emulate real-world physics and control dynamics. In this section, a HITL/PITL setup is proposed for testing flight control laws on an advanced autopilot system. The architecture is a HITL configuration but with the possibility to integrate VR systems and pilot controls to extend it to a PITL. This is currently an ongoing project, and the objectives of this section are limited to the theoretical presentation of the architecture. A more specific analysis of flight control system results gathered on a simplified HITL setup can be found in Ref. [176]. Figure 6.10 shows the adopted hardware, while the general system's architecture is depicted in Figure 6.11. The setup includes: a host computer running MatLab & Simulink (Release R2023a, in agreement with the latest Speedgoat software version), XPlane (Version 11.55) as a visualization tool, and QGround Control (Version 4.0) as a virtual ground station, a PixHawk 6X flight controller coupled with PX4 flight stack firmware, and a Speedgoat performance real-time target machine. In addition, the simulation setup is integrated with physical pilot controls (Thrustmaster Hotas Warthog and Thrustmaster TPR pedals), and virtual reality goggles (Meta Quest Pro) for a more immersive piloting experience.

The host computer is the core of the architecture and manages the communication between the real-time machine and the flight controller, as well as the integration of the external hardware. The connection with the Speedgoat is made with an ethernet cable and controlled by the Simulink Real-Time tool [177]. This external computer is used for running the aircraft flight dynamics on a separate machine with respect to the host computer and for synchronizing the simulation in real-time. An external monitor is connected to the Speedgoat for monitoring target variables. On the other side of the architecture, the host computer communicates with the PixHawk 6X, exchanging data on the aircraft state and control outputs. The connection is made through a serial port and controlled by the QGround Control station. This communicates with the PixHawk firmware in a "Monitor and Tune" mode, while the control algorithms are generated using the Matlab embedded coder [178].

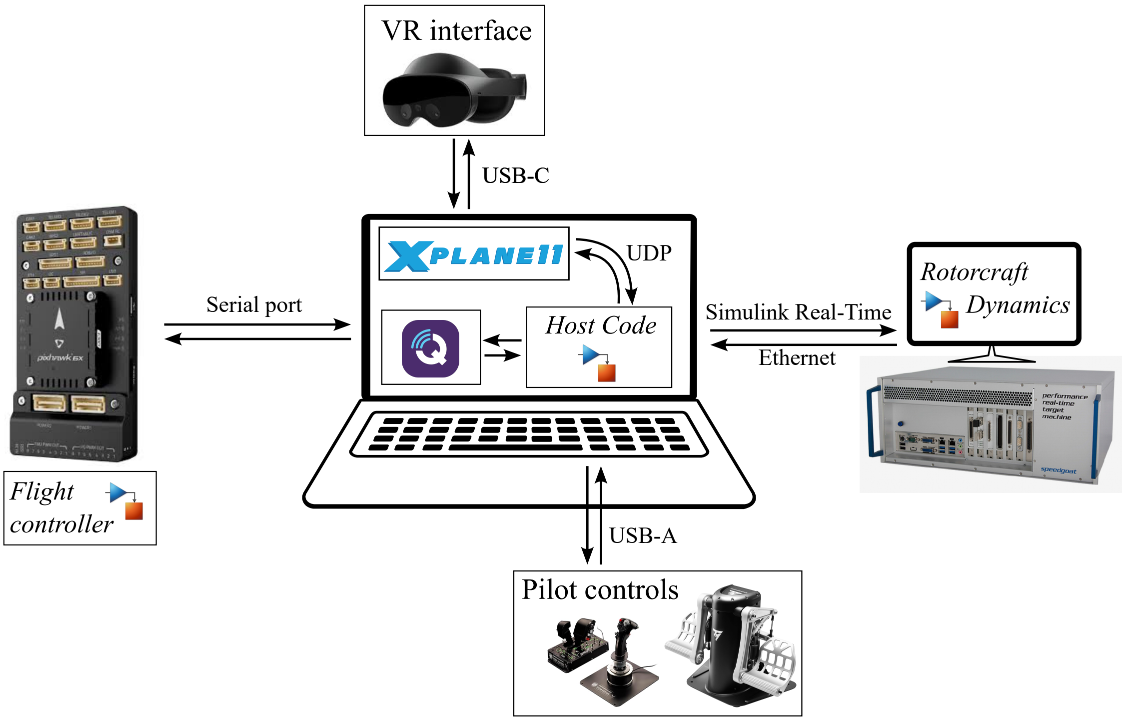

Figure 6.11: Hardware-in-the-loop architecture

Data visualization is made through the flight simulation software XPlane: this high-resolution videogame allows for exchanging data via UDP (User Datagram Protocol) port and visualizing the aircraft state in a virtual world. In addition, XPlane enables the wireless/USB-C connection with virtual reality goggles, for a 360° representation of the flight simulation and aircraft geometry. The pilot input is provided by a set of external hardware, connected from a USB-A port to the host computer, and read by the suitable Simulink blocks (see the Aerospace Toolbox [179]).

The host computer manages the PITL/HITL simulation with the Simulink scheme provided in Figure 6.12. To communicate with the PixHawk controller, the setup adopts the UAV Toolbox Support Package for PX4 Autopilots (see Ref [180]) and its *uORB Read* and *uORB Write* blocks: these two blocks exchange massages by creating Simulink nonvirtual buses that correspond to specific input/outputs of the controller. The data are exchanged by simulating the signal of distinct sensors, such as the GPS (for positions and velocity), the accelerometer (for linear accelerations), the magnetometer (for the aircraft's attitude), and the gyroscope (for the aircraft's angular rates). Similarly, *uORB* blocks are used for transferring pilot inputs from the host computer to the flight controller. The PixHawk elaborates the aircraft's state and desired attitude/velocities/rates with the implemented feedback loop (see Figure 6.13) and sends the control action (i.e. the main rotor swashplate controls) back to the host. UDP protocols are used for exchanging data to/from the Speedgoat machine: the control action is re-directed to the real-time target which computes the aircraft state according to the rotorcraft flight dynamics model (see Figure 6.14). This is built on the Speedgoat computer with the Simulink Real-Time tool and provides the aircraft state at each time step of the simulation. *Target plot* blocks are used to represent sensible data on the external monitor.

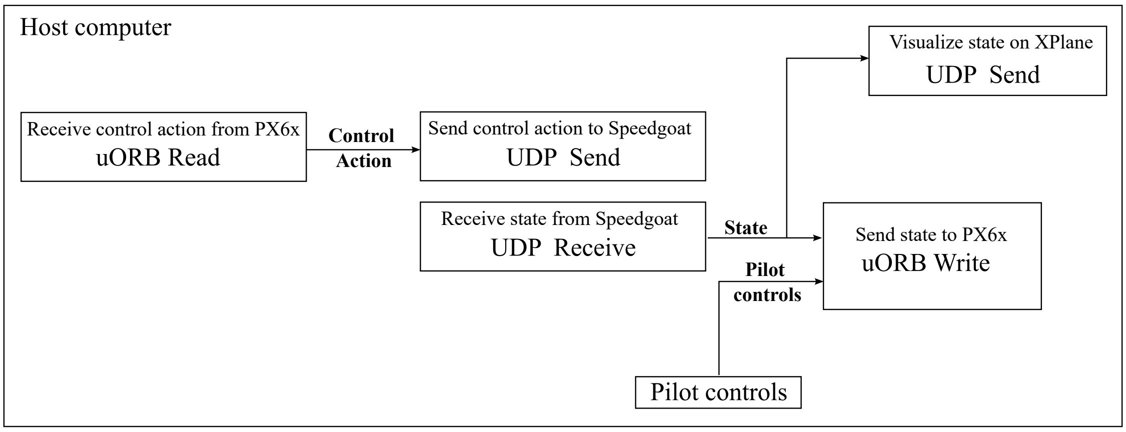

Figure 6.12: Host computer simulink code

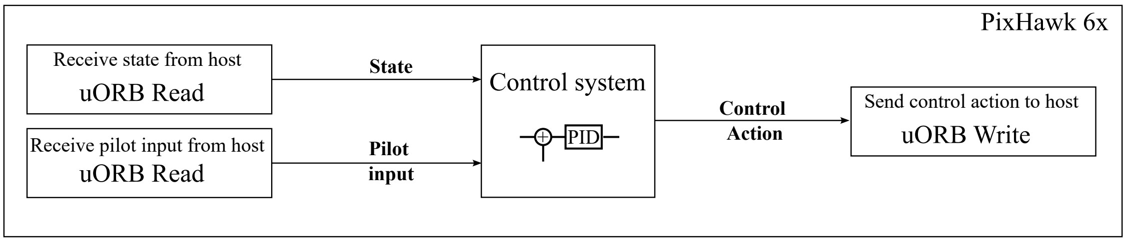

Figure 6.13: Controller architecture built on PixHawk 6x hardware

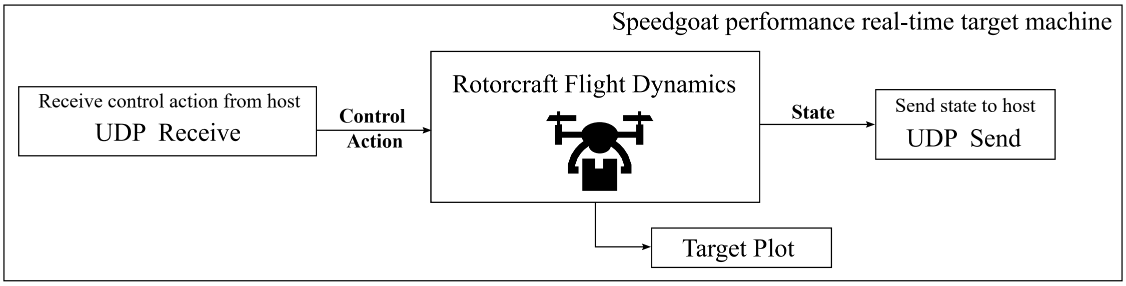

Figure 6.14: Simulink code built on Speedgoat performance real-time target machine

The PITL/HITL architecture outlined in this appendix is designed to serve as a simulation benchmark for future flight dynamics and control applications. While its full capabilities are still under validation, the communication between individual components has already been successfully tested independently. Specifically, the interactions between the host computer, flight controller, and real-time target machine have been confirmed to function correctly and synchronously. The next phase of this research involves assessing the flight performance calculations executed on the external real-time machine. Although the behavior of the side-by-side helicopter in a Software-in-the-Loop setup has been thoroughly evaluated in this thesis, it remains to be validated whether the integration with a real-time system yields comparable results. Furthermore, the flight control law described in Section 6.2 must be implemented on the external hardware, with the tuning parameters verified within the HITL framework. Once these steps are completed, the HITL architecture will be utilized as a physical platform for evaluating the flight performance of various vehicles. This platform will provide critical insights into the capabilities, handling qualities, and control characteristics of multiple VTOL configurations, thereby contributing to the development of advanced solutions for Urban Air Mobility.

Chapter 7

Conclusions

Urban Air Mobility (UAM) is an emerging aviation sector aimed at addressing critical societal challenges such as climate change, traffic congestion, safety, and efficiency. The growing demand for sustainable transport solutions, driven by the alarming increase of greenhouse gas emissions, has motivated significant research efforts in this field. Despite advancements in conceptual design and performance analyses of Vertical Take-Off and Landing (VTOL) aircraft, a definitive solution for UAM transport remains elusive. This thesis focuses on the modeling and simulation of a side-by-side helicopter configuration as a candidate VTOL for UAM applications. The primary objective is to define and justify the aircraft selection and perform a detailed analysis of its performance, trim, stability, and flight dynamic properties. The work is divided into three sub-goals: addressing the aircraft performance with different propulsion systems, providing a conceptual design and performance assessment of similar rotary wing configurations, and developing a numerical platform for flight dynamic simulations.

The first part of the thesis is dedicated to the performance analysis and conceptual design of generic VTOL layouts, with a particular focus on the propulsion system and configuration selection. An analytical framework was developed for a preliminary assessment of the power requirements at specific flight conditions: the model is based on the actuator disc and momentum theories and is adapted for considering either single or multirotor configurations. The propulsion system's performances are investigated on a conventional helicopter, by providing 3 plug-in hybrid (fuel cell and battery) systems and a full battery-electric layout. The powertrains are carefully designed by considering power and mission requirements, selecting suitable components, and including residual energy parameters for a safe landing. The hybrid configurations are named: Hybrid 70, which means a 70 kW fuel cell, coupled with a 10.3 kWh battery and 4.9 kg of hydrogen stored onboard; Hybrid 80, composed of an 80 kW fuel cell, a similar battery pack, and 4.0 kg of hydrogen onboard; Hybrid 90, with an oversized fuel cell providing 90 kW, the same battery pack and 3 kg of hydrogen stored. On the other hand, a battery-electric design is produced with a 44 kWh Li-S battery which aims at maximizing the endurance of the helicopter by increasing the total capacity. The four powertrains are compared along three mission scenarios, reproducing the travel between strategic locations (urban and regional missions) and a standard scenario for rotorcraft design (standard mission). The latter is used to define the minimum requirements for the four configurations, and to identify the maximum range achievable by each of them: more than 100 km are reached by Hybrid 70, while approximately 90 km and 60 km are reached at maximum by Hybrid 80 and Hybrid 90. The battery-electric reaches the minimum mission requirement of 50 km, but achieves considerable performance in the urban scenario, where it outperforms Hybrid 70 and matches Hybrid 80 with 5 routes completed. Hybrid 90 has the optimal outcomes in the urban mission, where the oversized fuel cell allows this rotorcraft to perform more than 7 travels.

On the other hand, a Hybrid 70 is the only configuration able to complete more than 3 regional routes, where low-power phases are dominant. Key findings from this study are here summarised:

1. While the battery-electric is designed to achieve the 50 km range, it is clear that a suitably sized fuel cell can be adopted as a range extender for low-power duties. Considering the three hybrid configurations, the highest range can be achieved by maximizing the hydrogen stored, thus reducing the fuel cell power as much as possible.
2. The optimal powertrain design is strictly related to the specific mission scenario: high-power missions with short ranges and frequent vertical flights, require powertrains with high specific powers, thus, with an oversized fuel cell or a large battery. On the contrary, mission scenarios with long cruise phases, call for large useful energy densities.
3. The battery electric design shows decent performance in all mission scenarios, with good performance in high-power duties where the very high specific power of the battery pack can be much better exploited.
4. In a UAM context, urban missions are predominant, requiring rotorcraft with high specific power to perform such operations efficiently. The choice of propulsion system narrows down to either a battery-electric design or a hybrid configuration with an oversized fuel cell. Considering the objectives of this thesis, along with the inherent advantages of a battery-electric powertrain (such as design simplicity, cost-effectiveness, and availability, particularly for small-scale models), this latter solution is chosen as the reference propulsion system for this work.

Once the electric powertrain is selected, various rotorcraft configurations are evaluated to identify the most suitable layout for Urban Air Mobility (UAM) operations in densely populated areas. For this study, three rotary-wing VTOL configurations are considered: a conventional helicopter, a side-by-side helicopter, and a multirotor. The goal is to develop preliminary design concepts that meet minimum performance criteria and are comparable in their capabilities. Similarly to the previous analysis, the conventional helicopter serves as the reference configuration from which the side-by-side and multirotor designs are derived by adjusting specific design parameters. A detailed battery design methodology and specific battery discharge models are provided at this stage. The performance of the three rotorcraft are compared in terms of power at different flight conditions, theoretical endurance and range on the standard mission profile. As expected, the conventional helicopter is the most efficient configuration and reaches the highest performance: at the best specific endurance speed, it achieves more than 1h of flight, against the 53 minutes of the side-by-side and the 34 min of the multirotor. On the other hand, both single and dual rotor layouts provide similar maximum range (around 90 km), while the multirotor only 66 km. Even if it is evident that from a performance point of view, the single rotor configuration with low disc loadings has the optimal results, the selection of a configuration for UAM services must include qualitative aspects that are relevant for the impact on the society. The key findings from the configuration selection process are summarised here:

1. The rotorcraft performance at hover and low-speed regimes (below the minimum power) is directly proportional to the disc loading of the configuration. Being the maximum size a fixed parameter in the design methodology, a single rotor configuration allows for reducing the total power required by the system, leading the helicopter to outperform the other two configurations.
2. From a design point of view, the variable RPM system of the multirotor and the symmetry in the side-by-side helicopter make these two vehicles mechanically simpler than a conventional helicopter, a property which is fundamental in UAM to reduce the empty mass ratio and to increase the available space for energy storage.
3. Societal acceptance is of primary importance: citizen's confidence in a VTOL configuration is determinant for the development of a solid UAM market and the spread of UAM technologies in urban areas. From this point of view, safety, noise, and sustainability are the primary concerns of future users.

4. While the helicopter configuration can always rely on an autorotation maneuver in case of engine failure, multirotors implement safety measures through the redundancy of their systems, and residual controllability is guaranteed in case of failure of a single engine. The side-by-side helicopter potentially merges these two characteristics and includes ducted rotors in its design, resulting in the safest configuration among the three.
5. Even if a deeper analysis would be required to assess the noise levels produced by each configuration, it is highlighted how an outboard position of the main rotors and the avoidance of rotor-rotor and rotor-fuselage interactions can substantially reduce the noise impact.

According to the performance analysis and qualitative discussion carried out in this part, the side-by-side helicopter is selected as a reference vehicle for future UAM services.

The second part of the thesis is dedicated to the modeling and simulation of the side-by-side helicopter flight dynamics, and the analysis of its trim and stability properties. The objective of this study is to characterize the flight dynamics of the rotorcraft and provide a methodology for modeling with different levels of complexity. Two different mathematical models are developed for this goal: the idea is to provide meaningful insights, not only on the characteristics of the rotorcraft but also on the necessary modeling approach for different tasks. In addition, in the absence of experimental evidence and profound literature knowledge on this particular configuration, a comparative approach between different frameworks would allow for a cross-validation of the results, and generate a greater confidence in the accuracy of the simulation. The analysis is divided into two separate steps. The first one is to develop an analytical framework, with a low level of complexity, that allows for studying the steady-state solutions at variable flight conditions and the stability properties in forward flight and variable center of gravity. The second step is instead to develop a numerical framework with an advanced modeling approach: the aim is to employ this model to study the effects of rotor dynamics on rigid body stability. Fuselage loads, shroud effect, and blade's aerodynamics are modeled separately.

The analytical model has 14 degrees of freedom and is based on 16 nonlinear ODEs: 6 for the rigid body dynamics, 6 for a second-order main rotor flapping, 2 for a first-order uniform inflow, and 2 for taking into account the control mix relations. It is named "analytical" because of the formulation of the main rotor forces, moments, and rotor flap equation coefficients, which are based on nonlinear equations defined on a rotor disc in a non-rotating frame of reference. The steady-state solutions of the rotorcraft dynamics are computed with a Newthon-Rapson method, while an 8-state-space linearized model is produced with a manual linearization algorithm. The trim and stability of a small-scale model are studied with the analytical framework: at trim, the rotorcraft absorbs around 1.5 kW in hovering conditions, while requiring around 9 degrees of collective in both rotors and around 1.2 kW at the best specific endurance speed of 12 m/s. Key findings are summarised here:

1. In general, the side-by-side helicopter controlled with the proposed control mix, behaves as a conventional helicopter without the need for a tail rotor: typical trim curves are obtained, showing how a positive longitudinal cyclic control can be applied to increase the rotorcraft speed and pitch down attitude. Similarly, the lateral cyclic is coupled with the pedal command to move the rotorcraft laterally.
2. Even if without considering the aerodynamic interactions at forward flight, the effect of the shrouds is taken into account on the production of thrust, reducing the main rotor collective for specific flight conditions.
3. The side-by-side helicopter flight dynamics is characterized, showing multiple similarities with conventional helicopters. Eigenvector analysis provided a clear view of the poles map at different conditions: rotorcraft stability is characterized by a couple of high-frequency, stable, and real poles, defining converging roll and short-period dynamics. Two couples of low-frequency, slightly unstable, oscillatory poles define the phugoid and dutch-roll modes,

while spiral and heave-subsidence dynamics are present at a very low frequency and stable location.

4. Forward flight stability is assessed: the longitudinal speed has a positive effect on the high-frequency modes (i.e. roll and short period) and a negative influence on the low-frequency oscillatory poles, creating a dangerous later-directional divergence from the dutch-roll.
5. The position of the CG is fundamental for the stability of the system, and so is the location of the batteries. At hover, the dutch-roll can be stabilized by moving the CG backward enough. On the contrary, such an adjustment should be carefully calibrated since the phugoid mode might become an unstable divergence. Similarly, in forward flight, the backward location of the CG helps the lateral mode to become stable, and an optimal location at -0.1 m is found: in this situation, the dutch-roll is stable, while the phugoid is still a low-frequency oscillatory mode. Short period and heave subsidence merge into a couple of oscillatory, high frequency, and stable poles.

The "take-home message" of this study, beyond the mathematical results, is that an analytical modeling approach can be adopted for studying the trim and stability properties of a specific VTOL configuration and derive considerations on its design and behavior at different flight conditions. What is missing from this analysis, is the influence of rotor parameters on the overall stability of the system, and the effect that an advanced modeling approach has on the results. Whenever a particular behavior arises, a more detailed mathematical framework may provide additional motivations for its origins and developments. Validation is another theme: in the absence of experimental evidence, a cross-comparison with a higher complexity model, can provide an increased confidence in the results produced with this approach. For these reasons, an advanced modeling methodology is proposed in this thesis.

The numerical model has 24 degrees of freedom and the system's dynamics is described by a set of 26 ODEs: 6 for the rigid boy motion, 12 for the main rotor dynamics (i.e. 6 for the second order flap, and 6 for the second order lead-lag), 6 for the first order nonuniform inflow dynamics and 2 for taking into account the control mix relations. The model is numerical, meaning that the single blades are divided into a finite number of sections, each of them governed by 2D aerodynamics and having its own position and orientation in time. The aerodynamic loads are integrated along the span, creating a system of forces and moments represented in a rotating frame of reference. A similar approach is also applied to the rotor dynamics, with the blade's flapping and lead-lag angles computed through generalized moments equilibrium. This approach brings with it several criticalities, related to the time-dependency of the loads, their numerical integration, and the non-linearity of the equation: because of them, a specific trim and linearization procedure was developed. For the first one, an iterative algorithm with two separate loops is adopted, while for the second a linearization methodology is proposed to produce a 38-state-space representation of the rotorcraft flight dynamics. The results and important outcomes produced with this framework are summarised here:

1. A comparison with the analytical model contributed to gaining confidence in the steady solutions at variable forward flight and the stability picture of the case study. In steady conditions, the aircraft modeled with a numerical framework behaves similarly to the analytical representation. At the lowest level of complexity, both the mathematical models agree on the low-frequency, oscillatory, and unstable poles, while a considerable discrepancy is observed in their frequency.
2. Considering the effect of flap dynamics, the lateral and longitudinal disc tilts are added at the first step of the analysis, showing how this rotor feature contributes to the increase of the roll and short period frequency, and the oscillation of both dutch-roll and phugoid. The relative discrepancy between the two models at this stage, is quite well improved.
3. Lead-lag dynamics is an additional level of complexity: it is observed that this rotor dynamics has a beneficial effect on the stability of the high-frequency poles, while it is quite low effective on the low-frequency ones. Flap and lead-lag coupling is essential to be

addressed at this stage, since the effectiveness of the lead-lag on the rigid body modes is directly related to its coupling with the rotor disc tilt.

4. The inflow model is another factor that has a strong influence on the stability outcomes. It is observed that a nonuniform inflow modeling provides different results with respect to the simpler uniform case. The coupling between rigid body and longitudinal inflow component generates a shifting of the phugoid modes from a slightly unstable oscillatory location to a more dangerous longitudinal divergence.
5. The pure rotor dynamics is studied with this model as well. The analysis revealed the presence of a collective flap oscillating at approximately the angular frequency of the rotor and a couple of advancing/regressive modes. Similarly, a collective lead-lag with its advancing/regressive modes is also present at a higher frequency. Inflow poles characterize the response of the rotorcraft to an inflow perturbation, confirming, as expected by the side-by-side arrangement, its coupling with both heave velocity and roll rate.

In general, the development of a numerical model has contributed to the partial validation of the analytical results and provided an advanced, modular, tool for simulation and flight dynamics analysis. The framework contains a higher number of degrees of freedom and allows for considering additional rotor features. With the single-blade representation, it is possible to perform a detailed rotor and blade design, without considering a unique and uniform disk like in the analytical one. The responsible for the longitudinal instability has been identified in the longitudinal inflow component, even if a complete validation is still required.

To the best of the author's knowledge, the original contributions provided by this thesis to the scientific community are:

1. The evaluation of sustainable propulsion systems in a UAM context, complemented by a detailed electrification methodology of a conventional rotorcraft (see Ref. [89]);
2. The comparison methodology between different VTOL configurations: while multiple conceptual design studies have already been developed, a unique procedure for designing comparable rotary wing VTOLs starting from a baseline layout was still missing (see Ref. [112]);
3. The characterization of side-by-side helicopter flight dynamic properties: even if some of the methods adopted are well-established ones, their application to an innovative side-by-side configuration remained unexplored (see Ref. [75]);
4. The trim and linearization methods, and the resulting outcomes, are innovative and specific for a high-complexity numerical modeling approach (see Ref. [139]).

To conclude, this thesis presents a comprehensive study of a side-by-side helicopter, identified as a viable candidate for future Urban Air Mobility (UAM) services. The work begins with a thorough review of the current state of UAM technologies, systems, and the motivations driving this transformative aviation sector. From this foundation, various VTOL candidates were evaluated through a detailed performance analysis and conceptual design study, ultimately converging on a single configuration. Starting from the analysis of different propulsion systems, and moving on to alternative rotorcraft configurations, the thesis provided and employed mathematical tools to identify the most promising candidate, both from a quantitative and a qualitative point of view. The side-by-side helicopter emerged as the optimal choice for this study. To analyze its unique flight dynamic characteristics and stability, two distinct modeling frameworks were developed. These frameworks enable a deeper understanding of the effects of design and modeling features on the aircraft's open-loop behavior, providing insights into its stability and flight dynamics properties. The thesis' contribution to the scientific community is represented by the tools and methodologies developed for the analysis, design, and simulation of VTOL aircraft in the context of UAM, as well as the results of the specific case study. The developed frameworks not only address the unique challenges of the side-by-side helicopter configuration but also lay the groundwork for broader studies on VTOL performance and flight dynamics. By advancing the understanding of these innovative rotorcraft, this research supports the realization of a solid UAM ecosystem that has the potential to transform modern societies, enhance urban connectivity, and address critical challenges.

Bibliography

[1] H. Ritchie, L. Rodes Guirao, E. Mathieu, *et al.* “Population growth.” Accessed: 14 November 2024. (2023), [Online]. Available: `https://ourworldindata.org/population-growth`.

[2] D. o. E. United Nations and S. D. Social Affairs. “Agenda 2030 - goal 11: Sustainable cities and communities.” Accessed: 14 November 2024. (2022), [Online]. Available: `https://unstats.un.org/sdgs/report/2023/goal-11`.

[3] European Union Aviation Safety Agency (EASA). “What is UAM.” Accessed: 14 November 2024. (2021), [Online]. Available: `https://www.easa.europa.eu/en/what-is-uam`.

[4] J. T. Doo, M. D. Pavel, A. Didey, *et al.*, “NASA Electric Vertical Takeoff and Landing (eVTOL) Aircraft Technology for Public Services - A White Paper,” NASA Ames Research Center, Tech. Rep. Document ID: 20205000636, 2021.

[5] L. Preis, M. Husemann, and M. Shamiyeh, “Time- and energy-saving potentials of efficient urban air mobility airspace structures,” *AIAA Journal*, vol. 61, no. 12, pp. 5571–5583, 2023. DOI: `10.2514/1.J062390`.

[6] O. Cokorilo, “Urban air mobility: Safety challenges,” *Transp. Res. Proc.*, vol. 45, pp. 21–29, 2020. DOI: `10.1016/j.trpro.2020.02.058`.

[7] C. Al Haddad, E. Chaniotakis, A. Straubinger, K. Plötner, and C. Antoniou, “Factors affecting the adoption and use of urban air mobility,” *Transportation Research Part A: Policy and Practice*, vol. 132, pp. 696–712, 2020. DOI: `10.1016/j.tra.2019.12.020`.

[8] International Energy Agency (IEA). “Greenhouse gas emissions from energy data explorer.” Accessed: 31 October 2024. (2024), [Online]. Available: `https://www.iea.org/data-and-statistics/data-tools/greenhouse-gas-emissions-from-energy-data-explorer`.

[9] Q. Long, J. Ma, F. Jiang, and C. J. Webster, “Demand analysis in urban air mobility: A literature review,” *J. Air Transp. Manag.*, vol. 112, p. 102 436, 2023. DOI: `10.1016/j.jairtraman.2023.102436`.

[10] Morgan Stanley Research. “Are flying cars preparing for takeoff?” Accessed: 14 November 2024. (2019), [Online]. Available: `https://www.morganstanley.com/ideas/autonomous-aircraft`.

[11] R. Goyal, C. Reiche, C. Fernando, *et al.*, “Urban Air Mobility (UAM) Market Study,” NTRS Research Center, Tech. Rep., 2018, Document ID: 20190001472.

[12] M. Chae, S. H. Kim, M. Kim, H. Park, and S. H. Kim, “Potential market based policy considerations for urban air mobility,” *J. Air. Transp. Manag.*, vol. 119, p. 102 654, 2024. DOI: `10.1016/j.jairtraman.2024.102654`.

[13] Northeast UAS Airspace Integration Research Alliance (NUAIR), “High-Density Automated Vertiport Concept of Operations,” NASA Ames Research Center, Tech. Rep. Document ID: 20210010603, 2021.

[14] Skyports. “Our vertiports.” Accessed: 15 November 2024. (2018), [Online]. Available: `https://skyports.net/vertiports/`.

[15] D. Thipphavong, R. Apaza, B. Barmore, *et al.*, "Urban air mobility airspace integration concepts and considerations," in *AIAA Aviation Technology, Integration, and Operations Conference, Atlanta, Georgia*, 2018.

[16] Federal Aviation Administration (FAA). "Urban Air Mobility (UAM) Concept of Operations." Accessed: 15 November 2024. (2023), [Online]. Available: `https://www.faa.gov/air-taxis/uam_blueprint`.

[17] A. Bauranov and J. Rakas, "Designing airspace for urban air mobility: A review of concepts and approaches," *Prog. Aerosp. Sci.*, vol. 125, p. 100 726, 2021. DOI: `10.1016/j.paerosci.2021.100726`.

[18] H. Smith. "Air Traffic Management - eXploration (ATM-X) Description." Accessed: 19 November 2024. (2024), [Online]. Available: `https://www.nasa.gov/directorates/armd/atm-x-description/`.

[19] V. L. Stouffer, W. B. Cotton, R. A. DeAngelis, *et al.*, "Reliable, Secure, and Scalable Communications, Navigation, and Surveillance (CNS) Options for Urban Air Mobility (UAM)," NASA Glenn Research Center, Tech. Rep. Document ID: 20205006661, 2020.

[20] J. Serrao, S. Nilsson, and S. Kimmel, "A Legal and Regulatory Assessment for the Potential of Urban Air Mobility (UAM)," UC Berkeley, Tech. Rep. submitted to: National Aeronautics and Space Administration, 2021.

[21] European Union Aviation Safety Agency (EASA). "Prototype Technical Specifications for the Design of VFR Vertiports for Operation with Manned VTOL-Capable Aircraft Certified in the Enhanced Category." Accessed: 15 November 2024. (2022), [Online]. Available: `https://www.easa.europa.eu/en/document-library/general-publications/prototype-technical-design-specifications-vertiports`.

[22] European Union Aviation Safety Agency (EASA). "Special condition for VTOL and means of compliance." Accessed: 15 November 2024. (2024), [Online]. Available: `https://www.easa.europa.eu/en/document-library/product-certification-consultations/special-condition-vtol`.

[23] C. Lee, B. Bae, Y. L. Lee, and T. Y. Pak, "Societal acceptance of urban air mobility based on the technology adoption framework," *Technol. Forecast. Soc. Change*, vol. 196, p. 122 807, 2023. DOI: `10.1016/j.techfore.2023.122807`.

[24] European Union Aviation Safety Agency (EASA), "Study on the societal acceptance of urban air mobility in europe," Tech. Rep., 2023, Accessed: 31 October 2024. [Online]. Available: `https://www.easa.europa.eu/en/full-report-study-societal-acceptance-urban-air-mobility-europe`.

[25] A. P. Cohen, S. A. Shaheen, and E. M. Farrar, "Urban air mobility: History, ecosystem, market potential, and challenges," *IEEE Trans. Intell. Transp. Syst.*, vol. 22, no. 9, pp. 6074–6087, 2021. DOI: `10.1109/TITS.2021.3082767`.

[26] S. Shaheen, A. Cohen, and E. Farrar, "The Potential Societal Barriers of Urban Air Mobility (UAM)," UC Berkeley, Tech. Rep. submitted to: National Aeronautics and Space Administration, 2018.

[27] E. Çetin, A. Cano, R. Deransy, S. Tres, and C. Barrado, "Implementing mitigations for improving societal acceptance of urban air mobility," *Drones*, vol. 6, no. 2, p. 28, 2022. DOI: `10.3390/drones6020028`.

[28] A. Bacchini and E. Cestino, "Electric VTOL configurations comparison," *Aerospace*, vol. 6, no. 3, p. 26, 2019. DOI: `10.3390/aerospace6030026`.

[29] Volocopter. "VoloCity the air taxi that's a cut above." Accessed: 18 November 2024. (2024), [Online]. Available: `hhttps://www.volocopter.com/en/solutions/volocity`.

[30] EHang AAM. "EHang AAV The Era of Urban Air Mobility is Coming." Accessed: 18 November 2024. (2024), [Online]. Available: `https://www.ehang.com/ehangaav/`.

[31] Vertical Flight Society. "Airbus Helicopters CityAirbus (technology demonstrator)." Accessed: 18 November 2024. (2024), [Online]. Available: `https://evtol.news/airbus-helicopters/`.

[32] "Advanced drone air traffic management system "Skye UTM"." Accessed: 17 December 2024. (2022), [Online]. Available: `https://www.maritimegateway.com/advanced-drone-air-traffic-management-system-skye-utm/`.

[33] Leonardo Elicotteri. "AW609 Tilt your Perspective." Accessed: 18 November 2024. (2024), [Online]. Available: `https://helicopters.leonardo.com/it/products/aw609`.

[34] "Boeing CH-47 Chinook." (2024), [Online]. Available: `https://en.wikipedia.org/wiki/Boeing_CH-47_Chinook`.

[35] "Kamov Ka-27." Accessed: 16 December 2024. (2024), [Online]. Available: `https://it.wikipedia.org/wiki/Kamov_Ka-27`.

[36] AIRBUS. "CityAirbus NextGen." Accessed: 18 November 2024. (2024), [Online]. Available: `https://www.airbus.com/en/innovation/energy-transition/hybrid-and-electric-flight/cityairbus-nextgen`.

[37] Uber Elevate. "Aerial ridesharing at scale." Accessed: 18 November 2024. (2024), [Online]. Available: `https://www.uber.com/kr/ko/elevate/vision/`.

[38] Vertical Flight Society. "Wisk aero cora (generation 5) (prototype)." Accessed: 18 November 2024. (2024), [Online]. Available: `https://evtol.news/kitty-hawk-cora/`.

[39] Vertical Flight Society. "eVTOL Aircraft Directory." Accessed: 18 November 2024. (2024), [Online]. Available: `https://evtol.news/aircraft`.

[40] Boeing. "V-22 Osprey: Unlike any aircraft in the world." Accessed: 18 November 2024. (2024), [Online]. Available: `https://www.boeing.com/defense/v-22-osprey`.

[41] Archer. "The flight of a lifetime, every day." Accessed: 18 November 2024. (2024), [Online]. Available: `https://archer.com/aircraft`.

[42] Vertical. "Electric flight is on the horizon." Accessed: 18 November 2024. (2024), [Online]. Available: `https://vertical-aerospace.com/meet-the-vx4/`.

[43] Joby Aviation. "Electric Aerial Ridesharing." Accessed: 18 November 2024. (2024), [Online]. Available: `https://www.jobyaviation.com/`.

[44] Wisk Aero. "Introducing Generation 6." Accessed: 18 November 2024. (2024), [Online]. Available: `https://wisk.aero/aircraft/`.

[45] Lilium. "The Lilium Jet." Accessed: 18 November 2024. (2024), [Online]. Available: `https://jet.lilium.com/`.

[46] Dufour aerospace. "Aero2 The Swiss Army Knife of Drones." Accessed: 18 November 2024. (2024), [Online]. Available: `https://www.dufour.aero/aero2`.

[47] R. Rothfeld, A. Straubinger, M. Fu, C. Al Haddad, and C. Antoniou, "Chapter 13 - Urban air mobility," in *Demand for Emerging Transportation Systems*, Elsevier, 2020, pp. 267–284. DOI: `https://doi.org/10.1016/B978-0-12-815018-4.00013-9`.

[48] W. Johnson, C. Silva, and E. Solis, "Concept vehicles for VTOL air taxi operations," in *Proceedings of the AHS Specialists Conference on Aeromechanics Design for Transformative Vertical Flight*, San Francisco, CA, USA.

[49] W. Johnson and C. Silva, "Observations from Exploration of VTOL Urban Air Mobility Designs," Tech. Rep., 2018, NTRS Research Center: Ames Research Center (ARC), Document ID: 20180007847.

[50] A. R. Kadhiresan and M. J. Duffy, "Conceptual design and mission analysis for eVTOL Urban Air Mobility flight vehicle configurations," in *in proceedings of the AIAA Aviation Forum*, Dallas, TX, USA, 2019.

[51] G. Palaia, K. A. Salem, V. Cipolla, V. Binante, and D. Zanetti, "A Conceptual Design Methodology for e-VTOL Aircraft for Urban Air Mobility," *Appl. Sci.*, vol. 11, no. 22, p. 10 815, 2021. DOI: `10.3390/app112210815`.

[52] C. Theodore and R. Celi, "Helicopter Flight Dynamic Simulation with Refined Aerodynamics and Flexible Blade Modeling," *J. Aircr.*, vol. 32, no. 4, pp. 577–586, 2012. DOI: `10.2514/2.2995`.

[53] G. Guglieri and R. Celi, "Some Aspects of Helicopter Flight Dynamics in Steady Turns," *J. Guid. Control Dyn.*, vol. 21, no. 3, pp. 383–390, 1998. DOI: `10.2514/2.4270`.

[54] P. D. Talbot, B. E. Tinling, W. A. Decker, and R. T. N. Chen, "A mathematical model of a single main rotor helicopter for piloted simulation," Tech. Rep., 1982, NASA Ames Research Center, Document ID: 19830001781. [Online]. Available: `https://ntrs.nasa.gov/citations/19830001781`.

[55] S. Taamallah, "Small-Scale Helicopter Blade Flap-Lag Equations of Motion for a Flybarless Pitch-Lag-Flap Main Rotor," in *AIAA Modeling and Simulation Technologies Conference*, Portland, Oregon, United States, 2011.

[56] A. K. Shastry, M. Kothari, and A. Abhishek, "Generalized Flight Dynamic Model of Quadrotor Using Hybrid Blade Element Momentum Theory," *J. Aircr.*, vol. 55, no. 5, pp. 2162–2168, 2018. DOI: `10.2514/1.C034899`.

[57] C. Malpica, P. Suh, and C. Silva, "Flight dynamics conceptual design exploration of multi-rotor evtol," in 80th *Vertical Flight Society's (VFS) Annual Forum and Technology Display, Montréal, Québec*, 2024.

[58] D. Barcelos, G. Bramesfeld, and S. Waslander, "Prediction of the Flight Dynamics of Maneuvering Multirotor Aircraft," *Int. J. Aerosp. Eng.*, vol. 1, p. 2 850 269, 2024. DOI: `10.1155/2024/2850269`.

[59] G. Hoffmann, H. Huang, S. Waslander, and C. Tomlin, "Quadrotor Helicopter Flight Dynamics and Control: Theory and Experiment," in *AIAA Guidance, Navigation and Control Conference and Exhibit, Hilton Head, South Carolina*, 2007.

[60] K. Ferguson and D. Thomson, "Flight Dynamics Investigation of Compound Helicopter Configurations," *J. Aircr.*, vol. 52, no. 1, pp. 156–167, 2015. DOI: `10.2514/1.C034899`.

[61] U. Saetti, J. Enciu, and J. F. Horn, "Flight Dynamics and Control of an eVTOL Concept Aircraft with a Propeller-Driven Rotor," *J. Am. Helicopter Soc.*, vol. 67, no. 3, pp. 153–166, 2022. DOI: `10.4050/JAHS.67.032012`.

[62] K. Lu, C. Liu, C. Li, and R. Chen, "Flight Dynamics Modeling and Dynamic Stability Analysis of Tilt-Rotor Aircraft," *Int. J. Aerosp. Eng.*, vol. 1, p. 5 737 212, 2019. DOI: `10.1155/2019/5737212`.

[63] M. Miller and J. Narkiewicz, "Tiltrotor modelling for simulation in various flight conditions," *J. Theor. Appl. Mechanics.*, vol. 44, no. 4, pp. 881–906, 2006.

[64] W. Beitz, G. Pahl, J. Feldhusen, and K. H. Grote, *Engineering Design: A Systematic Approach.* Springer, 2014.

[65] International Civil Aviation Organization (ICAO), "Annex 16, Volume 1, Environmental Protection - Aircraft noise," Tech. Rep., 2017. [Online]. Available: `https://www.icao.int/environmental-protection/pages/reduction-of-noise-at-source.aspx`.

[66] M. Sripad and V. Viswanathan, "The promise of energy-efficient battery-powered urban aircraft," *Proceedings of the National Academy of Sciences*, vol. 118, no. 45, 2021. DOI: `10.1073/pnas.2111164118`.

[67] M. Shamiyeh, R. Rothfeld, F. Mazzeo, and H. M., "A performance benchmark of recent personal air vehicle concepts for urban air mobility," in 31st *Congress of the International Council of the Aeronautical Sciences*, Belo Horizonte, Brazil, 2018.

[68] G. Avanzini, E. de Angelis, and F. Giulietti, "Optimal cruise performance of a conventional helicopter," *J. Aerosp. Eng.*, vol. 236, no. 5, pp. 865–878, 2022. DOI: `10.1177/09544100211024091`.

[69] M. Gatti, F. Giulietti, and M. Turci, "Maximum endurance for battery-powered rotary-wing aircraft," *Aerosp. Sci. Technol.*, vol. 45, pp. 174–179, 2015. DOI: `10.1016/j.ast.2015.05.009`.

[70] G. Avanzini, E. L. de Angelis, and F. Giulietti, "Optimal performance and sizing of a battery-powered aircraft," *Aerosp. Sci. Technol.*, vol. 59, pp. 132–144, 2016. DOI: `10.1016/j.ast.2016.10.015`.

[71] A. Filippone, "Data and performances of selected aircraft and rotorcraft," *Prog. Aerosp. Sci.*, vol. 36, no. 8, pp. 629–654, 2000. DOI: `10.1016/S0376-0421(00)00011-7`.

[72] M. Costes, T. Renaud, and B. Rodriguez, "Rotorcraft simulations: a challenge for CFD," *Int. J. Comput. Fluid Dyn.*, vol. 26, no. 6–8, pp. 383–405, 2012. DOI: `10.1080/10618562.2012.726710`.

[73] R. J. Higgins, G. N. Barakos, S. Shahpar, and I. Tristanto, "A computational fluid dynamic acoustic investigation of a tiltwing evtol concept aircraft," *Aerosp. Sci. Technol.*, vol. 111, p. 106 571, 2021. DOI: `10.1016/j.ast.2021.106571`.

[74] R. Du Val and C. He, "FLIGHTLAB modeling for real-time simulation applications," *Int. J. Model. Simul. Sci. Comput.*, vol. 8, no. 4, p. 1 743 003, 2017. DOI: `https://doi.org/10.1142/S1793962317430036`.

[75] F. Mazzeo, M. D. Pavel, D. Fattizzo, G. Bertolani, E. de Angelis, and F. Giulietti, "Flight dynamic modeling and stability of a small-scale side-by-side helicopter for urban air mobility," *Aerosp. Sci. and Tech.*, vol. 148, p. 109 117, 2024. DOI: `10.1016/j.ast.2024.109117`.

[76] J. Li, B. Long, H. Wu, *et al.*, "Rapid evaluation model of endurance performance and its application for agricultural uavs," *Drones*, vol. 6, no. 8, p. 186, 2022. DOI: `10.3390/drones6080186`.

[77] M. Kotwicz Herniczek, D. Jee, B. Sanders, and D. Feszty, "Rotor blade optimization and flight testing of a small uav rotorcraft," *J. Unmanned Veh. Syst.*, vol. 7, no. 4, pp. 325–344, 2019. DOI: `10.1139/juvs-2017-0005`.

[78] W. Johnson, *Helicopter Theory.* Courier Corporation, 2012.

[79] D. Kunz, "Comprehensive rotorcraft analysis: Past, present, and future," in 46th *AIAA/ASME/ASCE/AHS/ASC Structures, Structural Dynamics and Materials Conference*, Austin, Texas, United States, 2005, p. 2244.

[80] R. Chen, Y. Yuan, and D. Thomson, "A review of mathematical modelling techniques for advanced rotorcraft configurations," *Prog. Aerosp. Sci.*, vol. 120, p. 100 681, 2021. DOI: `10.1016/j.paerosci.2020.100681`.

[81] J. Howlett, "UH-60A Black Hawk Engineering Simulation Program. Volume 1: Mathematical Model," Tech. Rep., 19081, NASA CR 166309, Document ID: 19840020737.

[82] S. Taamallah, "A flight dynamics helicopter UAV model for a single pitch lag flap main rotor," in 36th *European Rotorcraft forum*, Paris, France, 2010.

[83] 0. A. Bauchau and N. K. Kang, "A multibody formulation for helicopter structural dynamic analysis," *J. Am. Helicopter Soc.*, vol. 38, no. 2, pp. 3–14, 1993. DOI: `https://doi.org/10.4050/JAHS.38.2.3`.

[84] A. Savino, A. Cocco, A. Zanotti, M. Tugnoli, P. Masarati, and V. Muscarello, "Coupling mid-fidelity aerodynamics and multibody 540 dynamics for the aeroelastic analysis of rotary-wing vehicles," *energies*, vol. 14, no. 21, p. 6979, 2021. DOI: `10.3390/en14216979`.

[85] E. Quon, M. J. Smith, G. R. Whitehouse, and D. Wachspress, "Hierarchical Variable Fidelity Methods for Rotorcraft Aerodynamic Design and Analysis," in 67th *American Helicopter Society Annual Forum*, Virginia Beach, Virginia, United States, 2011.

[86] E. L. de Angelis, F. Giulietti, G. Rossetti, M. Turci, and C. Albertazzi, "Toward smart air mobility: Control system design and experimental validation for an unmanned light helicopter," *Drones*, vol. 7, no. 5, p. 288, 2023. DOI: `10.3390/drones7050288`.

[87] "Robinson R22." (2024), [Online]. Available: `https://en.wikipedia.org/wiki/Robinson_R22`.

[88] International Energy Agency (IEA). "Aviation - energy system." Accessed: 31 October 2024. (2024), [Online]. Available: `https://www.iea.org/energy-system/transport/aviation`.

[89] F. Mazzeo and G. Di Ilio, "Fuel cell hybrid electric propulsion system for a lightweight helicopter: Design and performance analysis in urban air mobility scenario," *Int. J. Hydrogen Energy.*, vol. 50, pp. 891–907, 2024. DOI: `https://doi.org/10.1016/j.ijhydene.2023.09.134`.

[90] J. G. Leishman, *Principles of Helicopter Aerodynamics.* Cambridge University Press, 2016.

[91] "Advanced Electric Motors." Accessed: 26 December 2024. (2024), [Online]. Available: https://www.h3x.tech/.

[92] L. Lohse-Busch, M. Duoba, K. Stutenberg, *et al.*, "Technology Assessment of a Fuel Cell Vehicle: 2017 Toyota Mirai," Argonne National Laboratory (ANL), Tech. Rep. ANL/ESD-18/12, 2018.

[93] M. N. Boukoberine, T. Donateo, and M. Benbouzid, "Optimized energy management strategy for hybrid fuel cell powered drones in persistent missions using real flight test data," *Trans. Energy Convers.*, vol. 37, no. 3, pp. 2080–2091, 2022. DOI: 10.1109/TEC.2022.3152351.

[94] S. Suewatanakul, A. Porcarelli, A. Olsson, *et al.*, "Conceptual Design of a Hybrid Hydrogen Fuel Cell/Battery Blended-Wing-Body Unmanned Aerial Vehicle - An Overview," *Aerosp.*, vol. 9, no. 5, p. 275, 2022. DOI: 10.3390/aerospace9050275.

[95] Y. Wang, D. F. Ruiz Diaz, K. S. Chen, Z. Wang, and X. C. Adroher, "Materials, technological status, and fundamentals of PEM fuel cells â A review," *Mater. Today*, vol. 32, pp. 178–203, 2020. DOI: 10.1016/j.mattod.2019.06.005.

[96] "U.S. DRIVE - Fuel Cell Technical Team Roadmap." Accessed: 26 December 2024. (2017), [Online]. Available: https://www.energy.gov/eere/vehicles/articles/us-drive-fuel-cell-technical-team-roadmap.

[97] "DOE Technical Targets for Onboard Hydrogen Storage for Light-Duty Vehicles." Accessed: 26 December 2024. (2019), [Online]. Available: https://www.energy.gov/eere/fuelcells/doe-technical-targets-onboard-hydrogen-storage-light-duty-vehicles.

[98] B. Samaniego, E. Carla, L. O'Neill, and M. Nestoridi, "High specific energy Lithium Sulfur cell for space application," *E3S Web of Conferences*, vol. 16, p. 08 006, 2017. DOI: 10.1051/e3sconf/20171608006.

[99] "Curti Zefhir." (2024), [Online]. Available: https://zefhir.eu/innovation/.

[100] "McDonnell XHJD-1 Whirlaway." (2015), [Online]. Available: https://modelplanes.de/u-s-navy/hubschrauber-u-s-navy/mcdonnell-xhjd-1-whirlaway-anigrand/.

[101] I. Raptis and K. Valavanis, *Linear and Nonlinear Control of Small-Scale Unmanned Helicopters.* Springer, 2011.

[102] J. Liu, R. Guan, Y. Yao, H. Wang, and L. Hu, "A novel comprehensive kinematic and inverse dynamic model for the flybar-less swashplate mechanism: Application on a small-scale unmanned helicopter," *Symmetry*, vol. 12, no. 11, 2020. DOI: 10.3390/sym12111849.

[103] S. Newman, "The helicopter – efficiency or efficacy?" *Aircr. Eng. Aerosp. Technol.*, vol. 78, no. 1, pp. 15–19, 2006. DOI: 10.1108/17488840610639636.

[104] M. Ishitobi, M. Nishi, and K. Nakasaki, "Nonlinear adaptive model following control for a 3-DOF tandem-rotor model helicopter," *Control. Eng. Pract.*, vol. 18, no. 8, pp. 936–943, 2010. DOI: 10.1016/j.conengprac.2010.03.017.

[105] . M. A. Peña, S. A. R. Paredes, J. S. V. Martínez, and Y. Aguilar-Molina, "A Laboratory Prototype Tandem Helicopter With Two Degrees of Freedom," *IEEE Access*, vol. 9, pp. 39 618–39 625, 2021. DOI: 10.1109/ACCESS.2021.3064568.

[106] J. L. Williams, "Directional Stability Characteristics of Two Types of Tandem Helicopter Fuselage Models," Tech. Rep., 1954, NTRS Research Center: Ames Research Center (ARC), Document ID: 19930083960.

[107] Y. Cao, G. Li, and Q. Yang, "Studies of trims, stability, controllability, and some flying qualities of a tandem rotor helicopter," *J. Aerosp. Eng.*, vol. 223, no. 2, pp. 171–177, 2009. DOI: 10.1243/09544100JAERO462.

[108] R. F. Stengel, J. R. Broussard, and P. W. Berry, "Digital flight control design for a tandem-rotor helicopter," *Automatica*, vol. 14, no. 4, pp. 301–312, 1978. DOI: 10.1016/0005-1098(78)90030-4.

[109] A. Dzul, T. Hamel, and R. Lozano, "Nonlinear control for a tandem rotor helicopter," *IFAC Proceedings Volumes*, vol. 35, no. 1, pp. 229–234, 2002.

[110] M. Rao, S. Biswas, B. Butz, and D. Miller, "Dynamic modeling and feedback control of a side-by-side tandem helicopter," in 5th *IEEE International Symposium on Intelligent Control*, Philadelphia, Pennsylvania, United States, 1990, pp. 780–785. DOI: `10.1109/ISIC.1990.128546`.

[111] J. Sagaga and S. Lee, "Acoustic predictions for the side-by-side air taxi rotor in hover," in *AIAA Aviation Forum*, San Diego, California, United States, 2023.

[112] F. Mazzeo, E. de Angelis, F. Giulietti, A. Talamelli, and F. Leali, "Performance Analysis and Conceptual Design of Lightweight UAV for Urban Air Mobility," *Drones*, vol. 8, no. 9, p. 507, 2024. DOI: `10.3390/drones8090507`.

[113] "UAV VTOL Herlea 200kg." (2015), [Online]. Available: `https://www.austars-model.com/uav-vtol-herlea-200kg-thrust-motor-bjo210s-combo-w400v160a-esc-1x-propeller-72-inch_g25277.html`.

[114] G. Avanzini, E. de Angelis, D. Fattizzo, and G. F, "Autorotation design and simulation for a small-scale helicopter," in 48th *European Rotorcraft Forum*, Winterthur, Switzerland, 2022.

[115] E. Fomaro, M. Cardone, V. D'Agostino, and A. Dannier, "An Aircraft Hybrid Electric Propulsion Model Experimentally Validated," in *2024 International Symposium on Power Electronics, Electrical Drives, Automation and Motion (SPEEDAM)*, Ischia, Italy: IEEE, pp. 1197–1203.

[116] N. Ivanov, S. Zhuravlev, O. Kharkina, *et al.*, "Electric Machines with High Specific Power," *Russian Electrical Engineering*, vol. 93, pp. 621–630, 2023.

[117] EMRAX. "Customized axial flux electric motors." Accessed: 31 May 2024. (2024), [Online]. Available: `https://emrax.com/`.

[118] Amprius. "Amprius Technologies Silicon Anode Batteries." Accessed: 22 November 2024. (2024), [Online]. Available: `https://amprius.com/`.

[119] K. Feng, M. Li, W. Liu, *et al.*, "Silicon-Based Anodes for Lithium-Ion Batteries: From Fundamentals to Practical Applications," *Small*, vol. 14, no. 1702737, 2018. DOI: `10.1002/smll.201702737`.

[120] J. Tang, "Progress in the application of silicon-based anode nanotechnology in lithium batteries," *International Conference on Ecological Protection and Environmental Chemistry (EPEC)*, vol. 553, p. 01 007, 2024. DOI: `10.1051/e3sconf/202455301007`.

[121] Y. Zhou, H. Zhao, and Y. Liu, "An evaluative review of the vtol technologies for unmanned and manned aerial vehicles," *Computer Communications*, vol. 149, pp. 356–369, 2020. DOI: `10.1016/j.comcom.2019.10.016`.

[122] R. W. Prouty, *Helicopter Performance, Stability, and Control.* R.E. Krieger Publishing Company, 1995.

[123] "Robinson R44." (2024), [Online]. Available: `https://en.wikipedia.org/wiki/Robinson_R44`.

[124] "Flying Basket FB3." (2024), [Online]. Available: `https://flyingbasket.com/fb3-order`.

[125] S. Vouros, I. Goulos, and V. Pachidis, "Integrated methodology for the prediction of helicopter rotor noise at mission level," *Aerosp. Sci. and Tech.*, vol. 89, pp. 136–149, 2019.

[126] K. Brentner and F. Farassat, "Helicopter Noise Prediction: The Current Status and Future Direction," *J. Sound Vib.*, vol. 170, no. 1, pp. 79–96, 1994. DOI: `10.1006/jsvi.1994.1047`.

[127] M. Gennaretti, J. Serafini, G. Bernardini, A. Castorrini, G. De Matteis, and G. Avanzini, "Numerical characterization of helicopter noise hemispheres," *Aerosp. Sci. and Tech.*, vol. 52, pp. 18–28, 2016, ISSN: 1270-9638. DOI: `10.1016/j.ast.2016.02.013`.

[128] F. Yunus, D. Casalino, F. Avallone, and D. Ragni, "Efficient prediction of urban air mobility noise in a vertiport environment," *Aerosp. Sci. Technol.*, vol. 139, p. 108 410, 2023. DOI: `10.1016/j.ast.2023.108410`.

[129] M. Barbarino, F. Petrosino, and A. Visingardi, "A high-fidelity aeroacoustic simulation of a VTOL aircraft in an urban air mobility scenario," *Aerosp. Sci. Technol.*, vol. 125, p. 107 104, 2022. DOI: `10.1016/j.ast.2021.107104`.

[130] W. E. Bausch, C. L. Munch, and R. G. Schlegel, *An experimental study of helicopter rotor impulsive noise.* Army Air Mobility Research and Development Laboratory, 1971.

[131] V. F. Kopiev, M. Y. Zaytsev, V. I. Vorontsov, S. A. Karabasov, and V. A. Anikin, "Helicopter noise in hover: Computational modelling and experimental validation," *Acoust. Phys.*, vol. 63, pp. 686–698, 2017. DOI: `10.1134/S1063771017060070`.

[132] B. Smith, F. Gandhi, and R. Niemiec, "A comparison of multicopter noise characteristics with increasing number of rotors," in 76th *Annual Forum of the Vertical Flight Society*, Virtual, 2020.

[133] J. Holden. "Fast-Forwarding to a Future of On-Demand Urban Air Transportation." Accessed: 8 August 2024. (2016), [Online]. Available: `https://uberpubpolicy.medium.com/fast-forwarding-to-a-future-of-on-demand-urban-air-transportation-f6ad36950ffa`.

[134] I. A. Abalakin, V. G. Bobkov, and T. K. Kozubskaya, "Numerical study of fuselage impact on acoustic characteristics of a helicopter rotor," *J. Supercomput.*, vol. 9, no. 4, pp. 100–113, 2022. DOI: `10.14529/jsfi220409`.

[135] J. Yin, "Investigation of rotor noise shielding effects by the helicopter fuselage in forward flight," *J. Aircraft*, vol. 56, no. 4, pp. 1677–1688, 2019. DOI: `10.2514/1.C035009`.

[136] H. S. Choi, E. T. Kim, D. I. You, and H. Shim, "Improvements in Small-scale Helicopter Rotor Modeling for the Real-Time Simulation of Hovering Flight," *Trans. Jpn. Soc. Aeronaut. Space Sci.*, vol. 54, no. 185+186, pp. 229–237, 2011. DOI: `10.2322/tjsass.54.229`.

[137] R. T. N. Chen, "A simplified rotor system mathematical model for piloted flight dynamics simulation," Tech. Rep., 1979, NASA Ames Research Center, Document ID: 19790015806. [Online]. Available: `https://ntrs.nasa.gov/citations/19790015806`.

[138] R. T. N. Chen, "Effects of primary rotor parameters on flapping dynamics," Tech. Rep., 1980, NASA Ames Research Center, Document ID: 19800006879. [Online]. Available: `https://ntrs.nasa.gov/citations/19800006879`.

[139] F. Mazzeo, M. D. Pavel, D. Fattizzo, E. de Angelis, and F. Giulietti, "Numerical Modeling, Trim, and Linearization of a Side-by-Side Helicopter in Hovering Conditions," *Aerosp.*, vol. 11, no. 11, p. 927, 2024. DOI: `10.3390/aerospace11110927`.

[140] D. A. Peters and N. Haquang, "Dynamic inflow for practical applications," *J. Am. Helicopter Soc.*, vol. 33, 1988.

[141] R. P. Coleman, "Theory of self-excited mechanical oscillations of helicopter rotors with hinged blades," Tech. Rep., 1957, NACA TN 3844, Document ID: 19930084623. [Online]. Available: `https://ntrs.nasa.gov/citations/19930084623`.

[142] J. C. Butcher, *Numerical methods for ordinary differential equations.* John Wiley & Sons, 2016.

[143] A. Batrakov, L. Garipova, A. Kusyumov, S. Mikhailov, and G. Barakos, "Computational fluid dynamics modeling of helicopter fuselage drag," *J. Aircr.*, vol. 52, no. 5, pp. 1634–1643, 2015. DOI: `https://doi.org/10.2514/1.C033019`.

[144] A. Filippone and J. A. Michelsen, "Aerodynamic drag prediction of helicopter fuselage," *J. Aircr.*, vol. 38, no. 2, pp. 326–333, 2001. DOI: `https://doi.org/10.2514/2.2765`.

[145] J. Y. Hwang, M. K. Jung, and O. J. Kwon, "Numerical study of aerodynamic performance of a multirotor unmanned-aerial-vehicle configuration," *J. Aircr.*, vol. 52, no. 3, pp. 839–846, 2015. DOI: `10.2514/1.C032828`.

[146] G. Gibertini, F. Auteri, G. Campanardi, C. Macchi, A. Zanotti, and A. Stabellini, "Wind-tunnel tests of a tilt-rotor aircraft," *Aeronaut. J.*, vol. 115, no. 1167, pp. 315–322, 2011. DOI: `10.1017/S0001924000005790`.

[147] G. D. Padfield, *Helicopter Flight Dynamics: The Theory and Application of Flying Qualities and Simulation Modelling.* John Wiley & Sons, 2008.

[148] J. Zhu, G. Xu, and Y. Shi, "An efficient method for helicopter fuselage shape optimization," *Aircr. Eng. Aerosp. Technol.*, vol. 95, no. 7, pp. 1069–1080, 2023. DOI: `10.1108/AEAT-06-2022-0152`.

[149] R. Amadio, "Analisi CFD delle azioni aerodinamiche sulla scocca di un drone birotore per diversi angoli di attacco e di sideslip," M.S. thesis, Alma Mater Studiorum Universitá di Bologna, Forlí, Italy, 2024.

[150] M. Pantieri, "Studio delle modalitá di semplificazione e meshing della fusoliera di un velivolo eVTOL per simulazioni CFD," M.S. thesis, Alma Mater Studiorum Universitá di Bologna, Forlí, Italy, 2024.

[151] V. Komornik and P. Loreti, *Fourier Series in Control Theory.* Springer, 2005.

[152] J. P. Corriou, *Numerical Methods and Optimization.* Springer, 2021.

[153] F. Mazzeo, D. Micheletto, A. Talamelli, and A. Segalini, "An experimental study on a wind turbine rotor affected by pitch imbalance," *energies*, vol. 15, no. 22, p. 8665, 2022. DOI: `https://doi.org/10.3390/en15228665`.

[154] R. Steijl, G. Barakos, and K. Badcock., "A framework for CFD analysis of helicopter rotors in hover and forward flight," *Int. J. Numer. Methods Fluids*, vol. 51, no. 8, pp. 819–847, 2006. DOI: `https://doi.org/10.1002/fld.1086`.

[155] L. Erickson, "Panel methods: An introduction," Tech. Rep., 1990, NASA TP 2995, Document ID: 19910009745.

[156] G. R. Hough, "Remarks on vortex-lattice methods," *J. Aircr.*, vol. 10, no. 5, pp. 314–317, 1973. DOI: `10.2514/3.44370`.

[157] J. Cook, "A strip theory approach to dynamic modeling of eVTOL aircraft," in *AIAA Science and Technology Forum and Exposition*, Virtual event, 2021.

[158] I. H. Abbott and A. E. V. Doenhoff, *Theory of Wing Sections, Including a Summary of Airfoil Data.* Dover Publications, 1959.

[159] L. A. Viterna and D. C. Janetzke, "Theoretical and experimental power from large horizontal-axis wind turbines," NASA Lewis Research Center, Cleveland, OH (United States), Tech. Rep., 1982. DOI: `10.2172/6763041`.

[160] W. Kruger, "On Wind Tunnel Tests and Computations Concerning the Problem of Shrouded Propellers," Tech. Rep., 1949, NTRS Research Center: Headquarters (HQ), Document ID: 20050241797. [Online]. Available: `https://ntrs.nasa.gov/citations/20050241797`.

[161] B. G. Jimenez and R. Singh, "Effect of Duct-Rotor Aerodynamic Interactions on Blade Design for Hover and Axial Flight," in 53rd *AIAA Aerospace Sciences Meeting*, Kissimmee, Florida, United States, 2015.

[162] A. I. Abrego, R. W. Bulaga, and M. Rutkowski, "Performance Study of a Ducted Fan System," Tech. Rep., 2002, NTRS Research Center: Ames Research Center (ARC), Document ID: 20020052231. [Online]. Available: `https://ntrs.nasa.gov/citations/20020052231`.

[163] B. N. Bourtsev and S. V. Selemenev, "Fan-in-Fin Performance at Hover Computational Method," in 26th *European Rotorcraft Forum*, The Hague, The Netherlands, 2000.

[164] M. Millidere, U. Karaman, S. Uslu, C. Kasnakoglu, and T. Cimen, "Newton-Raphson Methods in Aircraft Trim: A Comparative Study," in *AIAA Aviation Forum*, Virtual Event, 2020.

[165] B. L. Aponso, D. E. Johnston, and W. A. Johnson, "Identification of higher-order helicopter dynamics using linear modeling methods," *J. Am. Helicopter Soc.*, vol. 39, no. 3, pp. 3–11, 1994. DOI: `10.4050/JAHS.39.3.3`.

[166] J. Blackwell, R. A. Feik, and R. H. Perrin, "Identification of rotor dynamic effects in flight data," in 15th *European Rotorcraft Forum*, Amsterdam, The Netherlands, 1989.

[167] M. Diftler, "UH-60A helicopter stability augmentation study," in 14th *European Rotorcraft Forum*, Milan, Italy, 1988.

[168] S. R. Turnour and R. Celi, "Effects of Blade Flexibility on Helicopter Stability and Frequency Response," in 19th *European Rotorcraft Forum*, Cernobbio, Italy, 1993.

[169] G. C. Goodwin, S. F. Graebe, and M. E. Salgado, *Control system design.* Upper Saddle River: Prentice Hall, 2001.

[170] M. Baarspul, "A review of flight simulation techniques," *Prog. Aerosp. Sci.*, vol. 27, no. 1, pp. 1–120, 1990. DOI: `10.1016/0376-0421(90)90006-6`.

[171] H. M. Omar, "Hardware-In-the-Loop Simulation of Time-Delayed Anti-Swing Controller for Quadrotor with Suspended Load," *Appl. Sci.*, vol. 12, no. 3, p. 1706, 2022. DOI: `10.3390/app12031706`.

[172] I. H. B. Pizetta, A. S. Brandão, and M. Sarcinelli-Filho, "A Hardware-in-the-Loop Platform for Rotary-Wing Unmanned Aerial Vehicles," *J. Intell. Robot. Syst.*, vol. 84, pp. 725–743, 2016. DOI: `10.1007/s10846-016-0357-9`.

[173] M. Hancer, R. Bitirgen, and I. Bayezit, "Designing 3-DOF Hardware-In-The-Loop Test Platform Controlling Multirotor Vehicles," *IFAC - PapersOnLine*, vol. 51, no. 4, pp. 119–124, 2018. DOI: `10.1016/j.ifacol.2018.06.058`.

[174] B. Lundstrom, S. Chakraborty, G. Lauss, R. Bründlinger, and R. Conklin, "Evaluation of system-integrated smart grid devices using software- and hardware-in-the-loop," in *IEEE Power Energy Society Innovative Smart Grid Technologies Conference (ISGT)*, Minneapolis, Minnesota, United States, 2016.

[175] S. Demers, P. Gopalakrishnan, and L. Kant, "A generic solution to software-in-the-loop," in *MILCOM - IEEE Military Communications Conference*, Orlando, Florida, United States, 2007.

[176] G. Bertolani, D. Fattizzo, F. Mazzeo, G. F., and E. de Angelis, "Hardware-in-the-loop simulation for small-scale helicopter control systems assessment," in 50th *European Rotorcraft Forum*, Marseille, France, 2024.

[177] "Simulink Real-Time." Accessed: 20 December 2024. (2024), [Online]. Available: `https://it.mathworks.com/products/simulink-real-time.html`.

[178] "Embedded Coder." Accessed: 20 December 2024. (2024), [Online]. Available: `https://it.mathworks.com/products/embedded-coder.html`.

[179] "Aerospace Toolbox." Accessed: 20 December 2024. (2024), [Online]. Available: `https://it.mathworks.com/products/aerospace-toolbox.html`.

[180] "UAV Toolbox Support Package for PX4 Autopilots." Accessed: 20 December 2024. (2024), [Online]. Available: `https://it.mathworks.com/help/uav/px4-spkg.html`.